KINETIC AND SPECTROSCOPIC STUDIES OF COBALT- AND MANGANESE-SUBSTITUTED EXTRADIOL-CLEAVING HOMOPROTOCATECHUATE 2,3-DIOXYGENASES

A DISSERTATION
SUBMITTED TO THE FACULTY OF THE GRADUATE SCHOOL
OF THE UNIVERSITY OF MINNESOTA
BY

Andrew J. Fielding

IN PARTIAL FULFILLMENT OF THE REQUIREMENTS
FOR THE DEGREE OF
DOCTOR OF PHILOSOPHY

Professor Lawrence Que, Jr.

February 2013

Acknowledgements

I would like to thank all those who have helped me in my efforts here at graduate school at the University of Minnesota including: My advisors Professors Larry Que and John Lipscomb for their instruction and advice. I would also like to thank my comrades in the Que and Lipscomb labs, specifically Drs. Erik Farquhar, Van Vu, and Mike Mbughuni, and fellow graduate students Rahul Banerjee, Brent Rivard, and Anna Komor for their friendship and the time they spent helping me. I would also like to thank all the many postdoctoral research associates from the Que and Lipscomb labs who have taken time to talk to me about my chemistry including: Ass't Prof. Joseph Emerson, Dr. Elena Kovaleva, Ass't Prof. Tom Makris, Dr. Yuming Zhou, Ass't Prof. Aidan McDonald, Ass't Prof. Matthew Cranswick, Ass't Prof. Kathy Van Heuvelen, Dr. Williamson Oloo and Dr. Lisa Engstrom. I am also grateful for the generous support of the University of Minnesota Department of Chemistry, the University of Minnesota Chemical Biology Initiative and the National Institutes of Health.

I would also like to thank my parents Kurt and Patti Fielding who encouraged my interests in Science while growing up, where dinner table discussions regularly lead to referencing our copy of the *Encyclopedia Britannica*. I would also like to thank my many terrific chemistry and biology teachers throughout junior high, high school and college for making science fun and interesting as well as training me to think like a scientist. Finally I would like to give special thanks to my wife Meikjn and our kids for their support and giving my life and work meaning.

Abstract

Homoprotocatechuate (HPCA) 2,3-dioxygenase (HPCD) is an Fe(II)-dependent extradiol-cleaving dioxygenase, which oxidatively cleaves the aromatic C(2)-C(3) bond of its catecholic substrate. Here we compare the reactivity of Fe-HPCD with its Mn(II)- and Co(II)-substituted analogues. While Mn-HPCD exhibits steady-state kinetic parameters comparable to those of Fe-HPCD, Co-HPCD exhibits significantly higher K_M^{O2} and k_{cat} values. The high activity of Co-HPCD is surprising, given that cobalt has the highest standard M(III/II) redox potential of the three metals. These kinetic differences and the spectroscopic properties of Co-HPCD have proven to be useful in further exploring the unique O_2 activation mechanism associated with the extradiol dioxygenase family.

Employing the electron-poor substrate analogue 4-nitrocatechol (4NC), which is expected to slow down the rate of catechol oxidation, we were able to trap and characterize the initial O_2-adduct in the single-turnover reaction of 4-nitrocatechol by Co-HPCD. This intermediate exhibits an S = 1/2 EPR signal typical of low-spin Co(III)−superoxide complexes. Both the formation and decay of the low-spin Co(III)−superoxide intermediate are slow compared to the analogous steps for turnover of 4NC by native high-spin Fe(II)-HPCD, which is likely to remain high-spin upon O_2 binding. Possible effects of the observed spin-state transition upon the rate of O_2 binding and catechol oxidation are discussed.

Two transient intermediates were detected in the reaction of the [M-HPCD(4XC)] enzyme-substrate complexes (M = Mn or Co, and 4XC = 4-halocatechols, where X = F,

Cl, and Br) with O_2. The first intermediate (Co^{4XIC}Int1) exhibited an $S = 1/2$ EPR signal associated with an organic radical species. Based on the UV-Vis and EPR data, Co^{4XC}Int1 was assigned to a unique low-spin [Co(III)(4XSQ$^{\bullet}$)(hydro)peroxo] species where the semiquinone radical is localized onto C4 of the ring. M^{4XC}Int2 was observed to have a high-spin metal(II) center by EPR and exhibit intense chromophores similar to the independently synthesized halogenated quinones (4XQ). Based on the UV-Vis and EPR data, M^{4XC}Int2 is assigned to a [M(II)(4XQ)(hydro)peroxo] species. The M^{4XC}Int2 species were further characterized by resonance Raman spectroscopy. Resonance enhanced vibrations between 1350–1450 cm^{-1} suggest that M^{4XC}Int2 is a metal-semiquinone species, conflicting with the initial assignment of these intermediates as a quinone species. Based on the EPR and resonance Raman data, M^{4XC}Int2 might be assigned to a [M(II)(SQ$^{\bullet}$)$O_2^{\bullet-}$] diradical species.

Table of Contents

List of Tables

List of Figures

List of Schemes

Chapter 1

O_2 Activation and Substrate Oxidation Mechanisms of C-C Bond Cleaving Oxygenases and Oxidases

1.1 Introduction

Oxygenases and oxidases that oxidatively cleave the C-C bonds of their organic substrates must activate O_2 and then direct the oxidizing equivalents and generated reactive oxygen species in a chemo- and regioselective manner.[1-3] C-C bond cleaving oxygenases and oxidases catalyze a wide variety of important biochemical transformations. This group of enzymes can be subdivided into five classes, as shown in schemes 1.1–1.5. The first class consists of enzymes that catalyze the oxidative cleavage of aromatic C-C bonds, exemplified by the intra- and extradiol catechol cleaving dioxygenases[2, 4-9] (Scheme 1.1), which are key enzymes in the metabolism and biodegradation of aromatic compounds. In the second class are enzymes that cleave of C-C bonds of alkenes (Scheme 1.2), exemplified by carotenases.[10-12] These enzymes are important in the biosynthesis of pigments and odorous compounds of many plants and fruit from roses and carrots to lemons and saffron. In the third class are enzymes that cleave of aliphatic C-C bonds of hydroxyphosponates, diketones, vinyl alcohols and vicinal alcohols with concurrent C-H bond cleavage (Scheme 1.3) of an adjacent C-H bond. This class of enzymes is exemplified by 2-hydroxyethylphosponate dioxygenase[13-20] (HEPD) in the biosynthesis of the herbicide phosphinothricin.The fourth class of enzymes that carry out the oxidative decarboxylation of organic substrates (Scheme 1.4) like α-ketoglutarate by α-ketoglutarate-dependent dioxygenases[21-25] to generate an

Fe(IV)-oxo species. The fifth class is exemplified by aromatase, which catalyzes the demethylation and desaturation of testosterone to form estradiol (Scheme 1.5).[26-30] Remarkably, the mechanisms of these different classes of C-C bond cleaving oxygenases and oxidases proceed through a series of comparable steps to couple of the oxidation of the organic substrates with the reduction of O_2.

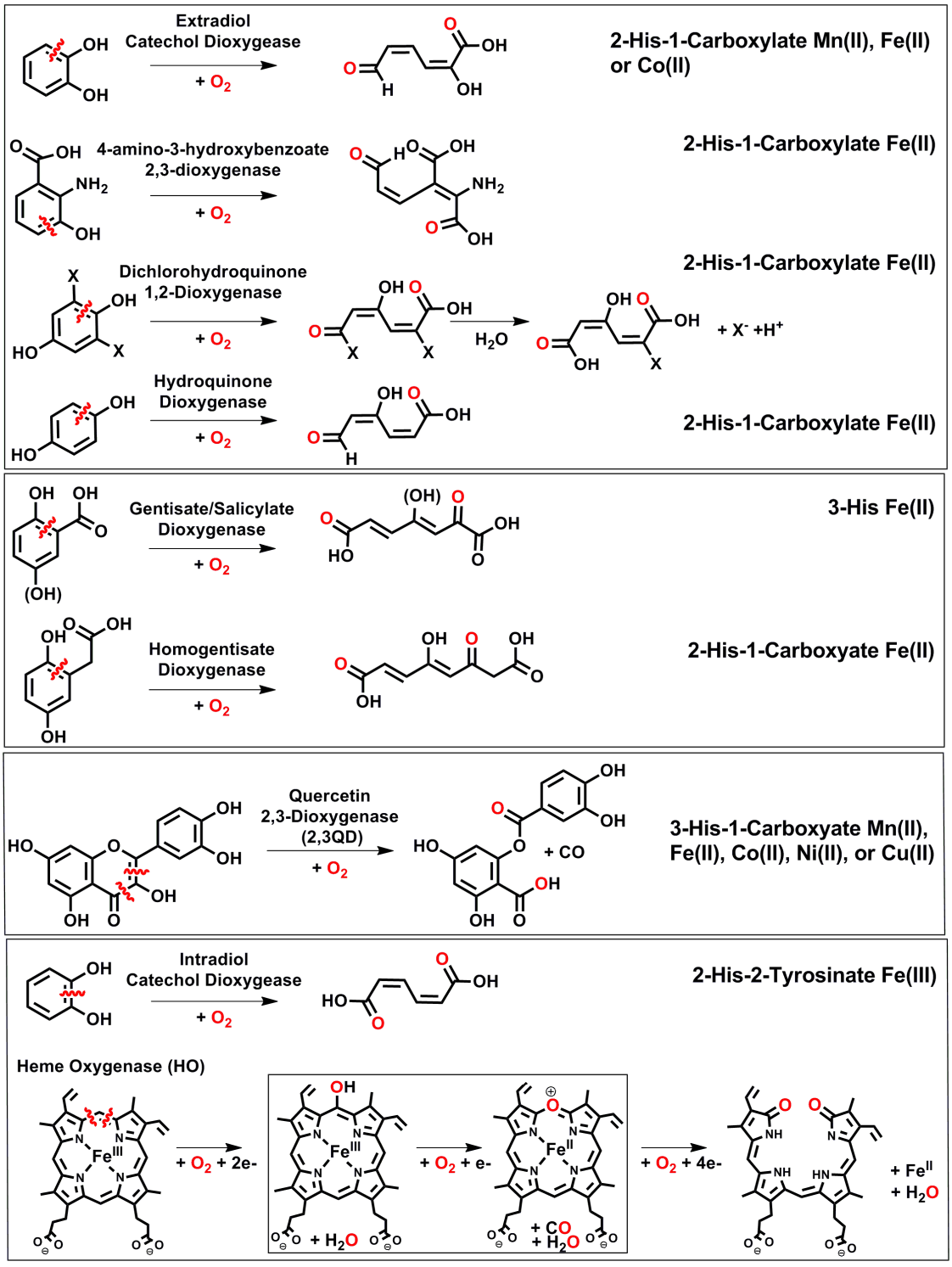

Scheme 1.1. Aromatic C-C bond cleaving dioxygenases including extradiol-cleaving catechol dioxygenases,[7] *o*-aminophenol dioxygenases,[31, 32] hydroquinone dioxygenases,[33-36] gentisate dioxygenases,[37, 38] quercetin, 2,3-dioxygenases.[39-43] intradiol cleaving dioxygenases,[4, 5] and heme oxygenase.[44-49]

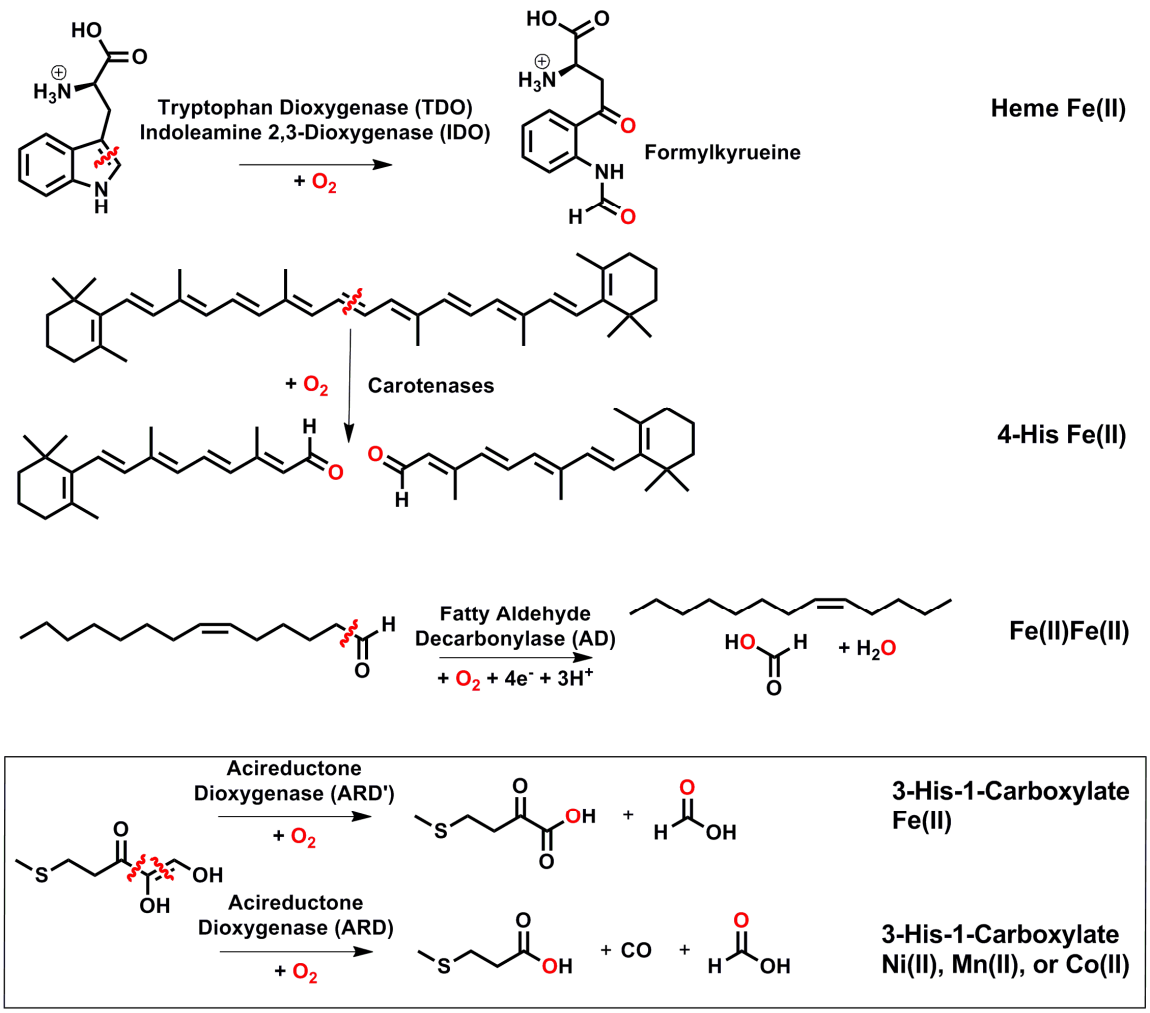

Scheme 1.2. C-C bond-cleaving oxygenases, which cleave the C-C bonds alkene substrates including: Tryptophan or indoleamine 2,3-dioxygenases,[50-58] carotenases,[10-12] fatty aldehyde decarbonylase,[59-65] and acireductone dioxygenases.[66-73]

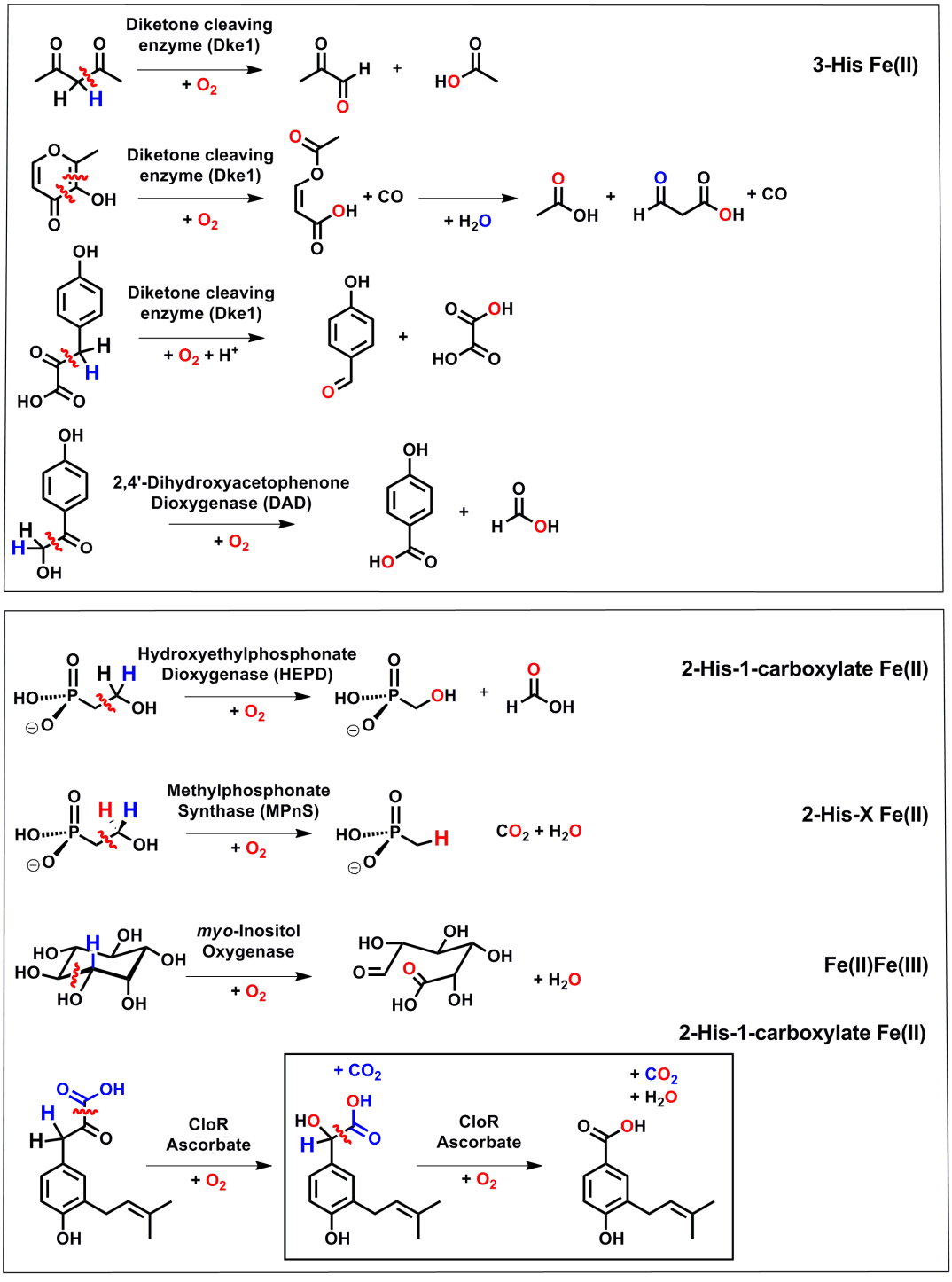

Scheme 1.3. Reactions of C-C bond-cleaving oxygenases, with concurrent C-H bond cleavage of an adjacent C-H bond. Including: diketone-cleaving enzyme (Dke1),[74-79] 2,4'-dihydroxyacetophenone dioxygenase (DAD),[80] 2-hydroxyethylphosphonate dioxygenase (HEPD),[13-20] methylphosphonate synthase (MPnS),[81] myo-inositol oxygenase (MIOX),[82-85] and CloR,[86] and alternate substrates[87, 88] cleaved by Dke1.

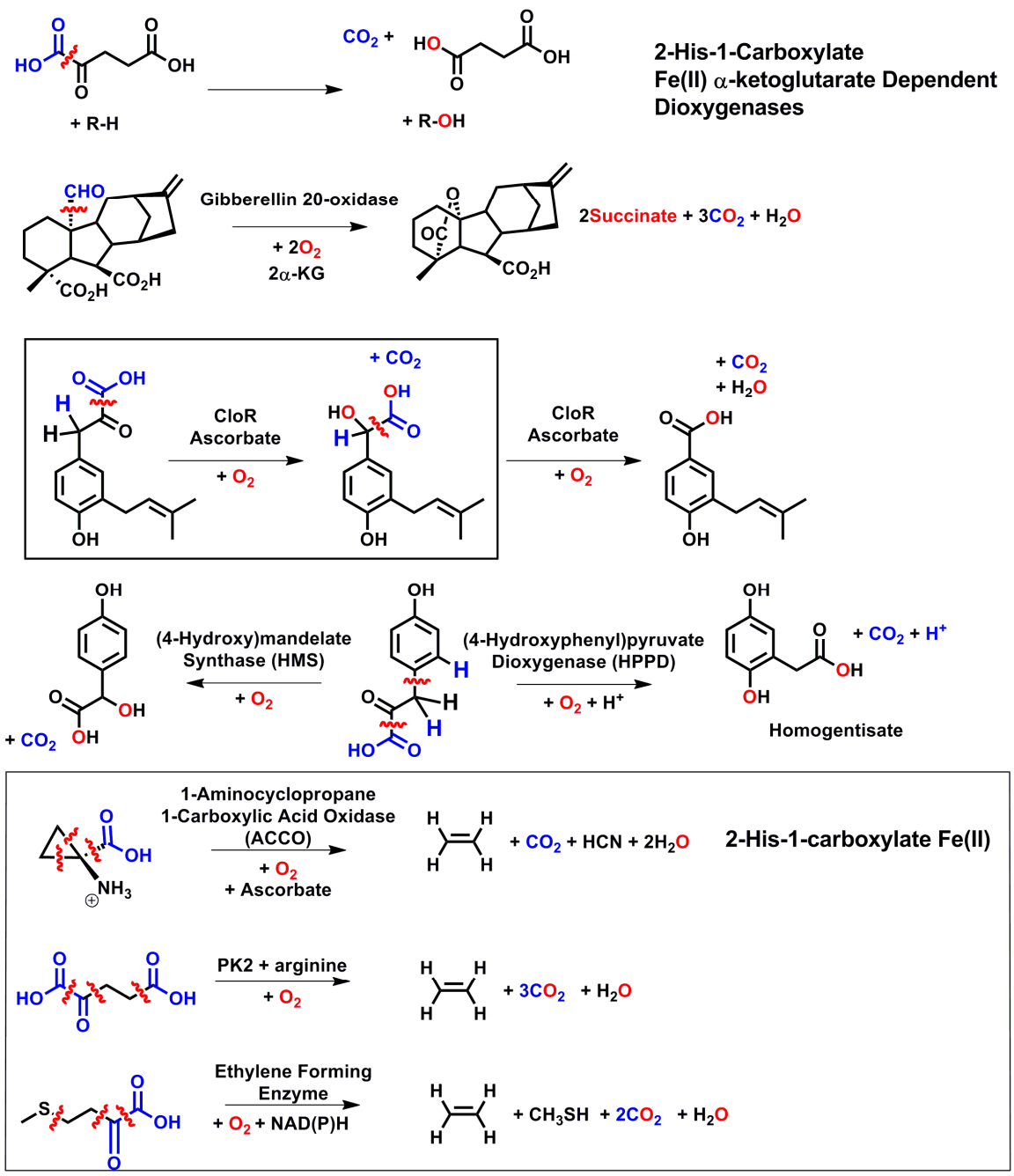

Scheme 1.4. C-C bond-cleaving oxygenases and oxidases that decarboxylate their organic substrates. Including: α-ketoglutarate dependent dioxygenases,[21-25] gibberellin 20-oxidase,[89-91] CloR,[86] (4-hydroxy)mandelate synthase (HMS),[92, 93] 4-hydroxyphenylpyruvate dioxygenase (HPPD),[92-96] 1-aminocyclopropane-1-carboxylic acid oxidase (ACCO),[97-106] PK2,[107, 108] and ethylene forming enzyme.[109-112]

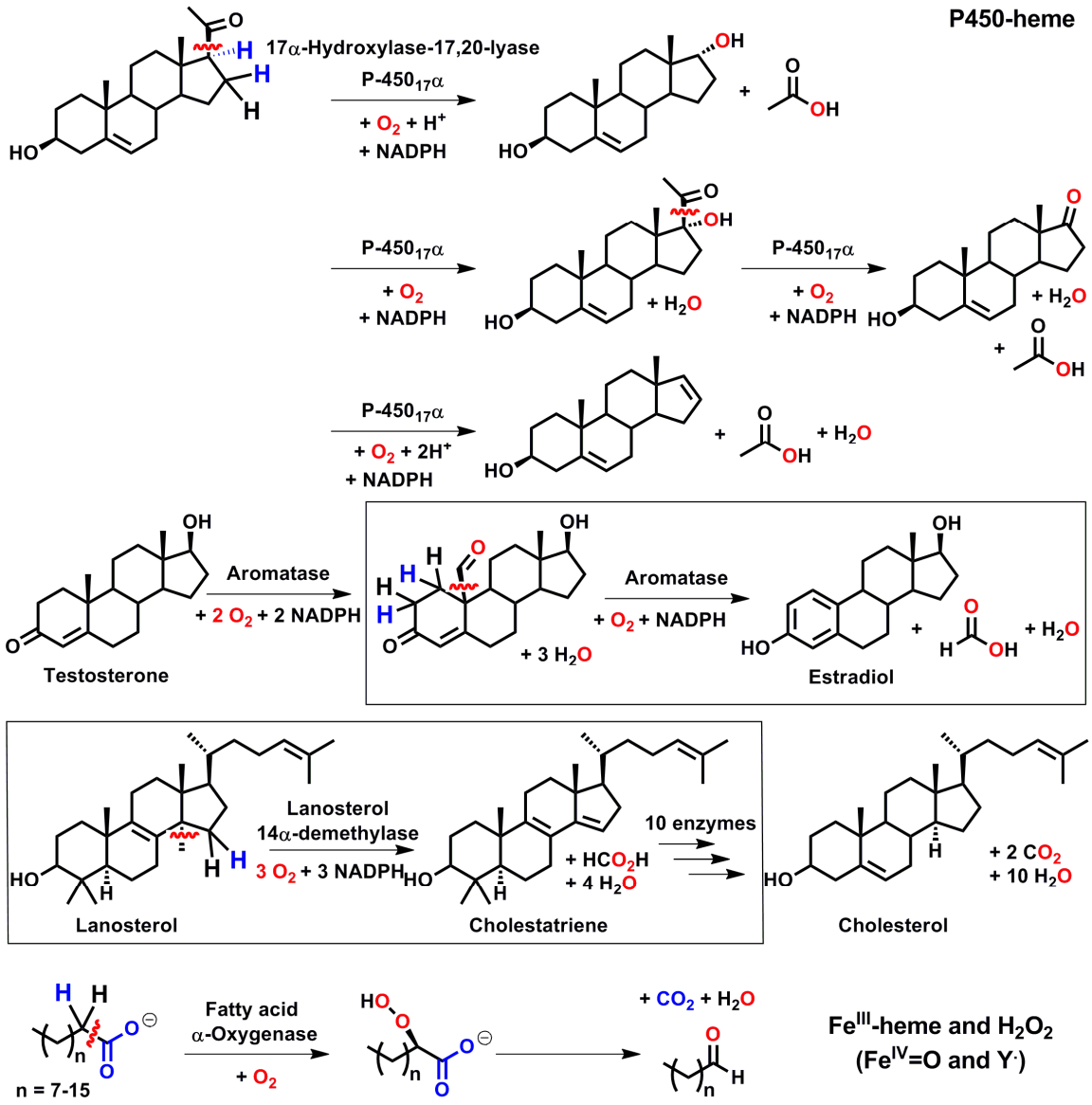

Scheme 1.5. Heme containing C-C bond-cleaving oxygenases, lanosterol 14α-demethylase[113] and aromatase,[28] which demethylate and desaturate their sterol substrates and fatty acid α-oxygenase,[114-116] which utilizes an Fe(III)-heme and H_2O_2 to generate a tyrosinyl radical in the decarboxylation of the fatty acid substrate to form an aldehyde product.

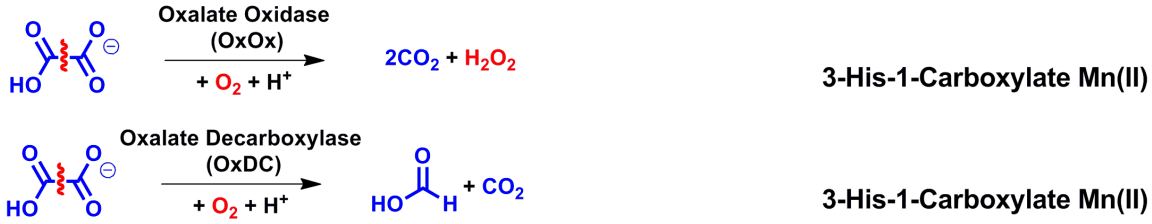

Scheme 1.6. Additional examples of C-C bond-cleaving enzymes that require O_2 including oxalate oxidase[117-119] and oxalate decarbonylase,[120-122]

1.2 Reductive O_2 activation and substrate oxidation.

As its name would suggest, O_2 (dioxygen) should be a strong oxidant. Yet the triplet ground state of O_2 makes it relatively unreactive and unselective in reactions with singlet organic substrates.[123, 124] This spin forbidden reaction requires either a large activation energy or a catalyst to lower the activation barrier. Enzymes catalyze the spin forbidden reaction by activating O_2, and/or the organic substrate to form some reactive pair. O_2 activation often entails the one- or two-electron reduction of O_2 to form a superoxo radical or peroxo species. The reductive activation of O_2 can be coupled to the oxidation of the organic substrate to form a substrate radical or electron deficient substrate species with which the reactive oxygen species can then react. Upon reacting the formed substrate-O_2 intermediate then undergoes a rearrangement step to break the O-O and C-C bonds of the substrates. The one-electron reduction of O_2 to superoxide is not a favorable reaction (-0.14 V vs SHE), so a good reducing agent is required.[123, 124] Many oxygenases utilize a redox-active paramagnetic metal cofactor like Fe(II) for reductive O_2 activation to generate an Fe(III)-$O_2^{\bullet-}$ species in a spin allowed manner.

1.3 Metal cofactor and active sites.

The active sites of C-C bond-cleaving dioxygenases and oxidases display a variety of metal cofactor binding sites (Figure 1.1). These active sites are classified here according to the metal cofactor and its coordinating protein amino acid residues. Mononuclear nonheme-Fe(II) binding sites motifs include: The 2-His-1-carboxylate (glutamate or aspartate) facial triad[3, 125] found in the extradiol catechol dioxygenases, α-ketoglutarate dependent dioxygenases[126] and 1-aminocyclopropane 1-carboxylic acid oxidase[97]

(ACCO). The 3-His binding motif is found in gentisate/salicylate dioxygenases and the diketone-cleaving enzyme[127] (Dke1) and the 4-His binding site is found in carotenases.[128] These metal binding motifs have basic histidine donors and anionic carboxylate ligands in some cases. The histidine and carboxylate ligands are thought to lower the redox potential of the metal center for initial reductive O_2 binding. Additionally, the facial coordination of the protein ligands leaves several *cis*-labile solvent sites to which the substrate and/or O_2 can coordinate. Binding of the organic substrate to the metal center can result in the displacement of the remaining solvent molecules. In this way the enzyme can control O_2 binding and activation, by only generating reactive oxygen species in the presence of the substrate. Similarly, the Fe(II)-heme containing tryptophan and indoleamine dioxygenases[129] regulate O_2 binding by displacing the labile distal solvent only upon substrate binding in the adjacent substrate binding pocket.

Some C-C bond-cleaving dioxygenases and oxidases like the extradiol catechol dioxygenases and quercetinase dioxygenases can incorporate or be substituted with other divalent first row transition metals other than Fe(II), including Mn(II), Co(II), Ni(II) and Cu(II) to produce active enzymes.[41, 68, 70, 130, 131] For the acireductone dioxygenases (Fe-ARD' and Ni-ARD) the metal cofactor present even affects the regioselectivity of the C-C bond cleaved (Scheme 1.1).[68, 70]

In contrast to the M(II)-extradiol-cleaving catechol dioxygenases, the intradiol catechol dioxygenases employ an Fe(III) center ligated by two histidines and two tyrosinates as protein ligands. The difference in metal oxidation state of the intra- and extradiol catechol dioxygenases is thought to result in an opposite mechanism of substrate activation. For the extradiol dioxygenases O_2 reduction by the Fe(II) center to

form an Fe(III)-$O_2^{\bullet-}$ species is followed by catechol oxidation to form a Fe(II)-$SQ^{\bullet}$-$O_2^{\bullet-}$ diradical pair has been proposed.[7] In the intradiol dioxygenases the order is reversed, such that the catechol is first activated by being oxidized by the Fe(III) center to form an Fe(II)-$SQ^{\bullet}$ radical species with which O_2 then reacts.[4]

Additional C-C bond-cleaving P450-like enzymes that employ Fe(III)-heme centers include aromatase,[28] 17α-hydroxylase-17,20-lyase[113] (Scheme 1.5), and fatty acid α-oxygenase[132] (Scheme 1.6). These enzymes require additional reducing equivalents or utilize H_2O_2 to generate a high valent-oxo species and/or tyrosine radical, to initiate substrate oxidation.

Nature has also been found to utilize nonheme diiron active sites for C-C bond cleaving enzymes. Myo-inositol oxygenase[82] (MIOX) has a unique mixed valiant diiron Fe(II)Fe(III) active site to which the inositol substrate coordinates to the Lewis acidic Fe(III) center while reductive O_2 activation occurs at the Fe(II) center. Another diiron enzyme fatty aldehyde decarbonylase[133] (AD) (Scheme 1.6) utilizes a diiron Fe(II)Fe(II) active site expected to generate an Fe(III)Fe(III)-peroxo species upon reductive O_2 activation.

Oxalate oxidase[117] (OxOx) and oxalate decarbonylase[122, 134] (OxDC) (Scheme 1.6) are Mn(II)-dependent enzymes with the Mn(II) bound by a 3-His-1-carboxylate (glutamate) combination of amino acid residues. Oxalate oxidase reduces O_2 by two electrons to H_2O_2 and cleaves the C-C bond of oxalate to form two equivalents of CO_2. Oxalate decarbonylase utilizes O_2 as a catalyst to generate a substrate radical, which rearranges to cleave the C-C bond of oxalate to form formic acid and carbon dioxide.

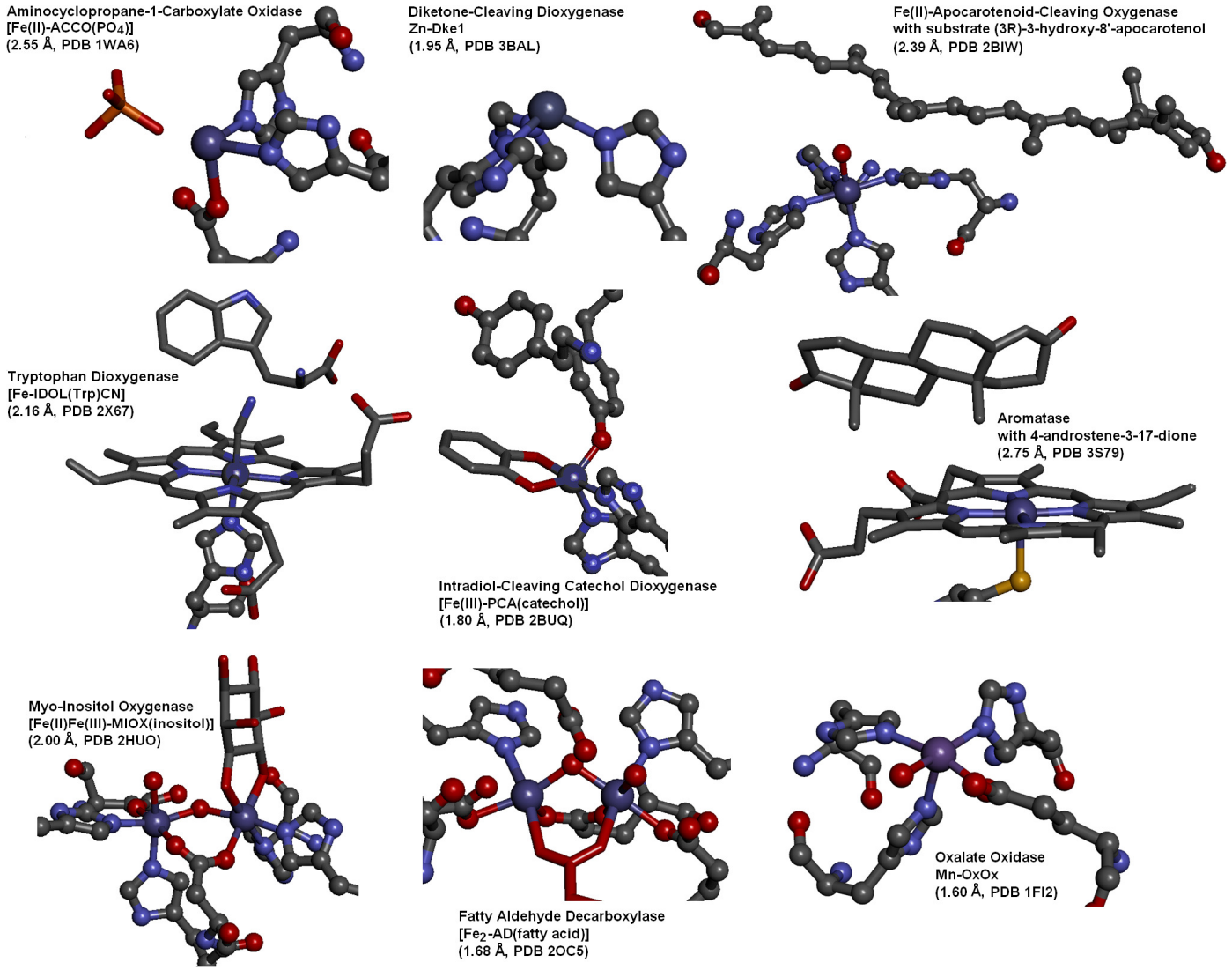

Figure1.1. Crystal structures of metal active sites of C-C cleaving dioxygenases and oxidases.[82, 97, 113, 117, 127-129, 133, 135, 136]

1.4 Common and divergent mechanistic themes.

In general C-C bond-cleaving dioxygenases and oxidases proceed through similar catalytic mechanisms (Scheme 1.7), which differ mainly by the type of reaction catalyzed (i.e. oxidase, monooxygenase or dioxygenase chemistry). The mechanisms often include but are not limited to the following steps and not necessarily in the following order: 1) substrate binding, 2) O_2 binding or reductive O_2 activation, 3) organic substrate activation or oxidation, 4) additional O_2 reduction and substrate oxidation steps to form a reactive pair 5) formation of an alkylperoxo or (hydro)peroxo intermediate,[7, 11, 18, 23, 58, 120] 6) rearrangement of the alkylperoxo or (hydro)peroxo intermediate by either a heterolytic O-O and C-C mechanism or homolytic O-O and C-C bond resulting in the formation of an Fe(II)-hydroxide, Fe(III)-hydroxide or Fe(IV)-oxo intermediate, 7) hydrolysis of organic products and release.[38, 75] The following sections will discuses these catalytic steps in further detail with schemes drawn from the proposed mechanisms of different C-C bond cleaving oxygenases and oxidases.

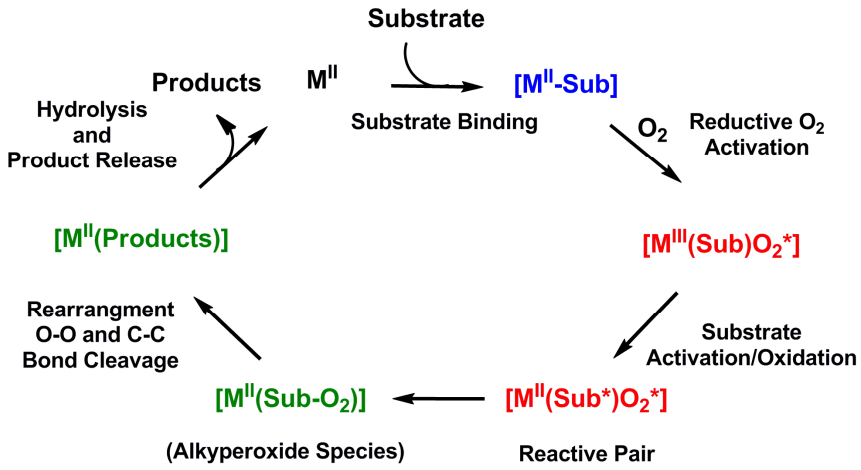

Scheme 1.7. Common catalytic cycle for C-C bond-cleaving dioxygenases and oxidases.

1.4.1 Organic substrate binding and activation. Binding of substrates and organic cofactors to the metal center or substrate binding pocket adjacent to the metal center can

prime the metal center for reductive O_2 activation by displacing coordinating solvent water molecules. Substrate binding can also lower the redox potential of the metal center for reductive O_2 activation by replacing the neutral water molecules with anionic donors of the coordinating substrate/cofactor.[125] Furthermore, binding of the substrate to the Lewis acid metal cofactor can activate the substrate for oxidation by deprotonating the donor alcohol groups and lowering the redox potential of the organic substrate.[125] Binding of the organic substrate to the Lewis acid metal cofactor can also promote keto-enol tautomerization of the substrate as proposed in the mechanisms of diketone-cleaving enzyme (Dke1), 2,4-dihydroxyacetophenone dioxygenases (DAD) and in the auto-oxidation of meso-hydroxyheme.[44, 47, 78-80, 87, 137] Additionally, binding of the organic substrate and O_2 to the metal active site in the ternary complex juxtaposes the two substrates with the correct alignment to react in a stereo- and regio-specific manner. Finally, binding of both the organic substrate and O_2 to metal center can allow the coupling of O_2 reduction to substrate oxidation by electron transfer via the metal center.[7]

1.4.2 Reductive O_2 activation and substrate oxidation. Reduction of O_2 by either one or two electrons to form the reactive oxygen species superoxide or peroxide, respectively, can proceed via several different mechanisms. If the organic substrate is easily oxidized (or a strong reducing agent) substrate oxidation and O_2 reduction can proceed without an inorganic catalyst by either a stepwise or concerted mechanism (Scheme 1.8). In a step-wise mechanism, O_2 is first reduced by outer sphere electron transfer from the substrate to O_2 to form a substrate radical and superoxide diradical pair. Pairing of the two radicals species results in the formation of the C-O bond of an alkylperoxide intermediate as has been proposed for 1H-3-hydroxy-4-oxoquinaldine 2,4-dioxygenase (Hod)

(Scheme 1.9).[138, 139] Alternatively, direct two-electron reduction of O_2 by nucleophilic attack from an electron rich substrate or cofactor in a concerted fashion (Scheme 1.8) would also yield an alkylperoxide species without the need of a metal cofactor catalyst. The proposed mechanisms of ranilla luciferase monooxygenase,[140] coproporphyrinogen oxidase (CPO),[141] and Baeyer-Villiger monooxygenase[139, 142, 143] are thought to proceed through concerted nucleophilic attack of the organic substrate on O_2 (Scheme 1.9).[144] Bayer-Villiger monooxygenase utilizes NADH as the reductant to form an alkylperoxo species that then attacks the carbonyl of the ketone substrate to form a bridging alkylperoxo species.[142, 144, 145]

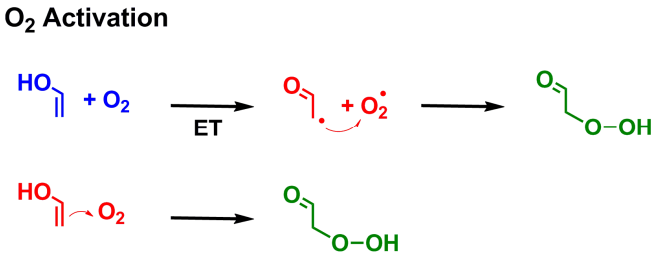

Scheme 1.8. Stepwise and concerted mechanism for O_2 activation and substrate oxygenation by organic molecules.

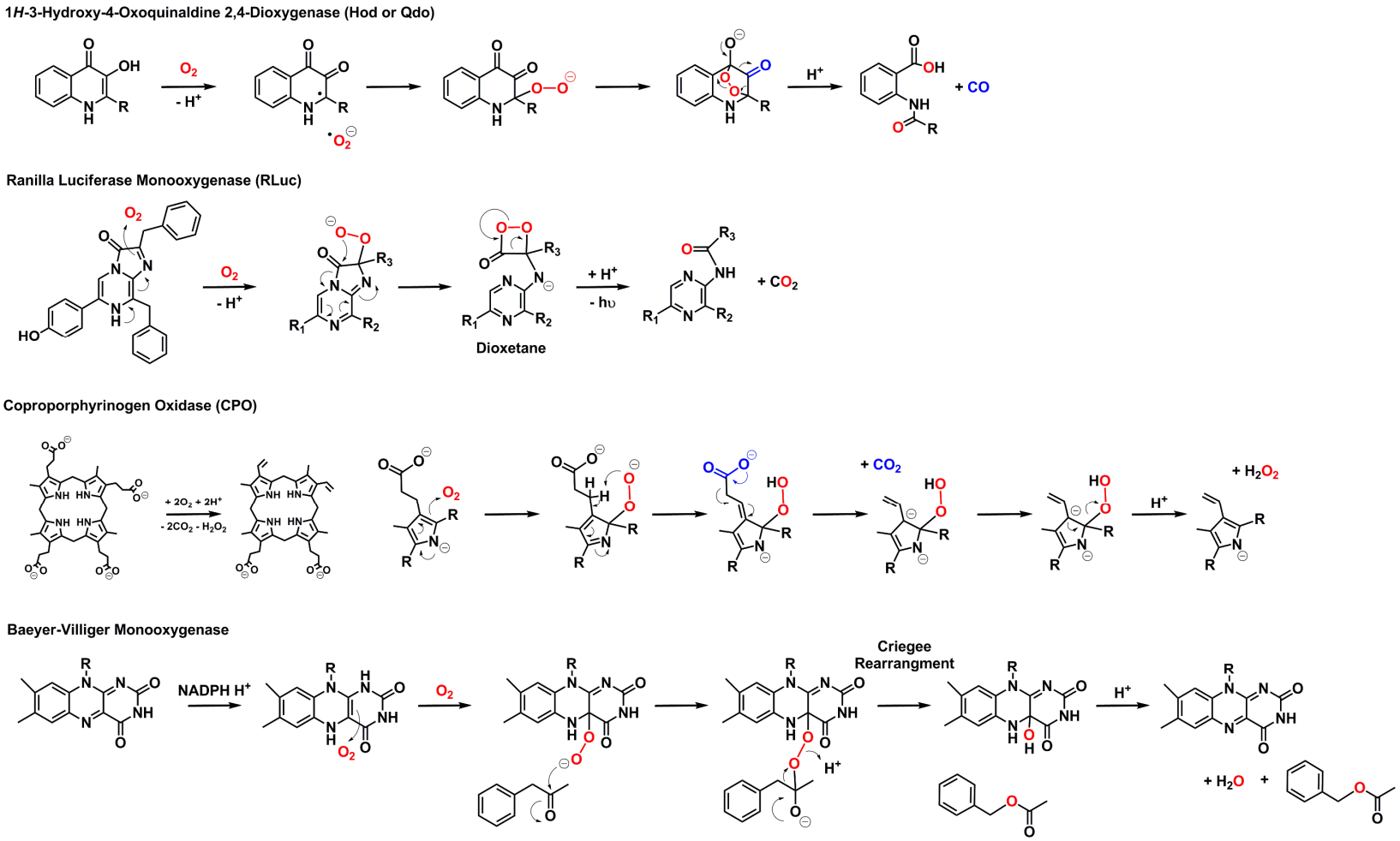

Scheme 1.9. Proposed mechanism for non metal cofactor C-C bond-cleaving oxygenases and oxidases.[138-142, 145-147]

1.4.3 Reductive O_2 activation by a metal cofactor. Similarly, metal catalyzed reductive O_2 activation by Fe(II) (Scheme 1.10) can proceed by either stepwise or concerted mechanisms. In a stepwise mechanism, O_2 is reduced via an Fe(II) center to form an Fe(III)substrate-superoxide intermediate followed by oxidation of the substrate to form a diradical pair. In a concerted mechanism the electron transfers from the substrate to the O_2 via the metal center, which may not necessarily require a "redox active" metal center to form a reactive diradical pair.[7] Further reduction of the Fe(III)-$O_2^{\bullet-}$ species by the metal center or an external reducing agent yields an Fe(IV) or Fe(III)-(hydro)peroxo species respectively.[23, 92] Homo- or heterolytic O-O bond cleavage of the Fe(III)-peroxo species, can yield high-valent Fe(IV)[54, 100, 101] and Fe(V)-oxo.[30, 148] species, respectively. Alternatively, the metal center may act solely as a Lewis acid to coordinate O_2 to position it near the bound substrate.[50, 57]

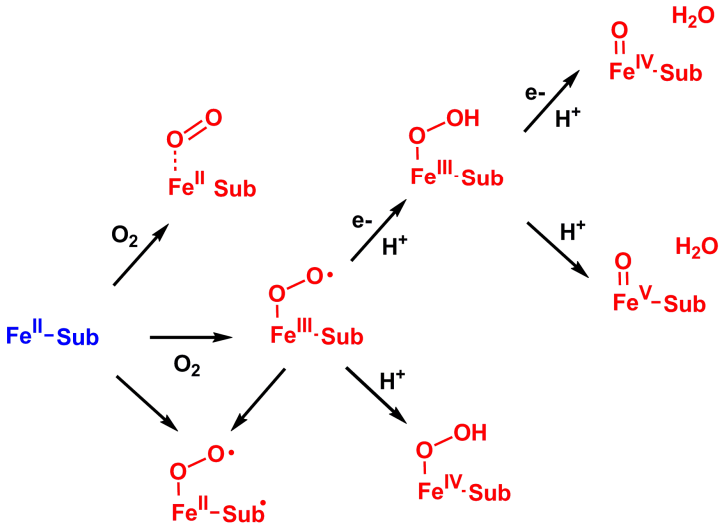

Scheme 1.10. Generic mechanisms for reductive O_2 activation and substrate oxidation at a metal cofactor.

1.4.4 Mechanism of substrate oxidation. For oxygenases O_2 is ultimately reduced by 4e- in the products. The mechanism of substrate oxidation differs mainly by the type of

substrate C-C bonds cleaved or oxidized during the reaction (i.e. aromatic, alkene, aliphatic C-C bonds). Some reactions also require the concurrent C-H bond cleavage of adjacent C-H bond,[81, 105] or loss of acidic C-H, N-H or O-H protons upon substrate binding or oxidation.[68, 79] Mechanisms of substrate oxidation (Scheme 1.11) can be classified as either electron transfer (ET), proton-coupled electron transfer (PCET) or hydrogen atom transfer/abstraction (HAT) reactions. Oxidation of the organic substrate by electron transfer include: 1) electron transfer from the substrate to an oxidized metal center, 2) outer sphere electron transfer from the substrate to O_2,[68] 3) electron transfer from the substrate to O_2 via the metal center,[7] or 4) further oxidation of a substrate radical by an Fe(III)-$O_2^{\bullet-}$ or Fe(III)-peroxide species. Proposed substrate oxidation mechanisms by proton-coupled electron transfer (Scheme 1.11) proceed by electron transfer to either the oxidized metal center and/or superoxide with proton transfer to an active site base.[1, 7] Oxidation of the substrate can also be accomplished by hydrogen atom abstraction resulting in both the cleavage of a C-H, N-H or O-H bond and simultaneous oxidation of the substrate Substrate oxidation by hydrogen atom abstraction have been proposed with HAT by an Fe(III)-$O_2^{\bullet-}$,.[81, 105] concurrent with homolytic O-O bond cleavage of an Fe(III)-(hydro)peroxide,[97] by a high-valent Fe(IV)-oxo[54, 100, 101] or an Fe(V)-oxo, [30, 148]. Lastly, hydrogen atom abstraction from an active site tyrosine by a high-valent Fe-oxo species can generate a tyrosyl radical species, which can then oxidize the organic substrate by a second hydrogen atom transfer step.[114-116]

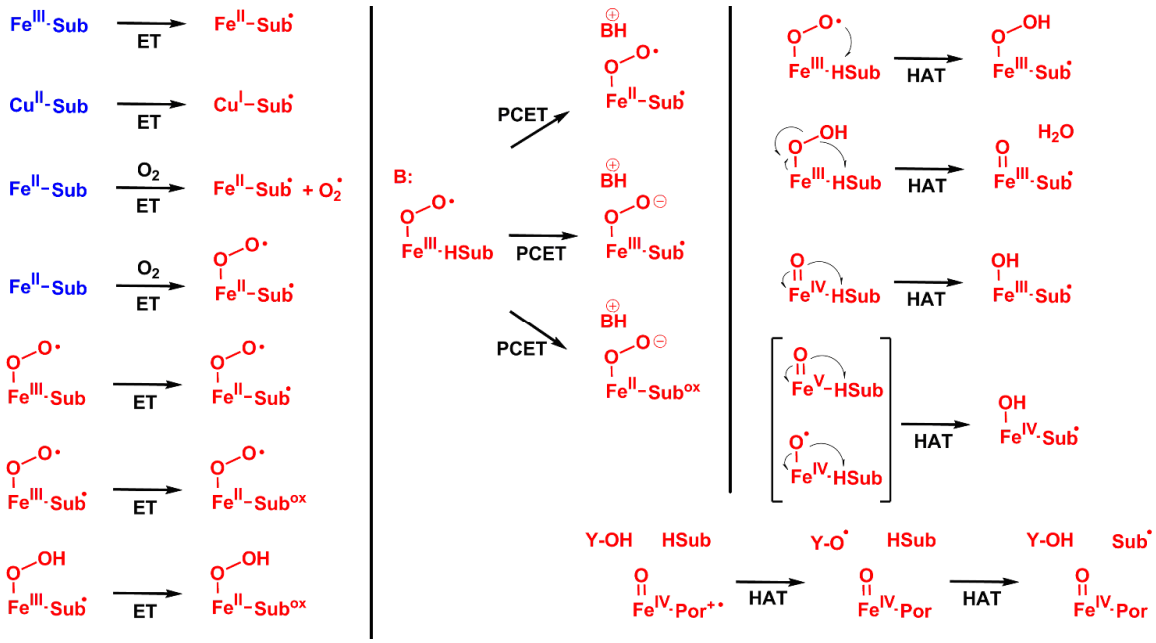

Scheme 1.11. General mechanisms of substrate oxidation/activation at a metal center by electron transfer (ET),[4, 5] proton-coupled electron transfer (PCET),[7] or hydrogen atom transfer/abstraction (HAT)[81, 105] to form a reactive O_2* and substrate* pair.

1.4.5 Reactive pairs. Here we will refer to the activated substrate* and O_2* species formed upon substrate binding or oxidation and/or reductive O_2 activation as the reactive pair. The reactive pair often reacts to form the C-O bond of an alkylperoxo species. Proposed reactive pairs differ mainly by the redox state of the two substrates and metal cofactor prior to reacting.

1.4.6 Formation of an alkylperoxo or (hydro)peroxo intermediate. A (hydro)peroxo or alkylperoxo species of some sort is formed in the proposed mechanism (Scheme 1.12) of all the C-C bond-cleaving dioxygenases and oxidases. In the peroxide intermediate, the double bond of O_2 has been reduced to a single bond en route to O-O bond cleavage. These peroxo species take the form of either Fe(II, III, IV)-(hydro)peroxides, which undergo O-O homolysis or heterolysis. Other proposed mechanisms lead to the formation of terminal alkylperoxo species via peroxylation[11, 12, 42] of an organic radical by an

Fe(III)(hydro)peroxo. Bridging alkylperoxo species (Fe-O-O-Sub) can form from the attack of an organic substrate radical by an Fe-$O_2^{\bullet -}$[149] or nucleophilic attack of the carbonyl of the substrate by an Fe-peroxo species.[18] Other proposed alkylperoxo species included dioxetane[12] and 1,2-dioxolane-4-one[41, 42, 68] intermediates.

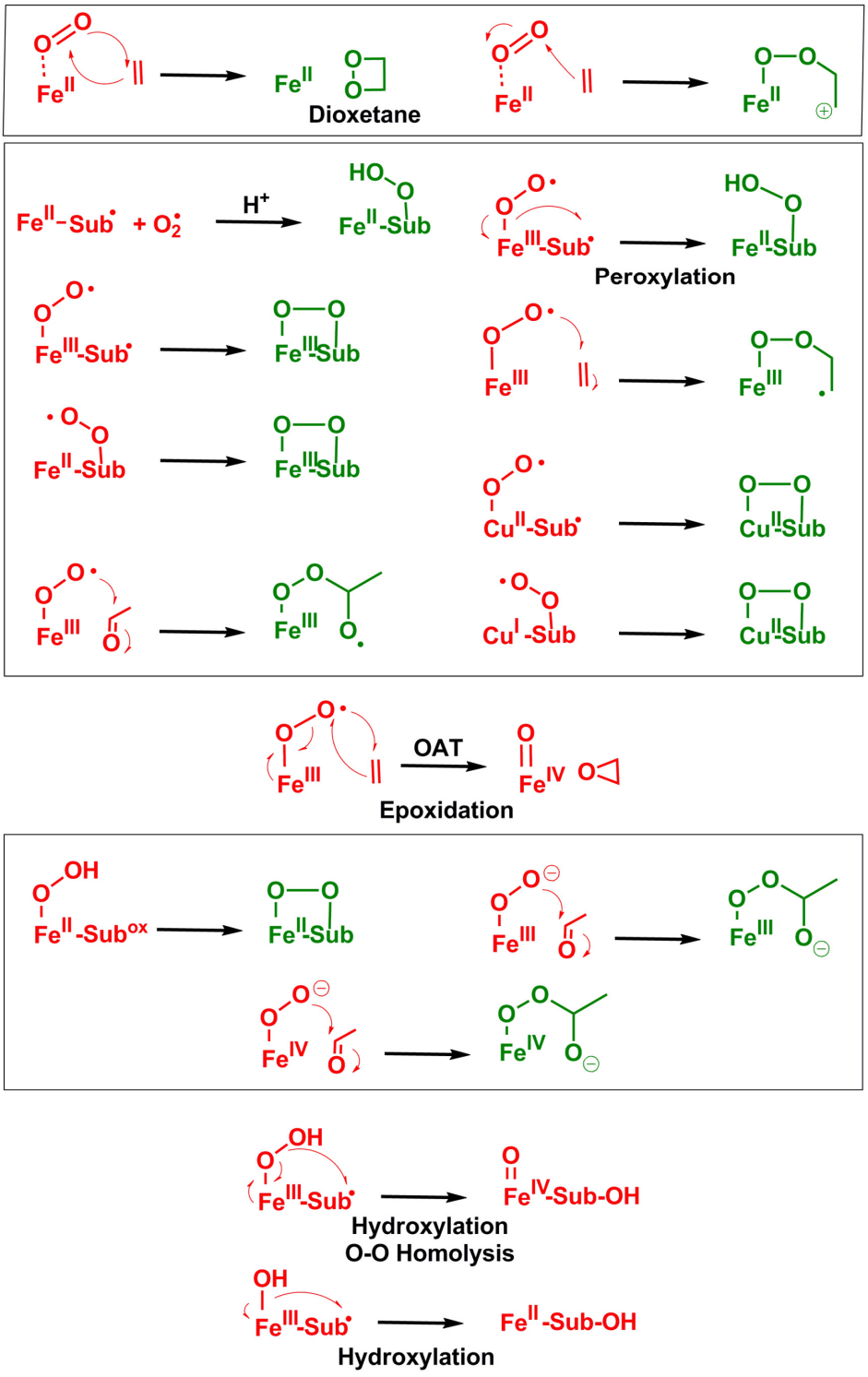

Scheme 1.12. General mechanisms for reaction between reactive O_2* and substrate* pairs (red) to form C-O bonds of alkylperoxide, epoxide, and hydroxylated products from proposed mechanisms of C-C bond-cleaving dioxygenases and oxidases.[11, 12, 18, 41, 42, 68, 149]

1.4.7 Rearrangement of the alkylperoxo or (hydro)peroxo intermediate. The proposed mechanisms of C-C bond cleavage by dioxygenases and oxidases are often initiated by or are concurrent with O-O bond cleavage of a peroxo or an alkylperoxo species. Proposed O-O and C-C bond cleavage mechanisms proceed by either heterolytic O-O and C-C bond cleavage[4, 9] or by homolytic O-O bond cleavage followed by C-C bond homolysis in a radical rearrangement mechanism.[150, 151]

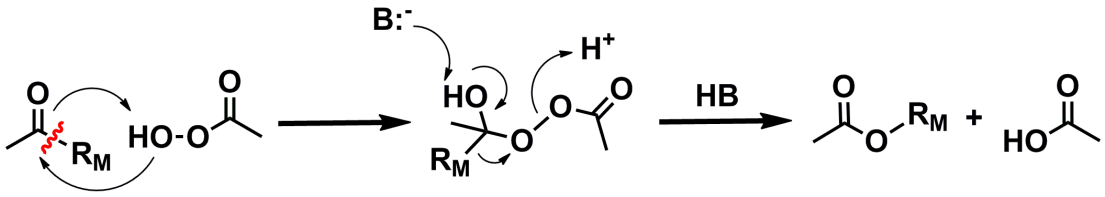

Scheme 1.13. Baeyer-Villiger Oxidation or "Criegee rearrangement" showing O-O and C-C bond cleavage with alkyl migration to form ester product.

Heterolytic O-O and C-C bond cleavage mechanisms have been proposed for dioxetane,[12] 1,2-dioxolene,[152] and terminal[102] or bridging[28, 119] peroxide intermediates as illustrated in Scheme 1.14. Heterolytic O-O bond cleavage with simultaneous C-C bond cleavage of bridging alkylperoxo intermediates may proceed through a Baeyer-Villiger oxidation mechanism also referred to as a "Criegee rearrangement" like mechanism (Scheme 1.13) due to its similarity to the Criegee rearrangement mechanism of primary ozonoides in the ozonolysis of olefins.[153, 154] The Criegee rearrangement may proceed via an alkyl or acyl migration of a C-C bond into the bridging peroxide to form an ester, or an anhydride intermediate species, respectively (Scheme 1.14). Furthermore, alkyl migration has been proposed to precede via either a π or σ mechanism.[4] A π-participation mechanism can occur by migration of the π bond of an adjacent double bond into the bridging peroxide to form an epoxide cation intermediate, which then opens to form an

ester. In the Criegee rearrangement mechanism protonation of the bridging peroxide at the proximal O is expected to aid in O-O bond heterolysis.

Homolytic O-O bond cleavage of the alkylperoxide intermediate can initiate the homolytic C-C bond cleavage of the organic substrate by a radical rearrangement mechanism (Scheme 1.15) via the rapid rearrangement of a series of radical species including geminol diol radicals, epoxide radicals, and ester radical species.[40, 105, 151, 155-159] Homolytic O-O bond cleavage of Fe(III)-hydroperoxide[49] or heterolytic cleavage of Fe(II)-hydroperoxide[87] intermediates yield high-valent Fe(IV)-oxo species, which can further oxidize the substrate and initiate C-C bond cleavage by hydrogen atom abstraction or oxygen atom transfer. Additionally, homolytic cleavage of an Fe(III)-hydroperoxide can generate a hydroxyl radical[105] able to abstract a hydrogen atom from the substrate to initiate a radical rearrangement mechanism and C-C homolysis.

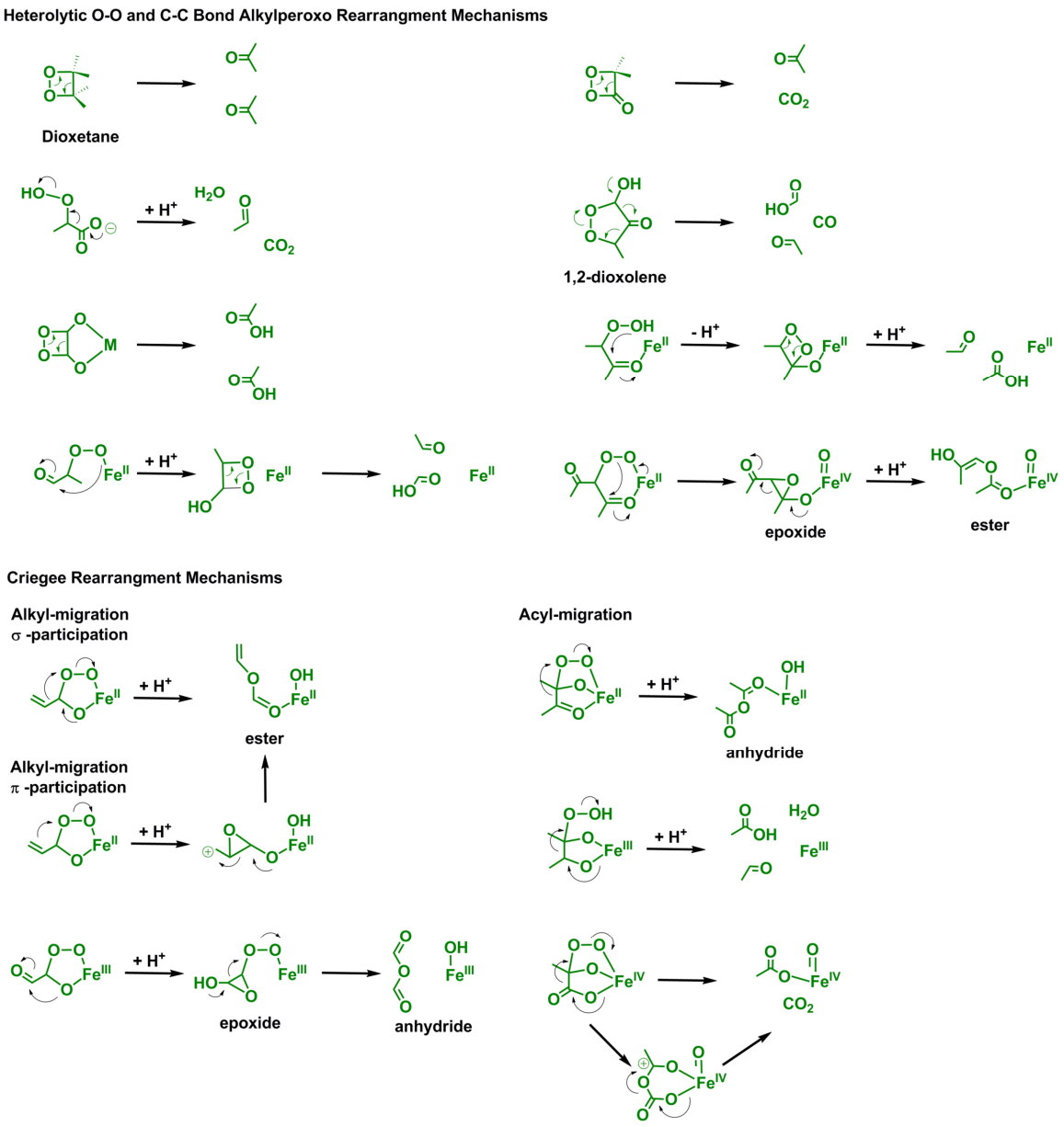

Scheme 1.14. Heterolytic O-O and C-C bond cleavage mechanisms of proposed alkylperoxide species.[4, 12, 28, 102, 119, 152]

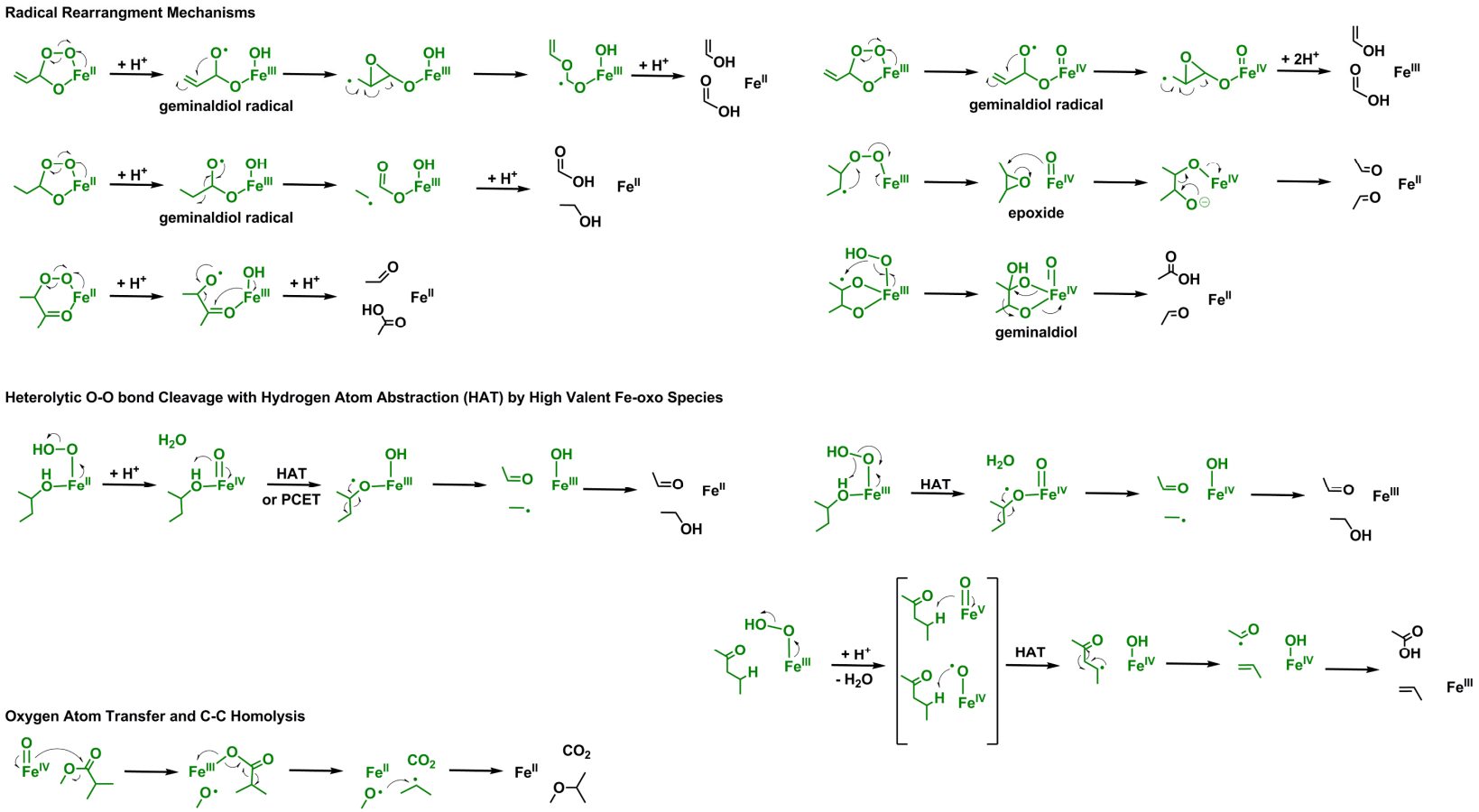

Scheme 1.15. Homolytic O-O and C-C bond cleavage radical rearrangement mechanisms of proposed alkylperoxide species.[40, 105, 151, 155-159] Proposed heterolytic O-O bond cleavage of Fe(III)-hydroperoxo species to generate high-valent Fe-oxo species followed by hydrogen atom abstraction (HAT)[160] or oxygen atom transfer (OAT)[29, 92] resulting in homolytic C-C bond cleavage of organic substrates.

1.4.8 Product formation and release. The proposed product from heterolytic O-O and C-C bond cleavage of the alkylperoxide intermediate by C-C bond-cleaving dioxygenases are ester-Fe(II)-hydroxide species. Hydrolysis and of the ester by water or the metal hydroxide is proposed to give the final product.[9] Alternately, oxygen atom transfer from an Fe(IV)-oxo to the ester can lead to the hydrolyzed product and reduced metal center in mechanism where heterolytic cleavage of an Fe(II)-peroxo results in the formation of an Fe(IV)-oxo species.[29, 92]

Homolytic O-O and C-C bond cleavage and radical rearrangement mechanisms result in organic product-radical species and Fe(III)-hydroxide. Hydroxyl radical rebound onto the organic radical product would both return the metal cofactor to it reduced state and give the final C-C cleavage product.[18, 81, 93, 151]

1.5 Mechanistic details of representative C-C cleaving oxygenases and oxidases.

The mechanism of C-C bond cleavage of organic substrates by dioxygenases and oxidases can be very complex. Many different reasonable mechanisms have been proposed for the different C-C bond cleaving dioxygenases and oxidases each proceeding through different substrate and O_2 activation mechanisms, reactive pairs and rearrangement mechanisms. This complexity can best be demonstrated by looking at the proposed mechanisms of the thoroughly studied catechol dioxygenases, described below. The proposed mechanisms for the catechol dioxygenases share similar mechanisms to other classes of C-C bond-cleaving dioxygenases and oxidases. Several O_2 intermediates have been trapped and characterized for the extradiol-cleaving catechol dioxygenases.[149, 161-165] Kinetic and spectroscopic studies employing substrate analogues, active site

mutants, and metal-substituted enzymes have given additional insights into the mechanism of the extradiol-cleaving catechol dioxygenases.[130, 131, 166-169]

1.5.1 Extradiol-cleaving catechol dioxygenases. A key step in the biodegradation of many aromatic compounds is catalyzed by a class of enzymes called catechol dioxygenases. These enzymes oxidatively cleave the strong C-C bond of their aromatic catechol substrate.[170, 171] Catechol dioxygenases play an important role in the carbon cycle and in the bioremediation of the environment. Microorganisms containing catechol dioxygenases are able to utilize aromatic hydrocarbons as a source of energy.[8] In humans, similar dioxygenases are involved in the metabolism of aromatic amino acids. Defects in these dioxygenases are associated with several severe diseases including the neurodegenerative disorder Huntington's chorea and degenerative arthritis.[172, 173]

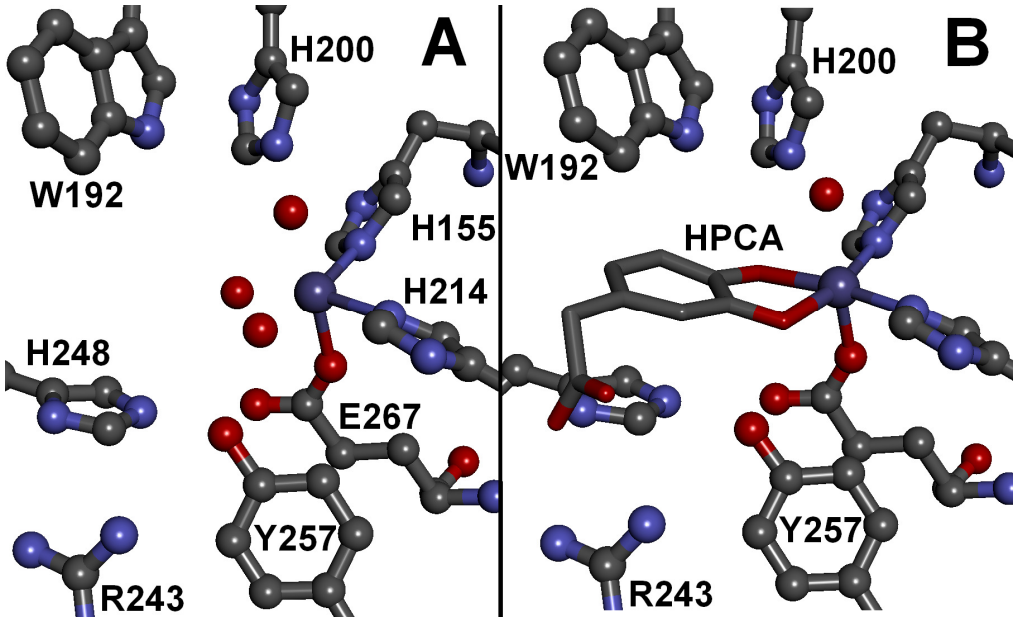

Figure 1.2. (A) Fe-HPCD (1.70 Å, PDB 3OJT) and (B) [Fe-HPCD(HPCA)] enzyme-substrate complex (1.50 Å, PDB 4GHG).

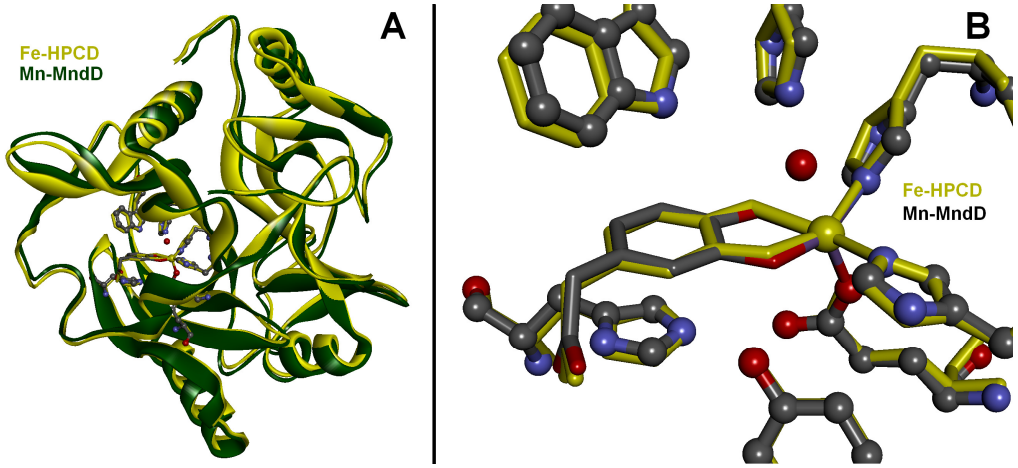

Figure 1.3. Overlays of [Fe-HPCD(HPCA)] (1.50 Å, PDB 4GHG)[163] and [Mn-MndD(HPCA)] (1.90 Å, PDB 1F1V)[174] enzyme-substrate complexes showing (A) protein fold and (B) first and second coordination sphere.

1.5.2 Metal substitution experiments. Homoprotocatechuate 2,3-dioxygenase (HPCD) isolated from *Brevibacterium fuscum* is an extradiol-cleaving catechol dioxygenase that catalyzes the cleavage of the C2-C3 bond of homoprotocatechuate (HPCA) with the incorporation of both oxygen atoms of O_2 into the ring-cleaved product.[175] HPCD has a six-coordinate Fe(II) center coordinated by two histidines and one glutamate in a 2-His-1-carboxylate facial triad motif (Figure 1.2A).[174, 176] This metal binding site leaves three *cis*-labile solvent occupied sites to which the catechol substrate and O_2 can then bind. The coordination of the anionic catechol substrate serves to lower the redox potential of the Fe(II) center and promote dissociation of the final solvent molecule for O_2 binding (Figure 1.2B). Another closely related extradiol catechol dioxygenase from *Arthrobacter globiformis* (MndD) utilizes Mn(II) instead of Fe(II) to cleave the same catechol substrate.[177] HPCD and MndD are very similar structurally, sharing 82% amino acid sequence identity, nearly identical protein folds (Figure 1.3A), and first and second coordination sphere structures (Figure 1.3B). However, these enzymes employ metals

with standard aqueous redox potentials for the M(III/II) couple that differ by 0.79 V (E^o = 0.77 V vs SHE for the Fe(III/II) couple and 1.56 V for the Mn(III/II) couple).[178] Metal-substitution experiments in which manganese was swapped for iron in HPCD and *vice versa* for MndD produced Fe-MndD and Mn-HPCD enzymes with similar catalytic activities.[131]

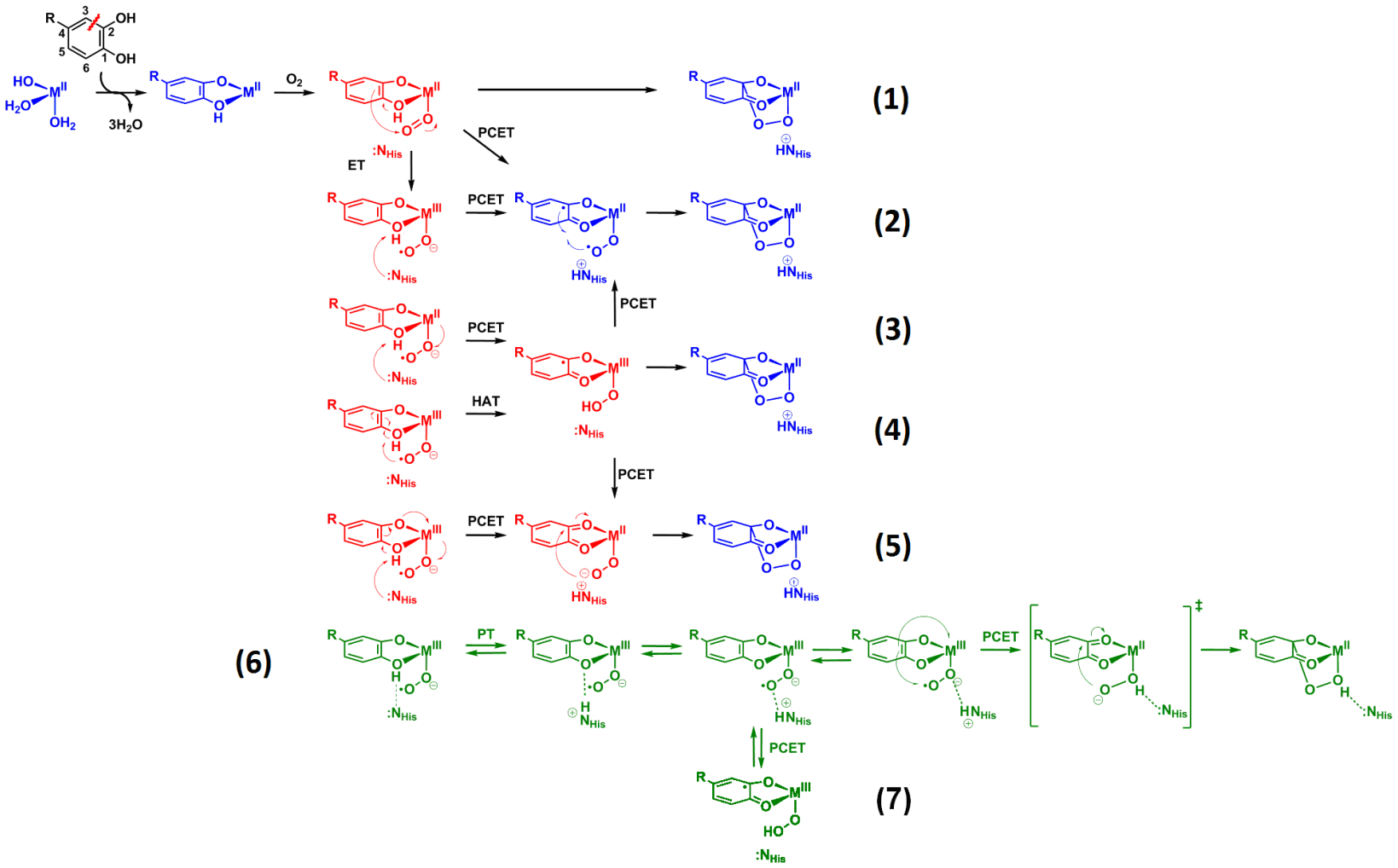

Scheme 1.16. Proposed catechol oxidation mechanisms for M-HPCDs to yield the alkylperoxo intermediate; (Red) species trapped and characterized in solution studies,[130, 149, 161, 162, 179] (Blue) species observed in X-Ray crystallography studies,[131, 165, 169, 174] (Green) proposed mechanism from DFT studies.[150, 151, 155, 157, 180]

1.5.3 Proposed mechanisms of reductive O_2 activation and substrate oxidation. Several different mechanisms of catechol oxidation and O_2 reduction can be envisioned (Scheme 1.16). These mechanisms differ with respect to the extent and mechanism of electron transfer between the two substrates to form a reactive pair. Mechanism (1) consists of direct nucleophilic attack of the coordinated catechol on coordinated O_2 to form a bridging alkylperoxo species. In this mechanism the metal acts solely as a Lewis acid base catalyst to bind and juxtapose the two substrates for the reaction.[50, 57] Mechanism (2) involves A proton-coupled electron transfer (PCET) mechanism to yield a [M(II)($SQ^{\bullet}$)-$O_2^{\bullet-}$] diradical pair (with the radical drawn localized on C2 of the catechol substrate). The diradical pair could be generated by either concerted electron transfer from the catechol substrate to O_2 via the metal center or via a M(III)-$O_2^{\bullet-}$ intermediate in a step-wise mechanism. Catechol oxidation and O_2 reduction are accompanied by proton transfer from the catechol substrate to the active site acid-base catalysis His200 by a PCET mechanism.[7] Recombination of the radicals would then result in the spin-allowed formation of the bridging alkylperoxo intermediate. The reaction could also proceed by mechanism (3) the two-electron reduction of O_2 to a peroxide is simultaneous with the one-electron oxidation of both the catechol and the metal center to yield a [M(III)($SQ^{\bullet}$)-hydroperoxo] intermediate.[149] Alternatively oxidation of the catechol to form a [M(III)($SQ^{\bullet}$)-hydroperoxo] intermediate could proceed by hydrogen atom transfer (HAT) from the catechol to the superoxide (Mechanism 4). Deprotonation of the hydroperoxo intermediate by His200 could result in a [M(III)($SQ^{\bullet}$)-peroxo], while further oxidation of the semiquinone by the metal center would result in a [M(II)(Q)-peroxo]

species (Mechanism 5).[161] Nucleophilic attack of the peroxo on either the semiquinone or quinone could form the C-O bond of the proposed alkylperoxo species.

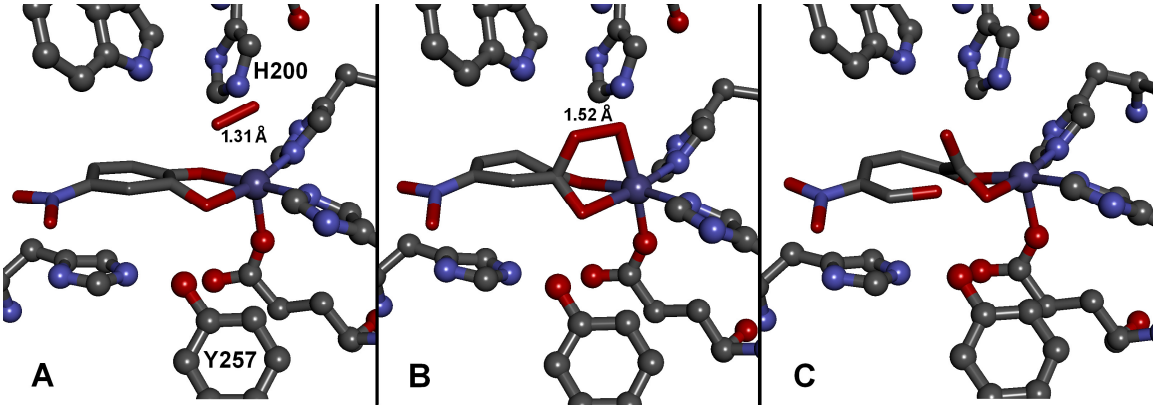

Figure 1.4. Intermediates species and enzyme-product complex observed in different subunits of the crystallographic unit cell of the homotetramere [Fe-HPCD(4NC)] enzyme-substrate complex reacting with O_2.[165] (A) Structure of [Fe-HPCD(4NSQ$^{\bullet}$)-$O_2^{\bullet-}$] exhibiting puckering of C2 of ring suggesting a localized semiquinone substrate radical, (B) [Fe-HPCD-alkylperoxide]intermediate, and (C) Enzyme-product complex with bound 4NC ring-cleaved product.

1.5.4 Trapped O_2 intermediates. Several of the proposed intermediates shown in Scheme 1.16 have been observed in crystallographic and solution studies with Mn-, and Fe-HPCD using active site mutants and electron-poor substrate analogues. Crystal structures consistent with the [Fe(II)(SQ$^{\bullet}$)-$O_2^{\bullet-}$] diradical pair (Figure 1.4A), the bridging alkylperoxo intermediate (Figure 1.4B), and the final ring-cleaved product (Figure 1.4C) were reported using the electron-poor substrate analogue 4-nitrocatechol (4NC).[165] M(III)-$O_2^{\bullet-}$ intermediates have been trapped and characterized in solution studies with Mn- HPCD and the H200N-Fe-HPCD mutant. Specifically, superoxide species were observed with [H200N-Fe(III)-HPCD(4NC)-$O_2^{\bullet-}$], and a probable Mn(III)-$O_2^{\bullet-}$ species with the native substrate HPCA, ([Mn(III)-HPCD(HPCA)-$O_2^{\bullet-}$]).[130, 162, 179]

The different electronic configurations of the three 3d transition metals have led to different observed electronic structures for the characterized M(III)-$O_2^{\bullet-}$ species. The [H200N-Fe(III)-HPCD(4NC)-$O_2^{\bullet-}$] species characterized by rapid freeze quench EPR and Mössbauer experiments has an $S = 2$ ground state arising from a high-spin Fe(III) center antiferromagnetically coupled to a superoxide radical.[162] The probable [Mn(III)(HPCA)-$O_2^{\bullet-}$] intermediate characterized by EPR formed rapidly in the first 15 ms to a ~5% yield. This species exhibited an $S = 5/2$ EPR signal with a feature at $g = 4.29$ displaying ^{55}Mn ($I = 5/2$) hyperfine splitting of only 60 G, much smaller than the 89 G splitting observed for the [Mn(II)-HPCD(HPCA)] enzyme-substrate complex. The small observed ^{55}Mn splitting suggested a high-spin Mn(III) center that is ferromagnetically coupled to a semiquinone or superoxide radical. Thus, it was assigned to either a [Mn(III)(catecholate)-$O_2^{\bullet-}$] or a [Mn(III)($SQ^{\bullet}$)(hydro)peroxide] species.[179]

1.5.5 Intermediates trapped with second sphere mutants. H200 and Y257 are observed to make hydrogen bonds with the O_2 adduct and the semiquinone intermediate respectively, in the crystal structure of the [Fe(II)($SQ^{\bullet}$)-$O_2^{\bullet-}$] diradical pair (Figure 1.4A).[165] Several intermediates were trapped and characterized in transient kinetic studies employing the H200N and Y257F mutants. When [H200N-Fe-HPCD(HPCA)] was rapidly mixed with O_2, a ($S = 2$) high-spin Fe(III) intermediate antiferromagnetically coupled to a radical was observed by EPR and Mössbauer spectroscopies.[149] In UV-Vis stopped-flow experiments, the observed intermediate was found to have absorption bands at 310, 395 and 610 nm, similar to the independently synthesized HPCA-$SQ^{\bullet}$. These experiments led to the assignment of the intermediate as a [Fe(III)($SQ^{\bullet}$)-(hydro)peroxo] species. The [Fe(III)($SQ^{\bullet}$)-(hydro)peroxo] species then

reacted to form the extradiol ring-cleaved product via a high-spin Fe(II) intermediate observed by Mössbauer spectroscopy, which was assigned to the bridging alkylperoxide species, as proposed in Scheme 1.16 (Mechanism 3).[149] A similar [Fe(III)($SQ^{\bullet}$)-peroxo] intermediate was observed to form from the initial Fe(III)-$O_2^{\bullet-}$ intermediate in the catalytic turnover of 4NC by H200N-Fe-HPCD. In this reaction the semiquinone and peroxide do not form a reactive pair. Instead, the 4NSQ is oxidized by the Fe(III) center to release 4NQ and hydrogen peroxide as the final products.[162] These studies suggested that the active site residue H200 plays several important roles in catalysis.[130, 149, 162, 167, 181] His200 is thought to facilitate electron transfer from substrate to the M-O_2 unit by a proton-coupled electron transfer mechanism where His200 acts as a base to remove the proton from the substrate to assist in catechol oxidation (Scheme 1.16). In turn, the protonated His200 residue can interact with the O_2 adduct as it forms and stabilize the developing negative charge on the dioxygen moiety. In the next step, the protonated His200 may help to align the superoxide moiety to optimize its attack on the substrate semiquinone radical to form the alkylperoxo intermediate (Figure 1.5). H200 may then act as a proton donor to promote O-O bond cleavage of the bridging alkylperoxide species by protonating the proximal oxygen (Scheme 1.17). The H200N mutant is no longer able to act as a catalytic base and the Asp side chain is too short to properly interact with the superoxide adduct. This misaligns the superoxo for attack on the substrate, and as a result led to the trapping of the M(III)-$O_2^{\bullet-}$ species with a H200N-Fe/Co-HPCD with the electron-poor 4NC[130, 162] substrate. Using the more easily oxidized native substrate, HPCA, a [H200N-Fe(III)($SQ^{\bullet}$)-(hydro)peroxo] intermediate was observed.[149]

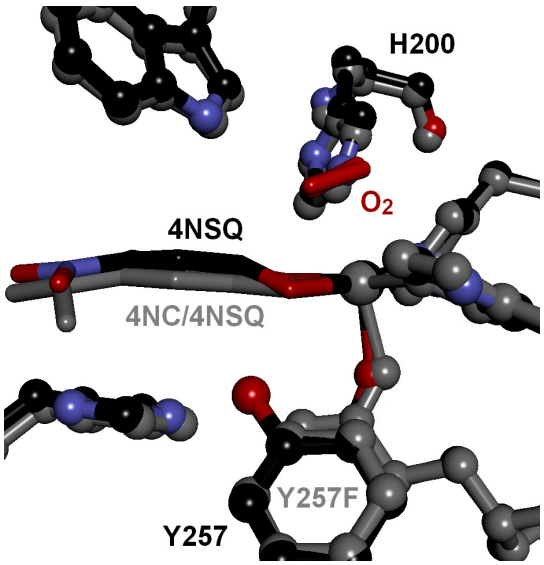

Figure 1.5. Structural overlays of [Fe-HPCD(4NSQ)O_2] (black, PDB 2IGA)[165] at 1.95 Å resolution and [Y257F-Fe-HPCD(4NC)O_2] (gray, PDB 4GHF)[163] at 1.67 Å resolution.

In single turnover transient kinetic experiments reacting [Y257F-Fe-HPCD(HPCA)] with O_2, two high-spin Fe(II) intermediates were characterized by UV-Vis and Mössbauer spectroscopies.[161] The first species had no unique chromophore in the visible region and its rate of formation showed linear O_2 concentration dependence with a non-zero y-intercept (at pH 7.5), suggesting that its formation is by reversibly O_2 binding. Intermediate 1 was thus assigned to the initially coordinated O_2 adduct [Y257-Fe(II)-HPCD(HPCA)-O_2]. At pH 5.5 the rate of formation of the O_2 adduct increases and became irreversible, suggesting that protonation of the H200 at low pH helped to stabilize the initial O_2 adduct.[161]

The second observed intermediate has an intense chromophore observed in stopped-flow experiments (ε_{425nm} = 10,500 M^{-1} cm^{-1}), which resembles the independently synthesized HPCA-quinone. Together with the Mössbauer data, this led to the assignment

of intermediate 2 as a [Y257-Fe(II)-HPCD(quinone)-(hydro)peroxo] species. In crystallographic studies Y257 is observed to hydrogen bond with the catechol at O(2C) and is observed to induce puckering of the catechol ring. Upon catechol oxidation, the hydrogen bonding interaction between Y257 and the catechol substrate effectively localizes the semiquinone radical to C2 of the ring (Figure 1.5), directing the attack by the superoxide on C2.[163, 165] The Y257F mutant is no longer able to hydrogen bond with the catechol ring to stabilize a localized semiquinone species. The Y257F mutant also was observed to have much lower apparent affinity for O_2, observed in both solution and crystallographic studies. The lower observed affinity for O_2 suggests that Y257 aids in the electron transfer from the catechol to superoxide by inducing puckering of the catechol ring. Y257 then localizes the semiquinone radical on C2 for attack by the superoxide.[163] The Y257F mutant is unable to localize the semiquinone radical and instead the substrate is oxidized by an additional electron to the planar quinone species, [Y257-Fe(II)-HPCD(HPCA-quinone)-(hydro)peroxo].[161] Attack of the peroxo on the quinone could then yield the proposed bridging alkylperoxo species as shown in Scheme 1.16 (Mechanism 5). Both the observed [H200N-Fe(III)(HPCA-$SQ^{\bullet}$)-(hydro)peroxo] and [Y257-Fe(II)-HPCD(HPCA-quinone)-(hydro)peroxo] intermediates are catalytically competent in forming the extradiol ring-cleaved product but at much slower rates than the native enzyme. The slow reactivity of these species suggests that they are probably not the reactive pairs in the native system but that the diradical $SQ^{\bullet}$-$O_2^{\bullet-}$ pair is most likely the operative reactive pair in the wild type system.[149, 161]

1.5.6 DFT calculations. DFT studies have been performed on the Fe- and Mn-enzymes.[150, 151, 155, 157, 180, 182] The most recent DFT study (Scheme 1.16, Mechanism 6) by

Gemma Christian, Shengfa and Frank Neese[150] modeled the reaction of [Fe-HPCD(HPCA)] with O_2. Their calculations predict that the initial O_2 adduct is an antiferromagnetically coupled high-spin Fe(III)-$O_2^{\bullet-}$, where the superoxide moiety is bound end-on to the metal center upon reductive O_2 activation.[150] The electronic structure is in agreement with the characterized Fe(III)-$O_2^{\bullet-}$ species observed with H200N-Fe-HPCD and 4NC. However, the O_2 adduct observed in crystallographic studies with the wild type enzyme are side-on bound seven-coordinate species (Figure 1.4A).[165] In the DFT study a proton is then transferred from the monoanionically bound catechol to His200, which then rotates to form hydrogen bonding interactions first with the distal oxygen and then the proximal oxygen of the Fe(III)-$O_2^{\bullet-}$ (Scheme 1.16, Mechanism 6).[150] They describe this reaction as proceeding by a PCET mechanism from the [Fe(III)(catechol)$O_2^{\bullet-}$] species where the superoxide is protonated at the proximal oxygen by His200 and the catechol substrate is oxidized by two electrons with one electron transferring directly from the catechol substrate to the superoxide while the other is transferred to the metal reducing it to Fe(II). This reaction proceeds through a high-spin [Fe(II)(quinone)-(hydro)peroxo] like transition state. Where the C-O bond of the alkylperoxo intermediate is formed by nucleophilic attack of the proximal peroxo oxygen on the C2 of the quinone.

Their calculations also predict the formation of a stable antiferromagnetically coupled high-spin [Fe(III)($SQ^{\bullet}$)-hydroperoxide] species.[150] This species forms by PCET, with protonation of the distal O of the Fe(III)-$O_2^{\bullet-}$ by the His200 followed by rapid electron transfer from the catechol to the superoxide via the metal center (Scheme 1.16, Mechanism 7). Their calculations suggest that the hydroperoxo and semiquinone are

unreactive with a barrier of 75 kJ mol^{-1} for the formation of the bridging alkylperoxo species. They suggest that the [Fe(III)($SQ^{\bullet}$)-hydroperoxide] species can convert back to the reactive [Fe(III)(catechol)$O_2^{\bullet-}$] species by deprotonation of the hydroperoxo by His200 and electron transfer from the peroxide back to the catechol substrate.

Unlike the traditional mechanism proposed for extradiol dioxygenase where the reactive pair has been described as a [Fe(II)($SQ^{\bullet}$)-$O_2^{\bullet-}$] species,[7] these DFT studies suggest that a [Fe(III)-catecholate-$O_2^{\bullet-}$] species constitutes the reactive pair, through a [Fe(II)(quinone)-(hydro)peroxide] like transition state.[150] Their DFT calculation also suggested that the observed [Fe(III)($SQ^{\bullet}$)-hydroperoxide] observed with the H200N is off pathway.

DFT studies were also performed by Valentin Georgiev, Tomasz Borowski, and Per E. M. Siegbahn.[151, 182] Their calculations used a smaller model, excluding second sphere amino acid residues Trp192 and Arg243, which interact with the catechol substrate.[150, 151] Their DFT study suggested rapid electron transfer from the catechol substrate to the O_2 adduct via the metal center to form an Fe(II)($SQ^{\bullet}$)-$O_2^{\bullet-}$ diradical pair with proton transfer to His200.[151, 155] Generation of the Fe(II)($SQ^{\bullet}$)-$O_2^{\bullet-}$ diradical pair was then followed by a barrier-less attack of the superoxide on the semiquinone at C2 of the HPCA substrate. Their DFT studies also looked at the attack of the superoxide at the "wrong position" (C1) of HPCA. O-O cleavage of the resulting bridging alkylperoxide was found to proceed through a 6.6 kcal/mol higher barrier then the O-O bond cleavage of the "correct" C2-O-O-Fe bridging alkylperoxo.[182] They calculated a barrier of 1.1 kcal between the "wrong" C1-O-O-Fe and "correct" C2-O-O-Fe bridging alkylperoxo species, suggesting a thermodynamic equilibrium between the two species. The lower barrier for

O-O bond cleavage from the correct species results in the preference for the correct alkylperoxo rearrangement pathway. They suggested that hydrogen bonding interactions from His200 and Tyr257, with the O_2 adduct and catechol substrate are important for creating an asymmetric active site. The asymmetric active site is important in directing the attack of the superoxide on the semiquinone ring at the correct position and in the subsequent rearrangement of the bridging alkylperoxo species to form the correct proximal extradiol ring-cleaved product. The trapped $O_2^{\bullet-}$-$SQ^{\bullet}$ species observed in crystallo with Fe-HPCD and 4NC (Figure 1.4 A) and experiments with the Y257F and H200N mutants in solution suggested that the preference for attack of the O_2 adduct on C2 of HPCA is directed by aligning the superoxide by hydrogen bonding from H200 to the proximal oxygen of the side-on bound superoxide, positioning the distal oxygen for attack on the substrate.[130, 149, 162, 163] On the other side, Y257 interactions with the substrate localize the semiquinone radical on C2, stabilizes the sp^3 hybridization of C2 of the substrate radical by hydrogen bonding with O(C2).[161, 163]

1.5.7 Mechanism of alkylperoxide rearrangement. DFT calculations suggest that the O-O bond of the [Fe(II)-alkylperoxo] intermediate is broken homolytically (Scheme 1.17),[150, 151] where electron transfer from Fe(II) into the σ* of the O-O bond forms an Fe(III)(oxyl-radical)-hydroxide species.[150, 151] Attack of the oxyl-radical on the substrate leads to the formation of an [Fe(III)(epoxide-radical)-hydroxide] species. The epoxide-radical then rearranges via homolytic C-C bond cleavage to form an [Fe(III)-hydroxide(lactone-radical)] intermediate. The [Fe(III)-hydroxide(lactone-radical)] intermediate is then hydrolyzed by attack of a hydroxide radical from the metal to form the ring-cleaved product and reduce the metal center to Fe(II). DFT calculations

suggested that the [Fe(III)-oxyl-radical] may also react with nearby Trp192 to abstract both a proton and an electron to form an off-pathway *gem*-diol Trp-radical species (Scheme 1.17). A stabilized *gem*-diol species was observed in crystallographic experiments using the surface mutant Glu323Leu-Fe-HPCD with the substrate analogue 4-sulfonylcatechol (Figure 1.6),[158, 164] where the combination of the substrate analogue and different crystal packing interactions between the different subunits apparently stabilized the observed intermediate in O-O bond cleavage.[164]

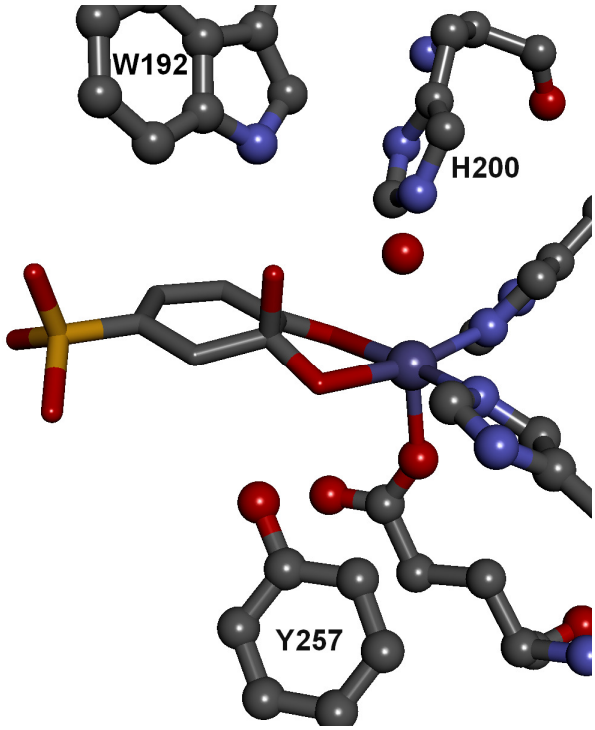

Figure 1.6. Crystal structure of [E323L-Fe-HPCD(4SC-*gem*-diol)] (1.60 Å, 3ECK).[164]

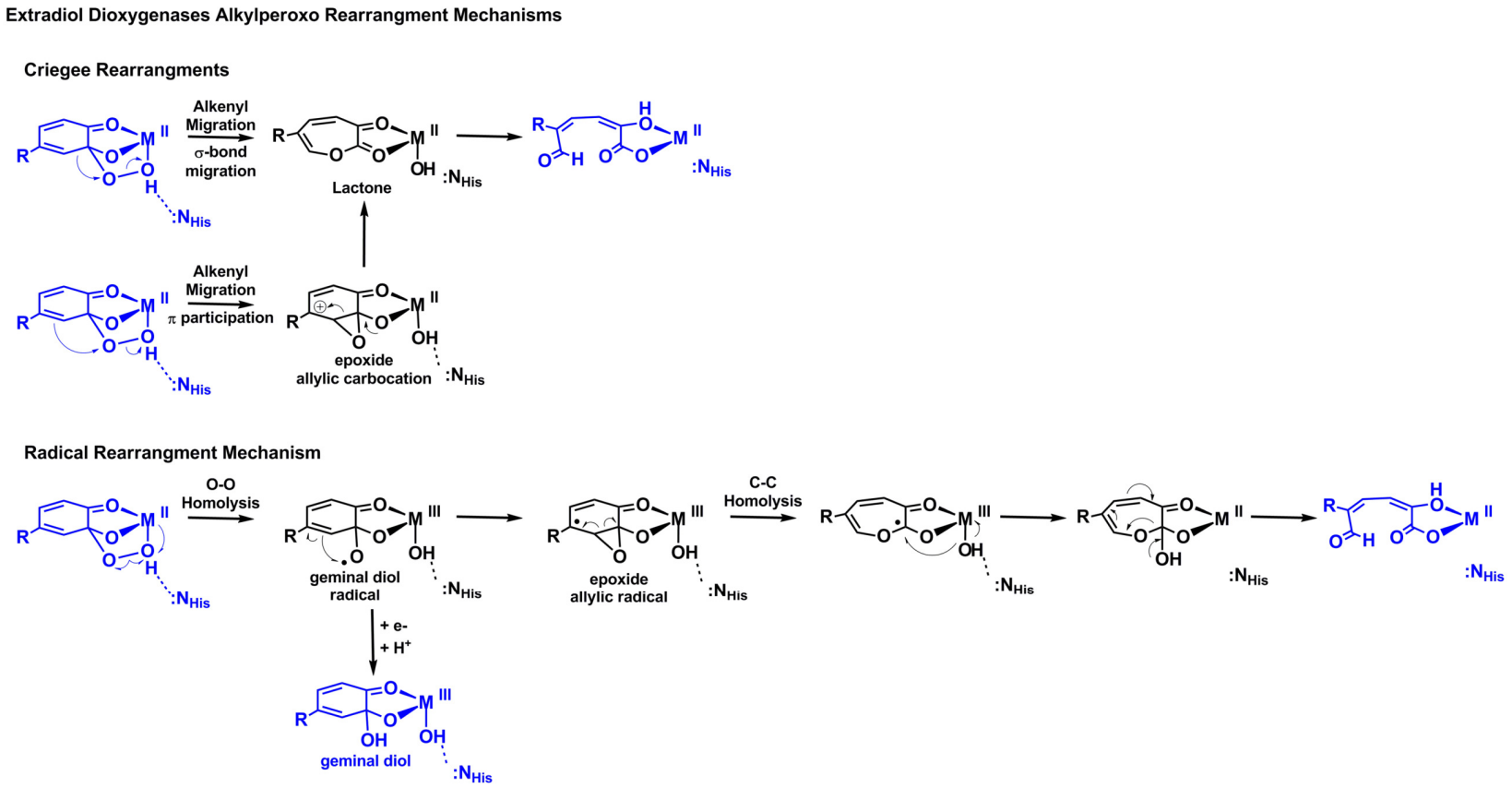

Scheme 1.17. Proposed Criegee type rearrangement of alkylperoxo intermediate to form the proximal extradiol ring-cleaved product from experimental[9, 164] and computational studies.[150, 151, 156, 158, 182] Species in blue have been observed in X-Ray crystallography studies.

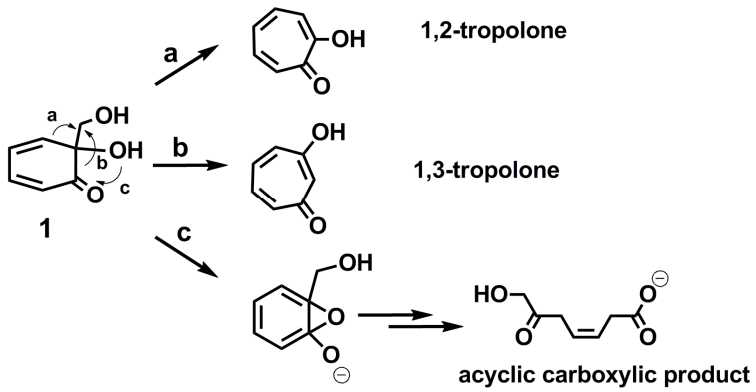

Scheme 1.18. Expected products of different rearrangements mechanisms of a) alkenyl migration b) acyl migration and c) epoxide formation followed by a benzene oxide-oxepin rearrangement of mechanistic probe (1) 6-hydroxymethyl-6-methylcyclohexa-2,4-dienone (Scheme adapted from Xin and Bugg, *J. Am. Chem. Soc.,* **2008**).[9]

Heterolytic O-O bond cleavage mechanisms of the bridging alkylperoxide species have also been proposed with alkenyl migration by Creigee-type rearrangement mechanisms (Scheme 1.17) via either σ bond migration or a π participation pathway.[4, 5, 9] The mechanism of heterolytic O-O bond cleavage was tested by Meite Xin and Timothy Bugg using the carba analogue of the bridging alkylperoxo intermediate, 6-hydroxymethyl-6-methyl-6-methylcyclohexa-2,4-dienone, as a mechanistic probe (Scheme 1.18).[9] Incubation of the mechanistic probe with the extradiol-cleaving catechol dioxygenase MhpB resulted in the product 2-tropolone, consistent with the alkenyl migration mechanism. This observation initiated further DFT studies, which found an unattainably large barrier for alkenyl migration by the carba analogue (32.8 kcal/mol).[156] Attempts to find the transition state for the alkenyl migration with the bridging alkylperoxo species were unsuccessful, converging to homolytic O-O bond cleavage, which has a calculated barrier of 11.3 kcal/mol for Fe-HPCD. It should be noted that O-O

bond homolysis would proceed through several Fe(III)-organic radical intermediates (Scheme 1.17). The formation of a trivalent intermediate upon O-O bond homolysis could affect the rate of these steps in the Mn- and Co-substituted extradiol dioxygenases due the expected higher M(III/II) standard redox potentials of these metals. It was found that this barrier could be overcome in the DFT studies with Mn-MndD by intersystem crossing from the sextet (high-spin Mn(II)-alkylperoxo, S = 5/2) to quartet (antiferromagnetically coupled high-spin Mn(III)(hydroxide)-substrate radical, S = 3/2) spin state during O-O homolysis.[156] A significant spin transition would also be expected during O-O bond homolysis between the high-spin Co(II)-alkylperoxo species and the Co(III)(hydroxide)-radical intermediate, as the Co(III) intermediate is likely be low-spin due to the d^6 electronic configuration of Co(III).

1.6 Aim and scope of thesis.

The research presented in this thesis focuses on understanding the mechanism of O_2 activation and catalysis by the Co- and Mn-substituted extradiol-cleaving catechol dioxygenases. Specifically, we hoped to probe the effects of the different physical and chemical properties of each metal and the catechol substrate on the mechanism and observable kinetic rates of the reaction. Employing the metal-substituted enzymes and electron-poor substrate analogues as well as the metal substituted H200N mutants we have been able to trap and characterize several transient intermediates in the O_2 activation and substrate oxidation steps. We then employed many different spectroscopic methods to characterize the observable species, including UV-Vis, EPR, resonance Raman, XAS and MCD.

Chapter 2

A Hyperactive Cobalt-Substituted Extradiol-Cleaving Catechol Dioxygenase

Portions of this chapter were previously published by Springer as: Andrew J. Fielding, Elena G. Kovaleva, Erik R. Farquhar, John D. Lipscomb, Lawrence Que Jr. "A Hyperactive Cobalt-Substituted Extradiol-Cleaving Catechol Dioxygenase" *J. Biol. Inorg. Chem.*, *16,* **2011,** 341–355.

2.1 Introduction

Catechol dioxygenases are essential microbial enzymes for the biodegradation of aromatic compounds.[170, 171] Homoprotocatechuate 2,3-dioxygenase (HPCD) isolated from *Brevibacterium fuscum* is an extradiol-cleaving catechol dioxygenase that catalyzes the cleavage of the C2-C3 bond of homoprotocatechuate (HPCA) with the incorporation of both oxygen atoms of O_2 into the product 5-carboxymethyl-2-hydroxymuconic semialdehyde (5-CHMSA) (Scheme 2.1)[175]. HPCD contains an active site Fe(II) center bound to a 2-His-1-carboxylate facial triad motif with solvent waters occupying the remaining three coordination sites.[174, 176, 183] Closely related is the homoprotocatechuate 2,3-dioxygenase from *Arthrobacter globiformis* (MndD), which is Mn(II)-dependent.[177] HPCD and MndD are very similar structurally, sharing 82% amino acid sequence identity, but they employ metals with standard aqueous redox potentials for the M(III/II) couples that differ by 0.79 V (E^o = 0.77 V vs SHE for the Fe(III/II) couple and 1.56 V for the Mn(III/II) couple).[178] Previously, we have described metal-substitution experiments in which manganese was swapped for iron in HPCD and *vice versa* for MndD, producing Fe-MndD and Mn-HPCD.[131] Remarkably, all four enzymes (Mn-MndD, Mn-HPCD, Fe-MndD and Fe-HPCD) exhibit nearly the same activity of *ca*. 400 turnovers/minute at (pH 7.8) (22 °C) when the metals are in their active reduced state. The electronic structures of the metal centers in each pair of enzymes are nearly indistinguishable, as demonstrated by the very similar EPR spectra for Mn-MndD vs Mn-HPCD, (Mn-MndD vs Mn-HPCD)/HPCA, and (Fe-MndD vs Fe-HPCD)/HPCA/NO complexes.[131] Moreover, high-resolution X-ray crystal structures of Fe-HPCD and Mn-HPCD are

indistinguishable,[131, 174] suggesting that the protein does not provide a means to tune the potentials of the Fe(II) and Mn(II) centers differentially, in contrast to the paradigm established by Fe- and Mn-superoxide dismutases.[184-186] For the latter enzymes, redox tuning is achieved by use of different second sphere residues that interact with the metal-bound solvent. Evidence that the Fe and Mn centers in HPCD and MndD maintain their redox potential differences also derives from the observation that only Fe-HPCD and Fe-MndD are inactivated by oxidants like hydrogen peroxide and ferricyanide,[131] consistent with the lower potentials expected for the iron centers. This ability to maintain high rates of reductive oxygen activation over a large range of metal redox potentials is unique to the extradiol dioxygenases and mechanistically related enzymes.[41, 71, 73, 187] In particular, it suggests that a mechanism is required that differs substantially from the classic heme oxygenase paradigm in which the metal center traverses through several redox states in the course of O_2 activation, implying a strong dependence on the metal redox potential.[188, 189]

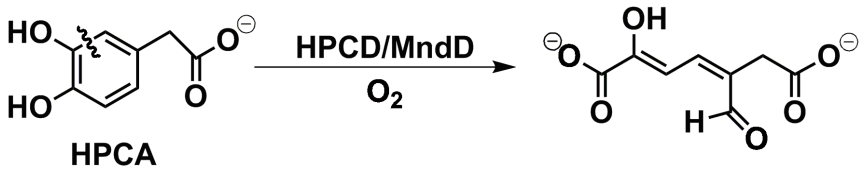

Scheme 2.1. Extradiol ring-cleavage of HPCA to product 5-CHMSA catalyzed by HPCD and MndD.

To harness the oxidizing power of triplet dioxygen, oxygenases generally activate O_2 by first reducing it to a more reactive superoxide or peroxide species.[123, 124] For many metalloenzymes, this entails the initial binding of O_2 to a divalent redox active metal

center to yield a M(III)-superoxo species. Upon transfer of an electron from a redox partner, the superoxo species is converted to a M(III)-peroxo species [125, 190] that may itself be reactive or undergo further activation to generate an even more reactive high-valent metal-oxo species. Based on our initial studies,[131] this paradigm does not appear to be followed by Fe-HPCD, Mn-MndD and their metal-exchanged homologs. While our recent spectroscopic evidence does show that short-lived M(III)-superoxo species can form in the reactions of O_2 with the ES complexes of Mn-HPCD and active site variants of Fe-HPCD,[162, 179] we postulate that formation of the reactive species requires subsequent electron transfer from the catechol substrate to the metal center leading to a [M(II)($SQ^{\bullet}$)$O_2^{\bullet-}$] species.[131, 175, 191] Recombination of the radicals would then result in a spin-allowed formation of an alkylperoxo intermediate that would rearrange to the observed ring-cleaved product (Scheme 2.2).[131, 155, 165, 181, 192] This type of mechanism does not require a net change in metal oxidation state between the M(II)-catecholate ES complex and the reactive [M(II)($SQ^{\bullet}$)$O_2^{\bullet-}$] intermediate, so the redox potential of the metal would not be critical so long as it is low enough for the initial O_2 complex to form.

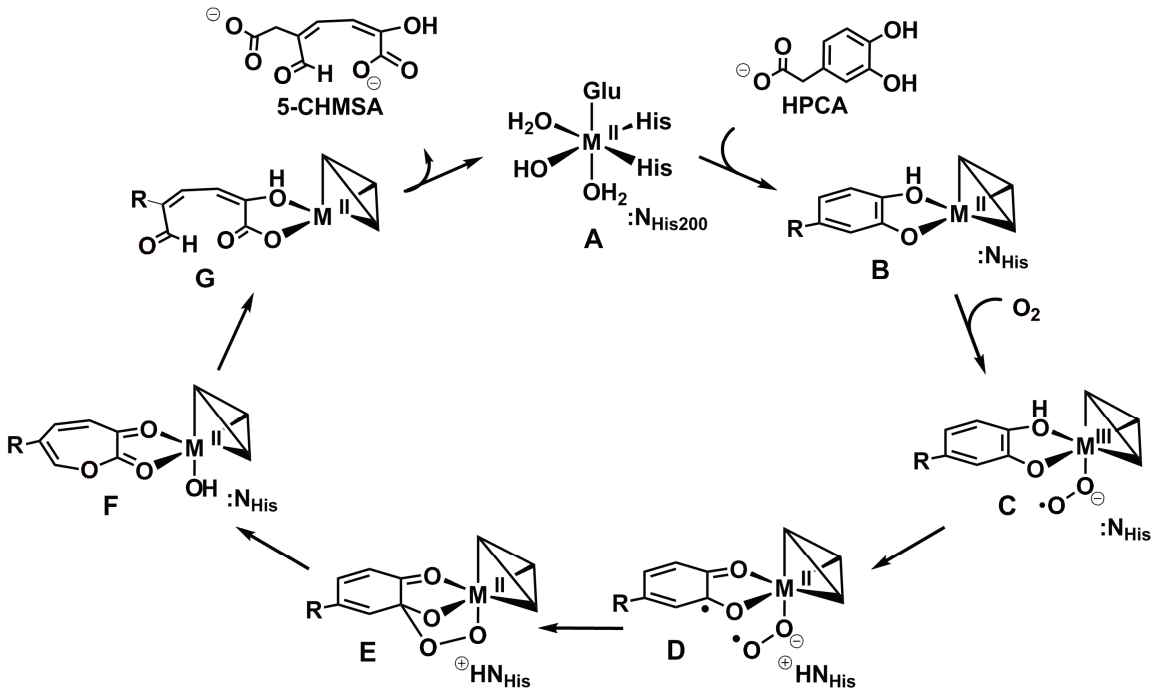

Scheme 2.2. Proposed reaction mechanism for the extradiol-cleaving catechol dioxygenases.[131]

As a further test of the hypothesis that the extradiol cleavage mechanism can operate with metal centers with significantly different redox properties, we have extended our investigation of metal-substituted HPCDs to other first-row transition metal ions. Remarkably, Co-HPCD is found to exhibit catalytic activity much higher than those found for Fe-HPCD and Mn-HPCD under O_2 saturating conditions. These results support the electron conduit hypothesis for the metal center in HPCD and provide new spectroscopic tools with which to further explore the unique mechanism of oxygen activation in the extradiol dioxygenase family.

2.2 Materials and Methods

2.2.1 Reagents and general procedures. Reagents and buffers were purchased from Sigma and were used as received. All reagent solutions and media were prepared using water treated with a Millipore MilliQ water system to minimize trace metal-ion contamination.

2.2.2 Preparation of M(II)-HPCD. Metal-substituted HPCDs were prepared by growing *E. coli* BL21(DE3) carrying plasmid pWZW204 containing the HPCD gene from *Brevibacterium fuscum* as previously described.[131, 181, 193] Upon inducing protein expression with isopropyl-β-D-thiogalactopyranoside (IPTG), the cultures were supplemented with 30 mg/L of an appropriate $M(II)Cl_2$ salt. In the procedure to obtain Cu-HPCD, $CuCl_2$ was added slowly, 10 mg/L at a time over 4 h, to avoid killing the cultures. The cells were then harvested and protein purified as previously described.[193]

2.2.3 Molar absorptivity of Co-HPCD. The molar absorptivity of Co-HPCD was determined by the Bradford assay using bovine serum albumin (BSA) as a standard and found to be 45,000 M^{-1} cm^{-1} per 42 kDa subunit at 280 nm.

2.2.4 ICP-AES metal analysis. Metal incorporation was measured by ICP-AES metal analysis at the Soil Research Analytical Laboratory (College of Food, Agricultural and Natural Resource Sciences, University of Minnesota). Samples were prepared for ICP-AES analysis by digesting 2 ppm protein in 5% HNO_3 overnight and then removing precipitated protein by centrifugation.

2.2.5 Steady-state kinetics. Enzyme activity was measured in air-saturated or oxygen-saturated 50 mM MOPS buffer (pH 7.8) at 22 °C using a Beckman DU 640

spectrophotometer. Reactions were followed by monitoring formation of the extradiol cleavage product 5-carboxymethyl-2-hydroxymuconic semialdehyde at 380 nm (5-CHMSA, ε_{380} = 38,000 M^{-1} cm^{-1}) [131]. HPCA concentrations ranging from 1 μM to 4 mM were used to determine the K_M^{HPCA} for Co-HPCD. All other assays used 2 mM HPCA. Metal-substituted HPCDs (Mn, Co, Ni, Cu and Zn) were assayed after first incubating with 1 mM H_2O_2 for 5 min to inactivate any residual Fe-HPCD present in the preperation. Apparent K_M^{O2} values were determined using a Clark-type oxygen electrode (Oxytherm from Hansatech Instruments) at 22 °C with 2 mM HPCA in 50 mM MOPS buffer (pH 7.8). The apparent kinetic parameters k_{cat} and K_M were determined using nonlinear regression fits of initial velocities to the Michaelis-Menten equation from initial velocities. All k_{cat} values were normalized by dividing the average velocity from multiple assays by the average concentration from ICP-AES metal analysis for the metal of interest. Because of the limited sensitivity of the oxygen electrode at high oxygen concentrations (above 550 μM O_2), oxygen kinetic experiments were also performed by mixing different ratios of anaerobic, air-saturated, and oxygen-saturated buffers. Reactions were then performed by monitoring the formation of product at 380 nm. Some reactions were performed under 2.0 atm of oxygen in a sealed cuvette (30 psi or 2.75 mM dissolved oxygen at 22 °C) to obtain a higher concentration of dissolved oxygen.

2.2.6 Activation and inhibition studies. The effects of L-ascorbate, H_2O_2, potassium persulfate, and potassium ferricyanide were studied by incubating Fe-, Mn-, or Co-HPCD with 1 mM reagent for 5 min before assaying for enzyme activity.

2.2.7 Transient kinetic experiments. Anaerobic [Mn- or Co-HPCD(HPCA)] was rapidly mixed with oxygenated 50 mM MOPS buffer (pH 7.8) using an Applied Photophysics model SX.18MV stopped-flow device at 22 °C. The concentrations of reagents after mixing were 20 μM HPCA and 50 μM M-HPCD. The formation of the extradiol cleavage product was monitored at 380 nm. O_2 concentrations after mixing ranged from 36 to 685 μM O_2.[166]

2.2.8 X-ray crystallography. Crystals of Co-HPCD were grown by the hanging-drop method at 20 °C in 13% PEG6000, 0.05 M calcium chloride, 0.1 M Tris-HCl pH 6.5, and then were cryo-cooled in liquid nitrogen following a brief transfer into cryoprotectant solution containing 20–25% PEG400 in the mother liquor solution. For anaerobic [Co-HPCD(4NC)] complex preparation, crystals of Co-HPCD were transferred into mother liquor solution at higher pH (13% PEG6000, 0.1 M calcium chloride, 0.1 M Tris-HCl pH 7.0) to increase the occupancy of the bound 4NC in the active sites. All mother liquor solutions, crystals of Co-HPCD and 4NC stocks were equilibrated in the anaerobic glove box atmosphere (Belle Technology) for at least 18 hours prior to mixing. The soaking reaction was initiated by anaerobic addition of 20 mM 4NC to crystals of Co-HPCD. After 1-hour incubation, crystal complexes were rapidly transferred into mother liquor solution containing 25% PEG400 prior to cryo-cooling in liquid nitrogen inside the anaerobic glove box. Crystals of Fe-and Mn-HPCD were grown in 13% PEG 6000, 0.125 M calcium chloride, 0.1 M Tris-HCl, pH 6.5 and cryo-cooled in liquid nitrogen using 25% PEG400 as cryoprotectant. Buffers with superior buffering capacity to Tris-HCl at pH 6.5 were tested but were found to result in lower quality diffraction

data. Adequate buffering was provided by the combination of Tris-HCl, PEG6000 (pK_a ~ 6), and the high concentration of the enzyme itself. X-ray diffraction data were collected at 100 K under the stream of liquid nitrogen. All diffraction data were processed using the XDS package,[194] with Friedel pairs kept separate for anomalous difference datasets. For high-resolution datasets, the coordinates of the Fe-HPCD (PDB 2IG9) were used as an initial model in rigid body refinement followed by cycles of restrained refinement with Refmac5[195] as part of the CCP4 program suite[196] and model building using Coot.[197] TLS was used in the final round of restrained refinement, with a single monomer defined as a TLS group. Link restraints to the metal (Mn, Fe or Co) were removed from the refinement to avoid bias in the refined metal-ligand distances. NCS restraints were not used during refinement, and the 4 subunits of the single enzyme molecule present in the asymmetric unit were refined independently. Anomalous difference maps were calculated in CCP4[197] using the calculated phases from PDB 3OJJ (Co-HPCD), PDB 3OJT (Fe-HPCD) or PDB 3OJN (Mn-HPCD) and the relevant anomalous difference amplitudes. X-ray data processing and refinement statistics are summarized in Tables S1, S2 and S3. All structure figures were produced using PyMOL Molecular Graphics System, Version 0.99, Schrödinger, LLC

2.2.9 UV-Vis absorption spectroscopy. Concentrated solutions of Co-HPCD exhibit a salmon pink color arising from the weak d-d transitions of Co(II). To accurately determine the extinction coefficients arising from these formally forbidden transitions, the UV-Vis spectrum of a 60 μM Mn-HPCD, which has no chromophore in the visible region, was used as reference and subtracted from the spectra of 60 μM Co-HPCD

(40 μM Co) and its complexes to obtain the difference spectra shown in the Results section.

2.2.10 EPR sample preparation and spectroscopic methods. EPR samples were made to a volume of 300 μL, with 300 μM Co- HPCD in 50 mM MOPS buffer (pH 7.8). Samples were frozen by slow immersion in liquid nitrogen. Anaerobic samples were prepared by purging Co-HPCD and HPCA separately by reeated cycling under argon and vacuum before mixing, followed by anaerobic sample transfers into EPR tubes using cannula. EPR spectra were recorded on a Bruker Elexsys E-500 spectrometer equipped with an Oxford Instruments ESR-10 liquid helium cryostat at X-band (9.64 GHz). Spectra were acquired at 20 K over a magnetic field range of 100–6000 G using 2 mW power, 10 G modulation amplitude, and 100 kHz modulation frequency.

2.3 Results

2.3.1 Metal-substituted enzymes. Metal-substituted HPCDs were expressed in *E. coli* cells grown in M9 minimal media in the presence of added Co(II), Ni(II), Cu(II), or Zn(II) ions. Enzyme preparations were analyzed by ICP-AES for their iron, manganese, cobalt, nickel, copper and zinc metal contents. The average metal occupancies (Table 2.1) show the highest incorporation for Co(II) and Cu(II) with little incorporation of Ni(II) and Zn(II). Contaminating amounts of iron and manganese were found in all preparations, but were typically less than or equal to 0.13 and 0.04 equivalents, respectively.

Table 2.1. Apparent steady-state kinetic parameters[a] and metal composition analysis of HPCDs.

Metal = ($\Delta E°$, V)[b]	[Metal]/[Subunit]			K_M^{HPCA} (μM)	K_M^{O2} (μM)	k_{cat}/[Metal (min^{-1})	k_{cat}/K_M^{HPCA} (μM^{-1} min^{-1})	k_{cat}/K_M^{O2} (μM^{-1} min^{-1})
	Target Metal	Fe	Mn					
Fe[c] (0)	0.7	0.7	<0.1	31 ± 6	60	470 ± 20	15 ± 3	7.8 ± 0.3
Mn[c] (0.79)	0.8	<0.1	0.8	35 ± 5	50 ± 4	370 ± 10	11 ± 2	7.4 ± 0.6
Co (1.15)	0.6(2)	<0.02	<0.01	5 ± 1	1200 ± 100	215 ± 8[a] 590 ± 20[d] 1120 ± 70[e]	43 ± 9 120 ± 20 220 ± 50	0.18 ± 0.02 0.49 ± 0.05 0.9 ± 0.1
Ni (1.5)	0.1(2)	0.06	0.02	—	—	10 ± 9[f]	—	—
Cu (1.6)	0.5(1)	0.13	0.02	—	—	12 ± 10[f]	—	—
Zn (—)	0.1(6)	0.08	0.04	—	—	4 ± 1[f]	—	—

[a] measured under ambient O_2 at 22 °C in 50 mM MOPS (pH 7.8); unless otherwise noted, apparent k_{cat} has been normalized by metal content from ICP-AES results. [b] difference in standard electrode potentials (in water at 298.15 K, pH = 0.0) from E° for Fe(III/II) (+0.77 V vs SHE).[178] [c] data from reference.[131] [d] measured in O_2-saturated buffer at 22 °C. [e] V_{max} extrapolated from Figure 2.3. [f] protein incubated in 1 mM H_2O_2 prior to being assayed; activity due to contaminating manganese detected by ICP-AES has also been subtracted.

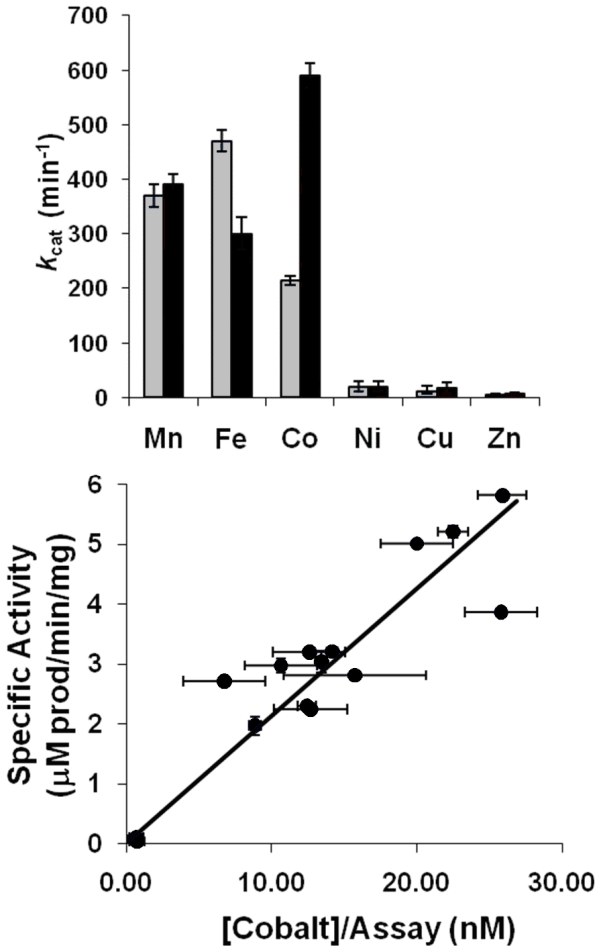

Figure 2.1. (Top) Comparison of activity of metal-substituted HPCDs measured in air-saturated (260 μM O_2, gray bars) and oxygen-saturated buffer (1.37 mM O_2, black bars) in 50 mM MOPS (pH 7.8) at 22 ºC determined by monitoring formation of the 5-CHMSA product (ε_{380} = 38,000 M^{-1} cm^{-1}). k_{cat} values have been normalized by metal content from ICP-AES results. Error bars were calculated from both the standard deviation in metal concentration measured from multiple samples submitted for ICP-AES metal analysis and from observed rates from multiple assays. (Bottom) Correlation between cobalt concentration determined from ICP-AES analysis and specific activity of Co-HPCD assayed in the presence of 1 mM H_2O_2. The black line was obtained from a linear regression fit of the data (R^2 = 0.87). Error bars represent ±1 standard deviation in average cobalt concentration determined from multiple samples for ICP-AES analysis.

2.3.2 Activation and inhibition studies. The activities of metal-substituted HPCD enzymes in the presence of reducing or oxidizing agents were examined to correlate the specific metal present with dioxygenase activity. The residual activity due to contaminating Fe-HPCD could be removed by incubating protein with 1 mM H_2O_2 or another oxidant for 5 minutes before the assay. The activity due to contaminating manganese was calculated by assuming that all Mn detected by ICP-AES gave rise to active Mn-HPCD. Of the various metal-substituted enzymes studied, only Co-HPCD showed significant HPCA cleavage activity (Figure 2.1, top) that could not be accounted for by contaminating iron or manganese. The Co-HPCD preparations also showed a good correlation between metal content and specific activity (Figure 2.1, bottom), while preparations with other metals showed no such correlation. Consequently, the Cu(II)-, Ni(II)-, and Zn(II)-substituted enzymes are not considered further here.

As previously reported, Fe-HPCD was found to be susceptible to inactivation by oxidants such as H_2O_2, $[Fe(CN)_6]^{3-}$ and even O_2, but regained full activity after incubation with ascorbate (Table 2.2).[131] In contrast, Co-HPCD, like Mn-HPCD, was essentially unaffected by treatment with the strong oxidizing agents H_2O_2 and potassium persulfate, as only a small decrease in activity was observed for both the Mn-HPCD and Co-HPCD samples assayed. This decrease can presumably be attributed to inactivation of contaminating Fe(II)-HPCD in the samples. Indeed, a small increase in activity was also observed for both Mn-HPCD and Co-HPCD upon incubation with L-ascorbate, reflecting activation of air-oxidized Fe(III)-HPCD contaminant. Figure 2.2 illustrates the sensitivity of Fe- Mn- and Co-HPCDs to O_2. Fe-HPCD afforded only 1,000–2,500 turnovers in

air-saturated buffer, while both Mn- and Co-HPCD consumed all the HPCA (33,000 turnovers) under these conditions. The latter observations clearly show that the activity of these metal-substituted enzymes is not due to contamination by Fe-HPCD. The resistance of Co-HPCD to H_2O_2-induced inactivation suggests that the cobalt center retains a high redox potential relative to iron when it is bound in the protein.

Table 2.2. Effect of various reagents on the activity of M-HPCDs compared to full activity in the presence of L-ascorbate. Standard deviations in percent activities ranged from 2 to 5%.

	Percent Activity		
Reagent	**Fe-HPCD**	**Mn-HPCD**	**Co-HPCD**
As isolated	83	93	99
L-ascorbate	100	100	100
Hydrogen peroxide	7	93	93
Potassium persulfate	11	92	91
Potassium ferricyanide	9	100	100

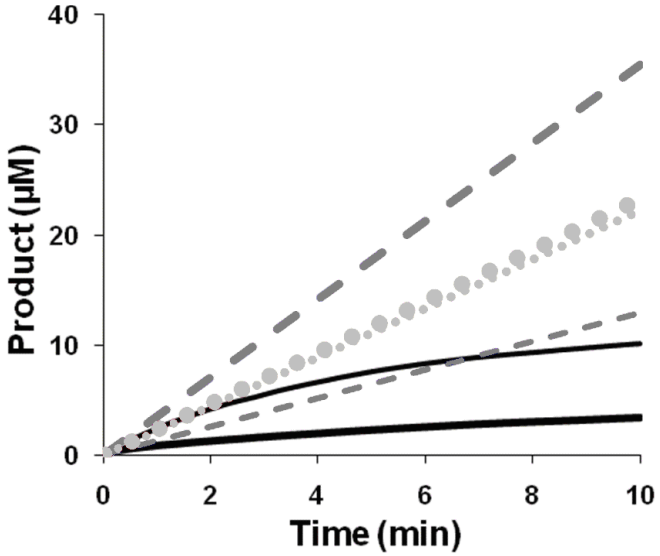

Figure 2.2. Representative progress curves for HPCA turnover by metal-substituted HPCDs carried out in air-saturated (thin lines) and O_2-saturated (thick lines) buffer. Mn-HPCD (light gray, dotted lines), Fe-HPCD (dark gray, solid lines), Co-HPCD (blue, dashed lines). Reactions contained 6 nM M-HPCD and 2 mM HPCA in 50 mM MOPS (pH 7.8) at 22 °C.

2.3.3 Steady-state kinetics. The apparent Michaelis-Menten kinetic parameters for reactions of Fe-, Mn-, and Co-HPCD enzymes with HPCA are reported in Table 2.1. The apparent k_{cat} for Co-HPCD (215 ± 8 min^{-1}), is approximately half the values reported for Fe-HPCD (470 ± 20 min^{-1}) and Mn-HPCD (370 ± 20 min^{-1}) in air-saturated (260 μM O_2) 50 mM MOPS buffer at pH 7.8, 22 °C. However, during the course of efforts to measure the K_M^{O2} for Co-HPCD, we found that the k_{cat} continued to increase even as O_2 approached saturation (1.37 mM at 22 °C) (Figure 2.3). Mn-HPCD showed zero-order kinetics at these O_2 concentrations, and the Fe-HPCD activity decreased slightly (280 ± 10 min^{-1}), presumably due to oxidation of the Fe(II) cofactor (Figure 2.1 top). Co-HPCD was found to be the most active (590 ± 20 min^{-1}) of the three enzymes under these high O_2 conditions (Figure 2.1).

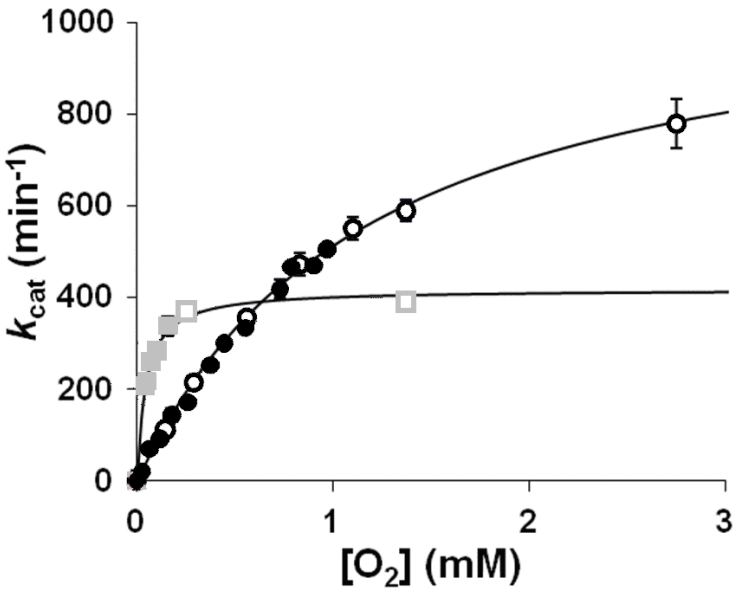

Figure 2.3. Michaelis-Menten plot of varying O_2 concentration for Co-HPCD (black ●) and Mn-HPCD (gray, ■) in the presence of 2 mM HPCA measured at 22 ºC. k_{cat} was calculated from initial velocities at different oxygen concentrations. Data points with closed symbols were measured using a Clark-type oxygen electrode, while points with open symbols were obtained by following product formation by UV-Vis spectroscopy. O_2 dependence data were fit to the Michaelis-Menten equation (solid lines).

From fitting the Michaelis-Menten plot for oxygen dependence (Figure 2.3) a maximum rate of 1120 ± 70 min^{-1} for Co-HPCD under truly oxygen saturating conditions is possible. The apparent K_M^{O2} for Co-HPCD is 1200 ± 100 μM (Figure 2.3, Table 2.1), twenty-fold higher than those for either Fe-HPCD (50 μM) or Mn-HPCD (60 μM). The catalytic efficiency (k_{cat}/K_M^{O2}) of 0.9 ± 0.1 μM^{-1} min^{-1} for Co-HPCD is an order of magnitude smaller than the corresponding-values for Fe- and Mn-HPCD (7.8 ± 0.3 and 7.4 ± 0.6 μM^{-1} min^{-1}, respectively). This suggests that [Co-HPCD(HPCA)] has a lower effective O_2 affinity, but the overall rate limiting step for Co-HPCD must be more efficient than those of Mn- and Fe-HPCDs.

2.3.4 X-ray crystal structure comparisons. One possible explanation for the high activity of Co-HPCD is that the structure of the active site may differ from that of Fe-HPCD such that the redox potential of the Co(II) ion becomes more similar to that of Fe(II) in Fe-HPCD. Recently, we reported the full length structures of Fe-HPCD (PDB 2IG9) and for Mn-HPCD (PDB 3BZA).[131, 165] Higher resolution structures of Fe-HPCD (1.70 Å, PDB 3OJT) and of Mn-HPCD (1.65 Å, PDB 3OJN) are also reported here (Tables 2.5 and 2.6) and used for all comparisons. To evaluate the structural consequences of the cobalt substitution, the X-ray crystal structure of Co-HPCD was solved to 1.72 Å resolution (Table 2.4). The presence of cobalt in the active site of HPCD was confirmed by anomalous difference X-ray diffraction data collected at the cobalt K-absorption edge and pre-edge energies (Figure 2.4 and 2.9, and Table 2.4). Four strong anomalous difference peaks corresponding to the positions of the four active site metals in the Co-HPCD tetramer are observed in X-ray diffraction data collected at the cobalt K-edge X-ray absorption energy. Data collected for Fe-HPCD and Mn-HPCD at their respective metal K-edge energies show the metal binding in the same position as in Co-HPCD (Figure 2.9). The comparison of the resting state structures shows that the identity of the metal (Fe, Mn, Co) has no effect on the overall protein structure as indicated by the RMSD values of 0.18–0.20 Å for superposition of all atoms of the Fe-HPCD (PDB 3OJT), Mn-HPCD (PDB 3OJN) and Co-HPCD (PDB 3OJJ) structures. Moreover, no significant structural differences are observed locally in the active site environment as indicated by the RMSD values of 0.10–0.14 Å for superposition of all atoms within 15 Å of the metal center in the Fe-HPCD and Co-HPCD structures. As

illustrated in Figure 2.5A, cobalt substitution also preserves the distorted octahedral coordination geometry of the metal center in which solvent molecules occupy three coordination positions on one face of the metal as observed in the new, high-resolution structures of Fe-HPCD and Mn-HPCD. In addition, the presence of Co in the active site does not elicit any changes in the mode of substrate binding or in the conformational geometry of the active site residues in the enzyme-substrate complex (Figure 2.5B). These results suggest that the protein structure does not tune the redox potential of Co(II) into the range of Fe(II), and the observed activity is thus due to Co(II) with a much higher redox potential than that of Fe(II) in the active site. Therefore, any observed differences in activity must arise from the inherent electronic properties of the metal rather than from structural properties of the protein *per se*.

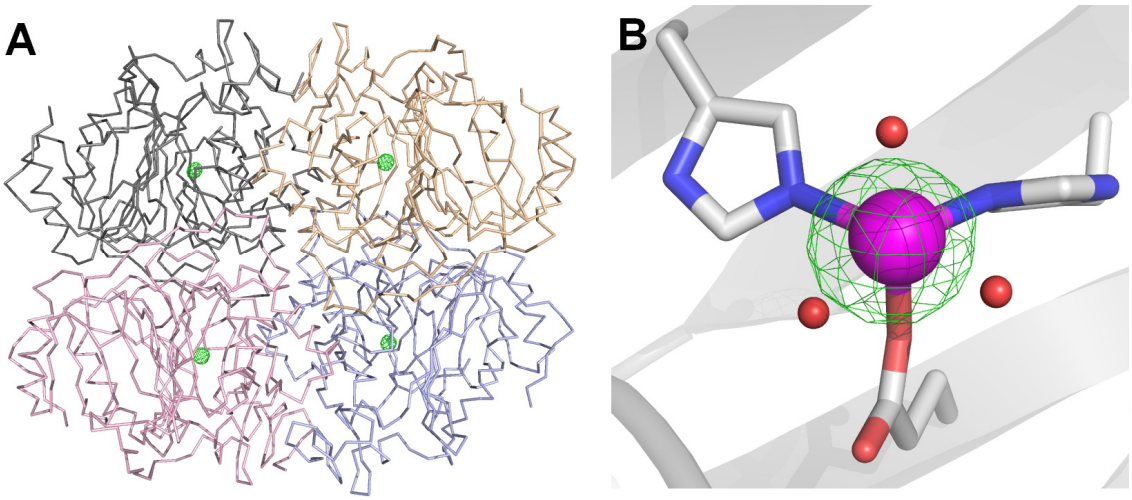

Figure 2.4. A) Model of Co-HPCD tetramer and anomalous difference map calculated from the X-ray diffraction dataset collected at the cobalt K-edge (1.6050 Å, 7.725 keV). The gray, gold, pink and blue ribbons depict backbone representations for the four subunits of Co-HPCD (PDB 3OJJ). The anomalous difference Fourier map (green mesh) is contoured at 8 σ. B) Active site of Co-HPCD (PDB 3OJJ). Anomalous difference maps were calculated from a dataset collected at the Co K-edge (1.6050 Å, 7.725 keV, green mesh, 8 σ contour) and pre-edge (1.6077 Å, 7.712 keV, red mesh, 5 σ contour). Model depicts the metal-(2-His-1-carboxylate) center in subunit C of Co-HPCD structure. Atom color-code: gray, carbon; blue, nitrogen; red, oxygen; magenta, cobalt.

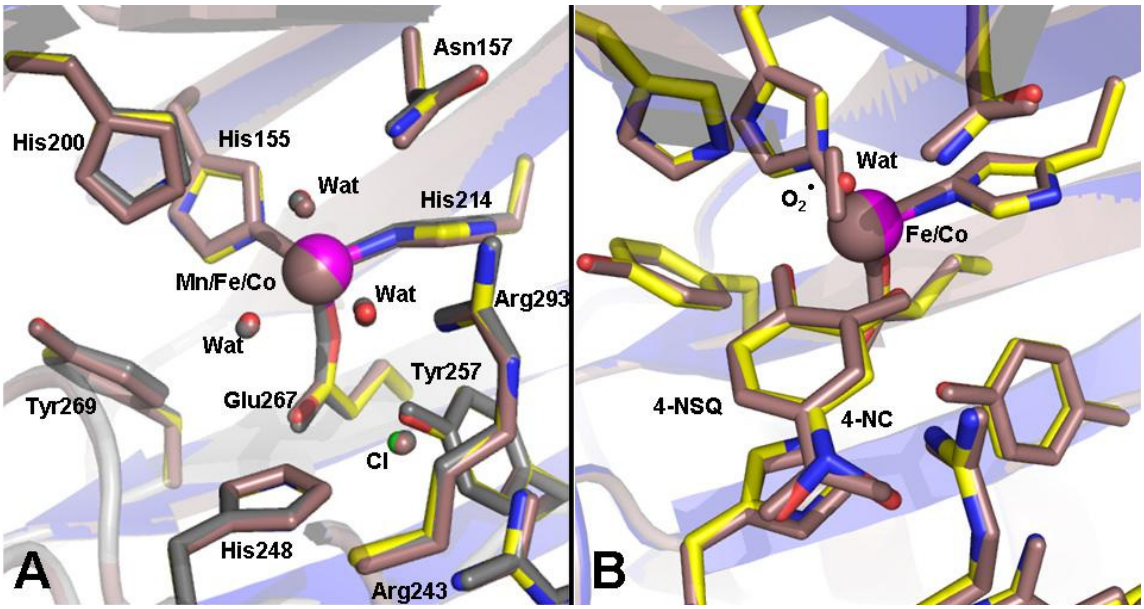

Figure 2.5. Structural comparison of the active site environments in HPCD enzymes with Fe(II), Mn(II) and Co(II) centers. A) Structure superposition of the metal centers in the resting state of Fe-HPCD (PDB 3OJT; bronze), Mn-HPCD (PDB 3OJN; gray) and Co-HPCD (PDB 3OJJ; color-coded). The bronze, gray and blue cartoons depict the secondary structure elements for Fe-HPCD, Mn-HPCD and Co-HPCD, respectively. B) Structural overlay of active sites in the [Co-HPCD(4NC)] complex (PDB 3OJK, color-coded) and [Fe-HPCD(4NSQ)superoxo] complex (PDB 2IGA, bronze). An RMSD value of 0.15 Å is found for the superposition of all protein-derived atoms within 15 Å from the metal center in the substrate-bound complex structures (PDB 2IGA and 3OJK). Atom colors: yellow, carbon; blue, nitrogen; red, oxygen; magenta, cobalt; green, chlorine.

2.3.5 Spectroscopic characterization.

2.3.5.A Electronic absorption spectra of high-spin Co(II) enzyme and enzyme-substrate complexes. It is also possible that the activity of the Co-HPCD stems from a perturbation of the protein structure in solution that is not revealed in the crystal structure, leading to a distinct redox potential tuning. The rich optical and EPR properties of Co-HPCD can be used to examine the electronic and geometric structure of the Co(II)

center. There is a well-established correlation between the coordination number and the extinction coefficients of the d-d transitions normally observed in the visible region from 450–750 nm of high-spin Co(II) model complexes.[198-200] As the coordination number and symmetry at the metal center decrease, the intensities of the forbidden d-d transitions increase due to greater p-d orbital mixing. Consequently, typical six-coordinate Co(II) complexes have molar absorptivities less than 50 M^{-1} cm^{-1}, while five-coordinate complexes have values between 50–250 M^{-1} cm^{-1} and four-coordinate complexes, greater than 300 M^{-1} cm^{-1}. Co-HPCD solutions exhibit a pale salmon pink color that is due to a broad visible absorption at 500 nm with a molar extinction coefficient of 60 M^{-1} cm^{-1}, suggesting either a five-coordinate or highly distorted six-coordinate high-spin Co(II) center (Figure 2.6).[198-200] The anaerobic addition of HPCA to Co-HPCD does not elicit a significant change in the visible spectrum, suggesting no change in the coordination number upon substrate binding. The fairly unstructured broad nature of the absorption bands in both complexes favors a six-coordinate over a five-coordinate center.[199] Therefore, our findings from the UV-Vis spectroscopy (Figure 2.6) are in agreement with the conclusions drawn from the X-ray crystal structure analysis (Figure 2.5 and Table 2.7), which revealed a distortion of the cobalt ligand environment away from an idealized six-coordinate geometry.

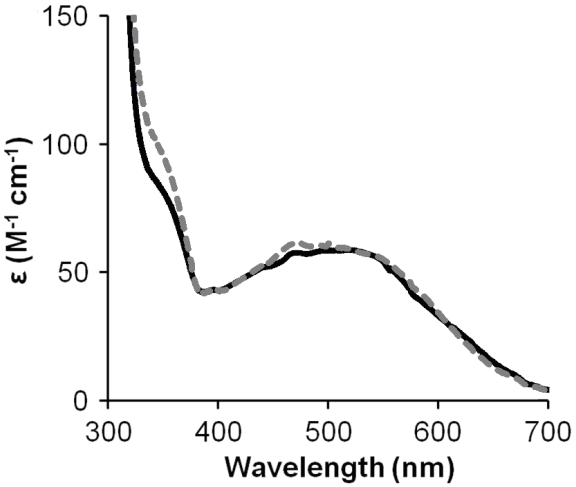

Figure 2.6. Visible absorption spectra of Co-HPCD (black line) and [Co-HPCD(HPCA)] (dashed, gray line). To accurately determine the extinction coefficients of the weak d-d transitions of Co(II), a solution of Mn-HPCD, which has no chromophore in the visible region, was used as a reference to correct the baseline of spectra in the visible region.

2.3.5.B EPR spectra of high-spin Co(II) enzyme and enzyme-substrate complexes. X-band EPR spectra of Co-HPCD and its complex with HPCA are shown in Figure 2.7. These spectra were collected under non-saturating conditions at 20 K, because at lower temperatures (*i.e.* 5 K) the spectra exhibited an absorption-like appearance due to rapid-passage effects commonly observed for cobalt complexes at 4 K due to slow relaxation.[201, 202] Co-HPCD exhibits a dominant rhombic signal with *g*-values at 6.7, 3.4 and 2.4 (Figure 2.7), arising from the ground Kramers doublet of a high-spin d^7 Co(II) center (S = 3/2).[199, 202, 203] The low-field signal exhibits well-resolved 8-fold hyperfine splitting with A = 80 G, due to the nuclear spin of ^{59}Co (I = 7/2). Anaerobic addition of HPCA drastically perturbs the spectrum (Figure 2.7), leading to an increase in both the rhombicity of the EPR signal (g = 7.6, 2.5, 1.9) and the magnitude of the ^{59}Co hyperfine splitting of the low-field signal (A = 98 G) (Figure 2.7).[177, 204]

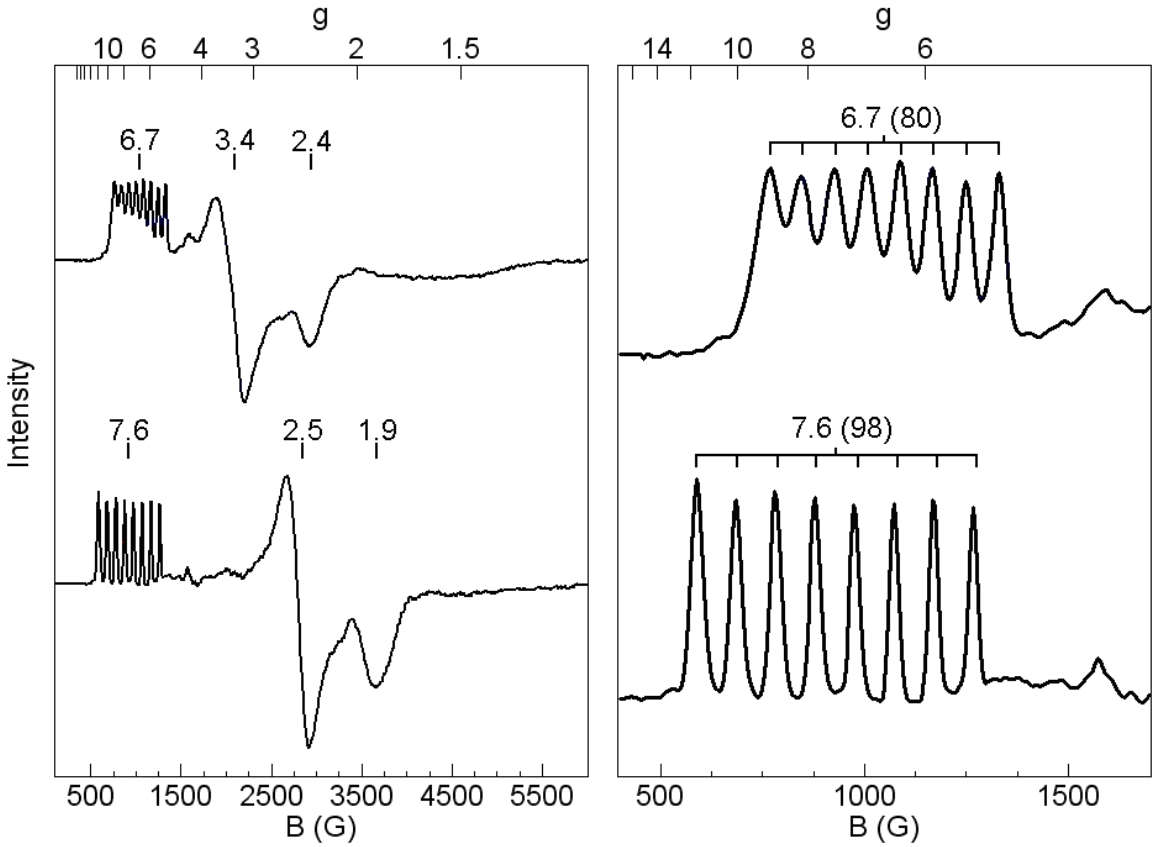

Figure 2.7. (Left panel) EPR spectra obtained at 9.64 GHz and 20 K of Co-HPCD at pH 7.8 (top), and [Co-HPCD(HPCA)] (bottom). The small signal at g = 4.3 derives from contaminating Fe(III). (Right panel) Magnification of the low-field regions of Co-HPCD (top) and [Co-HPCD(HPCA)] (bottom).

Table 2.3 compares the EPR parameters of Co-HPCD complexes with those found for other cobalt containing enzymes as well as several model complexes. This collection of data reveals that S = 3/2 Co(II) centers can exhibit a large range of rhombicities that give rise to g-values as high as 9 and as low as 1. The spectra of Co-HPCD and [Co-HPCD(HPCA)] have rhombicities comparable to those observed for Co-glyoxalase I, [CoZnAAP(LPA)], and [ZnCoAAP(LPA)].[200, 204, 205] Co-HPCD and [Co-HPCD(HPCA)] both exhibit ^{59}Co hyperfine splitting with large A-values of 80 and

98 G, respectively. In general, octahedral and square pyramidal complexes exhibit well-resolved hyperfine features with large *A*-values, while trigonal bipyramidal and tetrahedral complexes have smaller values.[199, 206] Thus, the EPR data support a coordination number of six for the metal centers in Co-HPCD and [Co-HPCD(HPCA)], consistent with visible absorption spectral data as well as the results obtained from X-ray crystallography.

Table 2.3. EPR and visible absorption data for Co(II)-substituted enzymes and Co(II) complexes.

Sample[a]	Coord#	*g*-values	*A*(G)[b]	λ_{max} (nm)(ε, $M^{-1}cm^{-1}$)	Ref
Co-HPCD	**6**	**6.7, 3.4, 2.4**	**80**	**500 (60)**	45
[Co-HPCD(HPCA)]	**6**	**7.6, 2.5, 1.9**	**98**	**500 (60)**	45
Co-TauD	6			530 (70)	46
[Co-TauD(taurine)(α-KG)]	5			552 (200), 565 (204)	46
Co-QueD'		6.5, 4.3, 3			14
Co-QueD	*5 (TBP)*	6.16, 3.8, 2.37.16	76 95		13
[Co-QueD(quercetin)]	*5/4*	6.94, <1.5 6.23	39 95		13
Co-glyoxalase I	6	6.6, 3, 2.5	81	493 (35), 515 (33)	38
[CoZnAAP(LPA)]	*6/5*	6.66, 3.05, 1.90	70	525 (68)	42 43
[ZnCoAAP(LPA)]	6	6.23, 3.40, 1.95	49.5	500 (63)	42 43
Co-MBP-VanX	5	5.92, 2.57, 1.69		520, 550, 580 (~100)	47
CoZn-HLADH	4 (Td)	6.5, 2.2, 1.6	37	520 (200), 655 (600)	48 49 50
$Co(Tp)_2$	6	8.48, 1.02	93	460(13.4), 515(1.3)	40 51 52
$[Co(Tp^{Ph,Me})(3,4\text{-HOPO})]$	5 (SP)	8.18, 1.42, 0.98	102	445 (379), 555 (89)	44
$[Co(imidazole)_2(acetate)_2]$	4 (Td)	4.49, 4.23, 2.16	15/38	550(155)	36, 53
$[Co(imidazole)_2(C_2H_5CO_2)_2]$	4 (Td)	5.37, 3.43, 2.06	14/38	550(155)	36

[a]Abbreviations used: TauD taurine/α-ketoglutarate dioxygenase from *Escherichia coli*; QueD', Quercetin 2,3-dioxygenase from *Bacillus subtilis*; QueD, 2,3-dioxygenase from *Streptomyces sp.*; AAP, aminopeptidase from *Aeromonas proterolytica*; LPA, L-leucine phosphonic acid; MBP-VanX, fusion protein of gene product of vancomycin-resistance gene X from *Enterococcus* and maltose-binding protein; HLADH, horse liver alcohol dehydrogenase; Tp, tris(pyrazolyl)borate; $Tp^{Ph,Me}$, hydrotris(3,5-phenylmethylpryrazolyl)borate; 3,4-HOPO, 3-hydroxy-1,2-dimethyl-4-pyridinone; Td, tetrahedral; SP, square pyramidal; TBP, trigonal bipyramidal. [b]*A*-values listed are for the lowest-field signal, except for the last two entries where hyperfine splitting was also observed for the highest-field signal.

2.3.5.C Electronic absorption spectra of enzyme complexes with wt- and H200N-Co-HPCD. The enzyme and enzyme-substrate complexes of Co-HPCD and [Co-HPCD(HPCA)] exhibit very similar weak chromophores from the forbidden d-d transitions (ε_{500nm} ~50 M^{-1} cm^{-1}) consistent with six-coordinate high-spin Co(II) complexes (Figure 2.8).[198-200] Addition of the competitive inhibitor 3-hydroxyphenylacetic acid (3HPA, K_I = 95 ± 10 μM, Figure 2.9) results in an increase in the intensity and shift to slightly lower energy of the well-resolved bands at 350, 475, 510, 574 and 609 nm (ε = 175–230 M^{-1} cm^{-1}). The increase in intensity and shift to lower energy of the d to d transitions suggest that the enzyme-inhibitor complex is five-coordinate. Typically five-coordinate high-spin Co(II) complexes have extinction coefficients values between 50–250 M^{-1} cm^{-1} and similarly well-resolved multiple absorption bands (Tables 2.3 and 2.4).[198-200] The inhibitor likely binds by displacing two of the solvent ligands in the same position as the native substrate HPCA (3,4-dihydroxyphenylacetic acid) due to specific interactions between the acetic acid substituent and the anion-binding pocket His248/Arg293/Arg/243 of both HPCA and 3HPA.[207] 4-hydroxyphenylacetic acid (4HPA) also acts as a competitive inhibitor for turnover of HPCA by Co-HPCD but has a much lower affinity (K_I of 1.2 ± 0.1 mM) than 3HPA. The difference in affinities for 3HPA and 4HPA has been argued to imply asymmetric binding of the substrate or monoanionic binding of HPCA (HPCA = 3,4-dihydroxyphenylacetic acid), where the catechol is protonated at HO(C4) and deprotonated at O(C3) upon binding to the metal center. The asymmetric substrate-binding pocket may also influence the affinities for 3HPA and 4HPA where Y257 forms a short strong 2.57 Å hydrogen bond with O(C3) and H200 forms a weaker 3.05 Å

hydrogen bond with O(C4) in the crystal structure of [Fe-HPCD(HPCA)] enzyme-substrate complex (PDB 4GHG).[163, 177]

The second sphere H200N mutation perturbs the Co(II) ligand-field environment as seen by comparing electronic spectra of the weak d to d transitions of the wt- and H200N-Co-HPCD enzyme, enzyme-substrate, and enzyme-inhibitor complexes (Figures 2.8 and 2.10, Table 2.4). For the enzyme complexes the transition has shifted from ~500 to 575 nm with the H200N mutation. Two distinct bands are now observed with the H200N enzyme-substrate complex with bands at 525 and 600 nm. The transitions also shift to slightly lower energies with the H200N enzyme-inhibitor complex to 350, 490, 515, 575, and 612 nm. The shifts in the d to d transition observed with the H200N mutation suggest a weaker ligand-field environment for the H200N mutant. The overlay of the crystal structures of the [wt- and H200N-Co-HPCD(4NC)] enzyme-substrate complexes (Figure 2.11) show that the mutation results in a change in the hydrogen bonding network to the axial aqua ligand and elongation of the Co-O(H_2O) distance from 2.27 to 2.87 Å due to the shorter side chain of Asn200 then His200.

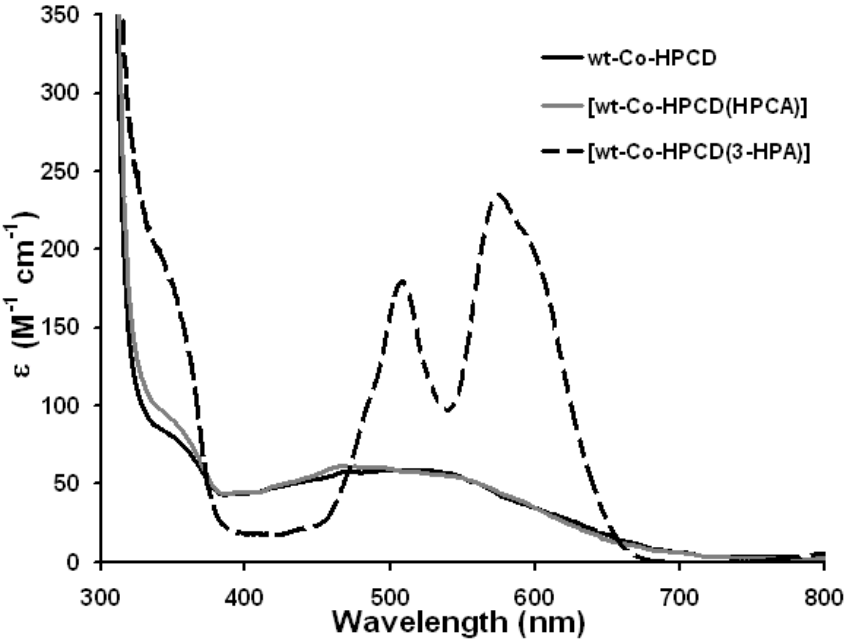

Figure 2.8. Visible absorption spectra of Co-HPCD (black line) and [Co-HPCD(HPCA)] (gray line) and [Co-HPCD(3HPA)] (dashed, black line).[169] To accurately determine the extinction coefficients of the weak d-d transitions of Co(II), a solution of Mn-HPCD, which has no chromophore in the visible region, was used as a reference to correct the baseline of spectra in the visible region.

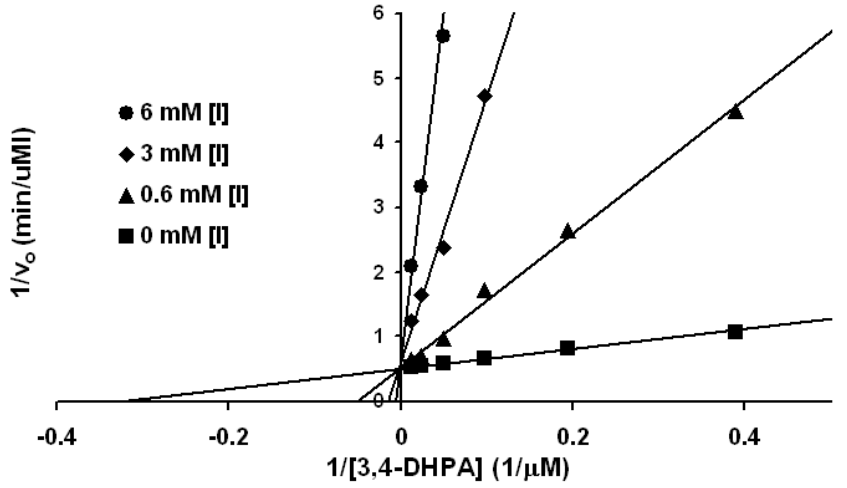

Figure 2.9. Lineweaver-Burk plot for inhibition of turnover of HPCA (2 mM) by Co-HPCD by competitive inhibitor 3-hydroxyphenylacetic acid (3HPA, K_I = 95 ± 10 μM). Reaction conditions: 50 mM MOPS (pH 7.8), 22 °C.

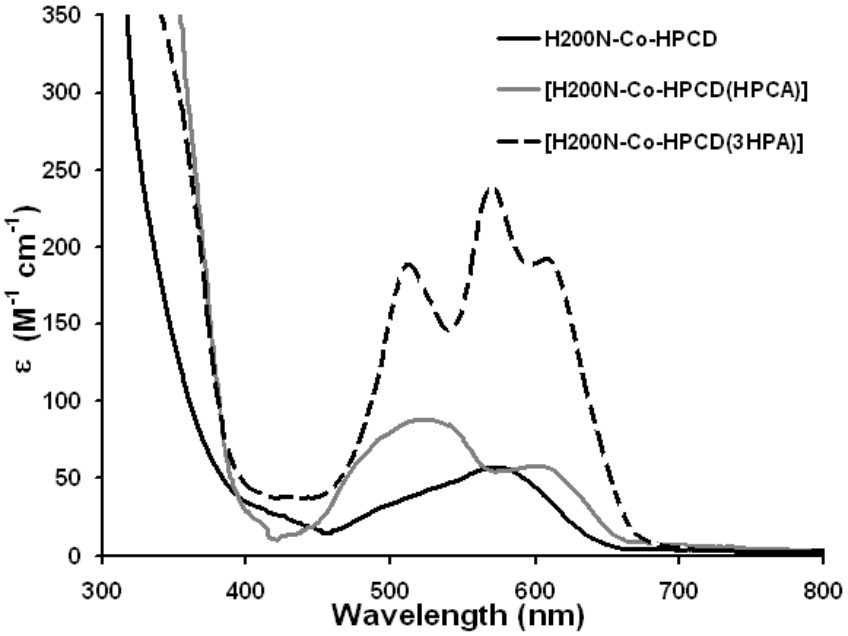

Figure 2.10. Visible absorption spectra of H200N-Co-HPCD (black line) and [H200N-Co-HPCD(HPCA)] (gray line) and [H200N-Co-HPCD(3HPA)] (dashed, black line). To accurately determine the extinction coefficients of the weak d-d transitions of Co(II), a solution of Mn-HPCD, which has no chromophore in the visible region, was used as a reference to correct the baseline of spectra in the visible region.

Table 2.4. Electronic absorption data for wt- and H200N-Co-HPCD and complexes.

Sample	λ and ε (nm / M^{-1} cm^{-1})	Ref
wt-Co-HPCD	500(~50)	[169]
H200N-Co-HPCD	575(~50)	This work
[wt-Co-HPCD(HPCA)]	500(~50)	[169]
[H200N-Co-HPCD(HPCA)]	525(88), 600(60)	This work
[wt-Co-HPCD(3HPA)]	475(50), 510(175) 574(235), 609(150)	This work
[H200N-Co-HPCD(3HPA)]	490(50), 515(185), 575(235), 612(190)	This work

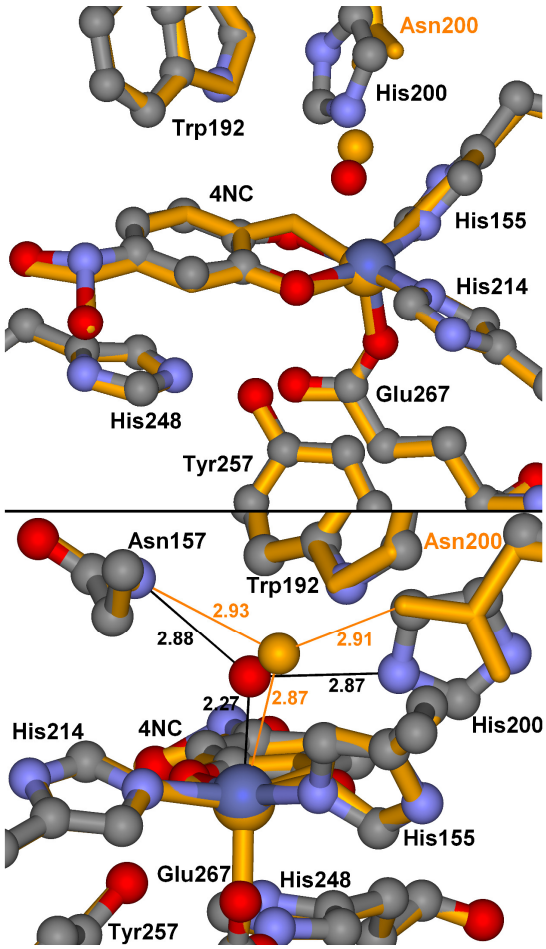

Figure 2.11. Overlays of crystal structures of [Co-HPCD(4NC)] (1.77 Å, PDB 3OJK) and [H200N-Co-HPCD(4NC)] (orange, unpublished work of Dr. Elena G. Kovaleva) from two different views.[169]

2.3.5.D X-ray absorption spectroscopy studies of Co-HPCD complexes. The results of the electronic absorption spectra reported here are consistent with X-ray absorption spectroscopy (XAS) experiments carried out by Dr. Erik R. Farquhar on the enzyme, enzyme-substrate and enzyme-inhibitor complexes reported in his doctoral thesis.[207] Most notably to the discussion here are the observed peak areas for the pre-edge features of the complexes in the X-ray absorption near edge structure (XANES) region (Figure 2.12 and Table 2.5). The pre-edge feature originates from the dipole forbidden 1s to 3d transitions.

The intensity of these symmetry forbidden transition increases with increased 3d to 4p orbital mixing as the geometry of the molecule distorts away from perfect centrosymmetric octahedral geometry. The three complexes all have similar edge and pre-edge energies expected for high-spin Co(II).[208-211] The relatively small peak areas (Table 2.5) of the pre-edge features for Co-HPCD and the [Co-HPCD(HPCA)] enzyme-substrate complex of 4.7 and 4.1 units respectively are consistent with six-coordinate high-spin Co(II) and suggest that only two of the three water ligands are lost upon substrate binding. Upon addition of 3HPA the pre-edge area increases to 18.2 units expected for a distorted five-coordinate high-spin Co(II) center.[207]

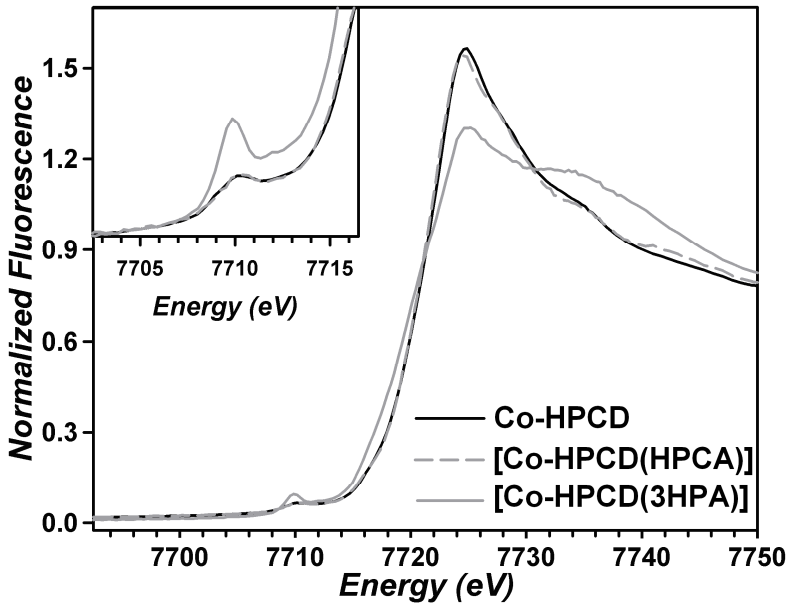

Figure 2.12. Comparison of the Co K-edge X-ray absorption edge and pre-edge (inset) features for Co-HPCD, [Co-HPCD(HPCA)] and [Co-HPCD(3HPA)].[207]

Table 2.5. Pre-edge analysis parameters for Co-HPCD, enzyme, enzyme-substrate and enzyme-inhibitor complexes.[207]

Species	E_{edge} (eV)	$E_{pre\text{-}edge}$ (eV)	Total Area
Co-HPCD	7722.77	7710.13	4.7
[Co-HPCD(HPCA)]	7722.47	7710.13	4.1
[Co-HPCD(3HPA)]	7723.08	7710.51	18.2

2.3.5.E Electron paramagnetic resonance spectra of 3HPA enzyme-inhibitor complexes. The EPR spectra of the two five-coordinate [wt- and H200N-Co-HPCD(3HPA)] enzyme-inhibitor complexes (Figure 2.13) have interesting EPR spectra distinctly different from the enzyme and enzyme-substrate complexes (Figure 2.7). The complexes have features at very low-field (g = 7.0) and very high-field (g = 1.1) with well-resolved ^{59}Co hyperfine in the low-field feature with relatively small ^{59}Co hyperfine splitting-values of 33 and 25 G for the wt and H200N complexes, respectively compared to the values of 80 and 90 G observed for the six-coordinate wt-Co-HPCD and [wt-Co-HPCD(HPCA)]. The 25–33 G ^{59}Co hyperfine splitting is similar to other five-coordinate high-spin Co(II) complexes (Table 2.3).[199, 206]

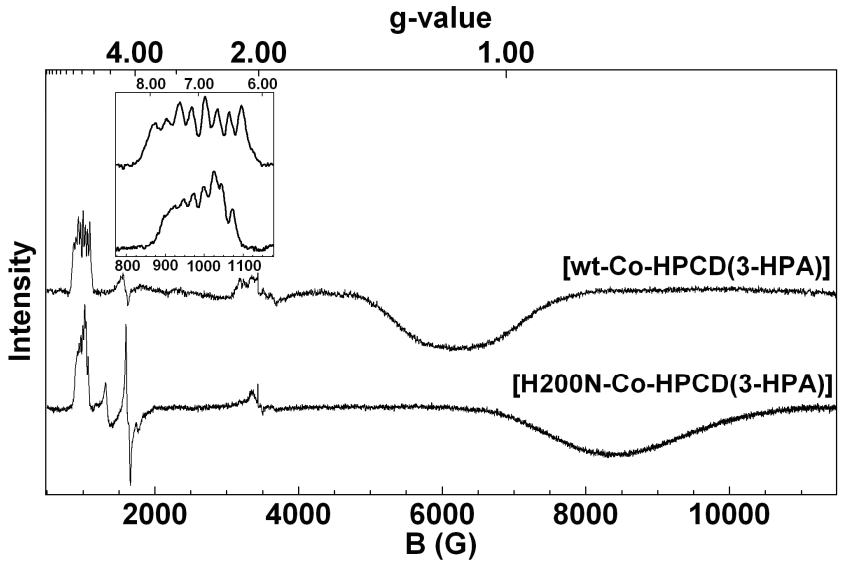

Figure 2.13. EPR spectra of [wt-Co-HPCD(3HPA)] (g = 7.1 and 1.1, ^{59Co}A = 33 G) and [H200N-Co-HPCD(3HPA)] (g = 7.0 and 0.8, ^{59Co}A = 25 G) enzyme-inhibitor complexes. The signal at g = 4.3 and 2.0 derives from contaminating Fe(III) and Mn(II), respectively.

2.3.6 Transient kinetic experiments. The lack of visible absorption features exhibited by the metal center and the native substrate (HPCA) of Fe-HPCD has complicated transient kinetic experiments in the past. One approach has been to monitor the time course of formation of the yellow ring-cleaved product after mixing anaerobic [Fe-HPCD(HPCA)] with oxygenated buffer.[166] In these experiments, a short lag phase prior to product formation was observed and the time course could be fit with two summed exponential phases, neither showing O_2 concentration dependence.[166] Preliminary stopped-flow experiments for the reactions of the [Co-HPCD(HPCA)] and [Mn-HPCD(HPCA)] enzyme substrate complexes with oxygenated buffer are shown in Figure 2.14. Like Fe-HPCD, both Co- and Mn-HPCDs exhibit a lag phase in product formation. While the Mn-HPCD time course shows only a small O_2 concentration

dependence, that of Co-HPCD is much more significant and exhibits multiple phases, the detailed analysis of which will be reported in a subsequent publication.

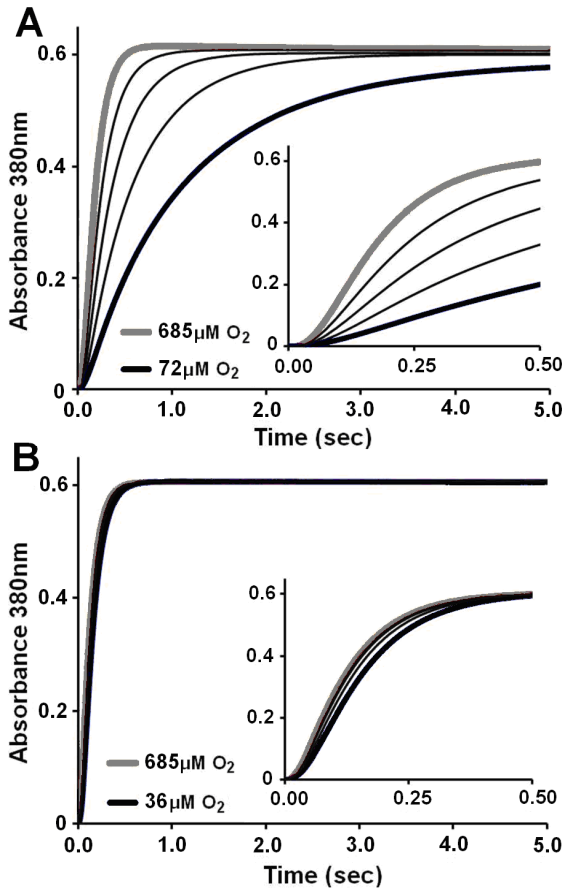

Figure 2.14. Single wavelength (380 nm) stopped-flow kinetic data for [Co-HPCD(HPCA)] (panel A) and [Mn-HPCD(HPCA)] (panel B) rapidly mixed with oxygenated buffer. O_2 concentrations upon mixing ranged from 36 to 685 μM O_2. Final concentrations of reagents after mixing: 20 μM HPCA and 50 μM M-HPCD. Reaction conditions: 50 mM MOPS (pH 7.8), 22 °C. Each inset highlights the observed lag phase that precedes product formation.

2.4 Discussion

Co(II) has been successfully incorporated into the active site of HPCD, producing the first example of an active cobalt-containing, extradiol ring-cleaving, catechol dioxygenase. In combination with our previous study of Mn-HPCD,[131] the results reported here show that the native Fe(II) center of HPCD can be replaced by the metal ions to both its left and right in the first-row transition metal series. Co(II)-HPCD is in fact highly active, having the largest k_{cat} yet found for any metal-HPCD preparation. Nevertheless, it is significant that in contrast to Mn-HPCD, Co-HPCD exhibits a K_M^{O2} value quite different from that observed for the native Fe-HPCD. This suggests that new insights into the chemical steps of oxygen activation and insertion by extradiol dioxygenases may be revealed by the study of this new metal-substituted enzyme form. This is discussed in the sections that follow in the context of the current proposal for the enzyme mechanism.

2.4.1 Mechanism proposed for extradiol dioxygenases. The mechanism proposed for the extradiol-cleaving catechol dioxygenases is depicted in Scheme 2.2.[131, 155, 165, 181, 192] In the resting, as isolated state, the high-resolution structure of the enzyme reported here shows that it has a six-coordinate Fe(II) center coordinated by three protein amino acid residues in a 2-His-1-carboxylate facial triad metal binding motif and three *cis*-labile solvent-derived ligands occupying the remaining three facial coordination sites (Scheme 2.2A).[53, 165, 174, 212] Catecholic substrate binds to the iron as a monoanionic bidentate ligand, displacing at least two of the bound waters (Scheme 2.2B).[213, 214] The third solvent is observed with variable occupancy in some crystal structures but is not observed in others,[174, 212, 215] suggesting that it becomes more labile upon substrate

binding. The coordination of the anionic substrate serves to lower the redox potential of the Fe(II) center and promote the dissociation of the final solvent and the binding of O_2 to form a transient Fe(III)-superoxo intermediate (Scheme 2.2C), following the heme paradigm.[188, 189] Although the putative Fe(III)-superoxo intermediate has not to date been directly detected in the wild type enzyme, it has recently been trapped in the case of the H200N mutant with 4-nitrocatechol as substrate.[162] This supports the hypothesis that the Fe(III)-superoxo species is formed, but it has a very short lifetime. At this point in heme enzyme mechanisms, an electron from an external reductant is introduced to form an Fe(III)-peroxo intermediate. Instead for HPCD, an electron is postulated to be transferred from the catecholate substrate to the iron center, generating a substrate radical-Fe(II)-superoxide species (Scheme 2.2D). Subsequent C–O bond formation between the semiquinone radical and superoxide leads to an alkylperoxo-Fe(II) species (Scheme 2.2E) that breaks down via a lactone intermediate (Scheme 2.2F) to afford the ring-opened product (Scheme 2.2G).

Strong support for this scheme derived from recent crystallographic studies where exposure of [Fe-HPCD(4NC)] to trace O_2 resulted in intermediates D, E, and G being trapped in different active sites present in the asymmetric unit.[165] The apparent stability of these intermediates *in crystallo* allowed them to be structurally characterized revealing geometries very close to those predicted from biochemical, chemical, and computational studies.[155, 165, 180]

Subsequent spectroscopic studies on the reaction of [Mn-HPCD(HPCA)] with O_2[179] also provided support for this mechanistic scheme. These studies applied rapid freeze-quench techniques and took advantage of the EPR properties of the $S = 5/2$ Mn(II)

center of Mn-HPCD to monitor intermediates formed during the reaction. At the shortest observable time after mixing (approximately 15 ms), an S = 5/2 species comprised of Mn(III) spin coupled to a radical was observed and proposed to originate from either a Mn(III)-superoxide (Scheme 2.2C) or a Mn(III)-peroxide-HPCA radical moiety. Within 30 ms this species converted to a second S = 5/2 species attributed to a Mn(II) species, which was tentatively assigned to the proposed alkylperoxo-Mn(II) intermediate (Scheme 2.2E).

2.4.2 Basis for the high turnover rate of Co-HPCD. The substitution of the native Fe(II) in HPCD with Mn(II) or Co(II) to produce comparably active enzymes is quite remarkable, given the redox process implied by intermediate C in the proposed extradiol dioxygenase mechanism (Scheme 2.2). The three metal ions that afford active HPCD have standard aqueous M(III/II) potentials that span a range of nearly 1.2 V (E° = +1.92 V vs SHE for Co(III/II), +1.51 V for Mn(III/II), and +0.77 V for Fe(III/II), so much slower rates would normally be expected for the Mn(II) and Co(II) containing enzymes relative to the native Fe-containing enzyme for the steps involving electron transfer. In contrast, we show in the current and previous studies that Fe-HPCD and Mn-HPCD exhibit similar rates,[131] while Co-HPCD shows a higher turnover rate. One possibility explored here is that the protein tunes the redox potentials to similar values, as seen in the case of the Fe- and Mn-superoxide dismutases where differences in second sphere residues affect the ionization state of a water-derived ligand, and in turn, the redox potential of the metal center.[184-186] However, based on the X-ray crystallographic analysis described above, the structure of resting Co-HPCD is indistinguishable from those of its iron and manganese counterparts (Figure 2.5A). More relevantly, the second sphere

amino acid residues of the enzyme-substrate complex [Co-HPCD(4NC)] and the [Fe-HPCD(4NSQ)superoxo] intermediate[165] show no significant structural differences as seen in Figure 2.5B. Thus, differential redox potential tuning of the metal centers in Fe-, Mn-, and Co-HPCDs is unlikely, and we expect the relative order in redox potential, i.e. Fe < Mn < Co, to be maintained. This notion is supported by the susceptibility of Fe-HPCD to inactivation by O_2 and H_2O_2 and the insensitivity of Mn- and Co-HPCD to these oxidizing agents (Table 2.2). The absence of differential redox potential tuning of the metal centers by second sphere residues is not unreasonable, considering that the Mn(II) and Co(II) forms of HPCD are created by altering growth conditions and have not evolved naturally.

It is notable that Co-HPCD, with a relatively inaccessible Co(III) state, is active, indeed hyperactive when compared to the native Fe(II)-containing enzyme. To rationalize these observations, one must either consider a non-redox-active role for the metal center (i.e. no intermediate C) or postulate that the metal center in HPCD acts primarily as a conduit for electron transfer between the catecholate substrate and O_2 (i.e. short lived intermediate C) in these dioxygenases. In the latter scenario, initial electron transfer from the divalent metal center to O_2 would elicit an immediate subsequent electron transfer from substrate to the nascent trivalent center to form the reactive [M(II)($SQ^{\bullet}$)$O_2^{\bullet-}$] species (Intermediate D). The redox potential of the metal employed would then affect these two steps in a self-compensating manner. The expected higher potentials of the metal centers of the Mn(II)- and Co(II)-substituted enzymes would make them poorer reducing agents in the reductive oxygen binding step than the Fe(II) center in the wild-type enzyme, but the resulting M(III)-superoxo intermediates would be stronger oxidizing agents, thereby

facilitating the subsequent oxidation of the bound substrate. The net result would be that the rate of conversion from the M(II)-catecholate to the reactive [M(II)($SQ^{\bullet}$)$O_2^{\bullet-}$] species would be largely unaffected by the specific metal present so long as the O_2 adduct with the metal complex could form. From the point of view of thermodynamics, the electron donor in this oxygen activation reaction is the substrate and the electron acceptor is the O_2, so the potential of the metal catalyst that connects these two redox active species has no effect on the position of equilibrium, provided that the M(III)-superoxo state is accessible.

Co(II) substitution in other dioxygenases can be used to illustrate the significance of the current proposal. Co(II) incorporated into quercetin 2,3-dioxygenase (QueD) from *Bacillus subtilis* (Co-QueD) also results in an active enzyme.[41] This enzyme utilizes a mechanism developed from that proposed in Scheme 2.2 for the extradiol dioxygenases in which substrate and oxygen bind to the active site metal and are simultaneously activated.[41] Thus, it is reasonable that the enzyme should use metals over a range of potentials. In contrast, taurine/α-ketoglutarate dioxygenase (TauD) generates an Fe(IV)=O intermediate from the reaction of oxygen with α-ketoglutarate bound to its Fe(II) center.[216] The required change in metal oxidation state from +2 to +4 in this case suggests that the mechanism would be very sensitive to the redox potential of the metal center, and indeed, Co-TauD is inactive.[217]

2.4.3 Effect of Co(II) substitution on reaction cycle rate constants. Co-HPCD exhibits a 20-fold larger K_M^{O2} value (1200 μM) than do Mn- and Fe-HPCD. To the extent that this value reflects affinity, it suggests that O_2 binds less tightly to Co-HPCD. A similarly high K_M^{O2} of 1230 μM is reported for the cobalt-substituted form of QueD.[187] In

its simplest form, the ordered bi uni mechanism of HPCD gives $K_M^{O2} = (k_{-2} + k_3)/k_2$, where the rate constants shown represent collections of rate constants for individual steps involved in O_2 binding (k_2), O_2 release (k_{-2}), and product release (k_3) (Scheme 2.3).[218] Thus, the higher K_M^{O2} of Co-HPCD reflects a lower rate constant for O_2 binding and/or a higher rate constant for the release of O_2 from the enzyme. Given the decrease in the electron sharing capability of the higher potential cobalt center, a lower affinity for O_2 would likely contribute significantly to the high K_M^{O2} values of Co-HPCD (and Co-QueD).

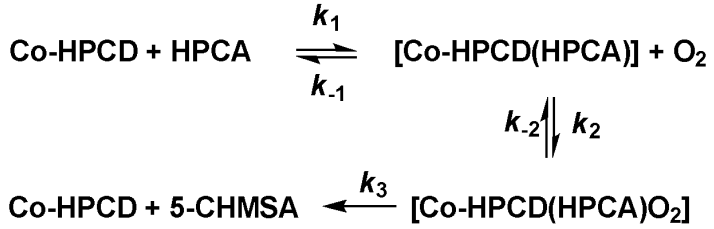

Scheme 2.3. Simplest form of the ordered bi uni mechanism for HPCD. Rate constants shown represent collections of rate constants involved in substrate and O_2 binding and product formation and release.

Transient kinetic studies of the reaction of [Fe-HPCD(HPCA)] with O_2 and more detailed studies of [Fe-HPCD(4NC)] with O_2 showed that none of the rate constants for the individual steps observed in the product formation and release portion of the cycle were dependent on O_2 concentration, indicating either effectively irreversible O_2 binding or an irreversible step between O_2 binding and the first observable step.[166, 167] A similar detailed analysis of the kinetics of Co-HPCD is complicated by the slow turnover of 4NC and the multiple, low-amplitude phases of the HPCA reaction, but it is clear that the overall product formation reaction exhibits a dependence on O_2 concentration

(Figure 2.8). Additionally, the true k_{cat} of Co-HPCD, nominally 1120 ± 70 min^{-1} under fully saturating O_2 conditions, is much higher than that of Fe-HPCD (470 ± 20 min^{-1}), showing that the rate of at least one previously rate limiting step has more than doubled upon incorporation of cobalt into the active site. For the reaction of [Fe-HPCD(HPCA)] with O_2, the rate limiting step is believed to be part of the product release sequence, perhaps the step immediately before the actual release of product from the active site.[166, 167] The increase in k_{cat} in the case of Co-HPCD shows that this step is at least 2.5 times faster and may be even faster if it is no longer rate limiting as discussed below.

The catalytic efficiency for the use of O_2 by Co-HPCD (0.9 ± 0.1 μM^{-1} min^{-1}) is an order of magnitude smaller than the k_{cat}/K_M^{O2} values for the Fe(II)- and Mn(II)-containing enzymes (7.8 ± 0.3, and 7.4 ± 0.6 μM^{-1} min^{-1}, respectively). The k_{cat}/K_M^{O2} value is comprised of all of the rate constants for steps between O_2 association through the first irreversible step, presumably either formation of the alkylperoxo-Fe(II) intermediate or the O–O bond cleavage step that follows.[219] Thus, the low value of k_{cat}/K_M^{O2} suggests that a step early in the O_2 activation process is significantly slowed in the Co-HPCD reaction. This is consistent with the expected higher potential of Co(II), which should decrease its affinity for O_2.

The k_{cat}/K_M^{O2} value can also be viewed as reflective of the second-order rate constant for the reaction of the enzyme-substrate complex with O_2. The first-order rate constant calculated by multiplying the observed k_{cat}/K_M^{O2} value by the O_2 concentration at which it was observed is very close to the turnover number under those conditions. For example, an apparent first-order rate constant of 670 ± 70 min^{-1} is calculated in oxygen-saturated buffer (1370 μM O_2; 22 °C; pH 7.8) compared to the observed k_{cat} of

590 ± 20 min^{-1}. This suggests that the rate-determining step has moved from a step in the product release sequence with Mn- or Fe-HPCD to an earlier step in the O_2 binding and activation sequence with Co-HPCD. This possibility was examined further in stopped-flow transient kinetic experiments in which [Co-HPCD(HPCA)] was rapidly mixed with oxygenated buffer over a range of O_2 concentrations (Figure 2.8A). Each kinetic time course shows a long lag phase when monitored at 380 nm as expected, because the chromophore results from formation of product in the active site. The fact that a lag phase is easily observed suggests that the steps before product formation are not exceptionally fast compared with the product-forming step itself. However, unlike Fe- and Mn-HPCDs (Figure 2.8B), the formation of product by Co-HPCD shows significant O_2 concentration dependence.[166] This observation rules out the possibility that the increases in K_M^{O2} and k_{cat} are due solely to an increase in product dissociation rate. The O_2 concentration dependence seen for Co-HPCD could be caused by either very weak (i.e. fully reversible) O_2 binding and/or a slow step early in the overall process of O_2 binding and product formation.[166] We argue here that both may be true for the Co-HPCD enzyme. In contrast, for Fe- and Mn-HPCD, the rate determining step occurs late in the process and transient kinetic experiments with Fe-HPCD and its His200 variants indicate that O_2 binding is fast and effectively irreversible.[166, 167]

2.4.4 Effects of Co(II) substitution on HPCD catalysis. It seems likely that the presence of cobalt in the active site of HPCD has two effects. First, its high potential slows one or more steps in the oxygen binding process so that it (they) becomes rate limiting and the k_{cat}/K_M^{O2} value falls. Second, it accelerates one or more steps in the product release sequence so that this portion of the reaction cycle is no longer rate

limiting. The net result of this is that the overall reaction is faster because the decrease in the O_2 binding sequence rate is not as large as the increase in the rate of the product release sequence.

The studies reported here do not suggest that Co-HPCD utilizes a mechanism different from that shown in Scheme 2.2 for Fe- and Mn-HPCD, but merely that the relative rates of intermediate steps have changed. This raises the prospect of trapping early reaction cycle intermediates for detailed spectroscopic characterization.

2.5 Supporting information: X-ray crystallographic studies

Crystallography work is done by collaborator Elena G. Kovaleva at the Institute of Molecular and Cellular Biology, University of Leeds, Leeds, LS2 9JT, UK.

X-ray data collection and refinement statistics for Co-HPCD, Fe-HPCD and Mn-HPCD are summarized in Tables 2.6, 2.7 and 2.8, respectively. Under crystallization conditions stated in the Materials and Methods section, HPCD enzymes crystallize in the $P2_12_12$ space group containing a single tetramer per asymmetric unit.

In addition to the first high-resolution crystal structures of Co-HPCD (PDB 3OJJ) and its anaerobic complex with 4-NC (PDB 3OJK) described in this work, structures of native Fe-HPCD (PDB 3OJT) and Mn-HPCD (PDB 3OJN) enzymes are also reported here. The X-ray crystal structure of Fe-HPCD was solved at 1.70 Å resolution, and it is indistinguishable from the previously reported structure of the full-length enzyme (PDB 2IG9, 1.90Å[165]) as indicated by RMSD values of 0.4 Å for superposition of all atoms in the entire tetramer. Similarly, the crystal structure of Mn-HPCD was solved at 1.65 Å resolution, and it is also indistinguishable from that reported previously.[131] Owing to the

higher resolution of these structures, Fe-HPCD (PDB 3OJT, Table 2.7) and Mn-HPCD (PDB 3OJN, Table 2.8), they were used for structural comparisons with Co-HPCD as well as for anomalous difference experiments. The observed coordination distances and angles for 2-His-1-carboxylate triad in the resting state structures of Co-, Mn- and Fe-HPCDs are summarized in Table 2.9.

In order to confirm the identity of the metal in the active site of native (Fe) and metal-substituted (Co, Mn, Cu, Zn and Ni) preparations of HPCD, a series of anomalous difference datasets were collected at the metal K-edge and pre-edge X-ray energies. The anomalous difference signal for Cu-, Zn- and Ni-HPCD enzymes was weak (less than 7 σ) and as such inconclusive (data not shown), albeit consistent with the significantly lower metal content in these preparations as indicated by ICP-AES analysis (Table 2.1). In contrast, active HPCD enzymes (Co, Mn, Fe) show strong anomalous difference signal in the active sites when X-ray diffraction data is collected at the K-edge of the incorporated metal. Examples of anomalous difference Fourier maps for data collected at the corresponding metal edge and pre-edge energies for Fe-, Mn- and Co-HPCDs are shown in Figure 2.9. Importantly, the presence of strong anomalous signal at the metal K-edge (green mesh, Figure 2.15) and absence of detectable anomalous signal at the metal pre-edge energies (red mesh, Figure 2.15) confirms the presence of the correct catalytic metal in the active sites of native (Fe) and metal-substituted (Co, Mn) HPCD enzymes.

The anaerobic [Co-HPCD(4-NC)] complex was formed by soaking Co-HPCD crystals with 4-NC substrate in the anaerobic glove box atmosphere. After about 1 hr incubation, significant accumulation of the 4-NC ligand was observed in the active sites

of subunits A, C and D (about 80% occupancy estimated from the average B-factors), whereas significantly lower occupancy of 4-NC was observed in subunit B. The same ligand distribution, occupancy and conformation were also observed in several additional independently refined structural datasets obtained from different crystal complexes prepared using the same *in crystallo* reaction procedure as described in the Materials and Methods section. Figure 2.16 shows multiple views of the representative enzyme-substrate complex.

Table 2.6. X-ray data collection and refinement statistics for Co-HPCD [a].

Dataset (PDB Code)	Co-HPCD (3OJJ)			[Co-HPCD(4-NC)] (3OJK)
	High Resolution	Co K-edge	Co K-pre-edge	High Resolution
Wavelength (X-ray Energy)	0.9763 Å (12.70 keV)	1.6050 Å (7.725 keV)	1.6077 Å (7.712 keV)	0.9801 Å (12.65 keV)
Synchrotron (beamline)	Diamond Light Source (beamline I03)	Synchrotron Soleil (Proxima I)	Synchrotron Soleil (Proxima I)	Synchrotron Soleil (Proxima I)
Cell dimensions (Å)	110.5, 152.1, 96.5	110.7, 151.6, 96.4	110.7, 151.7, 96.5	110.1, 150.4, 95.9
Cell angles (deg)	90, 90, 90	90, 90, 90	90, 90, 90	90, 90, 90
Resolution range[a] (Å)	29.9-1.72 (1.81)	41.5-2.50 (2.64)	41.5-2.50 (2.64)	41.2-1.68 (1.77)
Reflections (observed/unique)	590958/170151	211659/56126	191762/54517	1007797/175180
R_{rim} [a, b] (%)	12.2 (84.4)	6.4 (12.0)	6.7 (11.7)	13.7 (82.4)
R_{pim} [a, c] (%)	6.3 (43.7)	3.3 (6.2)	3.6 (6.4)	5.3 (34.6)
Mean $\langle I\rangle/\sigma\langle I\rangle$ [a]	9.0 (1.9)	21.0 (11.8)	21.1 (12.3)	10.6 (2.1)
Completeness (%) [a]	98.9 (98.7)	98.9 (98.7)	97.2 (91.7)	97.2 (91.7)
R, R_{free}, test (%) [d]	14.7, 17.6, 5.0			15.3, 18.1, 5.0
RMSD [e] bond length (Å)	0.014			0.013
RMSD [e] angles (deg)	1.442			1.460
ESU [f] (Å)	0.063			0.062
Ramachandran Plot				
Allowed regions (%)	99.6			99.7
Additional regions (%)	0.4			0.3

[a] Values for the highest resolution shell are given in parentheses. [b] Redundancy-independent merging R factor: $R_{r.i.m} = \sum_{hkl}[N/(N-1)]^{1/2}\sum_i|I_i(hkl)-\langle I(hkl)\rangle| / \sum_{hkl}\sum_i I_i(hkl)$, where $\langle I(hkl)\rangle$ is the mean value of $I(hkl)$.[220] [c] Precision-indicating merging R factor: $R_{p.i.m} = \sum_{hkl}[1/(N-1)]^{1/2}\sum_i|I_i(hkl)-\langle I(hkl)\rangle| / \sum_{hkl}\sum_i I_i(hkl)$, where $\langle I(hkl)\rangle$ is the mean value of $I(hkl)$.[220] [d] $R = (\sum||F_{obs}|-k|F_{calc}||)/\sum|F_{obs}|$, where k is a scale factor. The R_{free} value was calculated with the indicated percentage of reflections not used in the refinement. [e] Root-mean-square deviation (RMSD) from ideal geometry in the final models. [f] Estimated overall coordinate error (ESU) based on maximum likelihood.

Table 2.7. X-ray data collection and refinement statistics for Fe-HPCD [a].

Dataset (PDB Code)	Fe-HPCD (3OJT)		
	High Resolution	Fe K-edge	Fe K-pre-edge
Wavelength (X-ray Energy)	0.9999 Å (12.39 keV)	1.7394 Å (7.128 keV)	1.7428 Å (7.114 keV)
Synchrotron (beamline)	Swiss Light Source (PXII)	Synchrotron Soleil (Proxima I)	Synchrotron Soleil (Proxima I)
Cell dimensions (Å)	110.7, 151.2, 96.4	110.6, 150.9, 96.4	110.6, 150.8, 96.4
Cell angles (deg)	90, 90, 90	90, 90, 90	90, 90, 90
Resolution range[a] (Å)	89.3-1.70 (1.79)	41.4-2.60 (2.74)	41.35-2.61 (2.75)
Reflections (observed/unique)	586722/174363	261945/49461	187998/48753
R_{rim} [a, b] (%)	12.3 (81.1)	7.0 (17.7)	5.1 (17.8)
R_{pim} [a, c] (%)	6.4 (42.7)	3.0 (7.8)	2.5 (9.0)
Mean $\langle I\rangle/\sigma\langle I\rangle$ [a]	8.6 (2.0)	19.4 (8.5)	22.5 (7.8)
Completeness (%) [a]	98.3 (98.6)	98.6 (93.9)	97.9 (93.8)
R, R_{free}, test (%) [d]	16.0, 18.8, 5.0		
RMSD [e] bond length (Å)	0.015		
RMSD [e] angles (deg)	1.460		
ESU [f] (Å)	0.068		
Ramachandran Plot			
Allowed regions (%)	99.7		
Additional regions (%)	0.3		

[a] Values for the highest resolution shell are given in parentheses. [b] Redundancy-independent merging R factor: $R_{r.i.m} = \sum_{hkl}[N/(N-1)]^{1/2}\sum_i|I_i(hkl)-\langle I(hkl)\rangle| / \sum_{hkl}\sum_i I_i(hkl)$, where $\langle I(hkl)\rangle$ is the mean value of $I(hkl)$.[220] [c] Precision-indicating merging R factor: $R_{p.i.m} = \sum_{hkl}[1/(N-1)]^{1/2}\sum_i|I_i(hkl)-\langle I(hkl)\rangle| / \sum_{hkl}\sum_i I_i(hkl)$, where $\langle I(hkl)\rangle$ is the mean value of $I(hkl)$.[220] [d] $R = (\sum||F_{obs}|-k|F_{calc}||)/\sum|F_{obs}|$, where k is a scale factor. The R_{free} value was calculated with the indicated percentage of reflections not used in the refinement. [e] Root-mean-square deviation (RMSD) from ideal geometry in the final models. [f] Estimated overall coordinate error (ESU) based on maximum likelihood.

Table 2.8. X-ray data collection and refinement statistics for Mn-HPCD [a].

Dataset (PDB Code)	Mn-HPCD (3OJN)		
	High Resolution	Mn K-edge	Mn K-pre-edge
Wavelength (X-ray Energy)	0.9763 Å (12.70 keV)	1.8923 Å (6.552 keV)	1.8958 Å (6.540 keV)
Synchrotron (beamline)	Diamond Light Source (beamline I03)	Diamond Light Source (beamline I03)	Diamond Light Source (beamline I03)
Cell dimensions (Å)	110.5, 151.5, 96.4	110.3, 151.0, 96.1	110.2, 151.2, 96.1
Cell angles (deg)	90, 90, 90	90, 90, 90	90, 90, 90
Resolution range [a] (Å)	29.8-1.65 (1.74)	29.7-2.50 (2.64)	29.7-2.50 (2.64)
Reflections (observed/unique)	609411/188789	777971/56279	431606/56256
R_{rim} [a, b] (%)	11.2 (66.1)	16.9 (69.2)	13.1 (58.1)
R_{pim} [a, c] (%)	6.1 (35.7)	4.5 (18.6)	4.7 (21.5)
Mean $\langle I\rangle/\sigma\langle I\rangle$ [a]	7.3 (2.0)	14.2 (5.0)	13.6 (3.7)
Completeness (%) [a]	97.6 (98.5)	99.9 (100.0)	99.9 (100.0)
R, R_{free}, test (%) [d]	14.8, 17.7, 5.0		
RMSD [e] bond length (Å)	0.013		
RMSD [e] angles (deg)	1.403		
ESU [f] (Å)	0.055		
Ramachandran Plot			
Allowed regions (%)	99.7		
Additional regions (%)	0.3		

[a] Values for the highest resolution shell are given in parentheses. [b] Redundancy-independent merging R factor: $R_{r.i.m} = \sum_{hkl}[N/(N-1)]^{1/2}\sum_i|I_i(hkl)-\langle I(hkl)\rangle| / \sum_{hkl}\sum_i I_i(hkl)$, where $\langle I(hkl)\rangle$ is the mean value of $I(hkl)$.[220] [c] Precision-indicating merging R factor: $R_{p.i.m} = \sum_{hkl}[1/(N-1)]^{1/2}\sum_i|I_i(hkl)-\langle I(hkl)\rangle| / \sum_{hkl}\sum_i I_i(hkl)$, where $\langle I(hkl)\rangle$ is the mean value of $I(hkl)$.[220] [d] $R = (\sum||F_{obs}|-k|F_{calc}||)/\sum|F_{obs}|$, where k is a scale factor. The R_{free} value was calculated with the indicated percentage of reflections not used in the refinement. [e] Root-mean-square deviation (RMSD) from ideal geometry in the final models. [f] Estimated overall coordinate error (ESU) based on maximum likelihood.

Table 2.9. Comparison of metal coordination distances and angles for HPCD enzymes [a].

Distances/Angles	Co-HPCD	Mn-HPCD	Fe-HPCD
∠ H155-M-H214 (°)	102 ± 2	100 ± 2	101 ± 2
∠ H155-M-E267 (°)	91 ± 2	91 ± 1	92 ± 2
∠ H214-M-E267 (°)	86 ± 2	87 ± 2	87 ± 2
M-H155 (Å)	2.18 ± 0.03	2.27 ± 0.03	2.24 ± 0.07
M-H214 (Å)	2.15 ± 0.03	2.21 ± 0.04	2.23 ± 0.04
M-E267 (Å)	2.08 ± 0.05	2.08 ± 0.05	2.04 ± 0.02
M-Wat1 (Å)	2.17 ± 0.03	2.25 ± 0.03	2.23 ± 0.06
M-Wat2 [b] (Å)	2.27 ± 0.04	2.31 ± 0.08	2.19 ± 0.05
M-Wat3 (Å)	2.13 ± 0.03	2.18 ± 0.02	2.14 ± 0.08

[a] Average values and standard deviations for coordination distances and angles were calculated for 4 monomeric subunits of each type of HPCD enzyme: Co-HPCD, PDB 3OJJ; Mn-HPCD, PDB 3OJN and 3BZA; Fe-HPCD, 3OJT and 2IG9. Wat1, Wat2 and Wat3 designate solvent-derived ligands coordinated to the catalytic metal (M) in the resting state of the enzyme in the positions trans to the residues H214, H155 and E267, respectively. [b] In the high-resolution structures of all HPCDs (Co, Mn, Fe), slightly asymmetric rather than spherical electron density is apparent at Wat2 coordination sites. Since no small ligand accounting for the observed density is present in purification or crystallization solutions, a single solvent was modeled at these sites.

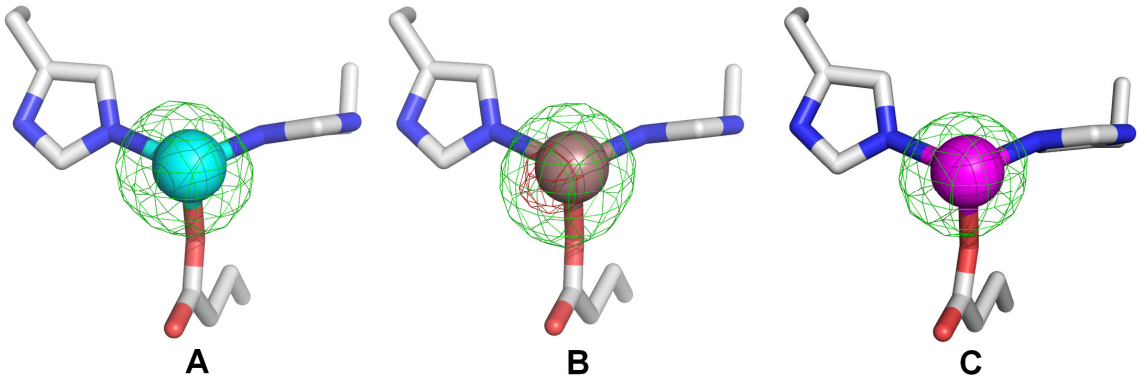

Figure 2.15. Representative anomalous difference Fourier maps for HPCD X-ray diffraction data sets collected at metal-specific K-absorption edges (Mn, Fe, Co). Models depict the metal-(2-His-1-carboxylate) center in subunits C of HPCD structures. Atom color-code: gray, carbon; blue, nitrogen; red, oxygen; magenta, cobalt; cyan, manganese; bronze, iron. The anomalous difference maps were calculated for datasets at the metal K-edge (green mesh, 8 σ contour) and pre-edge (red mesh, 5 σ contour). A) Active site of Mn-HPCD (PDB 3OJN). Anomalous difference maps calculated from dataset collected at the Mn K-edge (green, 1.8923 Å, 6.552 keV) and pre-edge (red, 1.8958 Å, 6.540 keV). B) Active site of Fe-HPCD (PDB 3OJT). Anomalous difference maps calculated from dataset collected at the Fe K-edge (green, 1.7394 Å, 7.128 keV) and pre-edge (red, 1.7428 Å, 7.114 keV). C) Active site of Co-HPCD (PDB 3OJJ). Anomalous difference maps calculated from data set collected at the Co K-edge (green, 1.6050 Å, 7.725 keV) and pre-edge (red, 1.6077 Å, 7.712 keV).

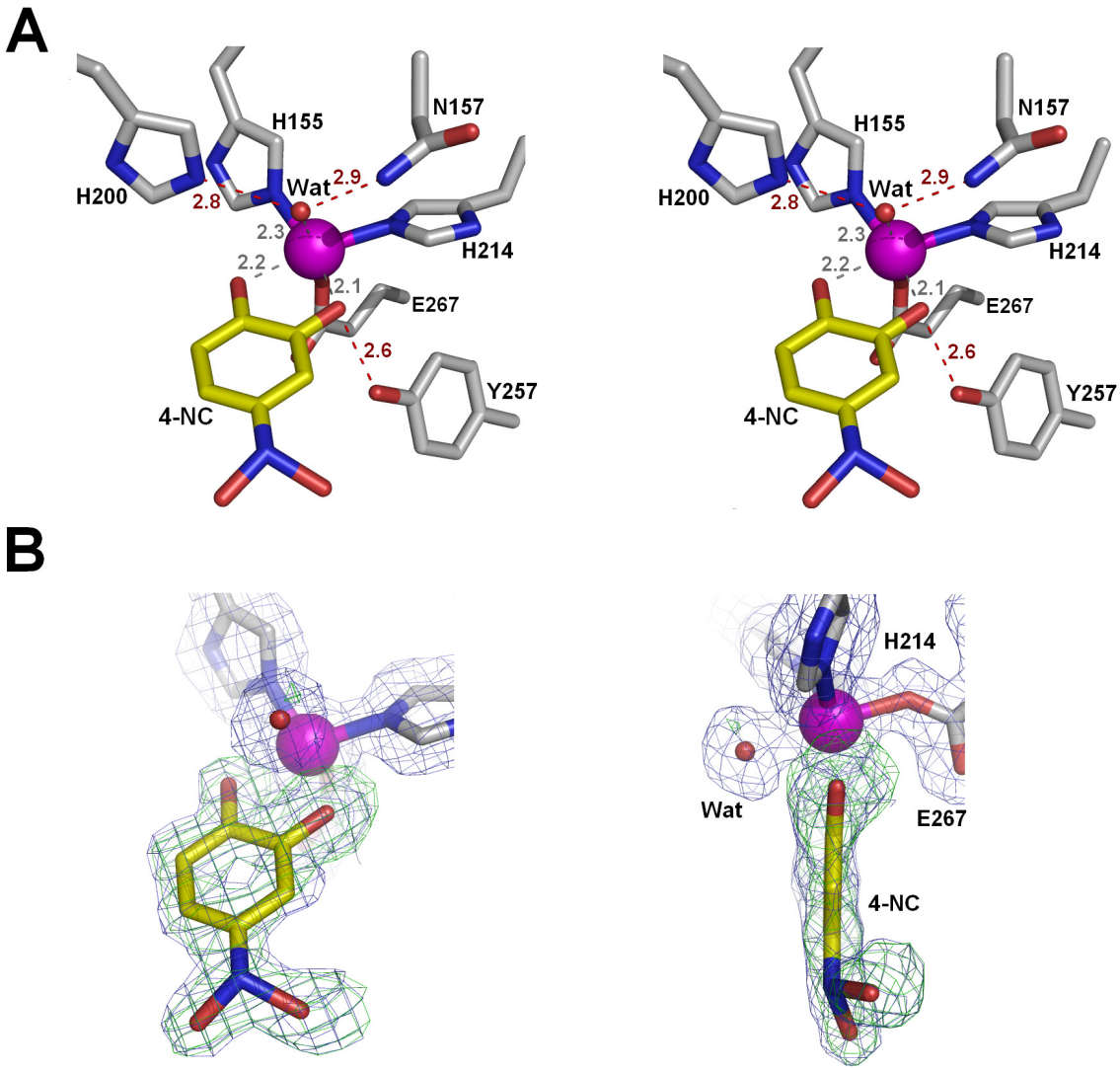

Figure 2.16. Representative structure of [Co-HPCD(4-NC)] complex (PDB 3OJK, subunit D). A) Cross-eyed stereoview of the hydrogen-bonding interactions in the active site. B) Electron density maps for bound 4-NC. The blue $2F_{obs}$-F_{calc} map is contoured at 1 σ. The green F_{obs}-F_{calc} ligand-omit difference map was calculated by removing 4-NC from the final model and it is contoured at +3 σ. Atom color-code: gray, carbon (enzyme residues); yellow, carbon (substrate); blue, nitrogen; red, oxygen; magenta, cobalt. Red dashed lines show hydrogen bonds (Å). Gray dashed lines indicate bonds or potential bonds to cobalt (Å).

Chapter 3

Characterization of an O_2 Adduct of an Active Cobalt-Substituted Extradiol-Cleaving Catechol Dioxygenase

Portions of this chapter were previously published by the American Chemical Society as: Andrew J. Fielding, John D. Lipscomb, and Lawrence Que Jr. "Characterization of an O_2 Adduct of an Active Cobalt-Substituted Extradiol-Cleaving Catechol Dioxygenase" *J. Am. Chem. Soc.,* **2012,** *134,* 796–799.

3.1 Introduction

Homoprotocatechuate 2,3-dioxygenase (HPCD) activates O_2 to carry out the extradiol ring-cleavage of homoprotocatechuate (HPCA) (Scheme 3.1) in the biodegradation of aromatic compounds by microorganisms.[170, 171, 175] Recently metal substitution experiments showed that the native Fe(II) metal cofactor can be substituted with Co(II) to yield Co-HPCD with comparable activity,[169] despite an apparent large difference in M(III/II) redox potential between Fe-HPCD and Co-HPCD as suggested by the observation that H_2O_2 oxidatively inactivates Fe-HPCD, but not Co-HPCD and the large difference in the M(III/II) standard potentials of these metals.[178] As the catalytic mechanism for Fe-HPCD involves O_2 binding to the Fe(II) center,[162, 149, 165] our observations raise the question as to how O_2 activation and extradiol cleavage can be carried out by the higher-potential Co(II) center of Co-HPCD.

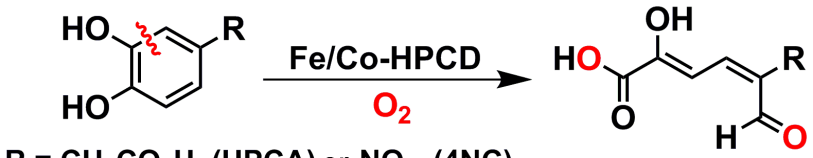

Scheme 3.1. Extradiol ring-cleavage of catechol substrates by Fe- or Co-substituted HPCD.

3.2 Experimental methods

3.2.1 Reagents. Reagents and buffers were purchased from Sigma and were used as received. All reagents and media were prepared using water treated with a Millipore Milli-Q water system to minimize trace metal-ion contamination.

3.2.2 Preparation of metal-substituted wt-HPCD and H200N-HPCD. Cobalt-substituted HPCD and H200N-HPCD mutants were overexpressed in *E. coli* strain BL21 (DE3) and purified as previously described.[167, 169, 193] Protein concentrations were measured using the absorbance at 280 nm (ε_{280} = 45,000 M^{-1} cm^{-1}).[169] Metal incorporation was measured by inductively coupled plasma atomic emission spectroscopy (ICP-AES) metal analysis at the Soil Research Analytical Laboratory (College of Food, Agriculture and Natural Resources Sciences, University of Minnesota). Samples were prepared for ICP-AES by digesting 2 ppm protein in 5% HNO_3 overnight and then removing precipitated protein by centrifugation.

3.2.3 EPR sample preparation and spectroscopic methods. EPR samples were made to a volume of 300 μL, with 300 μM Co-HPCD in 50 mM pH 7.5 MOPS buffer. Samples were frozen by slow immersion in liquid nitrogen. Anaerobic samples were prepared by purging Co-HPCD and substrate separately by repeated cycling under argon and vacuum before mixing, followed by anaerobic transfer of samples into EPR tubes in a glovebox. [H200N-Co-HPCD(4NC/HPCA)O_2] complexes were prepared by mixing anaerobic enzyme-substrate complex with O_2-saturated buffer or by placing the enzyme substrate complex under the desired pressure of O_2 for 10 minutes before transferring the protein to EPR tubes to be frozen. For high O_2 pressure samples, the EPR tube and sample were put under the desired pressure of O_2 for 10 minutes and then rapidly frozen in an isopentane bath (-160 °C). EPR spectra were recorded on a Bruker Elexsys E-500 spectrometer equipped with an Oxford Instruments ESR-10 liquid helium cryostat at X-band

(9.64 GHz). Spectra of Co-HPCD samples were acquired at 20 K over a magnetic field range of 100–6000 G using 2 mW power, 10 G modulation amplitude, and 100 kHz modulation frequency.

3.2.4 Determination of the dissociation constant for 4NC. The K_D for 4NC binding to Co-HPCD (Figure 3.1) was determined by monitoring changes in the optical spectrum of 4NC at 600 nm (ε_{600} = 3,000 M^{-1} cm^{-1}) upon binding, as previously described.[166]

3.2.5 Kinetic experiments. Enzyme used for 4NC experiments was first incubated with 2 mM H_2O_2 to inactivate any contaminating Fe-HPCD. Residual H_2O_2 was then removed by buffer exchange to prevent oxidation of 4NC to 4-nitroquinone. Single turnover reactions of 4NC by Co-HPCD were performed by rapidly mixing anaerobic [Co-HPCD(4NC)] in a sealed cuvette with O_2-saturated buffer (50 mM MES (pH 6.0) at 22 °C) to yield the final desired O_2 concentration and then placing the reaction under the desired O_2 pressure. For reactions above 1 atm O_2, Co-HPCD was first equilibrated in a sealed cuvette under the desired O_2 pressure to which 4NC was added, and the reaction solution was rapidly mixed. High dissolved O_2 concentrations were achieved by using a sealable cuvette with screw cap lid from Strana with Teflon/Silcon disc septum from Thermo Scientific. The cuvette was held under pressure using a 19 gage needle connected to an O_2 cylinder using vacuum hosing. The O_2 pressure in the cuvette was set by adjusted the pressure on the O_2 tank regulator. Dissolved O_2 concentrations were

calculated using Henrys Law and the van't Hoff equation.[221] The reactions were monitored by UV-Vis absorption spectroscopy on a photodiode array spectrophotometer.

3.2.6 Global analysis. The EPR and UV-Vis reaction progress curves (Figures 3.6 and 3.7) were fit simultaneously by global analysis to rate equations based on reaction Scheme 3.2 using the program DYNAFIT.[222] The O_2 concentration dependence data was obtained by monitoring the decay of the 4NC chromophore of the enzyme-substrate (ε_{516} = 8,700 M^{-1} cm^{-1}, ε_{390} = 5,600 M^{-1} cm^{-1}) and formation of the extradiol ring-cleaved product (ε_{516} = 1,600 M^{-1} cm^{-1}, ε_{390} = 16,500 M^{-1} cm^{-1}) complex. The EPR 4NC single turnover experiment has the advantage of being able to monitor the formation and decay of the intermediate directly.

$$\mathbf{ES + O_2} \underset{k_{-1}}{\overset{k_1}{\rightleftharpoons}} \mathbf{ESO_2} \xrightarrow{k_2} \mathbf{E + P}$$

$d[ES]/dt = -k_1[ES][O_2] + k_{-1}[ESO_2]$

$d[O_2]/dt = -k_1[ES][O_2] + k_{-1}[ESO_2]$

$d[ESO_2]/dt = k_1[ES][O_2] - k_{-1}[ESO_2] - k_2[ESO_2]$

$d[E]/dt = k_2[ESO_2]$

$d[P]/dt = k_2[ESO_2]$

Scheme 3.2. Reaction scheme and corresponding rate equations used to simultaneously fit the EPR freeze-quench experiments and UV-Vis experiments (Figure 3.6 and 3.7) by global analysis for the single turnover reactions of [Co-HPCD(4NC)] with O_2.

3.3.7 pH-Activity profiles. pH-Activity experiments were performed in a buffer mixture consisting of MES, bis-Tris, MOPS, Tris, CHES, and CAPS all at 25 mM concentrations with pHs ranging from 5.5–8.5. The final conductivity of each buffer was then adjusted to 6.4 mS using 2 M NaCl. The pH activity profile of Co-HPCD for the native substrate HPCA (180 nM Co-HPCD and 2 mM HPCA) was monitored in O_2-saturated buffer at 22 °C, at the pH-independent isosbestic point for the colored product (ε_{350} = 13,900 M^{-1} cm^{-1}). The background rate of the base-catalyzed substrate auto-oxidation reaction monitored at 350 nm was subtracted for pH > 8.[181] The pH activity profile data (Figures 3.13 and 3.14) were fit using equations 3.1 or 3.2 to determine apparent pK_a values.[223] The b variables in Equations 3.1 and 3.2 accounts for basal activity at high or low pHs observed in pH activity profiles (Figure3.13 and 3.14) in which the bulk solvent may be acting as the proton donor or acceptor.

Equation 3.1
$$k_{obs} = k - \left(\frac{k \cdot 10^{pK_a - pH}}{1 + 10^{pK_a - pH}} \right) + b$$

Equation 3.2
$$k_{obs} = \left(\frac{k \cdot 10^{pK_a - pH}}{1 + 10^{pK_a - pH}} \right) + b$$

3.2.8 EPR freeze-quench kinetic experiments. EPR freeze quench experiments were performed by rapidly mixing the anaerobic [Co-HPCD(4NC)] enzyme-substrate complex (pH 6.0 at 22 °C) with O_2-saturated buffer, and then stirring the reaction under 2 atm of O_2. Aliquots from the reaction were then taken every few minutes over the course of 120 min and rapidly frozen in EPR tubes. Initial concentration of reactants were 0.5 mM [Co-HPCD(4NC)] and 1.18 mM O_2.

3.2.9 Spin quantification. To quantify the yield of the $S = 1/2$ species, the spectra of the anaerobic enzyme-substrate complex and the final time point sample were each integrated to get the total cobalt concentration. For the O_2 adduct, the $g = 2$ region (3150–3550 G) was integrated separately from the rest of the spectrum. The yield of the O_2 adduct was quantified according to the procedure of Aasa and Vänngård, which corrects the intensity of the integrated areas of highly anisotropic EPR spectra by multiplying by a correction factor that scales the area based on the g-values of each species.[224] The yield of the $S = 1/2$ species was also checked by simply monitoring the change in intensity of EPR features unique to each species ($g = 4.8$ for [Co-HPCD(4NC)], at $g = 2.04$ and 1.975 for [Co-HPCD(4NC)O_2], and at $g = 8.9$ for [Co-HPCD]). This procedure yields the normalized concentration of these two species at each time point, allowing the yield to be calculated for the intermediate. (Normalized yield of ESO_2 = 1 - ES - E) This gave the same yield of the O_2 adduct as from the spin quantification method.

3.3 Experimental results

3.3.1 Turnover of 4NC. Steady-state kinetics measurements showed Co-HPCD to have a low apparent O_2 affinity (K_M^{O2} = 1.2 ± 0.1 mM vs 60 μM for Fe-HPCD at pH 7.8), perhaps reflecting the higher potential of the Co(II) center. However, under O_2-saturating conditions, Co-HPCD shows a higher HPCA ring-cleavage activity than Fe-HPCD (k_{cat} = 1120 ± 70 min^{-1} vs 470 ± 20 min^{-1} for Fe-HPCD at pH 7.8).[169] Comparisons of transient kinetic experiments indicate different rate-limiting steps for Fe-HPCD- and

Co-HPCD-catalyzed reactions. Whereas the rate-limiting step for Fe-HPCD occurs in the product release phase of the catalytic cycle,[162, 166, 167] that for Co-HPCD occurs in the O_2 binding and activation phase of the reaction. Investigation of these steps has been facilitated in our past studies of extradiol dioxygenases by the use of the slow substrate analogue 4-nitrocatechol (4NC).[162, 166, 167] This electron-poor substrate is cleaved in the same position as HPCA by Co-HPCD, but the rate of the reaction is slowed 1000-fold (pH 6.0, 22 °C and 2 atm O_2). This has allowed us to trap an O_2 adduct and characterize it as a low-spin Co(III)-superoxide complex, the first documented example of such a species for a functional cobalt oxygenase.

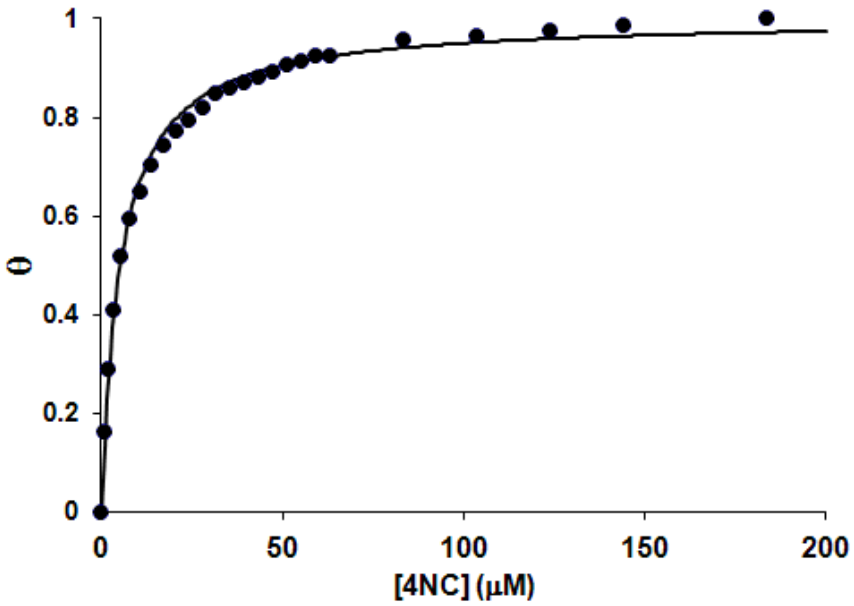

Figure 3.1. 4NC-binding curve from anaerobic titration of Co-HPCD with 4NC in 50 mM MES (pH 6.0). Solid line represents a hyperbolic fit to data (K_D^{4NC} = 5 ± 2 μM).[166] The y-axis (θ) is the fraction 4NC bound.

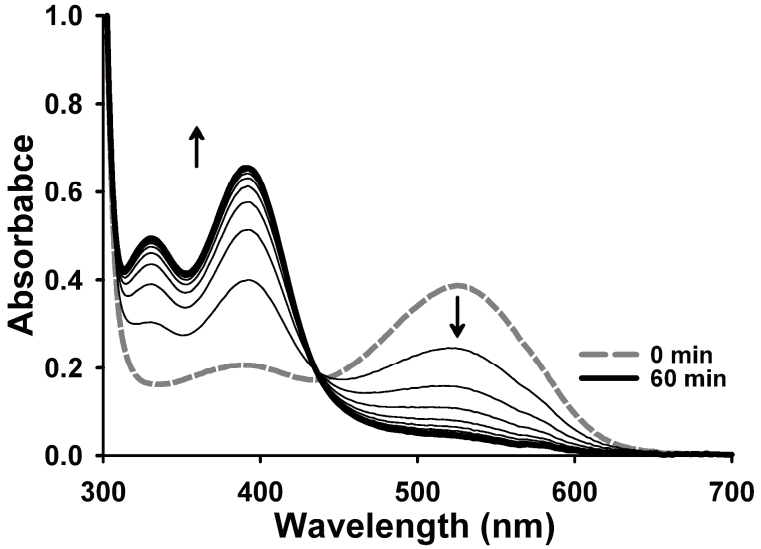

Figure 3.2. UV-Vis absorption spectra observed for the single-turnover reaction of [Co-HPCD(4NC)] (40 μM 4NC and 150 μM Co-HPCD) (gray dashed line) with O_2 to form the extradiol ring-cleaved product (thick black line). Reaction conditions: 50 mM MES, (pH 6.0), 2 atm O_2, and 22 °C. Intermediate lines were obtained at 5 min intervals.

3.3.2 O_2 concentration dependence. Co-HPCD binds 4NC (K_D^{4NC} = 5 ± 2 μM, Figure 3.1) in its purple dianionic form with an intense absorption band at 516 nm that slowly converts to the yellow extradiol ring-cleaved product with absorption bands at 330 and 390 nm at pH 6.0 (Figure 3.2).[166] Time-dependent traces of the reaction at 516 and 390 nm were fit satisfactorily with single-exponential equations to give nearly the same $1/\tau$ value at these two wavelengths (Figure 3.3). The conversion exhibited a linear dependence on O_2 concentration (Figure 3.3 inset), suggesting that O_2 binding is the first and rate-limiting step over the experimentally accessible [O_2] range. The slope of the plot gives a second-order rate constant for O_2 binding of 30 ± 3 M^{-1} min^{-1}, which is at least 6 orders of magnitude smaller than that for O_2 binding to [Fe-HPCD(4NC)].[166, 167] This is in accord with our previous proposal, based on steady-state kinetic analysis, that the O_2

binding step in HPCA turnover by Co-HPCD is slow and rate-limiting.[169] Because of the slow turnover of 4NC by Co-HPCD, the observed activity could originate from contaminating Fe-HPCD. To rule out this possibility, the enzyme was pretreated with H_2O_2 to inactivate any contaminating Fe-HPCD.[131] Furthermore, in the single turnover of 4NC by Fe-HPCD none of the observed kinetic phases show an O_2 concentration dependence, in contrast to our observations here for Co-HPCD (Figure 3.3).[166]

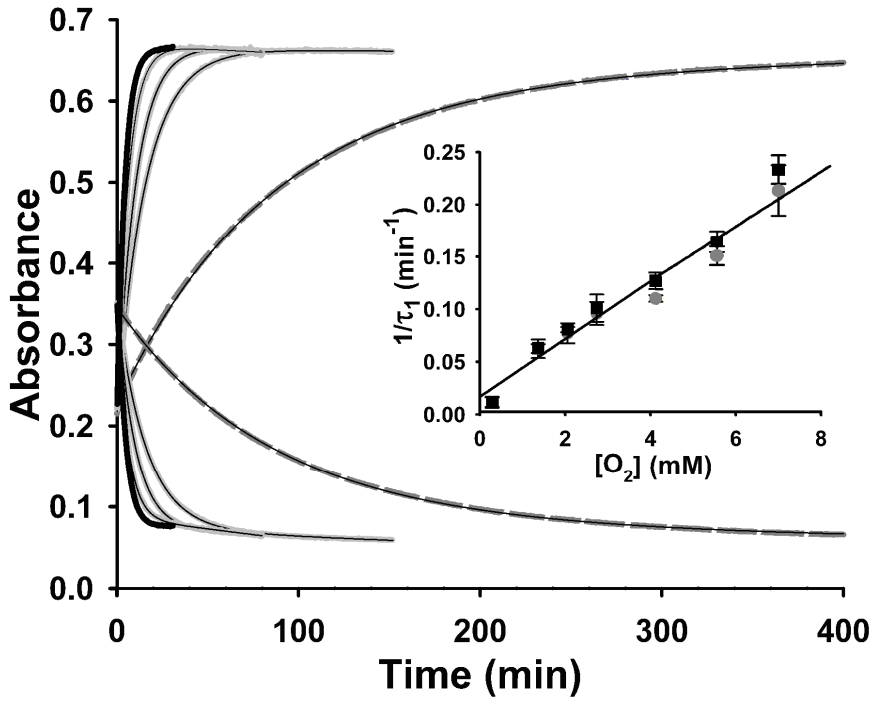

Figure 3.3. Single exponential fit of single wavelength traces for the single-turnover reactions of [Co-HPCD(4NC)] (30 μM 4NC and 150 μM Co-HPCD) with O_2 concentrations ranging from 0.29 mM (air-saturated buffer, gray dashed lines) to 6.86 mM O_2 (5 atm O_2, thick black lines). Reaction conditions: 50 mM MES (pH 6.0), and 22 °C (K_D^{4NC} = 5 ± 2 μM, Figure 3.1). The reaction was monitored by following the decay of the 516 nm band and the growth of the 390 nm band. Thin black lines are the single exponential fit of experimental data. **Inset.** O_2 dependence of average 1/τ values from single exponential fits of data at both 516 (black, ■) and 390 nm (gray, ●). The thin black line represents a linear fit of 1/τ data.

3.3.3 EPR freeze-quench experiments. Electron paramagnetic resonance (EPR) freeze-quench experiments were performed by rapidly mixing the anaerobic [Co-HPCD(4NC)] complex (pH 6 at 22 °C) with O_2-saturated buffer and then placing the reaction under 2 atm of O_2. Aliquots from the reaction were then taken every few minutes over the course of 60 minutes and frozen in EPR tubes. Figure 3.4 shows representative

EPR spectra from freeze-quench experiments. Co-HPCD exhibits an $S = 3/2$ EPR signal associated with a high-spin Co(II) center (Figure 3.5),[169] with the signal at $g = 6.7$ showing ^{59}Co ($I = 7/2$) hyperfine splitting ($A = 80$ G) (Table 3.1). The $S = 3/2$ signal changes upon anaerobic formation of the [Co-HPCD(4NC)] complex (Figure 3.4 and 3.5). Upon mixing with O_2, the amount of the $S = 3/2$ species decreases, as indicated by a decrease in the feature at $g = 4.8$, and a new $S = 1/2$ species forms with signals centered at $g = 2$. The new $S = 1/2$ species exhibits well-resolved eight-line hyperfine splitting from the ^{59}Co nucleus ($A = 24$ G). The intensity of the $S = 1/2$ species continues to increase over the first 2 minutes and then decreases as the $S = 3/2$ signal of Co-HPCD at $g = 8.9$ grew.

The reaction progress (Figure 3.6) was monitored by following changes in the intensities of EPR features unique to each species. A yield of ~10% for the $S = 1/2$ species was measured at 2 minutes by spin quantification.[224] The ability to observe the intermediate directly allowed accurate fitting of the time course to the appropriate equation for a two-step reaction. The EPR and UV-Vis reaction progress curves (Figures 3.6 and 3.7) were fit simultaneously by global analysis to rate equations based on the reaction scheme shown in Scheme 3.2. using the program DYNAFIT and the following rate constants were obtained: $k_1 = 40 \pm 5$ M^{-1} min^{-1}, $k_{-1} = 0.05 \pm 0.01$ min^{-1} and $k_2 = 0.72 \pm 0.06$ min^{-1}.[222] Under this model, $k_1[O_2]$ and k_2 values are comparable in magnitude, with $k_1[O_2] < k_2$ at experimentally accessible O_2 pressures (< 5 atm). The ~10% yield of the $S = 1/2$ species observed in the freeze-quench EPR experiments at 2 atm O_2 is fully consistent with the rate constants obtained.

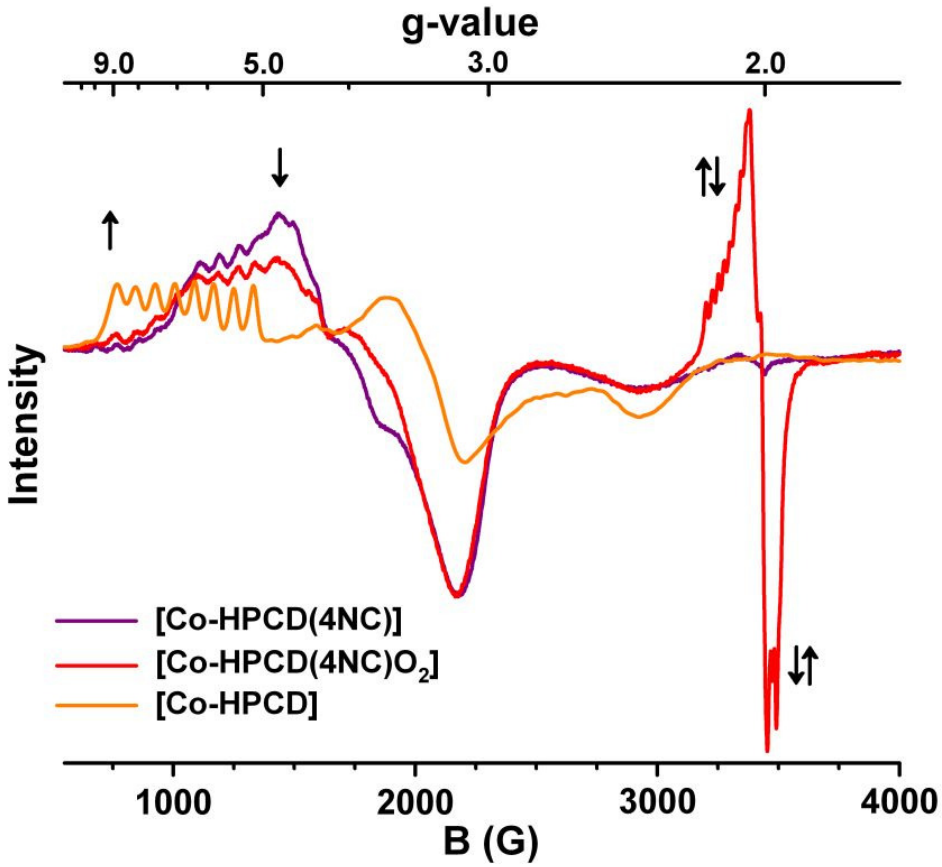

Figure 3.4. EPR spectra of freeze-quench samples of anaerobic enzyme-substrate complex [Co-HPCD(4NC)] (gray, dashed line) rapidly mixed with O_2-saturated buffer under 2 atm O_2 at 22 °C in 50 mM MES buffer (pH 6.0), showing formation of the [Co-HPCD(4NC)O_2] intermediate (black line) at 2 min and subsequent decay to Co-HPCD (solid, gray line) and the extradiol ring-cleaved product after 60 min. Initial concentration of reactants were 0.5 mM [Co-HPCD(4NC)] and 2.75 mM O_2.

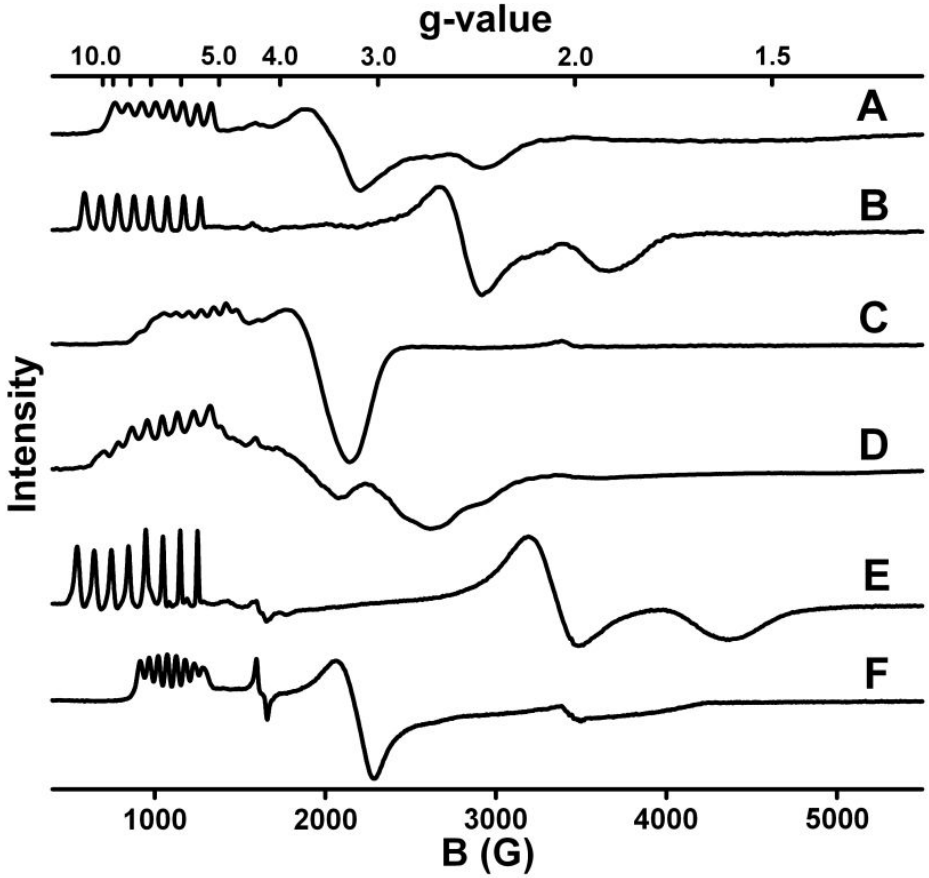

Figure 3.5. EPR spectra obtained at 9.64 GHz, 20 dB and 20 K in 50 mM MOPS pH 7.5. (A) wt-Co-HPCD[169] (B) anaerobic [wt-Co-HPCD(HPCA)][169], (C) anaerobic [wt-Co-HPCD(4NC)], (D) H200N-Co-HPCD, (E) anaerobic [H200N-Co-HPCD(HPCA)],and (F) anaerobic [H200N-Co-HPCD(4NC)].

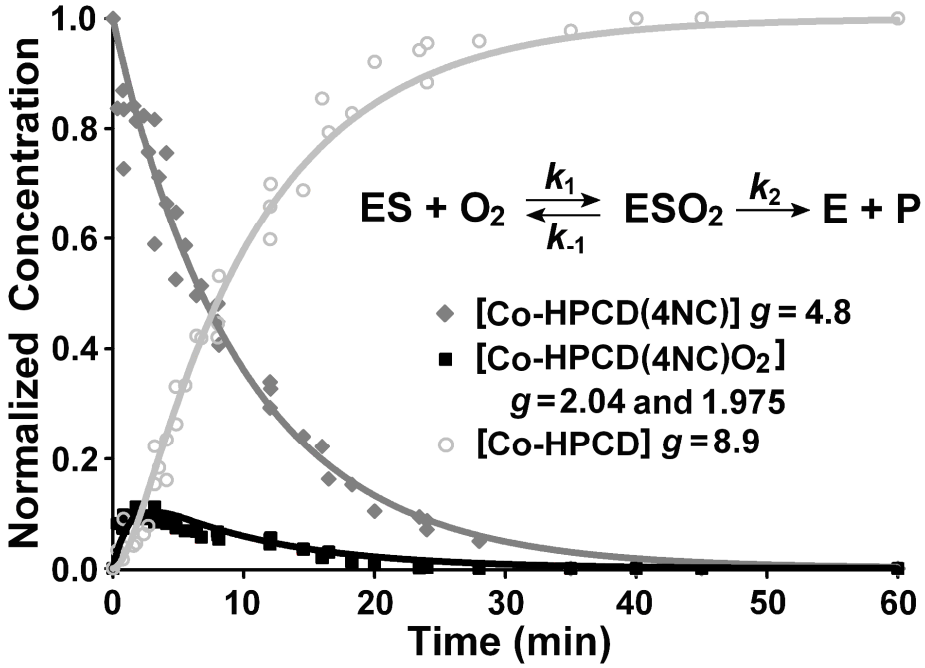

Figure 3.6. Time dependence of the various EPR-active species observed in EPR freeze-quench experiments. The change in concentration of each species was measured by monitoring the change in the intensity of EPR features unique to each species. The initial and final spectra were used to normalize the concentrations of [Co-HPCD(4NC)] and Co-HPCD, respectively. The maximum yield of [Co-HPCD(4NC)O_2] was measured by spin quantification and used to normalize its concentration.[224] Solid lines represent fits of data by global analysis to rate equations based on the reaction Scheme 3.2.

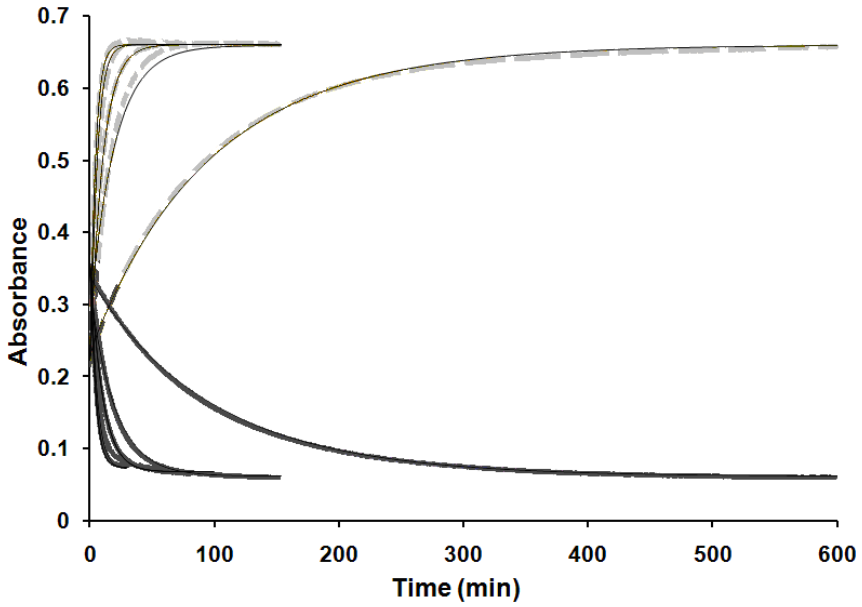

Figure 3.7. Global analysis fit of single-turnover reactions monitoring the decay of [Co-HPCD(4NC)] enzyme-substrate complex at 516 nm band (solid, dark gray lines) and the growth of the 4NC extradiol ring-cleaved product at 390 nm band (dashed, light gray lines). UV-Vis data was simultaneously fit with EPR data in Figure 3.6 to rate equations based on the Scheme 3.2. Reaction conditions: [Co-HPCD(4NC)] (30 μM 4NC and 150 μM Co-HPCD) in the presences of 0.29, 1.37, 2.74, 4.12 and 6.86 mM O_2 (0.21–5 atm O_2, Figure 3.3), 50 mM MES (pH 6.0), and 22 °C. Thin lines represent fits of data to the O_2 binding and activation mechanism illustrated in Scheme 3.2 with rate constants $k_1 = 40 \pm 5$ M^{-1} min^{-1}, $k_{-1} = 0.05 \pm 0.01$ min^{-1}, and $k_2 = 0.72 \pm 0.06$ min^{-1}.

3.4 [H200N-Co-HPCD(4NC)superoxide]

3.4.1 Reversible O_2 binding. The H200N-Co-HPCD mutant showed no extradiol ring-cleavage activity for 4NC at all pHs examined. Nevertheless, the [H200N-Co-HPCD(4NC)] complex could form an O_2 adduct with an S = 1/2 EPR spectrum similar to that of [Co-HPCD(4NC)O_2] (Figure 3.8). In fact, because $k_2 = 0$, the

intermediate is formed in higher yield (50% under 2 atm O_2), facilitating investigation of its properties. Interestingly, no significant UV-Vis spectral changes between [H200N-Co-HPCD(4NC)] and [H200N-Co-HPCD(4NC)O_2] were observed (Figure 3.9), suggesting that the 4NC chromophore is not affected by O_2 binding. Accordingly, O_2 binding to [H200N-Co-HPCD(4NC)] proved to be reversible, as purging the sample with argon caused the S = 1/2 species to disappear, restoring the EPR signal of the enzyme-substrate complex (Figure 3.10). O_2 binding experiments monitored by EPR spectroscopy (Figure 3.11) showed that [H200N-Co-HPCD(4NC)] has a low affinity for O_2, with a K_D^{O2} of 2.8 ± 0.2 mM O_2 at pH 7.5, similar to the value of 1.3 mM O_2 deduced for Co-HPCD from the kinetic fits described above.

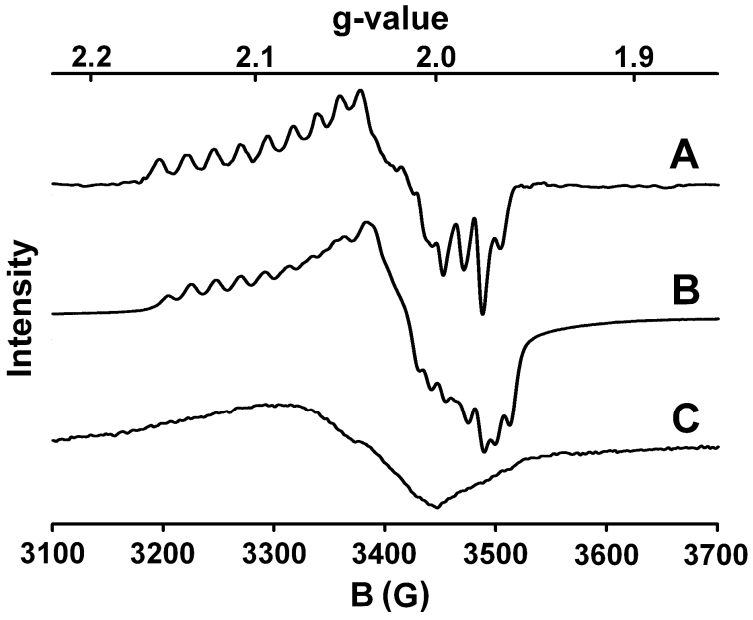

Figure 3.8. EPR spectra of (A) [Co-HPCD(4NC)$^{16}O_2$] at pH 6.0, (B) [H200N-Co-HPCD(4NC)$^{16}O_2$] at pH 7.5, and (C) [H200N-Co-HPCD(4NC)$^{17}O_2$] at pH 7.5 (prepared with 70% $^{17}O_2$). Spectra were obtained at 9.64 GHz, 20 dB microwave power at 20 K.

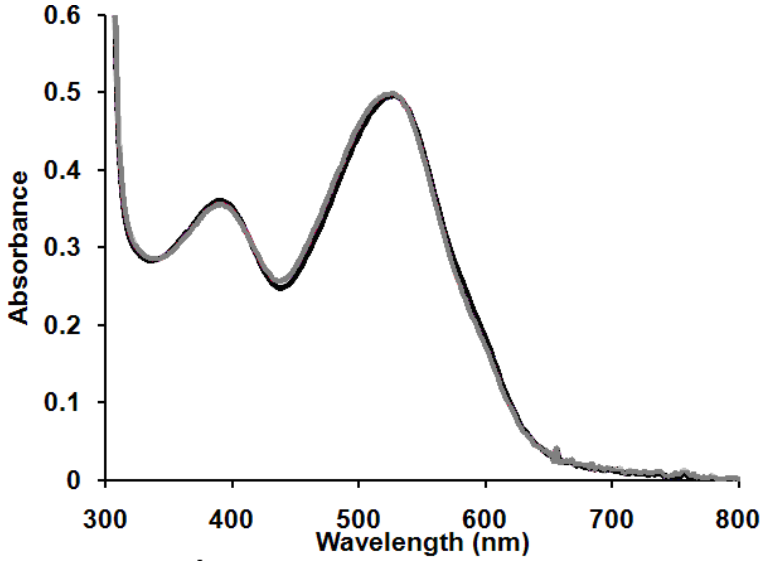

Figure 3.9. UV-Vis spectra of the anaerobic [H200N-Co-HPCD(4NC)] enzyme-substrate complex (black line), 40 μM 4NC and 150 μM H200N-Co-HPCD, and [H200N-Co-HPCD(4NC)O_2] (gray line), 40 μM 4NC, 150 μM H200N-Co-HPCD reacted under 2 atm O_2 for 2 hrs at 22 °C in 50 mM MOPS pH 7.5. A 50% yield of the O_2 adduct was measured by EPR for samples prepared under identical conditions (Figure 3.11).

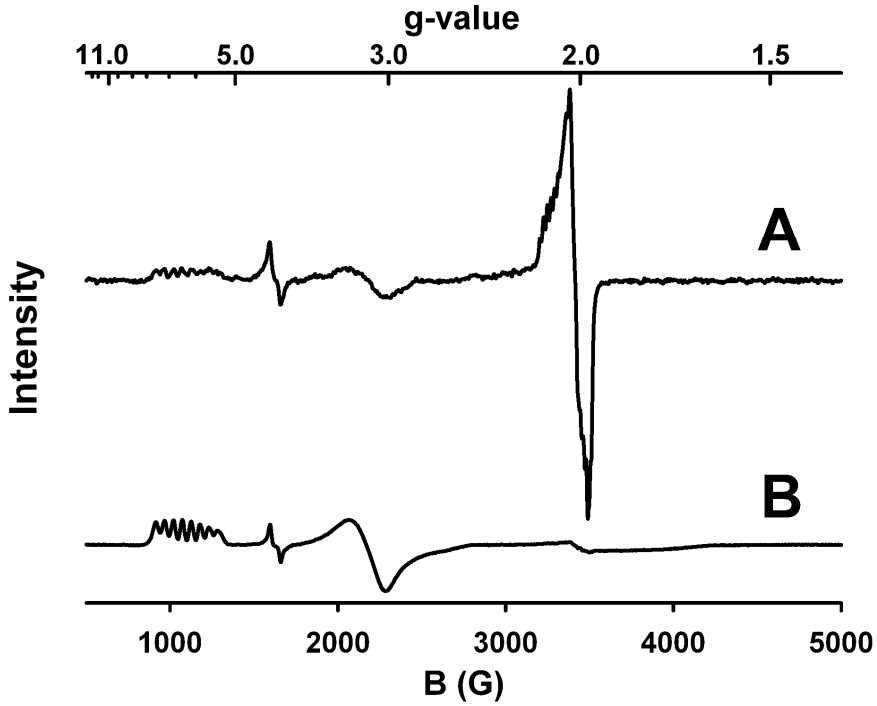

Figure 3.10. EPR spectra showing reversible binding of O_2 to [H200N-Co-HPCD(4NC)] in 50 mM MOPS pH 7.5. (A) Formation of the [H200N-Co-HPCD(4NC)] complex after exposure to 1 atm O_2 at 4 °C for 10 minutes to afford a ~40% yield of the S = 1/2 Co(III)-superoxide species, as measured by EPR spin quantification.[224] (B) Disappearance of the [H200N-Co-HPCD(4NC)O_2] complex after being purged with argon for 1 hr. Both spectra were obtained at 9.64 GHz, 20 dB and 20 K. The signal at g = 4.3 derives from contaminating high-spin Fe(III).

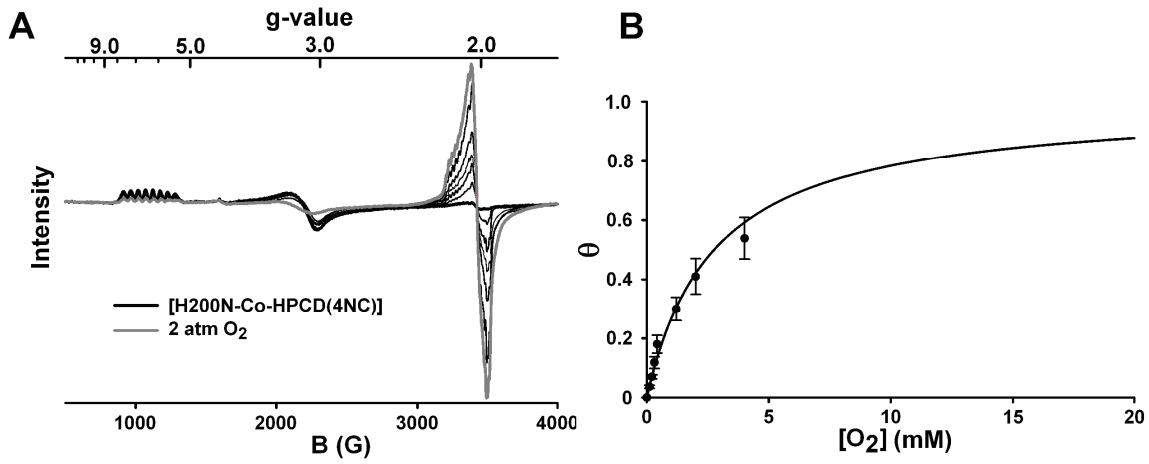

Figure 3.11. [H200N-Co-HPCD(4NC)] O_2 titration experiment monitored by EPR: **Panel A** EPR spectra of anaerobic [H200N-Co-HPCD(4NC)] incubated under increasing pressures of O_2 and then frozen in EPR tubes. Reaction conditions: 50 mM MOPS buffer pH 7.5 4 °C. **Panel B.** O_2-binding curve from EPR experiments K_D = 2.8 ± 0.2 mM O_2 (P_{50} = 1.4 ± 0.1 atm). The y-axis (θ) is the fraction O_2 bound.

3.4.2. $^{17}O_2$ EPR experiment. Both the H200N and wild-type [Co-HPCD(4NC)O_2] O_2-adducts exhibit small ^{59}Co hyperfine splittings of <25 G (Table 3.1). These are comparable to other characterized low-spin Co(III)-superoxide species (Table 3.1), where the unpaired electron is localized on the superoxide moiety and the observed ^{59}Co hyperfine splitting is attributed to spin polarization.[225-229] Furthermore, the use of $^{17}O_2$ (I = 5/2) results in significant broadening of the S = 1/2 EPR signals of both H200N- and wt-[Co-HPCD(4NC)O_2] O_2-adducts (Figures 3.8C and 3.12), in strong support of the low-spin Co(III)-superoxo description for the O_2-adducts.

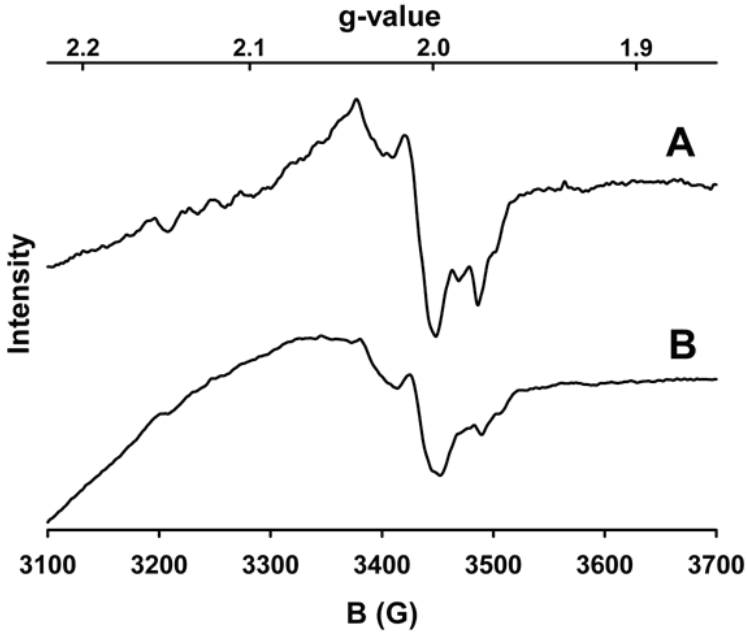

Figure 3.12. EPR spectra of (A) [Co-HPCD(4NC)$^{16}O_2$], and (B) [Co-HPCD(4NC)$^{17}O_2$] enriched with 45% $^{17}O_2$. Samples were prepared by mixing anaerobic [Co-HPCD(4NC)] in 50 mM MES at pH 5.5 with oxygenated buffer in EPR tubes and reacting the sample for ~5 min at 30 °C before freezing it in liquid nitrogen. Only the g = 2 regions are shown; spectra were obtained at 9.64 GHz, 20 dB microwave power at 20 K.

Table 3.1. Electron paramagnetic resonance data for Co(II)-complexes and their Co(III)-superoxide adducts.

Sample	*S* =	*g*-values	^{59Co}A (G)	^{17O}A (G)	References
Co-HPCD	3/2	6.7, 3.4, 2.4	80		[169]
[Co-HPCD(HPCA)]	3/2	7.6, 2.5, 1.9	98		[169]
[Co-HPCD(4NC)]	3/2	5.6, 3.5, 2.1	75		[130]
[Co-HPCD(4NC)O_2]	**1/2**	**2.10, 2.02, 1.99**	**24**		[130]
[H200N-Co-HPCD]	3/2	6.9, 3.7, 2.6	90		[130]
[H200N-Co-HPCD(4NC)]	3/2	6.3, 3.2, 1.9	53		[130]
[H200N-Co-HPCD(4NC)O_2]	**1/2**	**2.10, 2.02, 1.99**	**22**		[130]
Co-Mb	1/2	2.33, 2.32, 2.02	79, 6		[230]
[Co-Mb(O_2)] Species 1	1/2	2.081, 2.000, 1.99	-13.1, -23.5, -8.8	12, -72.5, 20	[230, 231]
[Co-Mb(O_2)] Species 2	1/2	2.079, 2.013, 1.985	-9.33, -16.7, -5.95	$O_{\perp}$ 5.0, -67.5, 2.4 $O_{\parallel}$ 5.4, -83.3, 30.3	[230, 231]
[Co-salMeDPT]	3/2	~ 4.3			[232]
[Co(salMeDPT)O_2]	1/2	2.086, 2.005, 1.999	18.7, 12.0, 13.6		[225, 232, 233]

Table 3.1 Continued.

Sample	S =	g-values	^{59Co}A (G)	^{17O}A (G)	References
[Co(saldpt)O_2]	1/2	2.085, 2.007, 2.000	22.7,13.3, 13.5		[226]
[Co(salen)THF]	1/2	2.4, 2.013	51, 127		[227, 234]
[Co(salen)O_2]	1/2	2.082, 2.024 1.996	25, 18		[227, 234]
[Co-(TPFC)O_2]	1/2	2.113, 2.017, 1.979	31.5, 10.3, 12.9		[235]
Vitamin B_{12r}	1/2	2.310, 2.190, 2.004	20, 26, 107		[236]
[Vitamin $B_{12r}(O_2)$]	1/2	2.089, 2.013, 1.993	-6.04, -23.0, -10.8	O_α43.3, 21.6, 21.6 O_β51.1, 25.6, 25.6	[236]
[Co(bzacen)pyO_2]	1/2	2.000, 2.085, 2.024	18, 19.2	60, 80	[227, 237-239]

[a]Abbreviations used: HPCD, Homoprotocatechuate 2,3-dioxygenase from *Brevibacterium fuscum*; HPCA, homoprotocatechuate; 4NC, 4-nitrocatechol; Co-Mb, cobalt-substituted sperm whale myloglobin; saldMeDPT, bis(salicy1idene-yiminopropyl)methylamine; saldpt, N,N'-bis(salicylidene)dipropylenetriamine; salen, N,N'-ethylenebis(salicylimine); THF, tetrahydrofuran; TPFC, 5,10,15-trispentaflurophenylcorrolato; bzacen, N,N′-ethylenebis(1-phenyl-3-imino-1-butanonato); py, pyridine.

3.5 Low-spin to high-spin transition

The binding of O_2 to the ES complexes of Co-HPCD results in an apparent spin-state change from high-spin Co(II) in the enzyme-substrate complex to low-spin Co(III) in the O_2 adduct. However, as expected, such a spin transition is not observed for the corresponding O_2-adducts of Fe- or Mn-HPCD because of the weak-field nature of the HPCD coordination environment.[162, 179] Co(III) differs from the other two metal centers, because of its d^6 electronic configuration and the consequent large ligand-field stabilization energy that favors the low-spin state, as found for all Co(III)-superoxide complexes characterized to date.[226, 227] The formation of the low-spin adduct is likely to be an important factor that promotes O_2 binding, despite the high Co(III/II) potential. However, the required reorganization that accompanies the spin transition as the O_2 adduct forms and the high Co(III/II) potential work together to raise the barrier for O_2 binding, which shifts the rate-limiting step to the O_2-binding phase of the catalytic cycle for Co-HPCD.[169]

The decay rate of the observed low-spin Co(III)-superoxide species is at least 7 orders of magnitude slower than the rate of the analogous step using Fe-HPCD,[166, 167] even though one may expect Co(III) to be a stronger oxidant than Fe(III) in the subsequent one-electron oxidation of 4NC. This slow rate of 4NC oxidation likely reflects the large kinetic barrier arising from an increase in the reorganization energy upon electron transfer as the low-spin Co(III)-superoxide converts to a high-spin [Co(II)($SQ^{\bullet}$)$O_2^{\bullet-}$] species (Scheme 3.3).[240]

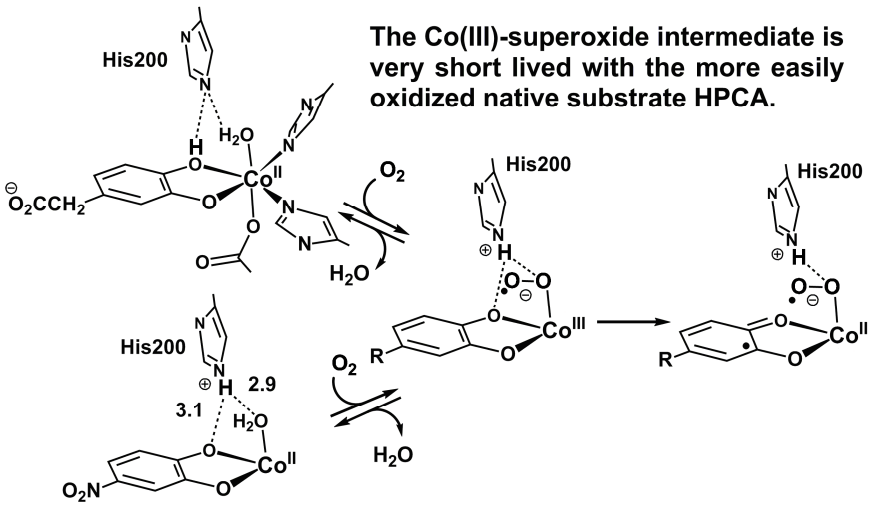

Scheme 3.3. Proposed O_2 activation mechanism by Co-HPCD with HPCA at pH 9.0 and 4NC at pH 5.5.[169]

3.6 Role of H200

His200 has been shown previously by site-directed mutagenesis to be a catalytically important residue for Fe-HPCD.[162 167, 168, 181] The fact that H200N-Co-HPCD is not catalytically active but is nonetheless able to bind O_2 reversibly when 4NC is bound to the cobalt center suggests that the H200 residue is not required for O_2 binding, but must be essential for a subsequent step. In Fe-HPCD crystal structures of the substrate complex and intermediates following O_2 binding, H200 is observed to be involved in weak hydrogen bonding interactions with the OH moiety of the monoanionically bound catecholate as well as stronger interactions with the various O_2-derived ligands.[165, 174, 213, 241] His200 has been proposed to facilitate electron transfer from substrate to the M-O_2 unit by a proton-coupled electron transfer mechanism, where it acts as a base to remove the proton from the substrate to assist in catechol oxidation. In turn, the protonated His200 residue can interact with the O_2 adduct as it forms and stabilize the developing negative charge on the dioxygen moiety.[165, 174] In the next step,

the protonated His200 may also help to orient the superoxide moiety to optimize its attack on the substrate semiquinone radical to form the alkylperoxo intermediate that leads to the extradiol cleavage of the substrate.[162, 165] These proposed roles are illustrated in Scheme 3.3.

3.6.1 [wt-Co-HPCD(4NC)] and [H200N-Co-HPCD(4NC)] pH titrations. Scheme 3.3 can also rationalize the dramatically different pH-activity profiles of Co-HPCD with HPCA and 4NC as substrates. Optimal extradiol cleavage of HPCA occurs at pH 9.0 (Figure 3.13), but for 4NC the pH optimum is at pH 5.5 (Figure 3.14). This may arise from the drastically different pK_a's of HPCA and 4NC,[242, 243] resulting in HPCA binding to Co-HPCD as a monoanionic catecholate and 4NC binding as a dianion.[166, 244, 245] In the case of the latter, the intensity of its characteristic 516 nm band of the dianion decreases and the rate of 4NC turnover increases as the pH is lowered (Figure 3.14 and 3.15A). However the decrease in the 516 nm band is not accompanied by the appearance of a 425 nm chromophore associated with the 4NC monoanion (Figure 3.15A),[244, 245] so lowering the pH from 9.0 to 5.5 does not result in the protonation of the bound 4NC. Instead, we suggest that H200 becomes protonated and then hydrogen bonds to the bound 4NC to affect its chromophore. This notion is consistent with the observation that the 4NC chromophore of the [H200N-Co-HPCD(4NC)] complex is much less sensitive to changes in pH (Figure 3.15B). As Asn200 has a shorter side chain and cannot be protonated in this pH range, it is unable to interact productively with 4NC. The differences in the pH-activity profiles for HPCA and 4NC as substrates can thus be rationalized by the key role proposed for H200 as an acid/base catalyst to promote

electron transfer from the substrate to the $M–O_2$ unit to advance the reaction cycle beyond the O_2 binding step. In the case of HPCA, protonation of H200 occurs upon extraction of the proton from the bound substrate concomitant with its oxidation. The analogous proton transfer to H200 cannot occur for 4NC, as it is bound as a dianion. However, H200 can be protonated by solvent at lower pH, resulting in the observed increase in the rate of 4NC cleavage (Figure 3.14). The H200N mutation prevents the ring-cleavage reaction by eliminating both protonation pathways as well as any effects on orientation of the oxy-moiety.

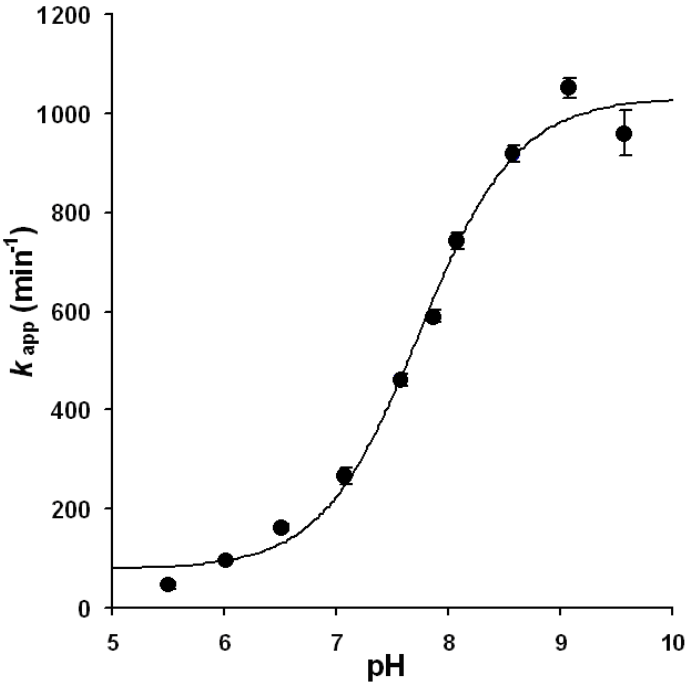

Figure 3.13. pH-Activity profile (black, ●) of extradiol ring-cleavage of HPCA by Co-HPCD. Reaction conditions: 22 °C, 1 atm O_2 (1.37 mM O_2), 180 nM Co-HPCD, and 2 mM HPCA. Product formation was monitored at the pH-independent isosbestic point for the colored product (ε_{350} = 13,900 M^{-1} cm^{-1}). The background rate of the base-catalyzed substrate auto-oxidation reaction monitored at 350 nm was subtracted for pH > 8.[181] The thin black line represents fit of data to equation 3.1 with an apparent pK_a of 7.74 ± 0.06.[223] Buffer mixtures consisting of MES, bis-Tris, MOPS, Tris, CHES, and CAPS, all at 25 mM concentrations were prepared at pH 5.5, 6.0 6.5, 7.0, 7.5, 8.0 and 8.5. The final conductivity of each buffer was then adjusted to 6.4 mS using 2 M NaCl.

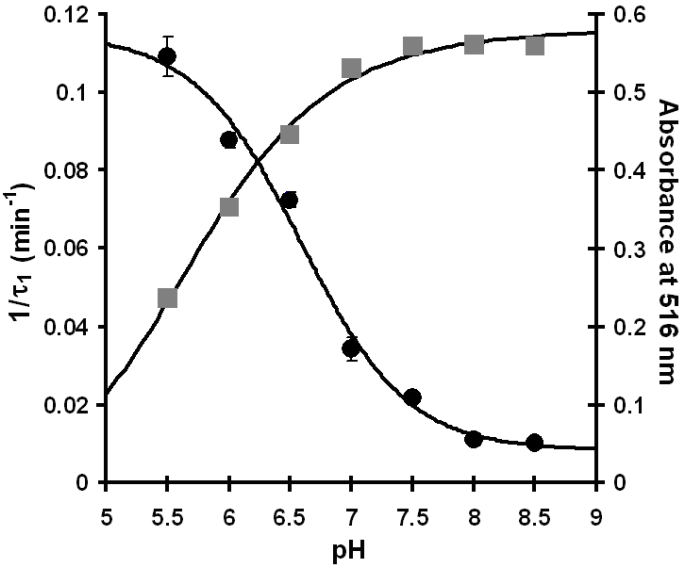

Figure 3.14. pH-activity profile (black, ●) of extradiol ring-cleavage of 4NC by Co-HPCD. Reactions conditions: 2 atm O_2 (2.75 mM O_2), 40 μM 4NC, 120 μM Co-HPCD and 22 °C. UV-Vis spectrophotometric pH titration curve (gray, ■) of anaerobic [Co-HPCD(4NC)] enzyme-substrate complex (40 μM 4NC 150 μM Co-HPCD) shown in Figure 3.15A by monitoring dianionically bound form at 530 nm. Thin black lines represent fit of data to equation 3.1 and 3.2 with apparent pK_a's of 6.59 ± 0.09 and pK_a = 5.72 ± 0.05 for the pH-activity profile and spectrophotometric pH titration respectively.[223] Co-HPCD rapidly precipitates at pH ≤ 5.0. Buffer mixtures consisting of MES, bis-Tris, MOPS, Tris, CHES, and CAPS, all at 25 mM concentrations were prepared at pH 5.5, 6.0, 6.5, 7.0, 7.5, 8.0, and 8.5. The final conductivity of each buffer was then adjusted to 6.4 mS using 2 M NaCl.

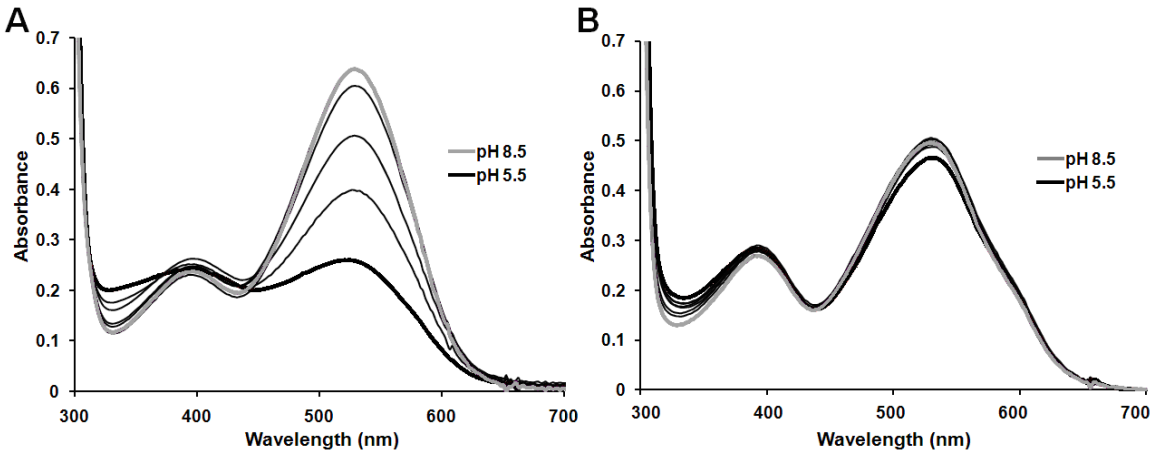

Figure 3.15. UV-Vis spectrophotometric pH titration of **(A)** anaerobic [Co-HPCD(4NC)] enzyme-substrate complex (40 μM 4NC and 150 μM Co-HPCD) and **(B)** [H200N-Co-HPCD(4NC)] (40 μM 4NC and 150 μM H200N-Co-HPCD). Buffer mixtures consisting of MES, bis-Tris, MOPS, Tris, CHES, and CAPS, all at 25 mM concentrations, were prepared at pH 5.5, 6.0, 6.5, 7.0, 7.5, 8.0 and 8.5. The final conductivity of each buffer was then adjusted to 6.4 mS using 2 M NaCl.

3.6.2 Effect of H200N mutation. The H200N-Fe-HPCD, mutant is similarly unable to catalyze extradiol cleavage of 4NC, but instead catalyzes the 2-e^- oxidation of 4NC to yield quinone and H_2O_2.[162, 166, 167] Initial O_2 binding to [H200N-Fe-HPCD(4NC)] is very rapid and reversible (k_1 = 9 ± 1.2 x 10^6 M^{-1} min^{-1}, and k_{-1} 3120 min^{-1} at 4 ^oC and pH 7.5) and leads to the formation of a long-lived Fe(III)-superoxo species analogous to the Co(III)-superoxo species observed in this study, This shows that the initial electron transfer step from M(II) to O_2 proceeds with either metal in the absence of H200. However, the subsequent electron transfer step from substrate to the M–O_2 unit is clearly blocked for the unreactive low-spin [H200N-Co-HPCD(4NC)O_2] species, but can still occur for the high-spin [H200N-Fe-HPCD(4NC)O_2] intermediate, (k = 1.32 min^{-1} at 4 ^oC and pH 7.5) to form a high-spin Fe(III)(4-nitrobenzosemiquinone)peroxo intermediate.[162, 167]

3.7 Summary

In summary, we have characterized the O_2 adduct of a cobalt-substituted iron dioxygenase that exhibits comparable activity to its iron analog. The O_2 adduct is best described as a low-spin Co(III)-superoxo complex,[225-229] the first example of such a species for a functional cobalt oxygenase. We have also shown that H200 plays a crucial role in promoting the subsequent oxidation steps that leads to extradiol cleavage of the substrate by acting as an acid/base catalyst and properly orienting the superoxide to attack the substrate. The substitution of Co(II) for the native Fe(II) center in HPCD shifts the rate determining step from the product release phase of the catalytic cycle in the case of the Fe(II) enzyme to the O_2 binding and catechol oxidation phase for the Co(II) enzyme.[166, 167] This shift probably results from the higher kinetic barrier associated with O_2 binding to Co-HPCD due to the higher M(III/II) redox potential of the cobalt center and the spin transition from high-spin Co(II) to low-spin Co(III) upon O_2 binding to Co-HPCD. It may also involve the reverse spin transition in the subsequent electron transfer from the electron-poor 4NC substrate to the low-spin Co-superoxo unit. A similar change in oxidation and spin state presumably occurs as [Co-HPCD(HPCA)] binds O_2, but this remains to be demonstrated. However, the fact that the HPCA reaction is at least 1000-fold faster than that for 4NC suggests that the lifetime of the putative low-spin Co(III)-superoxo intermediate significantly decreases as the electron-poor 4NC is replaced with the more easily oxidized substrate. Further efforts are aimed at trapping the analogous superoxo intermediate with substrates other than 4NC.

3.8 Inactivity of [Mn-HPCD(4NC)], [H200N-Mn-HPCD(4NC)], and [H200N-Mn-HPCD(HPCA)] complexes toward O_2 binding.

While Fe-HPCD turns over 4NC (0.4 sec^{-1}) 25 times slower than HPCA (10 sec^{-1}) and the turnover of 4NC by Co-HPCD is (0.012 sec^{-1}) ~33 times slower than by Fe-HPCD, Mn-HPCD does not turnover 4NC at any detectable rate even at high O_2 concentrations/pressures.[130, 166] At first, the inactivity of Mn-HPCD for 4NC turnover was not to surprising given that other characterized Mn-dependent 3,4-dihydroxyphenylacetate 2,3-dioxygenases from *Bacillus brevis* and Mn-MndD from *Arthrobacter globiformis* also do not turnover 4NC.[177, 246] The question of why Co-HPCD is able to turnover 4NC, while Mn-HPCD is not able to given the 0.36 V higher standard M(III/II) redox potential of Co than Mn is intresting.[178]

UV-Vis experiments show that 4NC binds dianionically to both wt-Mn-HPCD and H200N-Mn-HPCD. EPR (Figure 3.17) experiments also show that 4NC binds to both wt-Mn-HPCD and H200N-Mn-HPCD as observed from a decrease in the intensity of the signal at $g = 2$ and the appearance of new $S = 5/2$ EPR at g = 4.1 and 8.8 upon anaerobic addition of 4NC to the enzymes. No perceivable decrease in the intensity or line shape of the EPR spectra are observed after incubating the enzyme-substrate complexes under 1 atm of O_2 for 10 min at 4 °C. Given that the system starts with an odd number of electrons (high-spin Mn(II), $S = 5/2$ and triplet O_2, $S = 1$) the initial O_2 adduct and any conceived intermediate species are expected to give perpendicular mode EPR signals. The EPR experiment therefore gives no evidence that O_2 is even binding to the [Mn-HPCD(4NC)] complexes. No change in the 4NC chromophore is observed upon incubating the [Mn-HPCD(4NC)] enzyme-substrate complexes under 2 atm of O_2 for

extended periods of time as well. The H200N-Mn-HPCD mutant is also inactive in the turnover of the electron rich native substrate HPCA. The [H200N-Mn-HPCD(HPCA)] enzymes substrate does not even appear to bind O_2 by EPR (Figure 3.16). This is in contrast to the [Co-HPCD(4NC)] and [H200N-Co-HPCD(HPCA)] complexes, which form O_2-adducts reported in sections 3.4 and 4.2.3.E, respectively.

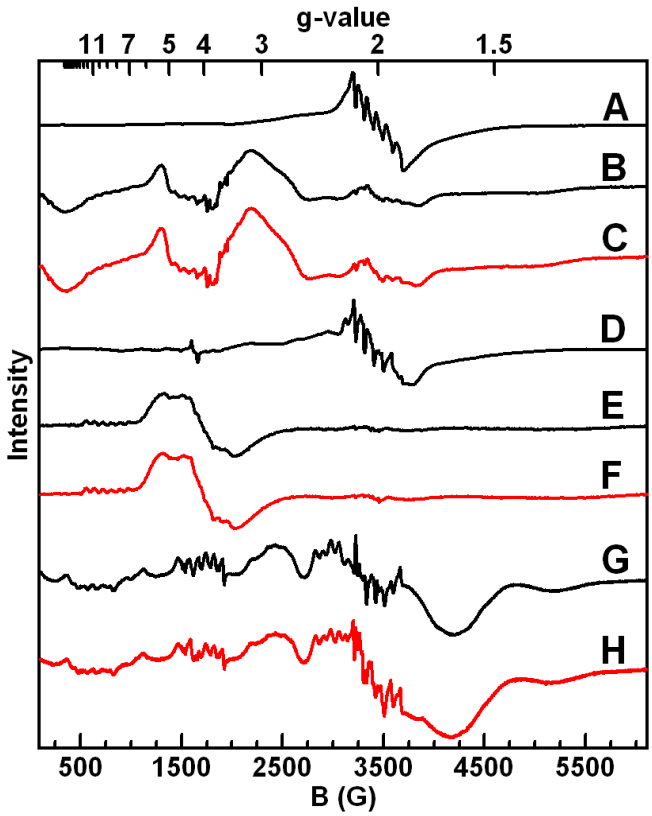

Figure 3.16. EPR spectra obtained at 9.64 GHz, 30 dB and 10 K in 50 mM MOPS pH 7.5. (A) wt-Mn-HPCD, (B) anaerobic [wt-Mn-HPCD(4NC)], (C) [wt-Mn-HPCD(4NC)] under 1 atm O_2 for 10 min, (D) H200N-Mn-HPCD (E) anaerobic [H200N-Mn-HPCD(4NC)], (F) [H200N-Mn-HPCD(4NC)] under 1 atm O_2 for 10 min, (G) anaerobic [H200N-Mn-HPCD(HPCA)] and (H) [H200N-Mn-HPCD(HPCA)] under 1 atm O_2 for 10 min. (wt- and H200N-Mn-HPCD protein was prepared by former Que lab member Dr. Erik R. Farquhar.)

3.9 Nitric oxide binding to Co-HPCD and Mn-HPCD enzyme-substrate complexes.

Similar differences in reactivity of [Mn-HPCD(HPCA)] and [Mn-HPCD(4NC)] where explored by Dr. Erik. .R. Farquhar in collaboration with the EPR spectroscopist Dr. Joshua Allen Hayden (former student of Professor Michael P. Hendrich at Carnegie Mellon) reported in Dr. Hayden's thesis.[247] They observed that while [Mn-HPCD(HPCA)] readily binds the O_2 surrogate nitric oxide (NO) to form an EPR silent [Mn-HPCD(HPCA)NO] complex, the [Mn-HPCD(4NC)] enzyme-substrate complex does not react with NO. They interpreted this difference in reactivity to be due to the difference in binding modes between HPCA and 4NC where HPCA binds to the metal center as a monoanionic catecholate and 4NC binds as the dianion. Upon substrate oxidation His200 is thought to deprotonate the monoanionic catecholate and then the protonated histidine cation is thought to help stabilize the growing negative charge on the O_2 adduct. Since 4NC binds dianionically it can not contribute a proton to His200 to stabilize the O_2 adduct.

We tested this hypothesis by attempting to bind NO to [Mn-HPCD(4NC)] at low pH (6.0). Since pH titrations of [wt/H200N-Mn-HPCD(4NC)] (Figure 3.17) suggest that His200 is protonated at low pH as was suggested from the analogous [wt-/H200N-Co-HPCD(4NC)] pH titration experiments (Figure 3.15). At pH 6.0 there was still no evidence by EPR of NO binding to the [Mn-HPCD(4NC)] complex.

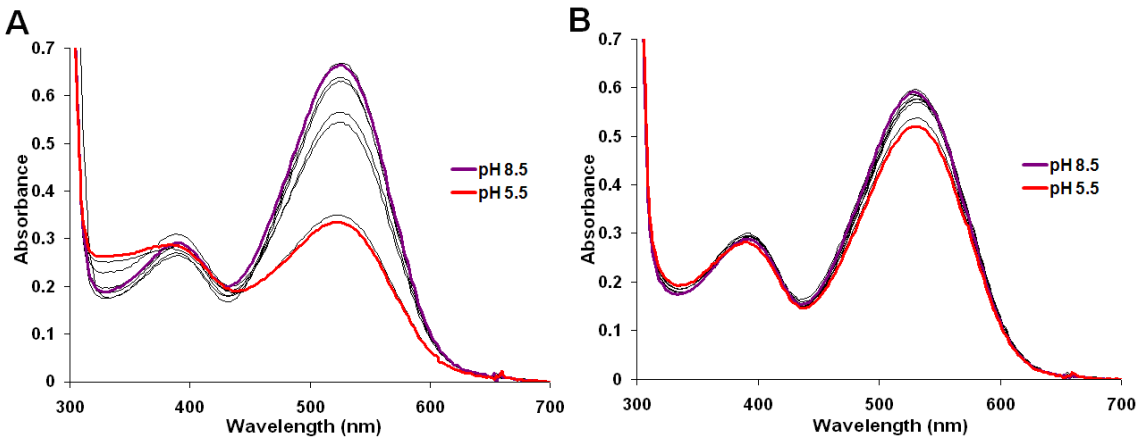

Figure 3.17. UV-Vis spectrophotometric pH titration of **(A)** anaerobic [Mn-HPCD(4NC)] enzyme-substrate complex (40 µM 4NC and 150 µM Mn-HPCD) and **(B)** [H200N-Mn-HPCD(4NC)] (40 µM 4NC and 150 µM H200N-Mn-HPCD). Buffer mixtures consisting of MES, bis-Tris, MOPS, Tris, CHES, and CAPS, all at 25 mM concentrations, were prepared at pH 5.5, 5.6, 6.0, 6.5, 7.0, 7.5, 8.0 and 8.5. The final conductivity of each buffer was then adjusted to 6.4 mS using 2 M NaCl.

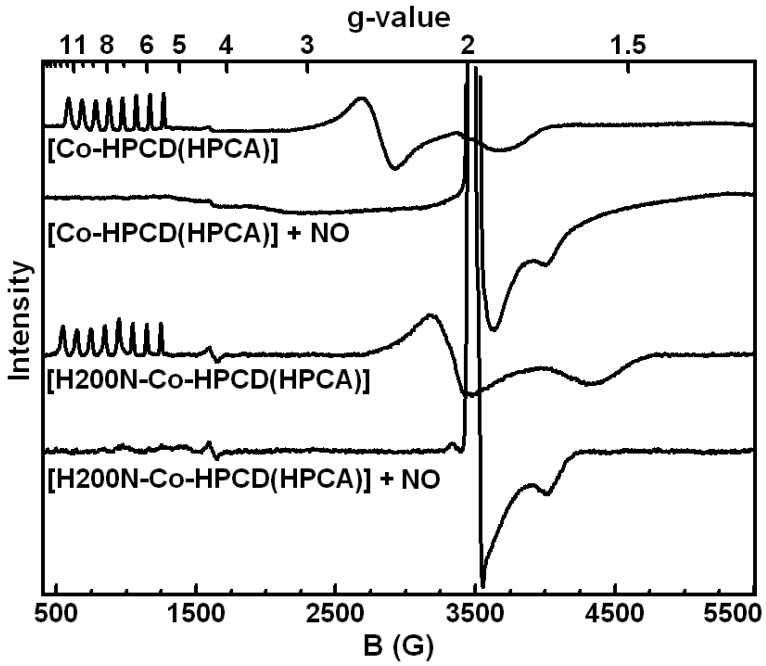

Figure 3.18. EPR spectra of [wt- and H200N-Co-HPCD(HPCA)] before and after the addition of NO. EPR spectra were obtained at 9.64 GHz, 20 dB and 20 K in 50 mM MOPS pH 7.5. EPR signal at $g = 2$ is from excess of NO.

Nitric oxide was observed to bind to [Co-HPCD(HPCA)] and [H200N-Co-HPCD(HPCA)] as observed by loss of the $S = 3/2$ EPR signals of the enzyme-substrate complexes upon addition of NO to form an EPR silent NO complex (Figure 18). Nitric oxide binding proved to be reversible as purging the sample with argon resulted in active Co-HPCD. The quantitative yield of the NO-adducts in solution should allow for further experiments characterize of the electronic and geometric structure of the Mn and Co NO-adducts by XAS and MCD.

3.10 Possible explanation for unexpected differences in reactivity of Mn and Co-HPCD.

One possible explanation for this difference in reactivity between Mn and Co 4NC enzyme-substrate complexes toward O_2 may be due to the high to low-spin transition observed upon binding O_2 to high-spin Co(II)-4NC to form low-spin Co(III)-4NC-superoxide while the probable [Mn(III)(HPCA)-superoxide] intermediate characterized by EPR contained a high-spin Mn(III) center ferromagnetically coupled to a radical.[179] The spin transition observed upon O_2 binding to Co-HPCD enzyme-substrate complexes adds an additional kinetic barrier from the required reorganization energy upon going low-spin. The low-spin state may actually help stabilize the O_2 adduct though allowing it to accumulate long enough for it to oxidize 4NC despite the higher Co(III/II) redox potential and harder to oxidize electron-poor substrate. In similar experiments employing a series of substituted catechol substrate analogues 4XC (X = F, Cl, and Br) with Mn- Fe- and Co-HPCD. We find that Mn-HPCD is the slowest of the three enzymes at turning over these substrates as well. DFT studies investigating the barrier and spin states of the reaction of the three [M-HPCD(4NC)] complexes with O_2 may give

additional insights into the effects of the different electronic configurations of the three metals in coupling the oxidation of the catechol substrate to the reduction activation of O_2.

3.11 Inactivity of Co-H200Q.

While Fe-HPCD H200A, Q, N, E and F mutants all show extradiol ring-cleavage activity for HPCA, though at decreased rates compared to wt-Fe-HPCD. Mn- or Co-substituted H200N and H200Q mutants do not turnover HPCA.[167, 247] It was found that [H200N-Co-HPCD(4NC)] does reversibly bind O_2 to form a low-spin Co(III)-superoxide species (Figure 3.11), [H200N-Mn-HPCD(4NC)] and [H200N-Mn-HPCD(HPCA)] do not appear to even bind O_2 (Figure 3.16). The Co-H200Q mutant does bind HPCA and 4NC but the enzyme-substrate complexes do not react with O_2 even at high concentrations in UV-Vis or EPR experiments (Figures 3.19 and 3.20). All three amino acid residues (His, Gln and Asn) can act as hydrogen bond donors to the O_2 adduct; the glutamine side chain is similar in length to histidine while the asparagine side chain is one carbon shorter. In DFT studies on [H200N-Fe-HPCD(4NC)O_2] the superoxide is thought to bind end-on while the observed superoxide species in the X-ray crystal structure with the wild-type enzyme was side-on bound.[162, 165] The shorter side chain of the H200N mutant may allow for more room for the O_2 adduct while the bulkier histidine residue may enforce the side-on binding of O_2. Histidine can also act as an acid-base catalyst where the protonated cationic histidine should better stabilize the developing negative charge on the activated O_2 species than Asn or Gln, which have neutral amide functional groups. The different activity of the Mn- Fe- and Co-substituted mutants may be an effect of the different redox potentials and electronic configurations of

the three metals as discussed in section 3.10 which are further exaggerated in the mutants.[247]

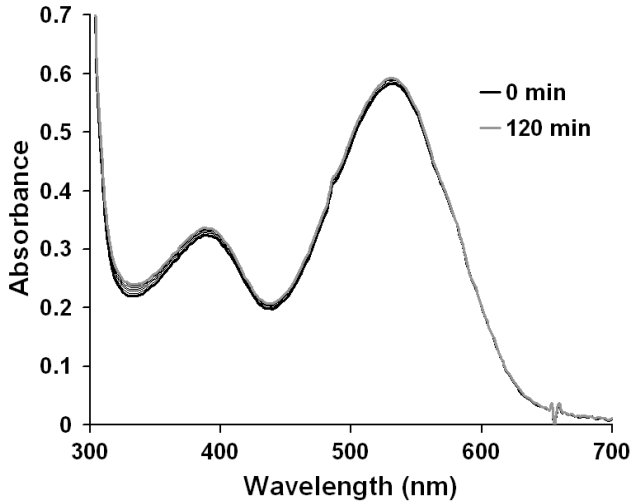

Figure 3.19. UV-Vis spectra of anaerobic [H200Q-Co-HPCD(4NC)] enzyme-substrate complex (Black), 40 μM 4NC and 150 μM H200Q-Co-HPCD, (gray) after incubating under 2 atm O_2 for 2 hrs at 22 °C in 50 mM MOPS pH 7.5.

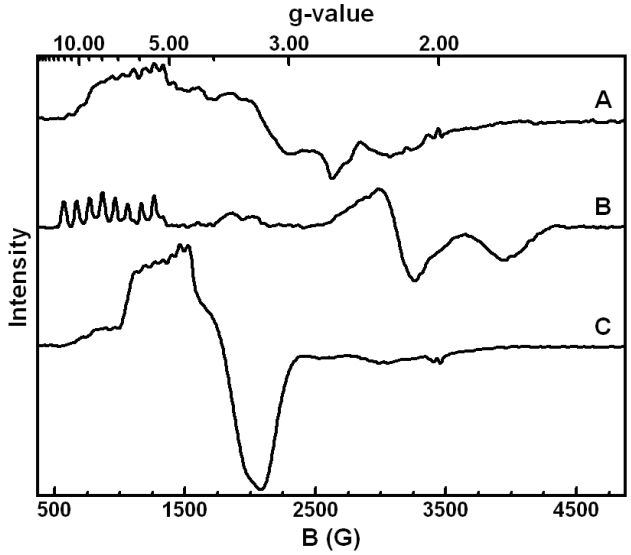

Figure 3.20. EPR spectra of: (A) H200Q-Co-HPCD pH 7.5 (g = 6.5 (^{59Co}A = 80 G), 3.3 and 2.2), (B) [H200Q-Co-HPCD(HPCA)] pH 7.5 incubated for 10 min under 2 atm O_2 at 4°C (g = 7.5 (^{59Co}A = 100 G), 2.2 and 1.7), and (C) [H200Q-Co-HPCD(4NC)] pH 7.5 incubated for 10 min under 2 atm O_2 at 4°C (g = 5.3 (^{59Co}A = 68 G), 3.8 and 3.3).

Chapter 4

Kinetic and Spectroscopic Experiments Characterizing Intermediate Species Observed in the Reaction of [Co-HPCD(4XC)] with O_2 (4XC = 4-Halogenated Catechols, X = F, Cl or Br).

4.1 Introduction

Homoprotocatechuate (HPCA) 2,3-dioxygenase from *Brevibacterium fuscum* (Fe-HPCD) has a six-coordinate Fe(II) center with two histidine and one glutamate amino acid ligands in a 2-His-1-carboxylate facial triad motif with three *cis*-labile solvent-derived ligands occupying the remaining three facial coordination sites.[53, 165, 174, 212] Monoanionic bidentate binding of the catechol substrate to the metal center displaces two of the bound waters.[213, 214, 248] The coordination of the anionic substrate serves to lower the redox potential of the Fe(II) center and promote the dissociation of the final solvent for O_2 binding. The Fe(II) center of HPCD can be replaced with either Mn(II) or Co(II).[131, 169] While both of these metals have higher M(III/II) standard redox potentials than Fe(II) they are still able to bind and activate O_2 to oxidatively cleave the aromatic ring of HPCA. Here we employ a series of the electron-poor halogenated substrate analogs (4XC, X = Br, Cl, or F) with Mn-, Fe- and Co-substituted HPCDs, to slow down the rate of catechol oxidation (Scheme 4.1). Two intermediates are observed in stopped-flow experiments with Co-HPCD upon mixing the anaerobic 4XC enzyme-substrate complexes with O_2-saturated buffer, these intermediate have been further characterized by EPR, as well as by steady-state and transient kinetic experiments.

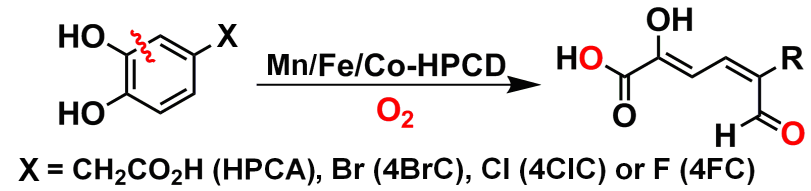

Scheme 4.1. Extradiol ring-cleavage of catechol substrates by Mn-, Fe- or Co-HPCD.

To harness the oxidizing power of triplet O_2, oxygenases generally activate O_2 by first reducing it to a more reactive superoxide or peroxide species.[123, 124] For many metalloenzymes, this entails the initial binding of O_2 to a divalent redox active metal center to generate a [M(III)-$O_2^{\bullet-}$] species. For catechol dioxygenases, O_2 binding and activation is proposed to be connected with catechol oxidation by concerted electron transfer from the catechol to O_2 via the metal center upon O_2 binding to produce a semiquinone-superoxide ($SQ^{\bullet}$-M(II)-$O_2^{\bullet-}$) diradical pair. The spin allowed reaction of the two radicals then forms the C-O bond of a bridging alkylperoxide intermediate (Scheme 4.2). Rearrangement of the alkylperoxide intermediate results in O-O and C-C bond cleavage to form the extradiol ring-cleaved product which has an intense yellow chromophore (~380 nm for HPCA cleavage product). To produce the chemoselective and regioselective proximal extradiol ring-cleavage product (Scheme 4.3), as opposed to the distal extradiol ring-cleaved product, intradiol ring-cleavage product, *ortho*-semiquinone, or *ortho*-quinone oxidation products, the generation and attack of the $O_2^{\bullet-}$ radical on the semiquinone ring and subsequent rearrangement mechanism must somehow be controlled by the enzyme.[2, 168, 249]

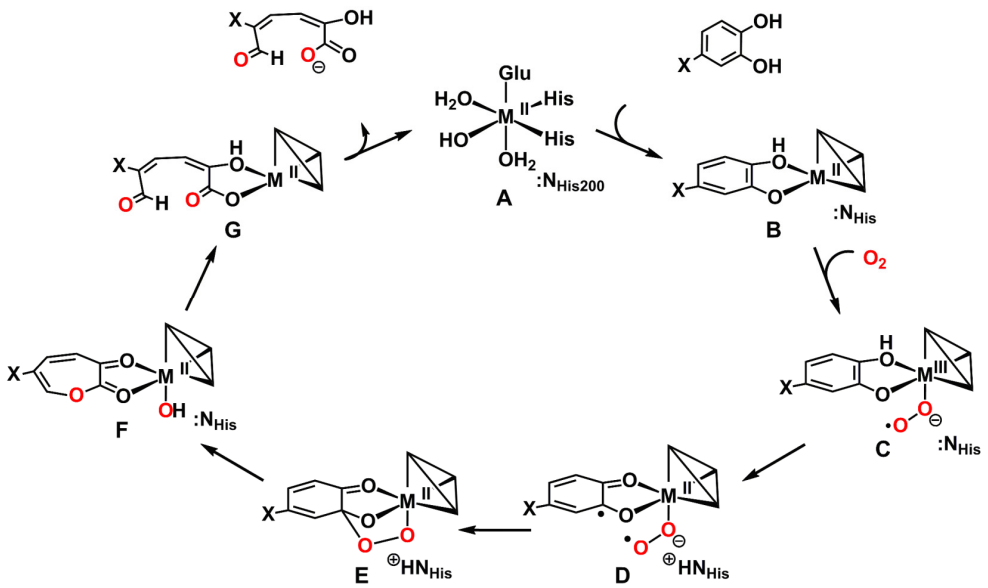

Scheme 4.2. Proposed mechanism of extradiol-cleaving catechol dioxygenases.

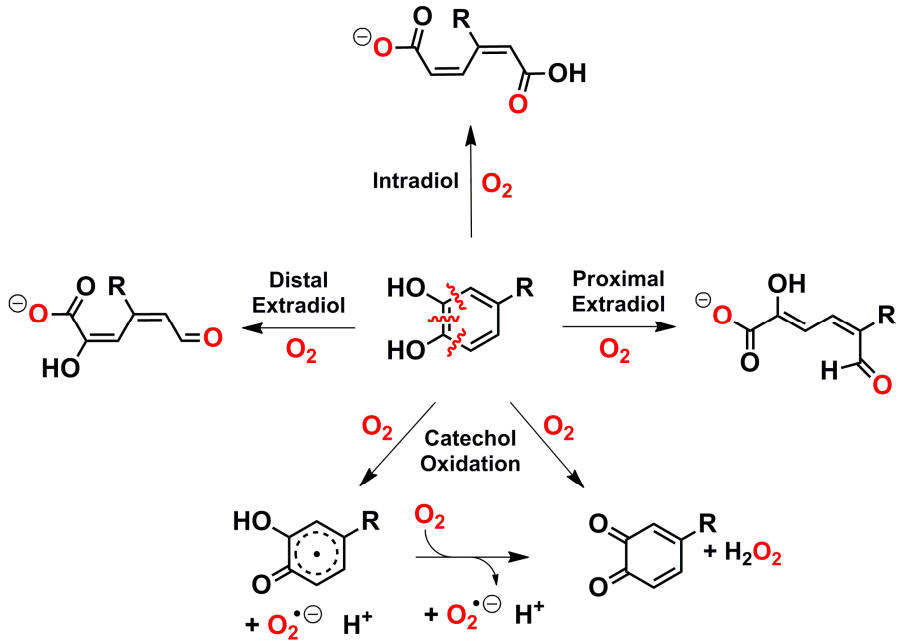

Scheme 4.3. Chemoselective and regioselective catechol oxidations.

Several of the proposed intermediates in Scheme 4.2 have been observed in crystallographic and solution studies with Mn-, Fe- and Co-HPCD using active site mutants and electron-poor substrate analogues.[130, 149, 161-165, 179] An X-ray crystal structure consistent with the [$SQ^{\bullet}$-Fe(II)-$O_2^{\bullet-}$] diradical pair (Scheme 4.2D) and the bridging

alkylperoxo intermediate (Scheme 4.2E) were reported with the electron-poor substrate analogue 4-nitrocatechol (4NC).[165] The structure of the [$SQ^{\bullet}$-Fe(II)-$O_2^{\bullet-}$] diradical pair (Figure 4.1) showed puckering of the semiquinone ring resulting in the apparent sp^3 hybridization of C2, suggesting localization of the semiquinone radical. The structure also showed a side-on bound O_2 adduct with hydrogen bonding interactions between the O_2 adduct and H200 positioning the superoxide for attack on the localized semiquinone radical at C2. In contrast crystal structures of semiquinone model complexes have planar semiquinone rings with the radical delocalized in a molecular orbital over the ring and dioxolene atoms.[250-259]

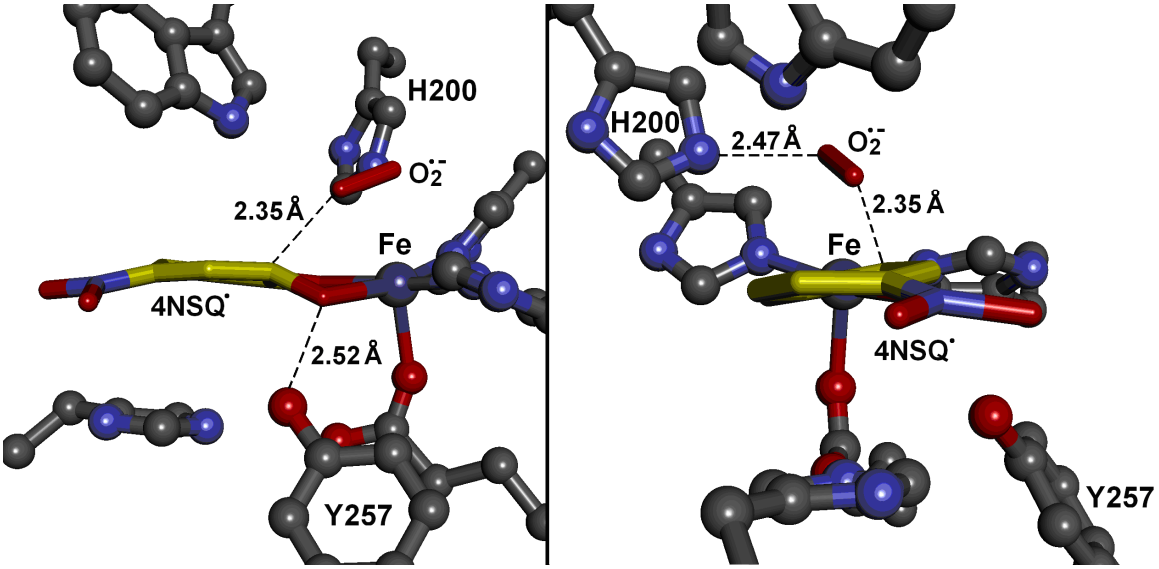

Figure 4.1. Structure of [Fe-HPCD(4NSQ$^{\bullet}$)$O_2^{\bullet-}$] (1.95 Å, PDB 2IGA) exhibiting puckering of C2 of the substrate ring suggesting a localized semiquinone substrate radical. Alternative view of [Fe-HPCD(4NSQ$^{\bullet}$)$O_2^{\bullet-}$] intermediate showing positioning of superoxide adduct above C2 of semiquinone ring.

Solution studies using active site mutants of H200 and Y257, both of which appear to have hydrogen bonding interaction with the O_2 adduct and the semiquinone intermediate respectively, in the crystal structure of the [Fe(II)($SQ^{\bullet}$)$O_2^{\bullet-}$] diradical pair

(Figure 4.1), were successful in trapping and characterizing several other early intermediates in reductive O_2 activation and substrate oxidation.[149, 163, 165] In transient kinetic experiments with [H200N-Fe-HPCD(HPCA)] rapidly mixed with O_2 a high-spin Fe(III) intermediate antiferromagnetically coupled to a radical was characterized by EPR and Mössbauer.[149] In UV-Vis stopped-flow experiments the observed intermediate exhibited absorption bands at 310, 395 and 610 nm similar to an independently synthesized HPCA-semiquinone.[149, 161] Based on the EPR and Mössbauer data the intermediate was assigned as a [Fe(III)($SQ^{\bullet}$)-(hydro)peroxo] species which then reacted to form the extradiol ring-cleaved product via a high-spin Fe(II) intermediate also observed by Mössbauer that was assigned to the bridging alkylperoxide species.[149] A similar [Fe(III)($SQ^{\bullet}$)-peroxo] intermediate was observed to form from the initial Fe(III)-$O_2^{\bullet-}$ intermediate in the catalytic turnover of 4NC by H200N-Fe-HPCD. In this reaction the semiquinone and peroxide do not form a reactive pair, instead the *o*-4-nitrosemiquinone ($4NSQ^{\bullet}$) is oxidized by the Fe(III) center to release *o*-4-nitroquinone (4NQ) and H_2O_2 as the final products. The Mn- and Co-substituted H200N mutants are inactive towards 4NC ring cleavage, the [H200N-Co-HPCD(4NC)] complex was found to reversibly bind O_2 to form a low-spin Co(III)-$O_2^{\bullet-}$ species.[130] These studies suggested that the active site acid base catalyst H200 plays an important role in aligning the superoxide adduct to optimize attack on the semiquinone radical to form the alkylperoxo intermediate. The shorter side chain of asparagine in the H200N mutants apparently misaligns the superoxide adduct for attack on the substrate leading to isolation of M(III)-$O_2^{\bullet-}$ species for H200N-Fe/Co-HPCD complexes with the electron-

poor 4NC substrate and formation of a [H200N-Fe(III)($SQ^{\bullet}$)-(hydro)peroxo] species with the more easily oxidized native substrate HPCA.

Transient kinetic studies of the Y257F mutant gave indirect evidence for the formation of a localized semiquinone radical in solution. In single turnover transient kinetic experiments, reacting [Y257F-Fe-HPCD(HPCA)] with O_2 produced two Fe(II) intermediates that were characterized by UV-Vis and Mössbauer spectroscopes.[161] The first species had no unique chromophore in the visible region and its formation showed a linear O_2 concentration dependence (at pH 7.5) with a non-zero y-intercept suggesting reversible O_2 binding, leading to its assignment as the initially coordinated O_2 adduct [Y257-Fe(II)-HPCD(HPCA)O_2]. The second species exhibited an intense chromophore (ε_{425nm} = 10,500 M^{-1} cm^{-1}) which resembles the independently synthesized quinone, leading to its assignment as a [Y257-Fe(II)-HPCD(quinone)(hydro)peroxo] intermediate.[149, 161, 260] In crystallographic studies Y257 is observed to hydrogen bond with the catechol at O(2C)-HPCA, (HPCA = 4-carboxymethylcatechol), thereby inducing puckering of the catechol ring, which effectively localizes the semiquinone radical to C2 of the ring upon catechol oxidation to direct the attack by the superoxide on C2.[163] The Y257F mutant is no longer able to hydrogen bond with the catechol ring to stabilize the localized semiquinone species, instead the substrate is oxidized by two electrons to form the observed planar quinone species [Y257-Fe(II)-HPCD(quinone)-(hydro)peroxo].[161, 163] Both the observed [H200N-Fe(III)($SQ^{\bullet}$-HPCA)(hydro)peroxo] and [Y257-Fe(II)-HPCD(Q-HPCA)-(hydro)peroxo] intermediates are catalytically competent going on to form the extradiol ring-cleaved product, although at much slower rates than the native

enzyme. This suggests that the reactive pair in the native system may be the [$SQ^{\bullet}$-Fe(II)-$O_2^{\bullet-}$] diradical pair, with the semiquinone radical localized to C2.[149, 161]

4.2 Results

4.2.1 Steady-state kinetics.

4.2.1.A Inactivation of Fe-HPCD during turnover of 4ClC. Fe-HPCD under steady-state conditions is observed to be quickly inactivated during turnover of 4ClC (Figure 4.2). While the initial rate of turnover of 4ClC by Fe-HPCD is very fast, it rapidly losses activity to yield only ~9 turnovers after a minute, suggesting that ~10% of the enzyme goes inactive for every turnover. Indeed iron-containing extradiol catechol dioxygenases including Fe-HPCD are known to inactivate slowly under air due to oxidation of the Fe(II) center.[131] Fe-HPCD was observed to also slowly lose activity during catalytic turnover of its native substrate HPCA.[169] Halogenated catechols have been described as potent inactivators of extradiol-cleaving catechol dioxygenases due to decoupling of O_2 reduction from catechol ring-cleavage resulting in formation of an inactive Fe(III)-catecholate complex with release of superoxide.[261] Indeed, addition of 5 mM 4ClC (40 equivalents) to 125 μM Fe-HPCD resulted in the formation of a stable intense chromophore at 680 nm within one minute, characteristic of an Fe(III)-catecholate ligand-to-metal charge transfer band (ε_{660nm} = 2,000 $M^{-1}cm^{-1}$, Figure 4.3). The cobalt- and manganese-substituted enzymes on the other hand do not show any loss of activity during catalytic turnover of HPCA or 4ClC (Figure 4.2).[169] This suggest that cobalt- and manganese-substitution of extradiol-cleaving catechol dioxygenases may be useful in the

biodegradation of halogenated aromatic pollutants like polychlorobiphenyls (PCBs), as this ring-cleaving step has been found to be a bottleneck in their degradation.[261-263]

This chapter will mainly focus on the experiments with Co-HPCD and the 4XC substrates. Chapter 5 will then describe further kinetic and spectroscopic experiments with Mn-HPCD and the 4XCs. Transient kinetic experiments with Fe-HPCD and the 4XCs have also been performed by Michael Mbughuni former member of the Lipscomb lab and will be reported elsewhere.

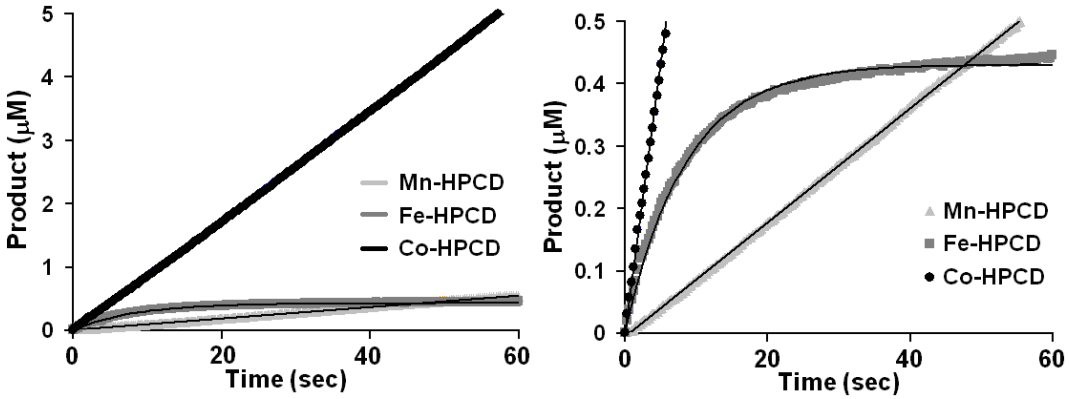

Figure 4.2. Representative progress curves for 4ClC turnover by metal-substituted HPCDs carried out in air-saturated buffer at pH 7.5 and 22 °C. Mn-HPCD, Fe-HPCD, and Co-HPCD. Reaction monitored by following formation of yellow extradiol ring-cleaved product at 380 nm (ε_{380nm} = 44,300 M^{-1} cm^{-1}). Reactions contained 50 nM M-HPCD and 3 mM 4ClC in 50 mM MOPS (pH 7.5). The Fe-HPCD trace was fit with a single exponential equation with a $1/\tau$ of 0.11 sec^{-1}. The total yield of 4ClC ring-cleaved product after 60 sec is ~430 nM suggesting the 50 nM Fe-HPCD only turns over ~9 times before it is inactive or that ~10% of the Fe-HPCD goes inactive each turnover.

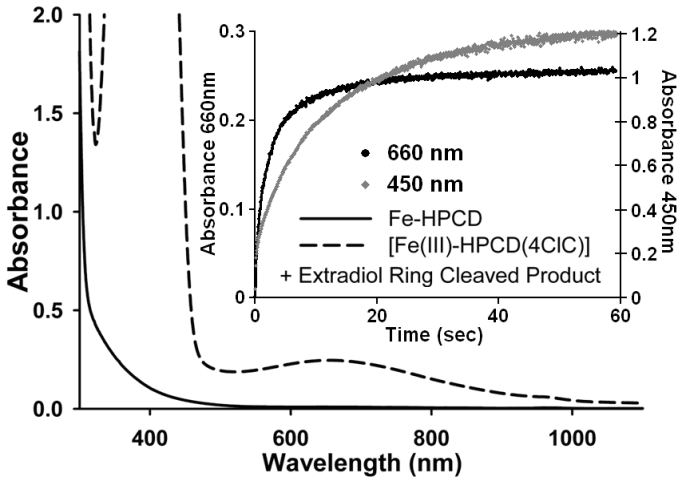

Figure 4.3. UV-Vis spectra of 125 μM Fe-HPCD before and after steady-state turnover reaction with 5 mM 4ClC. Reaction conditions: 100 mM MOPS (pH 7.5) 4 °C ~1 mM O_2. The extradiol ring-cleaved product absorbs at 385 nm and inactivated [Fe(III)-HPCD(4ClC)] absorbs at 660 nm. The inset shows formation of extradiol ring-cleaved product monitored at 450 nm and Fe(III)-catecholate at 660 nm fit. (Note: At these high enzyme concentrations O_2 is the limiting reagent.)

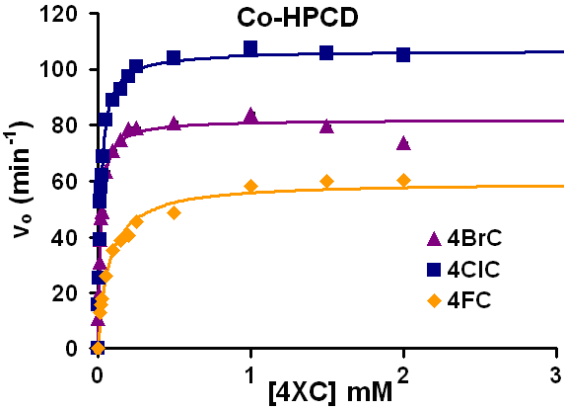

Figure 4.4. Michaelis-Menten plots varying 4XC concentration for the reaction of Co-HPCD with 4XC. Reaction conditions: air-saturated buffer (285 μM O_2), 22 °C, 50 mM MOPS buffer (pH 7.5). Rates were measured from initial velocities at different catechol concentrations by following the formation of the yellow extradiol ring-cleaved product by UV-Vis spectroscopy. Lines represent fits of data to the Michaelis-Menten equation.

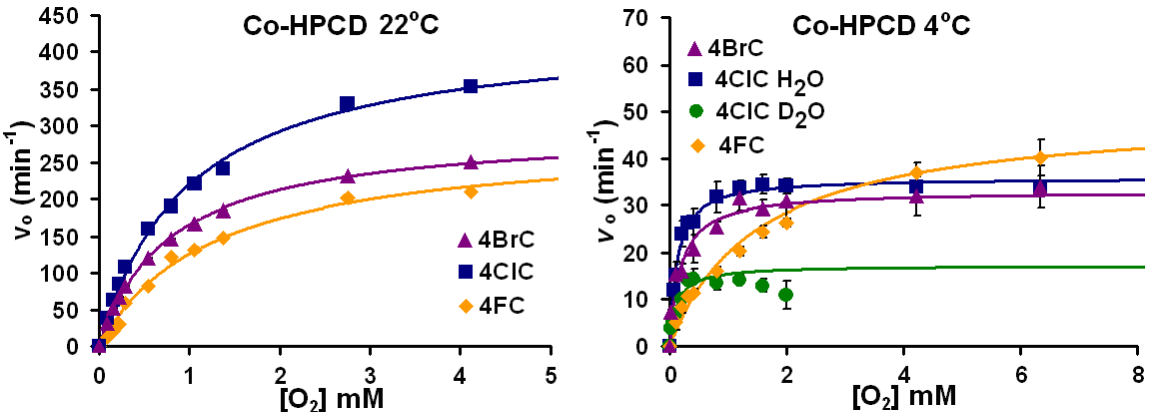

Figure 4.5. Michaelis-Menten plots varying O_2 concentration for the reaction of Co-HPCD with 3 mM 4XC. Reaction conditions 4 (right panel) and 22 °C (left panel), 50 mM MOPS buffer (pH/pD) 7.5). Rates were measured from initial velocities at different O_2 concentrations ranging from 0.086–4.12 mM (3 atm) by following the formation of the yellow extradiol ring-cleaved product by UV-Vis spectroscopy. Rates of the reaction were confirmed by monitoring the consumption of O_2 using a Clark-type oxygen electrode in air-saturated buffer. Lines represent fits of data to the Michaelis-Menten equation.

Table 4.1. Steady-state kinetic values measured for Co-HPCD in 50 mM MOPS buffer (pH 7.5) at 22 °C and 4 °C.

Temperature		Temperature	
Constant	**Substrate**	**22 °C**	**4 °C**
$K_M^{catechol}$ (mM O_2) †	4BrC	0.016 ± 0.001	
	4ClC H_2O	0.017 ± 0.001	
	4FC	0.070 ± 0.007	
	HPCA*	0.005 ± 0.001	
K_M^{O2} (mM O_2)	4BrC	0.79 ± 0.02	0.18 ± 0.04
	4ClC H_2O	0.98 ± 0.06	0.12 ± 0.01
	4ClC D_2O		0.12 ± 0.03
	4FC	1.25 ± 0.15	1.5 ± 0.2
	HPCA*	1.20 ± 0.10	
k_{cat} (min^{-1})	4BrC	297 ± 4	33 ± 1
	4ClC H_2O	436 ± 11	35.9 ± 0.6
	4ClC D_2O		17 ± 1
	KIE		2.1 ± 0.1
	4FC	284 ± 15	50 ± 3
	HPCA*	1120 ± 70	
k_{cat}/K_M^{O2} (mM^{-1} min^{-1})	4BrC	370 ± 10	180 ± 40
	4ClC H2O	440 ± 30	300 ± 30
	4ClC D_2O		140 ± 40
	4FC	230 ± 30	33 ± 5
	HPCA*	900 ± 100	
$k_{cat}/K_M^{catechol}$ (μM^{-1} min^{-1})	4BrC	18.6 ± 12	
	4ClC H_2O	25.9 ± 2.3	
	4FC	4.06 ± 4.6	
	HPCA*	224 ± 47	

* measured at pH 7.8.[8] † measured in air-saturated buffer (285 μM O_2). Reported error values for k_{cat} and K_M are from nonlinear regression fitting of data to the Michaelis-Menten equation. Error values for k_{cat}/K_M where calculated using error propagation.

4.2.1.B Steady-state kinetic parameters. The apparent Michaelis-Menten kinetic parameters for reactions of Co-HPCD with 4XCs both varying the catechol substrate (Figure 4.4) and O_2 concentrations (Figure 4.5) are reported in Table 4.1 for temperatures of at 4 °C and 22 °C. Co-HPCD has apparent affinities for the halogenated substrates (4XCs) that are an order of magnitude lower (higher $K_M^{catechol}$) than for the native

substrate HPCA. Turnover of the 4XCs (k_{cat}) by Co-HPCD is also an order of magnitude slower than the native substrate HPCA, with 4FC being the slowest at 4 °C. The higher $K_M^{catechol}$ values and lower k_{cat} values result in catalytic efficiencies ($k_{cat}/K_M^{catechol}$, or second order rate constants for substrate binding) that are an order of magnitude lower than for HPCA. However, the apparent affinities for O_2 (K_M^{O2}) and the catalytic efficiencies for O_2 (k_{cat}/K_M^{O2}) with the 4XC substrates are similar to that observed for the native substrate HPCA at 22 °C.

4.2.1.C Linear free-energy steady-state studies. A thorough linear free-energy type steady-state kinetic study was reported previously by Tetsuo Ishida and co-workers on the iron-dependent extradiol catechol dioxygenases Mpc from *Pseudomonas putida*.[262] They observed no strong trend in the k_{cat} values plotted against measured pK_{a1} values for the substituted catechols (4CH_3C, 4ClC, 4BrC, 4CHOC, and 3CHOC) at 25 °C, which suggested that the both steric and/or other factors affected the rate determining step to obscure the electronic effects of the substituents for turnover of these substrates by Mpc. This behavior is in contrast to the results observed with Co-HPCD, where there is a large difference in the observed k_{cat} values for the native substrate HPCA (1,120 ± 70 min^{-1}) compared to the 4-halogenated catechols (284–436 min^{-1}) and the very electron-poor substrate 4NC (0.72 ± 0.06 min^{-1}).[130, 169] We note that there is not a clear trend in the k_{cat} values observed for turnover of the various halogenated substrates by Co-HPCD. Ishida *et al.* did observe a trend in the catalytic efficiency ($k_{cat}/K_M^{catechol}$) values, or second order rate constants for catechol binding similar to the trend observed here where the more electron-withdrawing substituents reduced the rate of catechol binding, suggesting that less basic substrates bind more weakly to the metal center. They also observed trends in

the K_M^{O2} and k_{cat}/K_M^{O2} values similar to ours, in which the more electron-poor catechol substrates exhibit lower apparent and decreased catalytic efficiencies for O_2. This suggests that the electron withdrawing groups lower the highest occupied molecular orbital (HOMO) of the catechol substrate, thereby slowing electron transfer from catechol to O_2 via the metal center upon reductive O_2 binding, as has been suggested in transient kinetic studies of [Fe- and Co-HPCD(4NC)] reacting with O_2.[130, 162, 165-167]

4.2.1.D Temperature dependence of steady-state parameters. Interesting changes in the steady-state kinetic parameters for Co-HPCD and the 4XCs are observed upon decreasing the temperature from 22 to 4 °C. Under saturating substrate conditions Co-HPCD turns over 4ClC faster than 4FC at 22 °C (Figure 3), while at 4 °C Co-HPCD turns over 4FC faster than 4ClC. The apparent affinity of [Co-HPCD(4ClC)] for O_2 also increases (lower K_M^{O2}) by almost an order of magnitude, from 0.98 ± 0.06 mM at 22 °C to 0.12 ± 0.01 mM at 4 °C. On the other hand, the apparent affinity of [Co-HPCD(4FC)] for O_2 decreases only slightly (higher K_M^{O2}) with temperature from 1.25 ± 0.15 mM at 22 °C to 1.5 ± 0.2 at 4 °C.

4.2.1.E pH activity profiles. The pH activity profiles for the turnover of HPCA, 4ClC and 4NC (Figure 4.6) are distinctly different: the electron-rich HPCA is turned over fastest under basic conditions (pH 9), the less basic 4ClC is turned over fastest under neutral conditions (pH 7.8), and the electron-poor 4NC is turned over fastest under acidic conditions (pH < 5.5). The pH activity profile observed for Fe- and Co-HPCD is similar to the pH activity profile reported by Tetsuo Ishida and co-workers for turnover of 4ClC by Mpc.[262] Interestingly Mn-HPCD shows a slightly different pH activity profile than Fe- or Co-HPCD, with a maximum rate of 4ClC turnover observed at pH 6.5. Fe-HPCD

quickly becomes inactive while turning over 4ClC making it hard to accurately measure the initial rate. Fitting the pH activity profiles of Co-HPCD to Equation 4.1 gives pK_a values of 7.74 ± 0.06 for HPCA, 6.39 ± 0.09 and 9.17 ± 0.09 for 4ClC, and 6.59 ± 0.09 for 4NC.[130, 223]

The pH activity profile of 4ClC reflects the ionization state of the ternary (ESO_2) complex for optimum catalytic turnover.[262] pH titration experiments with [wt- and H200N-Co-HPCD(4NC)] enzyme-substrate complexes suggest that His200 has a pK_a of 5.72 ± 0.05. Co-HPCD binds 4NC as the dianionic catecholate; under acidic conditions H200 is protonated so that it can stabilize the incipient superoxide anion and increase the rate of 4NC turnover.[130] The bell-shaped pH activity profile of 4ClC indicates that for optimum turnover of 4ClC some ionizable group important for catalysis must be protonated and another ionizable group must be deprotonated at pH 7.8. At pH 7.8, H200 is deprotonated while 4ClC is expected to be bound monoanionically, remaining protonated at HO(C1). His200 can then act as base to deprotonate O(C1) to induce ketonization of the C1-O bond as well as stabilizing the O_2 adduct. At low pHs His200 and 4ClC would both be protonated, and His200 would not be able to assist in catechol oxidation by removing the proton from HO(C1). Under more basic conditions neither 4ClC nor His200 would be protonated and the stabilization of the O_2 adduct by the protonated histidine would be lost. The pK_a for optimum turnover of electron rich HPCA is higher as it is less acidic than either 4ClC or 4NC.

Equation 4.1
$$k_{obs} = \left[\left(\frac{k \cdot 10^{pK_{a1} - pH}}{1+10^{pK_{a1} - pH}}\right) + b_1\right] - \left[\left(\frac{k \cdot 10^{pK_{a2} - pH}}{1+10^{pK_{a2} - pH}}\right) + b_2\right]$$

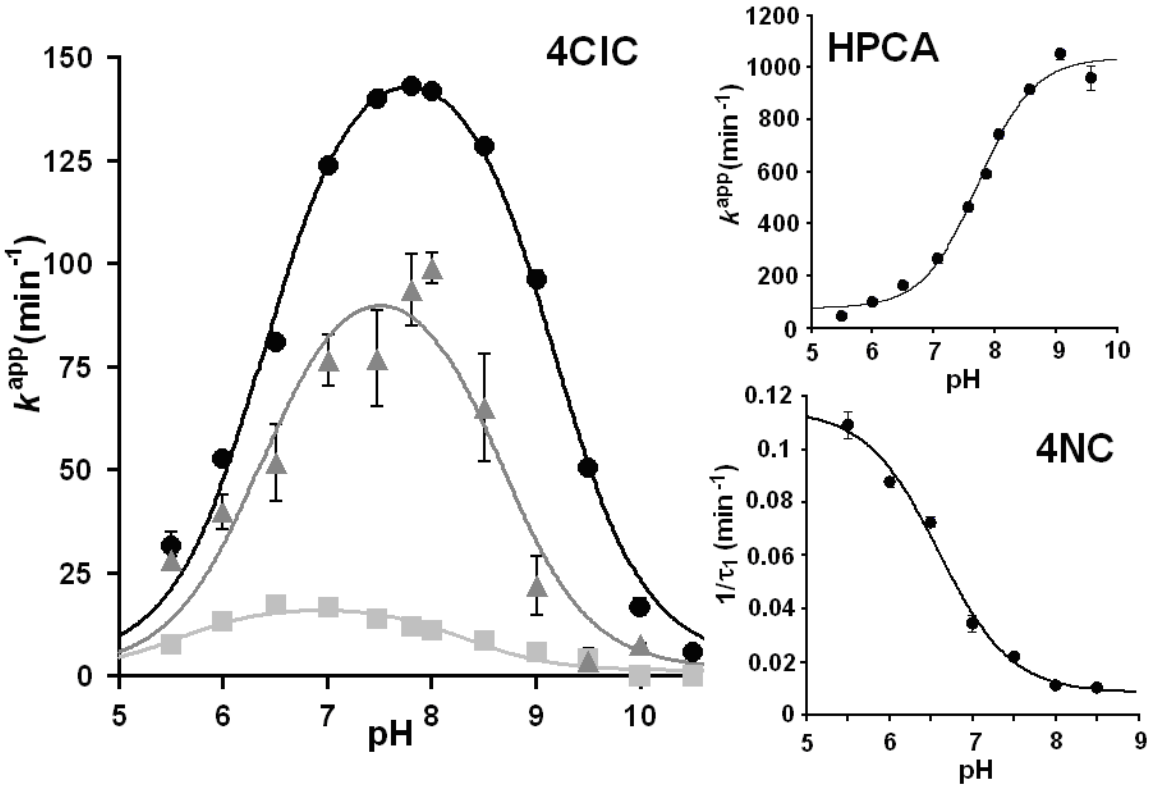

Figure 4.6. pH activity profile for turnover of (left) 4-chlorocatechol (4ClC), by Mn-HPCD (■), Fe-HPCD (▲) and Co-HPCD (●), (top, right) turnover of HPCA by Co-HPCD, and (bottom, right) single turnover of 4NC by Co-HPCD.[130] The 4ClC reaction was monitored at the pH independent isosbestic point of the ring-cleaved product (ε_{356nm} = 16,000 M^{-1} cm^{-1}) in air-saturated buffer at 22 °C (290 μM O_2). Reaction conditions: 300 nM [M] M-HPCD, 2 mM [4ClC] buffer mixture of MES, BisTris, MOPS, Tris, CHES, and CAPS, 25 mM each. The final conductivity of each buffer was then adjusted to 6.4 mS using 2 M NaCl. The background base-catalyzed auto-oxidation reaction of the catechol substrates to form a yellow product was subtracted for pH > 8. Fe-HPCD quickly becomes inactivated when turning over 4ClC. The lines represents fit of data to equation 4.1 with apparent pK_as for reactions with 4ClC of 6.39 ± 0.09 and 9.17 ± 0.09 for Co-HPCD, 6.4 ± 0.3 and 8.6 ± 0.3 for Fe-HPCD, and 5.6 ± 0.2 and 8.3 ± 0.2 for Mn-HPCD, and an apparent pK_a for Co-HPCD of 7.74 ± 0.06 with HPCA and 6.59 ± 0.09 with 4NC.[130]

4.2.2 Transient kinetic experiments.

4.2.2.A Stopped-flow experiments. Stopped-flow experiments were performed by rapidly mixing the anaerobic [Co-HPCD(4XC)] enzyme-substrate complex (pH 7.5 at 4 °C) with O_2 saturated buffer. [Co-HPCD(4ClC)] complexes react with O_2 to form an intermediate with an intense chromophore at 456 nm ($\varepsilon \sim 9{,}000\ M^{-1}\ cm^{-1}$, Figure 4.7). The intermediate decays to the yellow extradiol ring-cleaved product ($\varepsilon_{380} = 44{,}300\ M^{-1}\ cm^{-1}$), with an apparent isosbestic point at 433 nm. The single turnover reaction of [Co-HPCD(4ClC)] with O_2 (Figure 4.7) was monitored at 475 and 380 nm to follow the formation and decay of the intermediate species and the formation of the extradiol ring-cleaved product respectively. In the single wavelength traces a lag phase (~10 ms) was observed prior to the formation of the 456 nm intermediate. The single wavelength traces were fit with summed triple exponential equations (Figure 4.8), affording the same reciprocal relaxation times at both 475 and 380 nm. The faster phase shows linear O_2 concentration dependence (Figure 4.9) with a non-zero y-intercept, suggesting that this phase is associated with reversible O_2 binding. The second reciprocal relaxation time shows hyperbolic O_2 concentration dependence, suggesting that it follows the fast phase and is reversibly connected to O_2 binding. It was not possible from this data to tell whether the second step is also reversible (nonzero y-intercept) due to the quality of the data and due to the limited experimental O_2 concentration range of 0.2 and 1.0 mM O_2. The third phase shows no O_2 concentration dependence over the experimental O_2 concentrations and has a rate that corresponds to the observed steady-state rate under the same reaction conditions (4 °C and pH 7.5). The stopped-flow kinetics experiments suggest that two intermediates accumulate in the reaction of [Co-HPCD(4ClC)] with O_2

(Scheme 4.4). The first intermediate (Co^{4ClC}Int1) appears to be colorless, while the second intermediate (Co^{4ClC}Int2) has an intense yellow chromophore at 456 nm.

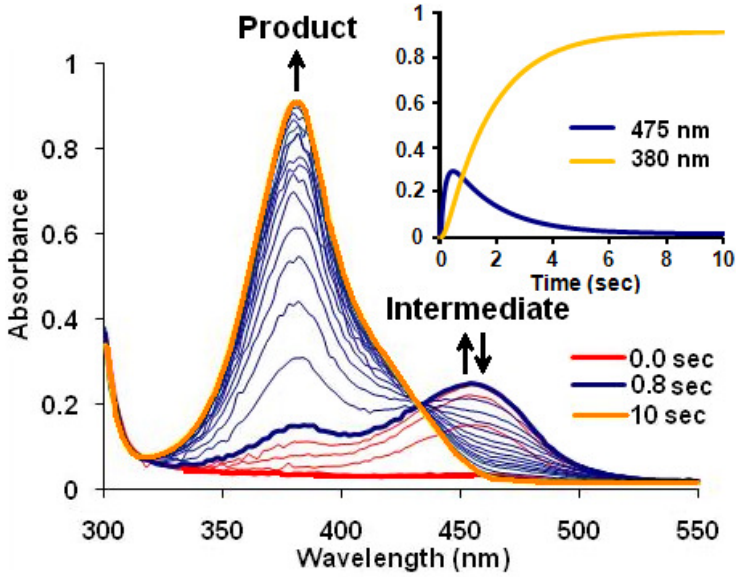

Figure 4.7. Photodiode array stopped-flow kinetic data for anaerobic [Co-HPCD(4ClC)] rapidly mixed with O_2-saturated buffer (1atm O_2). Final concentrations of reagents after mixing: 30 μM 4ClC, 65 μM Co-HPCD and 1 mM O_2. Reaction conditions: 100 mM MOPS (pH 7.5), 4 °C.

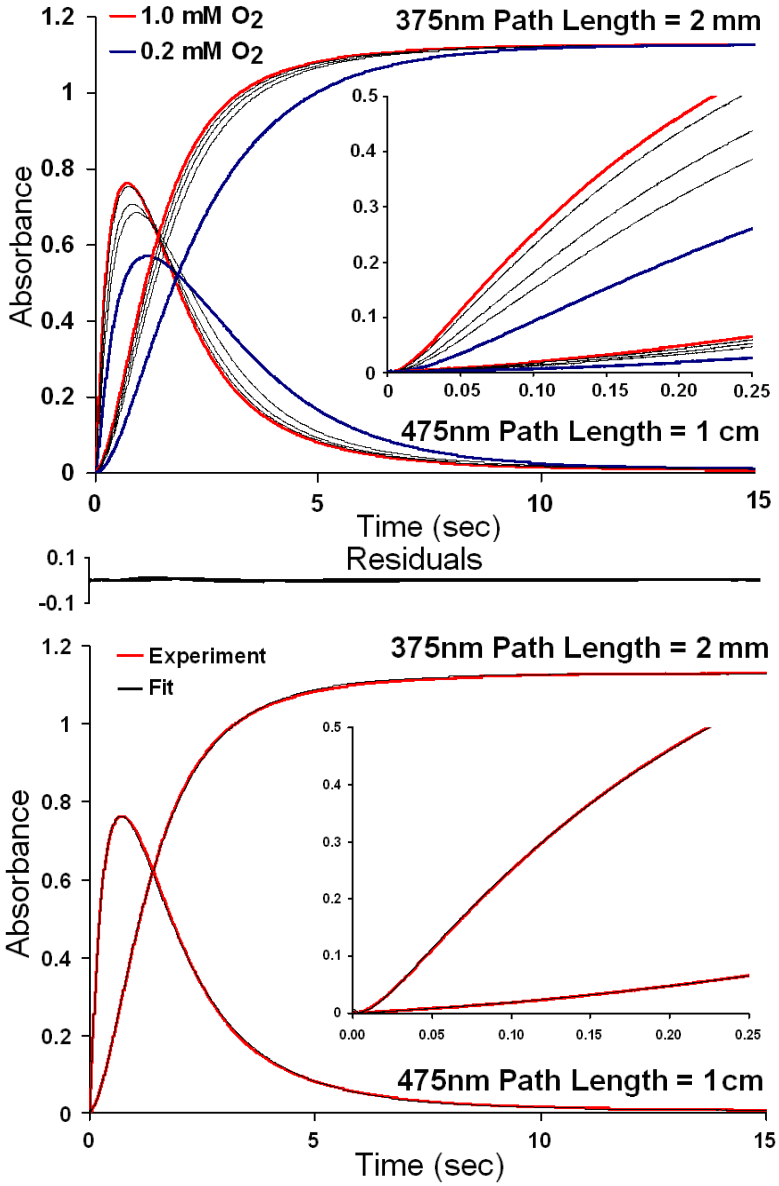

Figure 4.8. Stopped-flow kinetic data for [Co-HPCD(4ClC)] rapidly mixed with oxygenated buffer. (Top) Single wavelength traces monitoring formation and decay of intermediate at 475 nm (1 cm path length) and formation of extradiol ring-cleaved product at 380 nm (2 mm path length). Inset showing lag phase in formation of both intermediate and product. Final concentrations of reagents after mixing: 130 μM 4XC, 220 μM Co-HPCD and 200–1,000 μM O_2. Reaction conditions: 100 mM MOPS (pH 7.5), 4 °C. (Bottom) Representative fit of experimental data to summed triple exponential equations.

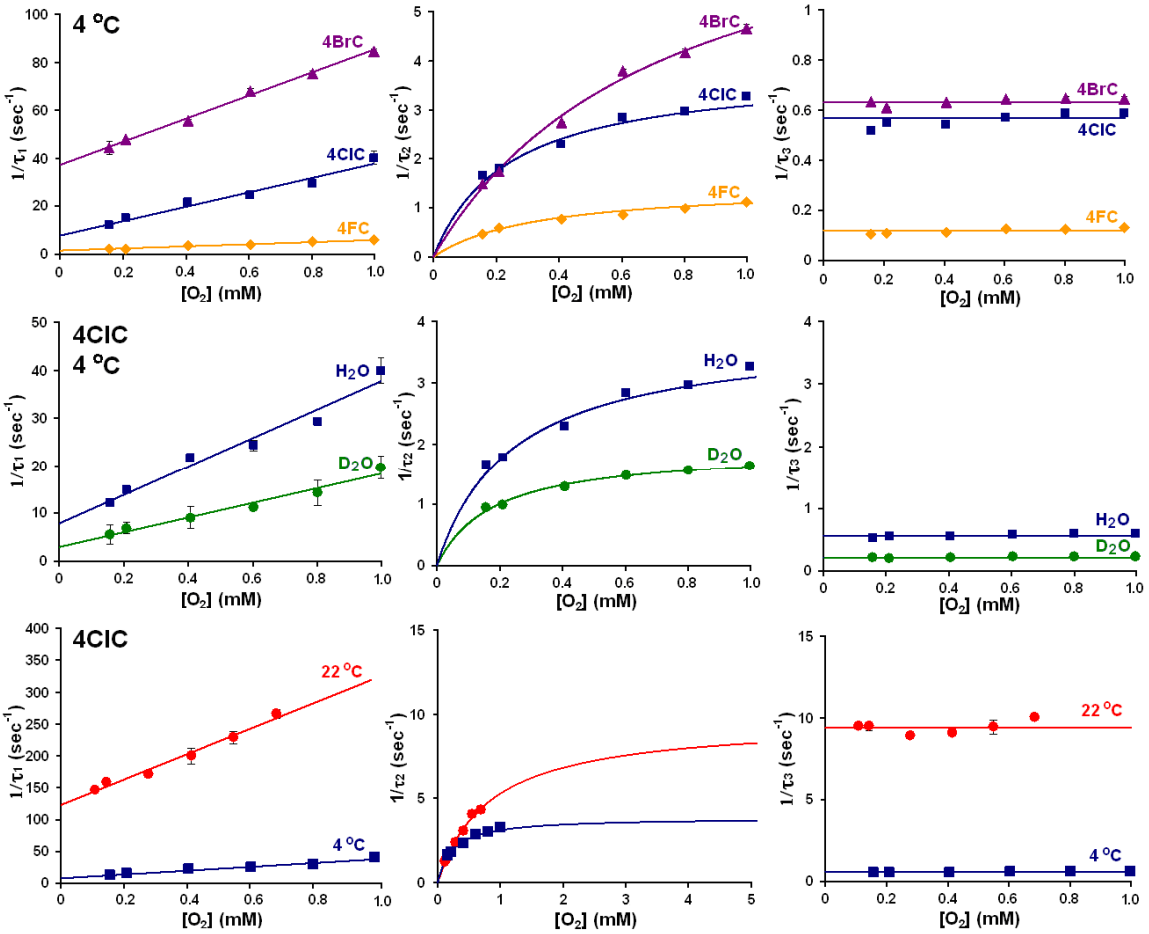

Figure 4.9. Reciprocal relaxation times for the observed phases in the reaction of [Co-HPCD(4XC)] with O_2 plotted as a function of O_2 concentration for reactions at 4 °C (top row), for the reaction of [Co-HPCD(4ClC)] in H_2O and D_2O (middle row), and for the reaction of [Co-HPCD(4ClC)] at 4 °C and 22 °C (bottom row). All reactions were monitored by following the chromophore of Co^{4XC}Int2 at 475 nm and fitting single wavelength time courses to summed triple exponential equations. Conditions: 100 mM MOPS (pH/pD 7.5), and 4 or 22 °C. Lines represent fit of data to linear or hyperbolic functions.

Table 4.2. Rate constants for the single turnover and stead state reactions of [Co-HPCD(4XC)] with O_2.

Reaction Conditions	Sub	k_1 (mM^{-1} sec^{-1})	k_{-1} (sec^{-1})	k_2 (sec^{-1})	k_3 (sec^{-1})	K_D^{O2} (mM)	k_{cat} (sec^{-1})
pH 6.0 22 °C	4NC	0.00067 ± 0.00008	0.00083 ± 0.00017	0.012 ± 0.001	---	1.24 ± 0.06	---
pH 7.5 4 °C	**4F**	**4.4 ± 0.2**	**1.5 ± 0.2**	**1.4 ± 0.1**	**0.12 ± 0.01**	**0.34 ± 0.05**	**0.83 ± 0.05**
pH 7.5 4 °C	**4Cl**	**30 ± 3**	**8 ± 2**	**4.0 ± 0.2**	**0.58 ± 0.03**	**0.27 ± 0.07**	**0.60 ± 0.01**
pD 7.5 4 °C	4Cl	15 ± 1	2.9 ± 0.9	1.9 ± 0.1	0.21 ± 0.01	0.19 ± 0.06	0.29 ± 0.02
k_H/k_D	4Cl	2.0 ± 0.2	2.8 ± 1.0	2.1 ± 0.2	2.8 ± 0.2	---	2.1 ± 0.1
pH 7.5 22 °C	4Cl	200 ± 13	123 ± 6	9 ± 1	9.4 ± 0.4	0.62 ± 0.05	7.3 ± 0.2
pH 7.5 4 °C	**4BrC**	**48 ± 2**	**37 ± 1**	**8.2 ± 0.8**	**0.64 ± 0.01**	**0.77 ± .04**	**0.55 ± 0.02**

$$\text{[Co-HPCD(4XC)]} + O_2 \underset{k_{-1}}{\overset{k_1}{\rightleftharpoons}} \text{Co}^{4XC}\text{Int1} \xrightarrow{k_2} \text{Co4XCInt2} \xrightarrow{k_3} \text{Co-HPCD} + \text{extradiol ring-cleaved product}$$

Scheme 4.4. Kinetic scheme for reaction of [Co-HPCD(4XC)] enzyme-substrate complexes with O_2.

4.2.2.B O_2 concentration dependence. Figure 4.9 shows the O_2 concentration dependence plots of the three observed reciprocal relaxation times for the reaction of [Co-HPCD(4XC)] with O_2. A clear trend is observed in the k_1 (slope) and k_{-1} (intercept) values for the linear $1/\tau_1$ vs O_2 plot where both the rate constants of the forward and reverse reactions increase down the series from 4FC to 4BrC (Table 4.2). The calculated K_D^{O2} values show that the series of halogenated catechol [Co-HPCD(4XC)] complexes exhibit similar low affinities for O_2 (0.27–0.77 mM) but higher affinities for O_2 and much higher second order rate constants for O_2 binding than is observed with the more electron-poor substrate 4NC (O_2 binding (k_1) to [Co-HPCD(4NC)] is rate limiting ($k_1 \bullet [O_2] < k_2$) for O_2 concentrations below ~18 mM).[130] For the reaction of the halogenated catechol [Co-HPCD(4XC)] complexes with O_2, k_2 and k_3 both show the same trend as k_1 and k_{-1} with increasing rates down the series from 4FC to 4BrC (Table 4.2). The magnitude of k_3 observed in transient kinetics is similar to that of the k_{cat} value measured under steady-state conditions at pH 7.5 and 4°C, suggesting that the decay of intermediate 2 leading to formation of the product is rate determining for turnover of the 4XCs by Co-HPCD.

4.2.2.C Solvent kinetic isotope effect. A kinetic solvent isotope effect (k_{H2O}/k_{D2O}) of 2.1 ± 0.1 was observed for the steady-state turnover of 4ClC by Co-HPCD under saturating O_2 concentrations (Figure 4.5) at 4 °C. The single turnover reaction of [Co-HPCD(4ClC)] with O_2 was also performed in D_2O (pD = 7.5) at 4 °C. Significant kinetic isotope effects ranging from 2.0 to 2.8 were observed for all four rate constants (Figure 4.9 and Table 4.2).

4.2.2.D Temperature dependence of rates. In the steady-state turnover of 4ClC by Co-HPCD a large increase in the value of K_M^{O2} was observed upon raising the temperature by 18 °C from 4 °C (0.12 ± 0.01 mM O_2) to 22 °C (0.98 ± 0.06 mM O_2, Figure 4.5). This 18 °C change in temperature was also accompanied by a 12-fold increase in the magnitude of k_{cat} under saturating O_2 conditions (Table 4.1). To better understand the observed changes in the steady-state parameters with temperature, the single turnover reaction of [Co-HPCD(4ClC)] with O_2 was also preformed at 22 °C (Figure 4.9, and Table 4.2). A 6.7-fold increase in the rate of O_2 binding (k_1) was observed upon increasing the temperature, and the reverse rate (k_{-1}) increased by 15-fold resulting in a significant decrease in the affinity for O_2 (or higher K_D^{O2}) from 0.19 ± 0.06 mM at 4 °C to 0.62 ± 0.05 mM O_2 at 22 °C. At 22 °C under the experimental O_2 concentrations (0.11–0.69 mM O_2) $1/\tau_2$ is slower than the rate of $1/\tau_3$, due to the reversible O_2 binding step, though under saturating O_2 concentrations $1/\tau_2$ and $1/\tau_3$ are predicted to be roughly equal. Using the Arrhenius equation (Equation 4.2) and the observed rates at 4 °C and 22 °C the activation energies of the forward and reverse reactions can be calculated. These calculations estimate a 72 kJ/mol activation energy for O_2 binding (Figure 4.10) with a larger 103 kJ/mol barrier for O_2 dissociation, along with a smaller 31 kJ/mol barrier for the forward reaction leading to the formation of intermediate 2. Decay of intermediate 2 to product is accompanied by a large 105 kJ/mol activation energy. Interestingly, the activation energy for the forward barrier from intermediate 1 to intermediate 2 (31 kJ/mol) is the same as the difference between the barrier for O_2 activation and O_2 dissociation (103 – 72 = 31 kJ/mol). This means there is

no net change in energy from the enzyme-substrate complex to the second transition state.

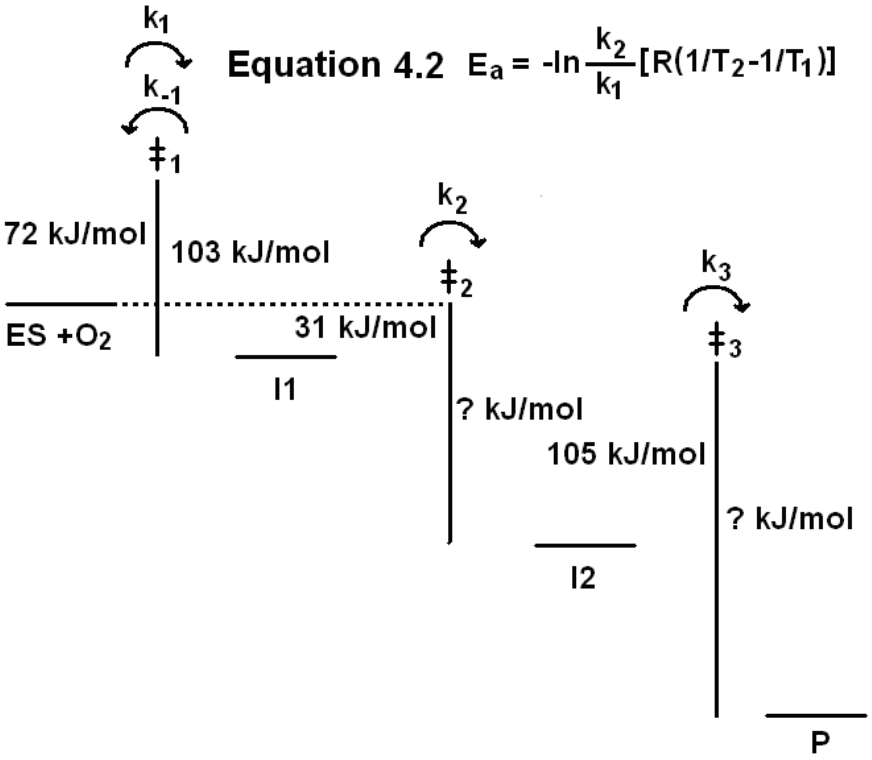

$$\text{Equation 4.2} \quad E_a = -\ln\frac{k_2}{k_1}[R(1/T_2 - 1/T_1)]$$

Figure 4.10. Calculated activation energies for transition states of the reaction of [Co-HPCD(4ClC)] with O_2 to form Co^{4ClC}Int1, Co^{4ClC}Int2 and the extradiol ring-cleaved product using Arrhenius equation (Equation 4.2).[264] Reverse activation energies for k_{-2} could not be determined from kinetic data while the conversion represented by k_{-3} is irreversible.

4.2.3 Spectroscopic characterization

4.2.3.A X-band EPR spectra of wt- and H200N-Co-HPCD enzyme-substrate complexes.

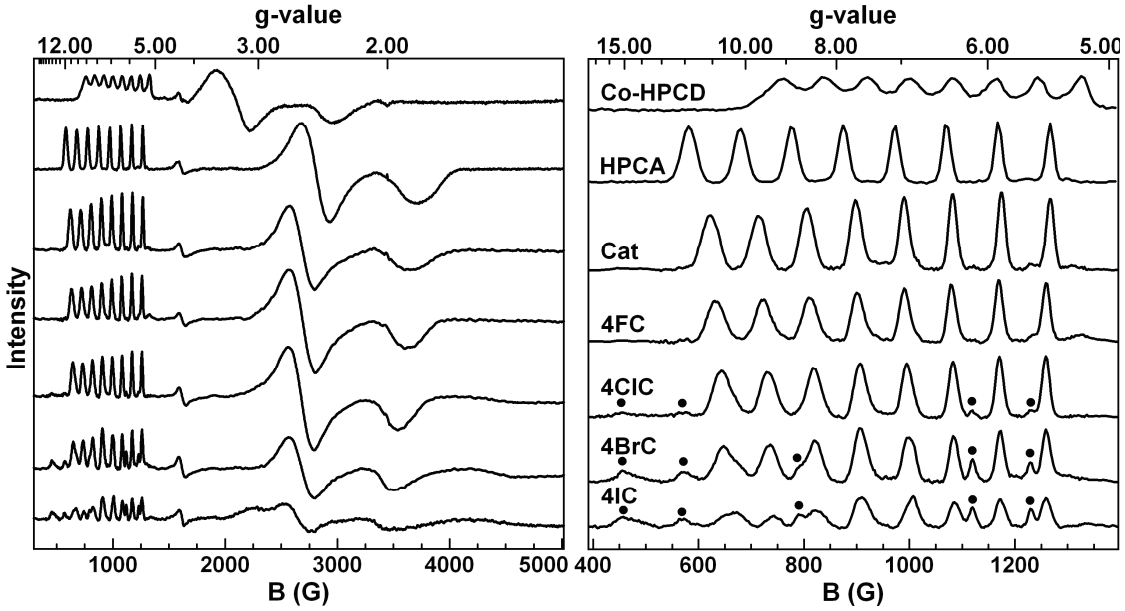

Figure 4.11. EPR spectra obtained at 9.64 GHz and 20 K of Co-HPCD and anaerobic enzyme-substrate complexes, in 100 mM MOPS (pH 7.5) for (top to bottom) Co-HPCD,[169] [Co-HPCD(HPCA)],[169] [Co-HPCD(catechol)], [Co-HPCD(4FC)], [Co-HPCD(4ClC)], [Co-HPCD(4BrC)], and [Co-HPCD(4IC)]. A decrease in the ^{59}Co hyperfine splitting is observed going from catechol to 4IC. A new S = 3/2 signal displaying ^{59}Co hyperfine (●) at g = 8.1 (112 G), ~2.9 and 1.4 appears for [Co-HPCD(4ClC)], [Co-HPCD(4BrC)], and [Co-HPCD(4IC)] enzyme-substrate complexes.

X-band EPR spectra of anaerobic [Co-HPCD(4XC)] enzyme-substrate complexes are shown in Figure 4.11. Co-HPCD exhibits an S = 3/2 rhombic EPR signal with g-values at 6.7, 3.4 and 2.4, typical of high-spin d^7 Co(II) centers.[130, 169, 199, 202, 203] The low-field signal (g = 6.7) exhibits well-resolved 8-fold hyperfine splitting with A = 80 G,

due to the nuclear spin of ^{59}Co (I = 7/2). Anaerobic addition of 4XC drastically perturbs the spectrum of Co-HPCD (Figure 4.11), leading to an increase in both the rhombicity of the EPR signal and the magnitude of the low-field signal's ^{59}Co hyperfine splitting (Table 4.3). While the enzyme-substrate complexes of Co-HPCD with the electron rich native substrate HPCA (g = 7.6, 2.5, and 1.9) and the electron-poor substrate 4NC (g = 5.6, 3.5, and 2.1) have very different g-values,[130, 169] the enzyme-substrate complexes in the series examined here all have similar g-values of ~7.2, 2.6 and ~2.0. However there is an apparent trend in the magnitude of the observed ^{59}Co hyperfine splitting, which decreases from 98 G with HPCA to 87 G with 4IC (Figure 4.11). This trend likely reflects the donor abilities of the substituted catechol ligand (Table 4.4) and the spin-polarization at the Co center.[130] Upon closer examination of the EPR spectrum of [Co-HPCD(4XC)] (X = Cl, Br, or I) (pH 7.5) a second set of ^{59}Co hyperfine-splitting (g = 8.1, ^{59Co}A = 112 G) is observed in the low-field signal, the intensities of which increase to represent ~30% of the population in [Co-HPCD(4IC)]. The population of this second S = 3/2 species with [Co-HPCD(4ClC)] is also affected by pH, decreasing at pH 6.0 and increasing at pH 8.0 (Figure 4.12). The increase in the population of the second species observed under basic conditions with [Co-HPCD(4ClC)] suggests that the species may be the dianionically bound catecholate. The population of the second S = 3/2 enzyme-substrate species also increases with the steric bulk of the substituent, suggesting a possible second substrate binding mode enforced by the bulky substituent. Mössbauer spectra of the enzyme-substrate complexes of [wt- and H200N-Fe-HPCD(HPCA)] also show two distinctly different high-spin Fe(II) species in roughly equal concentrations.[149]

Upon mixing with oxygenated buffer both observed enzyme-substrate complexes rapidly react with O_2 with rates that are indistinguishable in rapid freeze-quench Mössbauer experiments. This is in contrast to the EPR spectra of [wt- and H200N-Co-HPCD(HPCA)] enzyme-substrate complexes where only one high-spin Co(II) signal is observed for each complex.[130, 169] This difference between the Fe- and Co-HPCA complexes may be due to the different Lewis acidities of the two metal centers, which affects the binding mode of the catecholate.

Mössbauer spectra of [Fe-HPCD(4NC)] and [Y257F-Fe-HPCD(HPCA)] each exhibit only one high-spin Fe(II) species present in the enzyme-substrate complexes.[161, 162] 4NC is observed to bind to Fe-HPCD as the dianionic catecholate by optical spectroscopy and Y257 is observed to form a strong hydrogen bond with O(C2) in X-ray crystal structures.[163, 166] At pH 7.5 only one enzyme-substrate complex is observed in the EPR spectrum of [Co-HPCD(4NC)], while at pH 6.0 a second set of ^{59}Co hyperfine splitting appears and the rate of 4NC cleavage increases.[130] Optical pH titrations of [wt- and H200N-Co-HPCD(4NC)] complexes suggested that the second species may be due to protonation of His200 which then hydrogen bonds with the dianionically bound 4NC at O(C1).[130]

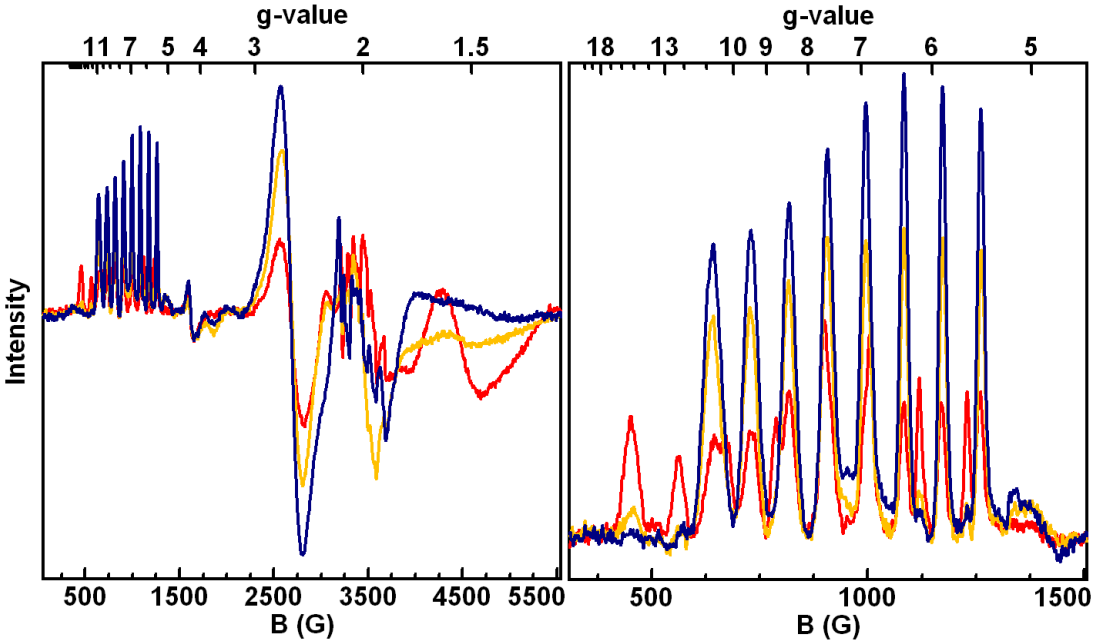

Figure 4.12. EPR spectra of (blue) [Co-HPCD(4ClC)] pH 6.0, (orange) [Co-HPCD(4ClC)] pH 7.5, (red) [Co-HPCD(4ClC)] pH 8.5. Hyperfine splitting at g = 2.0 comes from contaminating Mn(II) (I = 5/2) in enzyme preparation. The signal at g = 4.3 derives from contaminating high-spin Fe(III).

The EPR spectra of [H200N-Co-HPCD(4XC)] enzyme-substrate complexes (Figure 4.13) where all slightly more rhombic than the spectra of the wt-Co-HPCD enzyme-substrate complexes (Table 4.3).[130, 169] Only one S = 3/2 EPR signal is observed for enzyme-substrate complexes of H200N-Co-HPCD with HPCA, catechol and 4FC, as was observed with wt-Co-HPCD. Two different enzyme-substrate complexes are observed by EPR with H200N-Co-HPCD and the more bulky 4Cl, 4Br, and 4IC substrates, as evident from a new set of features at g = 6.4 and 2.7. Unlike the enzyme-substrate complexes observed with wt-Co-HPCD with 4Cl, 4Br and 4IC, which exhibited very large ^{59}Co hyperfine splitting values of ~88 and 112 G the second species observed with H200N-Co-HPCD display ^{59}Co hyperfine splitting of only 31 G (Table 4.3). The

small ^{59}Co hyperfine splitting is similar to that observed with the 5-coordinate enzyme-inhibitor complexes of wt- and H200N-Co-HPCD with 3-hydroxyphenylacetate (3HPA, Section 2.3.5.C). This suggests a drastically different substrate binding mode of these substrates to the H200N mutant than to the wild-type enzymes.

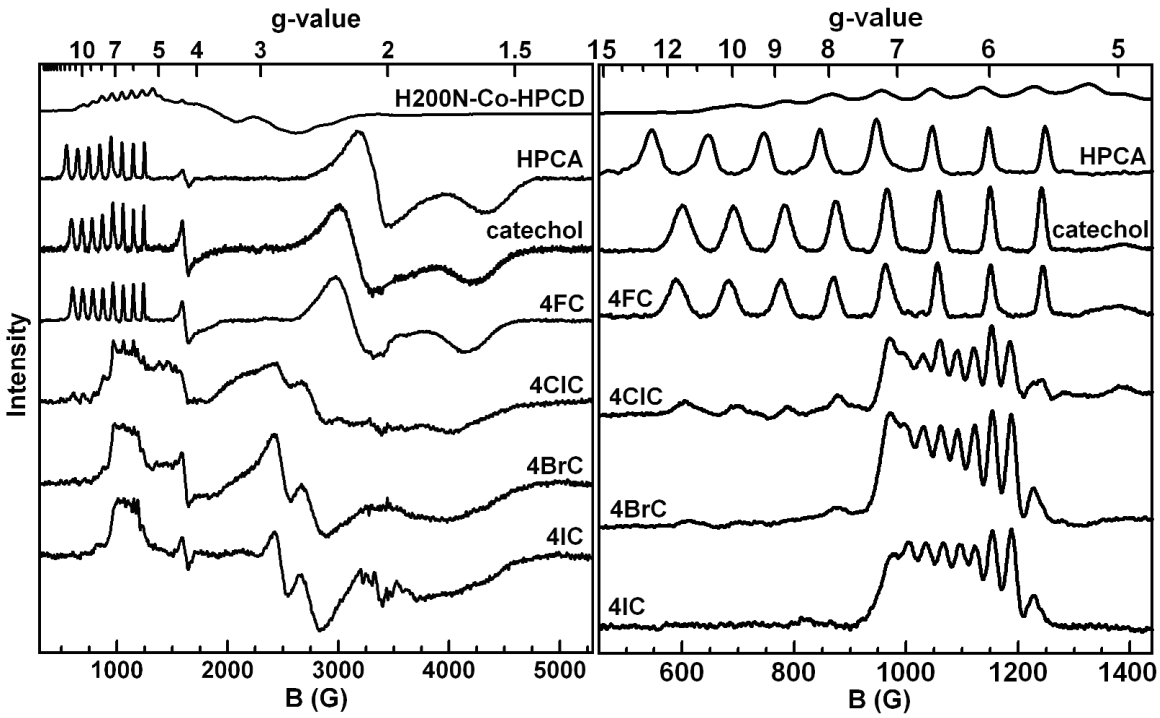

Figure 4.13. EPR spectra obtained at 9.64 GHz and 20 K of H200N-Co-HPCD and anaerobic enzyme-substrate complexes, in 100 mM MOPS (pH 7.5) for (top to bottom) H200N-Co-HPCD,[130] [H200N-Co-HPCD(HPCA)],[130] [H200N-Co-HPCD(catechol)], [H200N-Co-HPCD(4FC)], [H200N-Co-HPCD(4ClC)], [H200N-Co-HPCD(4BrC)], and [H200N-Co-HPCD(4IC)].

In an unpublished X-ray crystal structure by our collaborator Elena Kovaleva of [H200N-Fe-HPCD(4FC)] the substrate was observed to be bound in two different orientations where the substrate was apparently flipped by 180° from its normal binding position.[265] The misorientation of the substrate is likely due to a combination of factors

including the loss of the anionic acetic acid substituent's interactions with the protein's anion-binding pocket (His248/Arg293/Arg/243), in combination with loss of the interaction with His200. Though admittedly by EPR 4FC is observed to only form one enzyme-substrate complex with wt- and H200N-Co-HPCDs (Figures 4.11 and 4.13). Loss of the hydrogen bonding interaction between H200 and the catechol substrate in combination with the more bulky Cl, Br, and I substituents may lead to two different orientations of the substrate and explain the second enzyme-substrate species observed by EPR with these substrates and H200N-Co-HPCD. Experiments with H200F-Fe-HPCD mutant reported by Stepanie Groce and John Lipscomb, with the substrate analogue 2,3-dihydroxybenzoate (2,3-DHB) observed that while the mutant reacted with the native substrate HPCA to produce the normal distal extradiol ring-cleaved product it cleaved 2,3-DHB to afford the intradiol ring-cleaved product.[168] This loss of regiospecificity may be attributed to the missorentation of the substrate analog due to the positioning of the shorter benzoate side chain in combination with missorentation of the superoxide by the bulky side chain of Phe200.[168]

Further characterization of these wt- and H200N-Co-HPCD enzyme-substrate complexes by UV-Vis and MCD spectroscopes are underway with collaborators in the lab of Professor Thomas Brunold lab. Through these studies we hope to address the effects of the catechol substrate on the Co-ligand field. This is an important question due to the apparent spin-state transition observed upon binding O_2 to [wt- and H200N-Co-HPCD(4NC)] complexes. The different pK_as .(σ-basicity) of the different catechols and their different binding modes to the metal center, whether as the dianionic or

monoanionic catecholates (π-basicity) may have a significant effect on the Co ligand-field which in turn may effect the spin-transitions from high-spin Co(II) to low-spin Co(III) upon O_2 binding and back again upon catechol oxidation.

Table 4.3. Electron paramagnetic resonance data for Co-HPCD enzyme-substrate complexes.

Sample	*S* =	*g-values*	^{59Co}A (G)	References
Co-HPCD	3/2	6.7, 3.4, 2.4	80	[169]
[Co-HPCD(HPCA)]	3/2	7.6, 2.5, 1.9	98	[169]
[Co-HPCD(catechol)]	3/2	7.3, 2.6, 1.9	92	This work
[Co-HPCD(4FC)]	3/2	7.3, 2.6, 1.9	90	This work
[Co-HPCD(4ClC)] Species 1 Species 2 (pH 8.0)	3/2	7.2, 2.6, 1.9 8.1, 2.6, 1.4	88 112	This work
[Co-HPCD(4BrC)] Species 1 Species 2	3/2	7.2, 2.6, 2.0 8.1, 2.6, 1.4	87 112	This work
[Co-HPCD(4IC)] Species 1 Species 2	3/2	7.2, 2.6, 2.0 8.1, 2.7, 1.4	87 112	This work
[Co-HPCD(4NC)]	3/2	5.6, 3.5, 2.1	75	[130]
[H200N-Co-HPCD]	3/2	6.9, 3.7, 2.6	90	[130]
[H200N-Co-HPCD(HPCA)]	3/2	7.7, 2.1, 1.6	101	This work
[H200N-Co-HPCD(catechol)]	3/2	7.5, 2.2, 1.6	92	This work
[H200N-Co-HPCD(4FC)]	3/2	7.5, 2.2, 1.7	94	This work
[H200N-Co-HPCD(4ClC)] Species 1 Species 2	3/2	7.5, 2.5, 1.7 6.4, 2.7	91 31	This work
[H200N-Co-HPCD(4BrC)] Species 1 Species 2	3/2	7.5, 2.5, 1.7 6.4, 2.7	90 31	This work
[H200N-Co-HPCD(4IC)] Species 1 Species 2	3/2	7.5, 2.5, 1.8 6.4, 2.7	90 31	This work
[H200N-Co-HPCD(4NC)]	3/2	6.3, 3.2, 1.9	53	[130]

Table 4.4. Calculated and measured (*) pK_a, and sigma taft (σ^*), sigma meta (σ_m) and sigma para (σ_p) values for substituted catechols.[243, 262]

	HPCA	cat	4BrC	4ClC	4FC	4NC
pK_{a1}	9.5	9.83	8.96	9.01	9.07	6.69
pK_{a2}	13.7	12.37	11.88	11.83	12.24	10.85
σ^*	-0.06	0.49	2.84	2.96	3.21	4.25
σ_m	---	0	0.39	0.37	0.34	0.74
σ_p	---	0	0.22	0.24	0.06	0.78
***pK_{a1}**	---	9.32 ± 0.02	8.41 ± 0.02	8.51 ± 0.02	---	7.35 ± 0.09

4.2.3.B Rapid freeze-quench experiments: [Co-HPCD(4XC)] rapidly mixed with oxygenated buffer. Figure 4.14 shows representative EPR spectra from freeze-quench experiments with [Co-HPCD(4FC)] rapidly mixed with O_2 saturated buffer (pH 7.5 at 4 °C). The anaerobic [Co-HPCD(4FC)] enzyme-substrate complex exhibits an $S = 3/2$ EPR signal consistent with a high-spin Co(II) center. Upon mixing with O_2, the amount of the $S = 3/2$ species decreases as a new $S = 1/2$ species forms with signals centered at $g = 2.005$. Unlike the previously characterized low-spin Co(III)-$O_2^{\bullet-}$ complexes observed with [wt/H200N-Co-HPCD(4NC)O_2], the $S = 1/2$ species observed here with Co^{4FC}Int1 does not exhibit any resolved ^{59}Co hyperfine splitting; instead the signal is split into a doublet. The intensity of the $S = 1/2$ species continues to increase over the first 250 ms and then decreases as a new set of signals with ^{59}Co hyperfine ($g = 6.7$, $^{59Co}A = 75$ G) from an $S = 3/2$ species grow in the low-field region. The new $S = 3/2$ species, Co^{4FC}Int2 then decays slowly over 30 sec to another $S = 3/2$ species that corresponds to Co-HPCD. The new $S = 3/2$ intermediate is distinguishable from the [Co-HPCD(4FC)] enzyme-substrate complex and the final Co-HPCD product by its slightly different ^{59}Co hyperfine splitting of 75 G (Tables 4.3 and 4.5).

The reaction progress (Figure 4.15) was monitored by following changes in the intensities of EPR features unique to each species. A ~35% yield of the $S = 1/2$ Co^{4FC}Int1 species, was measured at 250 ms by spin quantification close to the ~40% yield of Co^{4FC}Int1 predicted from rate constant measured in stopped-flow experiments.[224] Co^{4FC}Int2 forms to ~70% yield at 2 sec, forming and decaying on the same time scale and yield as predicted from the stopped-flow experiments.

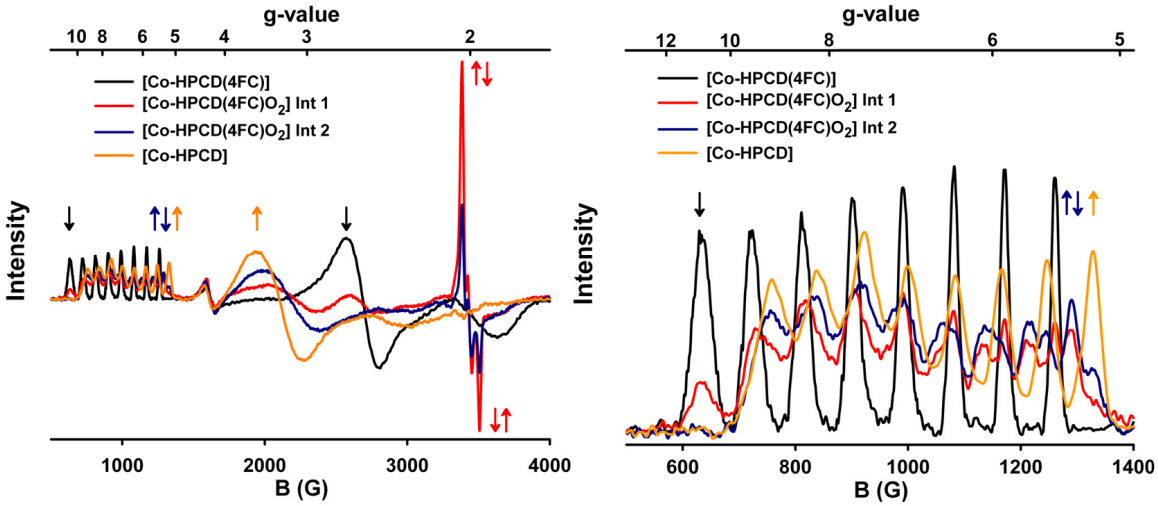

Figure 4.14. EPR spectra of rapid freeze-quench samples of anaerobic enzyme-substrate complex [Co-HPCD(4FC)] (black) rapidly mixed with O_2-saturated buffer, showing formation of Co^{4FC}Int1 (red) at 125 ms g = 2.036, 2.005, and 1.965, and formation of Co^{4FC}Int2 (blue) sample frozen at 2 sec g = 6.7 (A = 75 G), 3.1, and 1.9 and subsequent decay to Co-HPCD and the extradiol ring-cleaved product (orange) g = 6.7 (A = 80 G), 3.4, and 2.4 after 60 sec. Arrows indicate direction of change of each feature associated with each species over time. Spectra were normalized to high-spin Fe(III) contaminate at g = 4.3. Reaction conditions: 4 °C, 100 mM MOPS, pH = 7.5, final concentrations upon mixing: 0.32 mM Co-HPCD, 0.4 mM 4FC (~1.25 equivalents), and 1.0 mM O_2. EPR spectra were all collected at 20 K and 2 mW power.

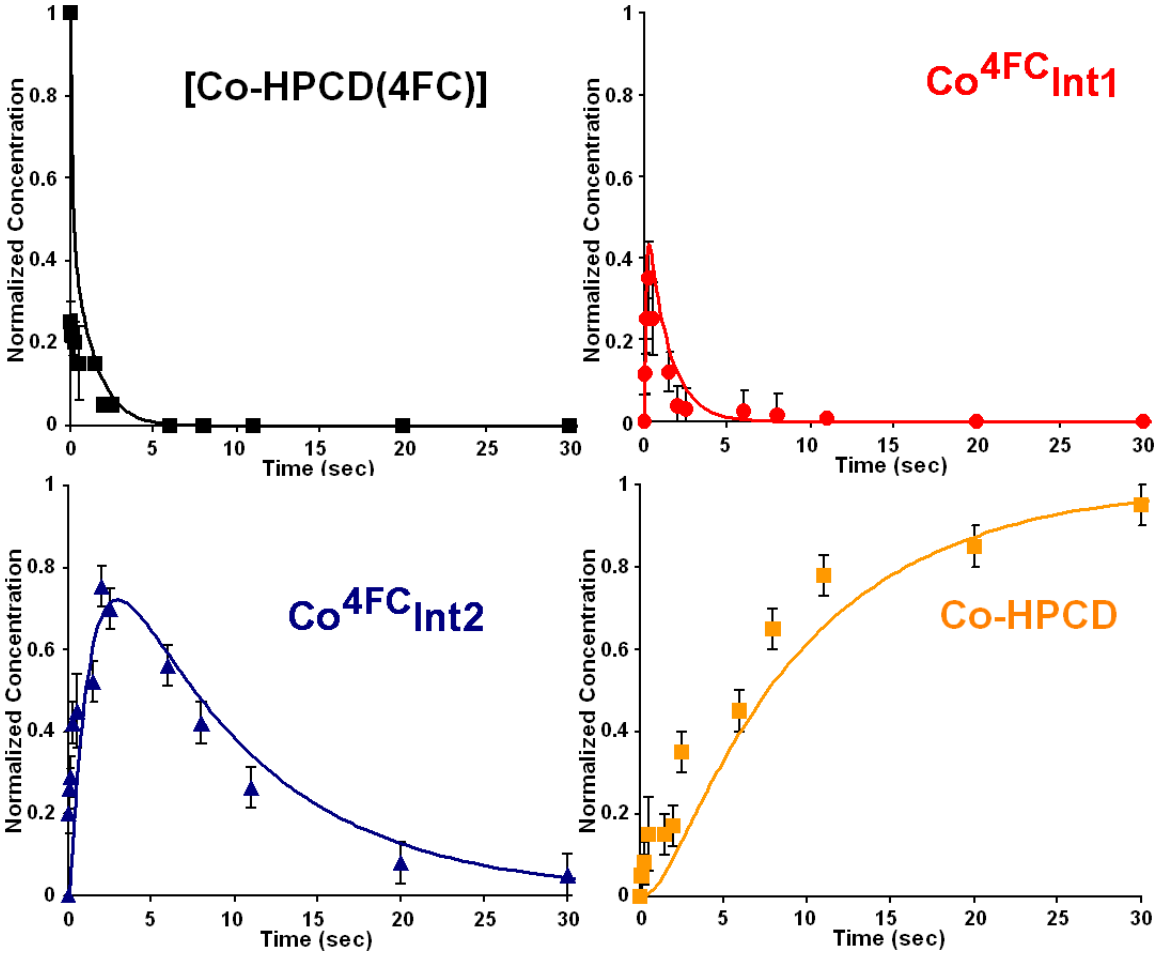

Figure 4.15. Time dependence of the various EPR-active species observed in EPR freeze-quench experiments. The change in concentration of each species was measured by monitoring the change in the intensity of EPR features unique to each species. ([Co-HPCD(4FC)] at g = 10.9, Co^{4FC}Int1 at g = 2.035 and 1.965, Co^{4FC}Int2 at g = 5.68, and Co-HPCD at g = 5.19.) Thick lines represent time courses for each species simulated using rates determined from stopped-flow experiments performed under similar reaction conditions.

Table 4.5. Electron paramagnetic resonance data for Co-HPCD O_2-adducts, trapped intermediate species and semiquinone model complexes.

Sample	*S* =	*g-values*	^{X}A (G)	Ref.
[Co-HPCD(4NC)O_2]	1/2	2.10, 2.02, 1.99	^{59}Co (24)	130
[H200N-Co-HPCD(4NC)O_2]	1/2	2.10, 2.02, 1.99	^{59}Co (22)	130
Co^{HPCA}Int1	1/2	2.00	---	This work
Co^{HPCA}Int2	3/2	6.7, 3.2, 1.9	75	This work
Co^{4FC}Int1	1/2	2.005	^{19}F (60), ^{59}Co (8.5)	This work
Co^{4FC}Int2	3/2	6.7, 3.2, 1.9	75	This work
Co^{4ClC}Int1	1/2	2.005	---	This work
Co^{4ClC}Int2	3/2	6.7, 3.2, 1.9	75	This work
[H200NCo-HPCD(HPCA)O_2]	1/2	2.00	^{59}Co (15)	This work
[H200NCo-HPCD(4ClC)O_2]	1/2	2.00	^{59}Co (19)	This work
[H200NCo-HPCD(4FC)O_2]	1/2	2.00	-	This work
[Sn(IV)(C_6H_5)$_3$-4FSQ]	1/2	2.00423	^{19}F (13.22), ^{1}HC3 (1.64), ^{1}HC5 (3.46), ^{1}HC6 (0.55)	266
[(CO)$_2$Rh(I)(DFDTBSQ)]	1/2	2.0032	^{19}F (10.88)	267
[K(FClDTBSQ)]	1/2	2.0054	^{19}F (8.03), ^{35,37}Cl (0.13)	268
[Co(III)(trien)3,5-DTBSQ]	1/2	2	^{59}Co (9.76), ^{1}HC4 (3.5)	269
[Co(III)(salen)3,5-DTBSQ] **295K** **77K**	1/2	2.58	^{59}Co (10.20), ^{1}H (3.50) ^{59}Co (17.50)	270
[Co(III)(triphos)3,5-DTBSQ]$^{2+}$	1/2	2.0039	^{59}Co (5.8), ^{1}H (2.9), ^{31}P (5.8)	253
[Co(III)(CTH) 3,5-DTBSQ](PF$_6$)$_2$	1/2	2.00	^{59}Co (9.5), ^{1}H (2.0)	271

Rapid freeze-quench experiments were also performed by rapidly mixing anaerobic [Co-HPCD(4ClC)] enzyme-substrate complex with O_2-saturated buffer (pH 7.5 at 4 °C). Two intermediate species were observed in this reaction with EPR spectra similar to that described for 4FC (Figure 4.16). The first Co^{4ClC}Int1 is an $S = 1/2$ species with an isotropic signal centered at $g = 2.005$ with no resolved splitting at 20 K. The second intermediate Co^{4ClC}Int2 is an $S = 3/2$ species nearly identical to Co^{4FC}Int2.

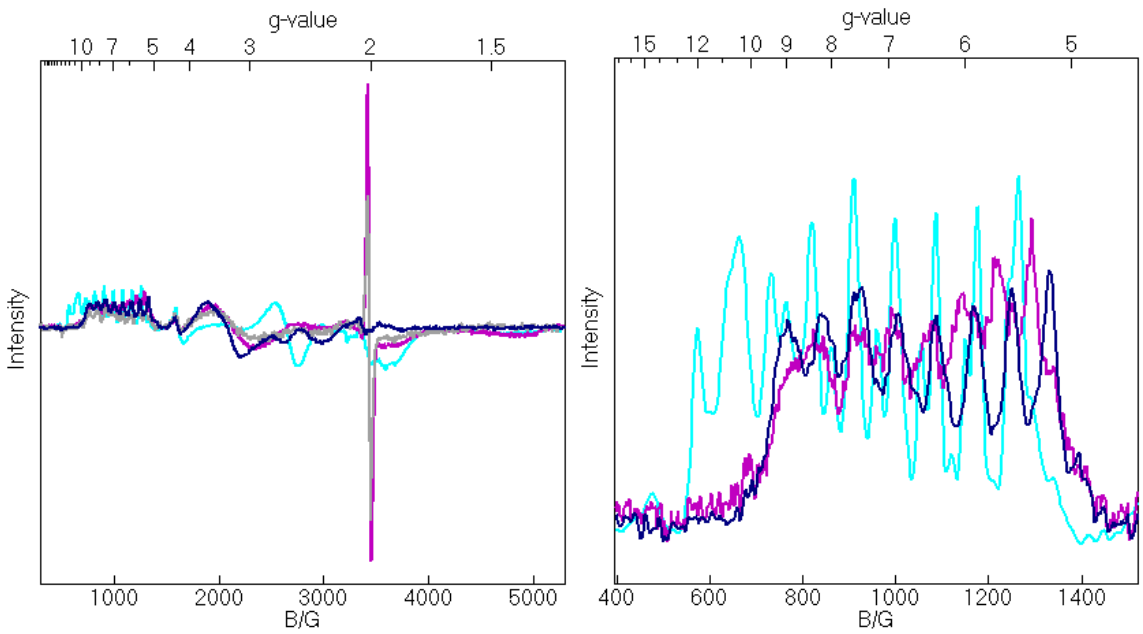

Figure 4.16. EPR spectra of rapid freeze-quench samples of anaerobic enzyme-substrate complex [Co-HPCD(4ClC)] (light blue) rapidly mixed with O_2-saturated buffer, showing formation of the S = 1/2, Co^{4ClC}Int1, and S = 3/2, Co^{4ClC}Int2 at 500 ms (purple). Co-HPCD (dark blue) g = 6.7(A = 80G), 3.4, and 2.4 and extradiol ring-cleaved product after 10 sec. Spectra were normalized to the high-spin Fe(III) contaminate at g = 4.3. Reaction conditions: 4 °C, 100 mM MOPS, pH = 7.5, final concentration upon mixing 0.24 mM Co-HPCD, 0.30 mM 4FC (~1.25 equivalents), and 1 mM O_2. EPR spectra were all collected at 20 K and 2 mW power.

4.2.3.C Transient kinetic experiments: [Co-HPCD(HPCA)] rapidly mixed with oxygenated buffer. In previously reported stopped-flow experiments in which the anaerobic enzyme-substrate complex [Co-HPCD(HPCA)] was rapidly mixed with oxygenated buffer (pH 7.8 at 22 °C), only the formation of the yellow ring-cleaved product at 380 nm was observed.[169] A 50 ms lag phase preceding the formation of the product in the single wavelength traces was observed when monitoring the formation of the product chromophore at 380 nm. Figure 4.17 shows the single wavelength traces for

the O_2 concentration dependence for the same reaction at pH 7.5 and 4 °C; under these conditions the lag phase is significantly longer (200 ms). A good fit of the single wavelength data could not be obtained, but the significant O_2 concentration dependence observed in product formation suggests that the rate determining step in the reaction is reversibly connected with O_2 binding as previously suggested.[169] The longer lag phase suggests the potential to trap accumulated intermediates at 4 °C.

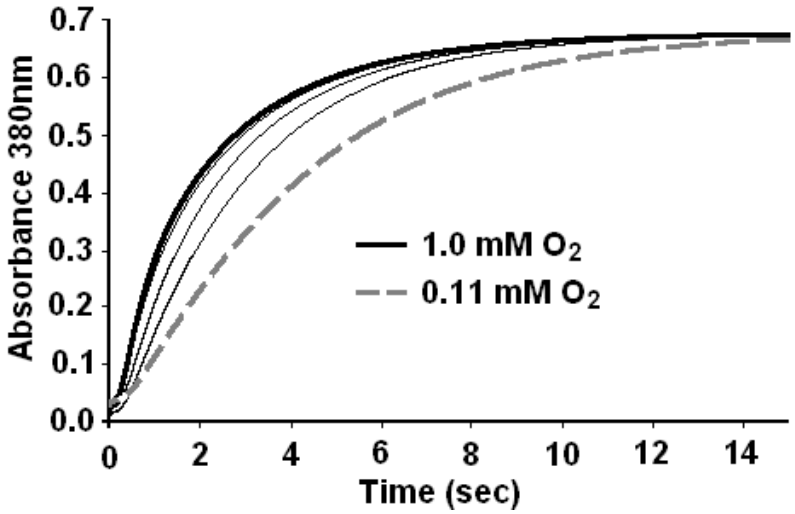

Figure 4.17. Single-wavelength stopped-flow kinetic data monitoring the formation of extradiol ring-cleaved product at 380nm for [Co-HPCD(HPCA)] rapidly mixed with oxygenated buffer. O_2 concentrations upon mixing range from 0.11 to 1.0 mM. Reaction conditions: 100 mM MOPS (pH 7.5), 4 °C, final concentration upon mixing 50 μM Co-HPCD, 20 μM HPCA.

Closer inspection of the photodiode array stopped-flow data for the reaction of [Co-HPCD(HPCA)] with O_2 at higher enzyme and substrate concentrations (Figure 4.18) shows the formation of a chromophore at 550 nm. The 550 nm chromophore forms in the first 150 ms and then decays over 20 sec with formation of the yellow ring-cleaved product at 380 nm (Figure 4.17). Single wavelength stopped-flow traces following the reaction at 550 nm (Figure 4.19) show a ~30 ms lag phase prior to the formation of the

chromophore at 550 nm suggesting the formation of two intermediate species in the reaction of [Co-HPCD(HPCA)] with O_2.

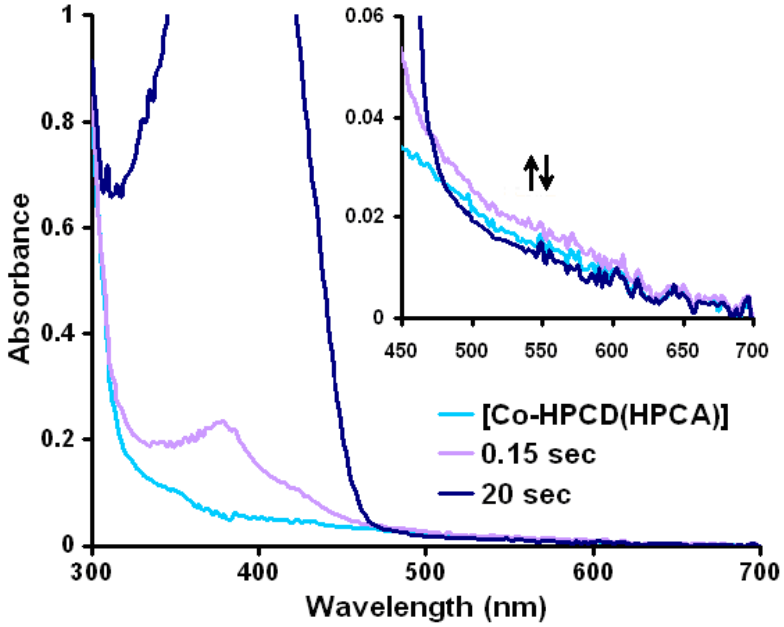

Figure 4.18. Photodiode array stopped-flow kinetic data for anaerobic [Co-HPCD(HPCA)] complex rapidly mixed with O_2-saturated buffer (1atm O_2). Final concentrations of reagents after mixing: 130 μM HPCA, 200 μM Co-HPCD and 1 mM O_2. Reaction conditions: 100 mM MOPS (pH 7.5), 4 °C with 1 cm path length. Inset showing small increase and decrease in absorption at 550 nm.

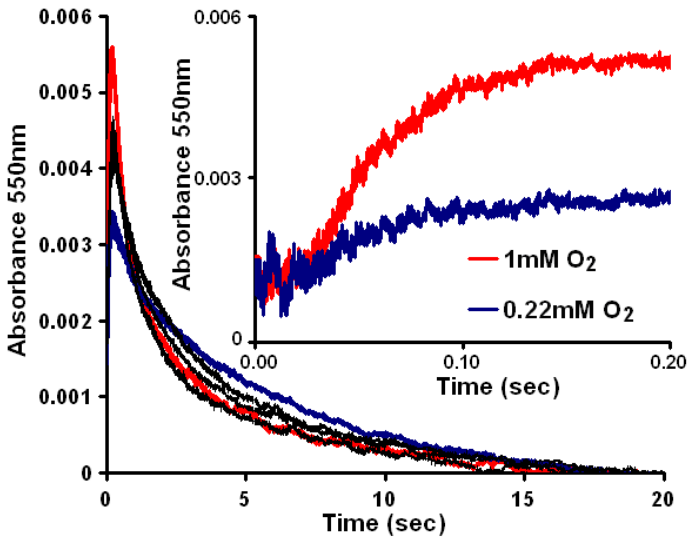

Figure 4.19. Stopped-flow kinetic data for [Co-HPCD(HPCA)] rapidly mixed with oxygenated buffer. Single wavelength traces monitoring formation and decay of chromophore at 550 nm (1 cm path length). Inset showing a 30 ms lag phase in formation of 550 nm chromophore. Final concentrations of reagents after mixing: 130 μM HPCA, 200 μM Co-HPCD and 1000–220 μM O_2. Reaction conditions: 100 mM MOPS (pH 7.5), 4 °C with a 1 cm path length.

EPR rapid freeze-quench experiments were also carried out using the native substrate by rapidly mixing the anaerobic [Co-HPCD(HPCA)] enzyme-substrate complex with oxygenated buffer (pH 7.5 at 4 °C, Figure 4.20). Similar to the experiments with [Co-HPCD(4FC)] and [Co-HPCD(4ClC)], two intermediates are observed. The first Co^{HPCA}Int1 is an S = 1/2 species with an isotropic signal centered at g = 2.005 with no resolved splitting at 20 K. Co^{HPCA}Int1 forms to ~15% yield at 50 ms and then decays by 0.5 sec. The second intermediate Co^{HPCA}Int2 forms to ~ 90% yield at 250 ms and exhibits an S = 3/2 species nearly identical to that of Co^{4FC}Int2 (Table 4.4).

Two intermediate species are observed in the reaction of both [Co-HPCD(4CC)] and [Co-HPCD(HPCA)] with O_2 by EPR. The EPR spectra of Co^{HPCA}Int1 and

Co^{HPCA}Int2 are nearly identical to Co^{4ClC}Int1 and Co^{4ClC}Int2 (Table 4.4), but while Co^{4ClC}Int2 exhibits an intense chromophore characteristic of the 4ClQ, Co^{HPCA}Int2 only displays a very weak chromophore in UV-Vis stopped-flow experiments.

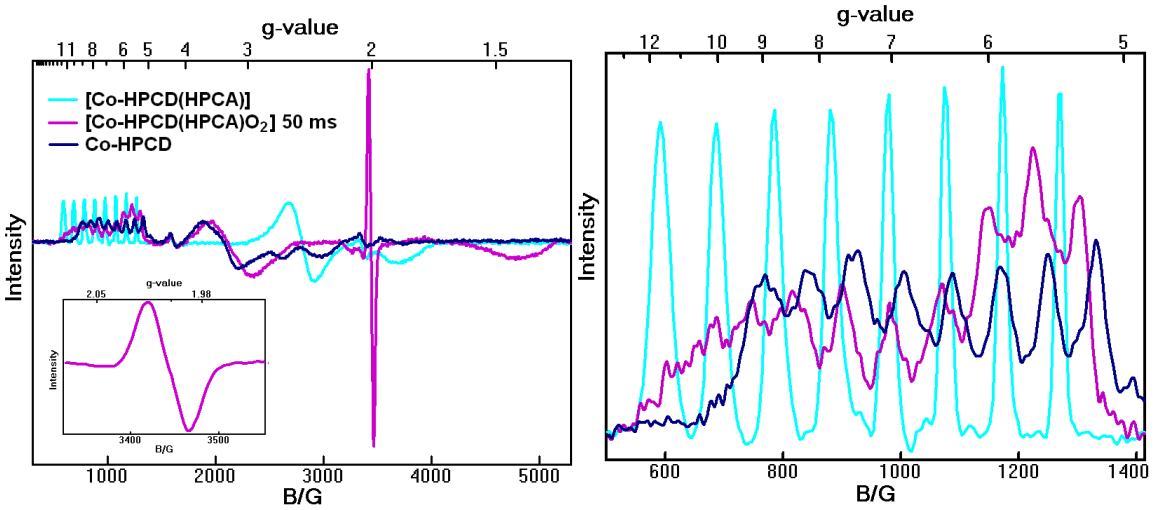

Figure 4.20. EPR spectra of [Co-HPCD(HPCA)] (light blue), [Co-HPCD(HPCA)O_2] (purple) sample frozen at 50 ms with a ~15% yield of S = 1/2 species (Co^{HPCA}Int1) and ~85% yield of S = 3/2 species (Co^{HPCA}Int2), (dark blue) [Co-HPCD] + HPCA extradiol ring-cleaved product. Reaction conditions: 4 °C, 100 mM MOPS, pH = 7.5, final concentration upon mixing 0.24 mM Co-HPCD, 0.30 mM HPCA (~1.25 equivalents), and 1 mM O_2.

4.2.3.D Characterization of the S = 1/2 intermediates. Figure 4.21 shows the overlay of the EPR spectra of the S = 1/2 intermediates of Co^{4FC}Int1 and Co^{4ClC}Int1 collected at 20 K. While the Co^{4FC}Int1 signal is split into a doublet, Co^{4ClC}Int1 appears to be just an isotropic signal at 20 K. The observed splitting of Co^{4FC}Int1 likely originates from coupling of the unpaired electron to the ^{19}F nucleus (I = 1/2). In contrast, the previously reported S = 1/2 complexes observed with [wt- and H200N-Co-HPCD(4NC)O_2] (Table 4.5) exhibit well-resolved ^{59}Co hyperfine (A = 22–24 G) centered at g = 2.1

typical of low-spin Co(III)-$O_2^{\bullet-}$ complexes.[130, 226-229, 272] In addition there is significant line broadening of the EPR signal in $^{17}O_2$ (I = 5/2, 70% ^{17}O) isotope labeling experiments of [H200N-Co-HPCD(4NC)O_2], confirming its identity as a low-spin Co(III)-$O_2^{\bullet-}$ species. On the other hand, $^{17}O_2$ isotope labeling experiments of Co^{4FC}Int1 (Figure 4.21) show no significant broadening or change to the shape of the S = 1/2 signal. An adequate simulation of the splitting observed in the Co^{4FC}Int1 can be obtained with the program Hyperfine Spectrum using ^{19F}A = 60 G and ^{59Co}A = 8.5 G coupling constants (Figure 4.22).[273]

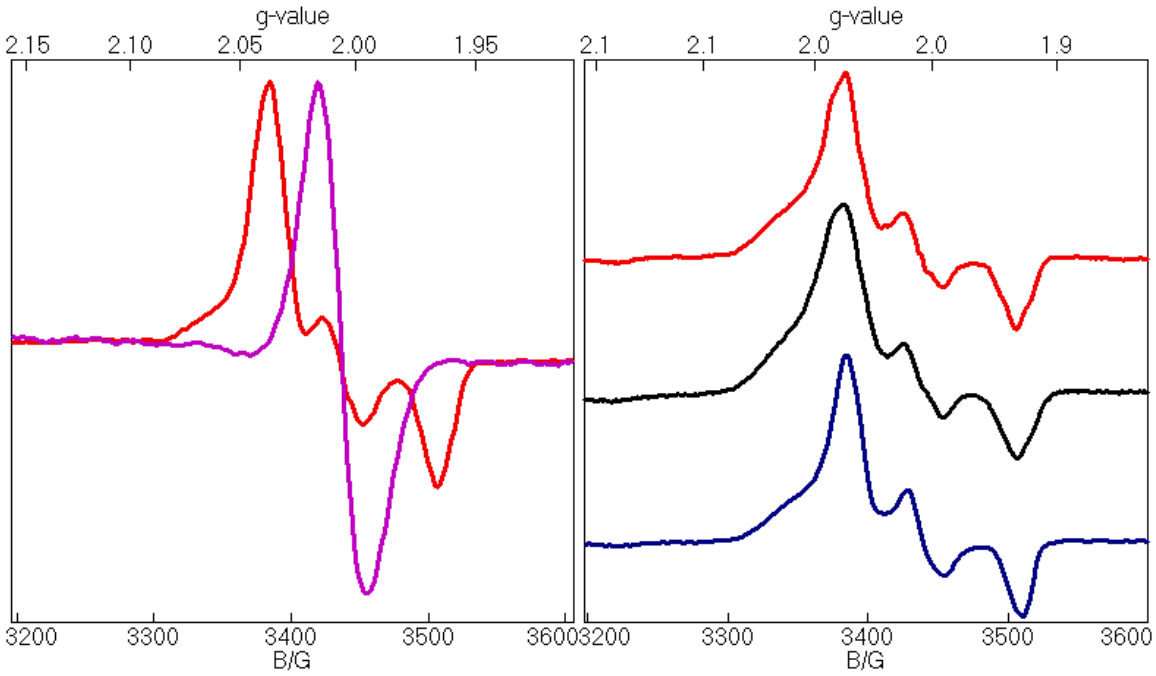

Figure 4.21. (Left) EPR spectra of S = 1/2 species; (purple) Co^{4ClC}Int1 sample frozen at 10 ms g = 2.005, (red) Co^{4FC}Int1 sample frozen at 50 ms g = 2.036, 2.005, and 1.965. (Right) EPR spectra of S = 1/2 species; (red) [Co-HPCD(4FC)$^{16}O_2$] (Co^{4FC}Int1), (black) [Co-HPCD(4FC)$^{17}O_2$] (70% ^{17}O), (blue) [Co-HPCD(d_3-4FC)O_2].

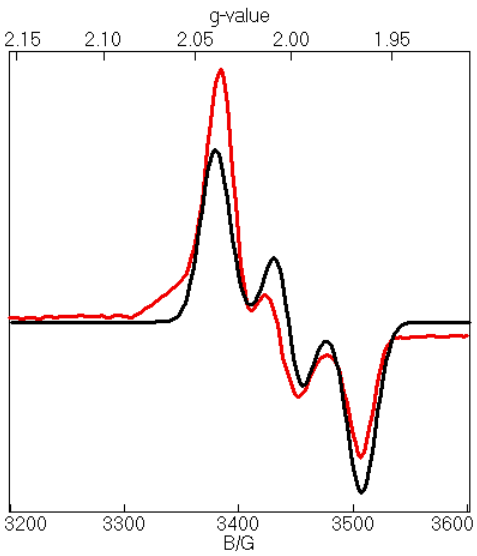

Figure 4.22. EPR spectra of S = 1/2 species; (red) Co^{4FC}Int1, (black) simulation of spectrum ^{59}Co (I = 7/2) A = 8.5 G, ^{19}F (I = 1/2) A = 60 G.

The 60-G ^{19}F splitting observed in Co^{4FC}Int1 is quite large. It is much larger than those observed in metal-fluorosemiquinone complexes, e. g. 13.22 G for [Sn(IV)$(C_6H_5)_3$-4FSQ$^{\bullet}$], 10.8 G for [$(CO)_2$Rh(I)(DFDTBSQ$^{\bullet}$)] (DFDTBSQ$^{\bullet}$ = 4,5-difluoro-3,6-di-*tert*-butyl-*o*-semiquinone), and 8.03 G for [K(FClDTBSQ$^{\bullet}$)] (FClDTBSQ$^{\bullet}$ = 4-fluoro-5-chloro-3,6-di-*tert*-butyl-*o*-semiquinone) (Table 4.6).[266-268, 274] The ^{19}F splitting observed in Co^{4FC}Int1 is similar to that for an sp^3 radical like $^{\bullet}CH_2F$ (64.3 G), but much larger than those for sp^2 radicals like the cis-2-fluorovinyl radical ($^{\bullet}CH=CHF$, 6.5 G) or for the 1-fluorovinyl radical ($^{\bullet}CF=CH_2$, 13.7 G).[275-277] These comparisons suggest that the radical observed in Co^{4FC}Int1 is localized on a sp^3 carbon of a nonplanar semiquinone, as seen in the crystal structure of the [Fe(II)HPCD(4NSQ$^{\bullet}$)$O_2^{\bullet-}$] intermediate. In this structure there is significant puckering at C2, suggesting localization of the semiquinone radical.[163, 165] The large ^{19}F splitting observed for Co^{4FC}Int1 leads us to suggest puckering at C4 of the semiquinone in this intermediate.[266]

The S = 1/2 species prepared with deuterated d_3-4FC (^{2H}I = 1) also did not result in any resolved ^{2}H hyperfine splitting at 20 K (Figure 4.21). This is not unexpected, given the small hyperfine splitting observed for the ^{1}H coupling (^{1H}I = 1/2) to the ring protons of [Sn(IV)$(C_6H_5)_3$-4FSQ$^{\bullet}$] of 0.55 G for ^{1}HC6, 1.64 G for ^{1}HC3 and 3.46 G for ^{1}H–C5.[266]

4.2.3.E H200N-Co-HPCD ESO_2 complexes. [H200N-Co-HPCD(HPCA)] samples slowly react with O_2 to form the yellow extradiol ring-cleaved product, but addition of H_2O_2 to the reaction greatly slows the rate of formation, suggesting that most of the observed activity is due to contaminating H200N-Fe-HPCD. However exposure of [H200N-Co-HPCD(HPCA)] to 2 atm of O_2 at 4 °C elicits an S = 1/2 species that is formed in ~25% yield (Figure 4.23). This signal is distinct from that previously reported for the reversible O_2 adduct of [H200N-Co-HPCD(4NC)] (Figure 4.25, inset), which is best described as a low-spin Co(III)-$O_2^{\bullet-}$ species.[130] The EPR signal of [H200N-Co-HPCD(HPCA)O_2] does exhibit some resolvable ^{59}Co hyperfine splitting, but the A-value of 15 G is half as big as that for [H200N-Co-HPCD(4NC)O_2]. Moreover, unlike for the 4NC adduct, its EPR signal is not broadened with the use of $^{17}O_2$ (Figure 4.23).[130] The two S = 1/2 species also exhibit different power saturation behaviors (Figure 4.24 and 4.25), with the S = 1/2 EPR signal of [H200N-Co-HPCD(HPCA)O_2] saturating at lower powers, between 2.5 and 35 K than that of [H200N-Co-HPCD(4NC)O_2]. Co^{4FC}Int1 exhibits similar EPR power saturation behavior (Figure 4.26) to the [H200N-Co-HPCD(HPCA)O_2] species, suggesting that both [H200N-Co-HPCD(HPCA)O_2] and Co^{4FC}Int1 S = 1/2 EPR signal derive from substrate radicals. Similar S = 1/2 species are also observed in the reaction of [H200N-Co-HPCD(4ClC/4FC)] enzyme-substrate complexes with O_2 by EPR (Figures 4.27 and 4.28).

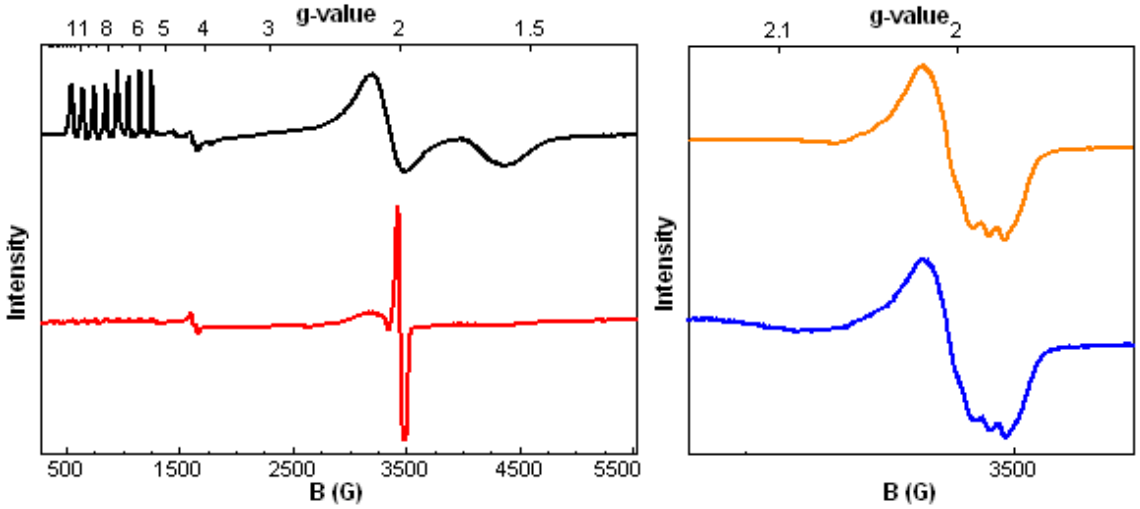

Figure 4.23. (Left) (black) [H200N-Co-HPCD(HPCA)], (red) [H200N-Co-HPCD(HPCA)O_2] pH 7.5 2 atm O_2, 4 °C ~25% yield. (Right) (orange) [H200N-Co-HPCD(HPCA)$^{16}O_2$], (blue) [H200N-Co-HPCD(HPCA)$^{17}O_2$]. Reaction conditions: 4 °C, 100 mM MOPS, pH = 7.5.

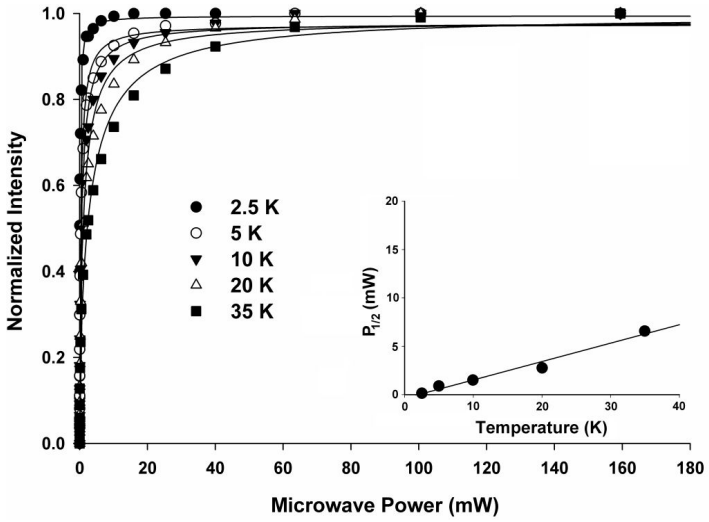

Figure 4.24. EPR power saturation experiment of S = 1/2 species [H200N-Co-HPCD(HPCA)O_2]. The sample was prepared by placing the enzyme-substrate complex (100 mM MOPS at pH 7.5) under 2 atm O_2 at 4 °C and then rapidly freezing the sample in liquid nitrogen cooled isopentane slurry. Data fit to equation 4.3 to determine $P_{1/2}$ values at each temperature.[278] Inset showing variation of $P_{1/2}$ with temperature.

$$\textbf{Equation 4.3} \quad S' = K\frac{\sqrt{P}}{\sqrt{1 + P/P_{½}}}$$

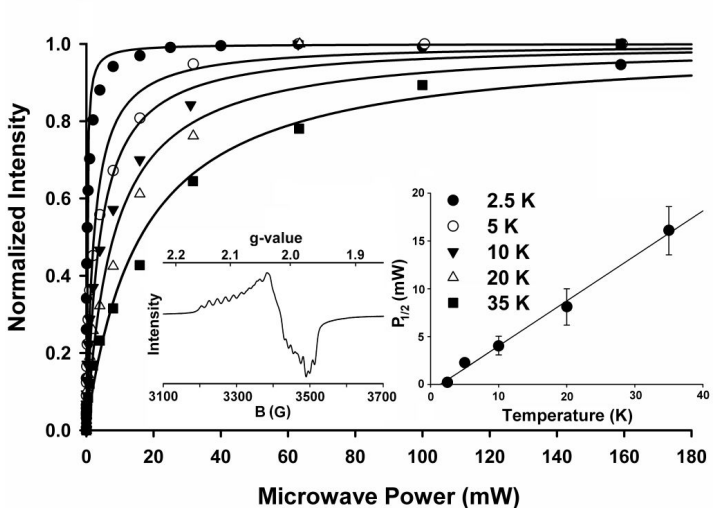

Figure 4.25. EPR power saturation experiment of $S = 1/2$ Co(III)-$O_2^{\bullet-}$ species, [H200N-Co-HPCD(4NC)O_2]. The sample was prepared by placing the enzyme-substrate complex (100 mM MOPS at pH 7.5) under 2 atm O_2 at 4 °C and then rapidly freezing the sample in liquid nitrogen cooled isopentane slurry. Inset EPR spectrum of Co(III)-$O_2^{\bullet-}$ species, [H200N-Co-HPCD(4NC)O_2] 2 atm O_2, pH 7.5 (~50% yield).[130] Data fit to equation 4.3 to determine $P_{1/2}$ values at each temperature.[278] Inset showing variation of $P_{1/2}$ with temperature.

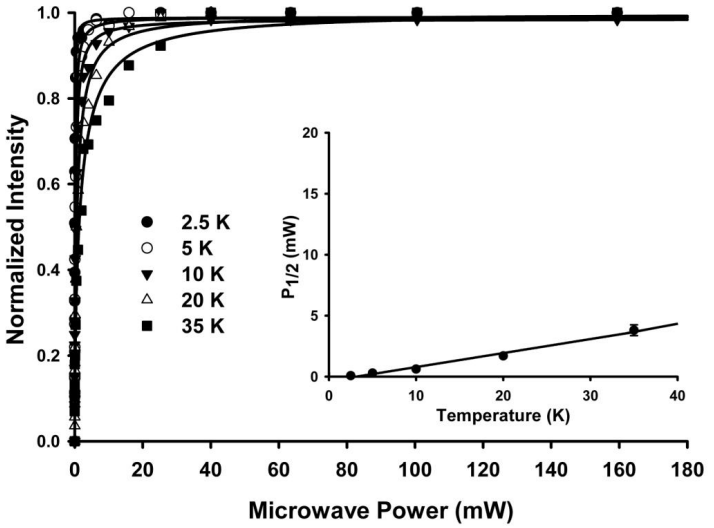

Figure 4.26. EPR power saturation experiment of Co^{4FC}Int1 frozen at ~3 sec in isopentane liquid N_2 bath following intensity of $S = 1/2$ species. Data fit to equation 4.3 to determine $P_{1/2}$ values at each temperature.[278] Inset showing variation of $P_{1/2}$ with temperature.

The EPR experiments suggest that these S = 1/2 species contain semiquinone radicals. The S = 1/2 species can be formulated as low-spin [Co(III)($SQ^{\bullet}$)(hydro)peroxo] complexes. This formulation accounts for all 11 valence electrons and the 5 unpaired electrons in the reactants (high-spin Co(II), the catechol substrate, and triplet O_2) in these S = 1/2 species, where the metal center has been oxidized by one electron to a diamagnetic d^6 low-spin Co(III) center, while the catechol has been oxidized by one electron to a semiquinone, resulting in the two-electron reduction of O_2 to a (hydro)peroxo species. Many low-spin Co(III)-$SQ^{\bullet}$ complexes have been characterized in the literature.[253, 270, 271, 279, 280] These complexes show distinctive S = 1/2 EPR spectra in solution at room temperature consisting of eight doublets originating from coupling to the ^{59}Co nucleus between (A = 5.8–10.2 G) as well as coupling to the protons *para* to the oxygens (A = 2.0–3.5 G, Table 5). In frozen glasses at liquid nitrogen temperatures (77 K) the low-spin Co(III)-$SQ^{\bullet}$ ^{59}Co hyperfine splitting value increase from 10.2 to 17.5 G for [Co(III)(salen)3,5-DTBS$Q^{\bullet}$)].[270] The ^{59}Co hyperfine splitting observed in the low-spin Co(III)-$SQ^{\bullet}$ complexes is thought to originate from the transfer of spin onto the cobalt center due to backbonding from a cobalt dπ orbital into the semiquinone π^*.[279] The suspected S = 1/2 Co(III)-$SQ^{\bullet}$ intermediates observed in EPR studies of wt-Co-HPCD complexed with HPCA, 4ClC, and 4FC do not show the expected ^{59}Co hyperfine splitting pattern in spectra collected at 20 K. There appears to be some resolved ^{59}Co hyperfine splitting in the S = 1/2 species observed upon placing the H200N-Co-HPCD enzyme-substrate complexes with HPCA, 4ClC, and 4FC under an atmosphere of O_2 (Figures 4.26–28). Indeed, collecting the EPR spectra of the these S = 1/2 species at higher temperature (80–150 K) resulted in a marked decrease in the intensity of the

S = 1/2 signal but with improved resolution of the ^{59}Co hyperfine splitting ranging from 15–19 G in the probable [H200N-Co-HPCD(SQ$^{\bullet}$)(hydro)peroxo] complexes. The observed A-value of 15–19 G agrees well with that observed for the semiquinone complex [Co(III)(salen)3,5-DTBSQ$^{\bullet}$)] (Table 4.5).[270]

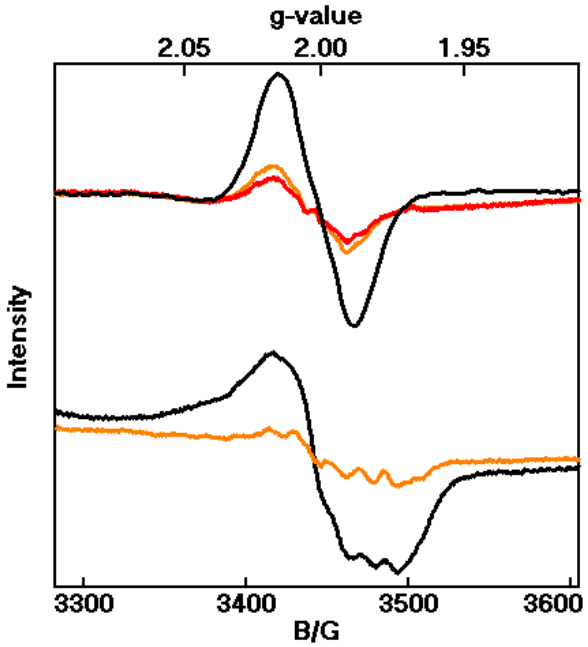

Figure 4.27. EPR spectra of S = 1/2 species, (top) [Co-HPCD(HPCA)O_2] and (bottom) [H200N-Co-HPCD(HPCA)O_2] collected at 20 K (black), 80 K (orange), and 120 K (red) at 2 mW power.

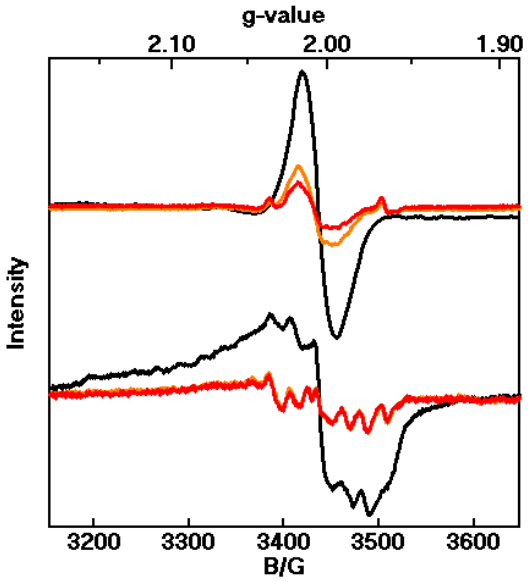

Figure 4.28. EPR spectra of S = 1/2 species, (top) [Co-HPCD(4ClC)O_2] and (bottom) [H200N-Co-HPCD(4ClC)O_2] collected at 20 K (black), 80 K (orange), and 150 K (red) at 2 mW power.

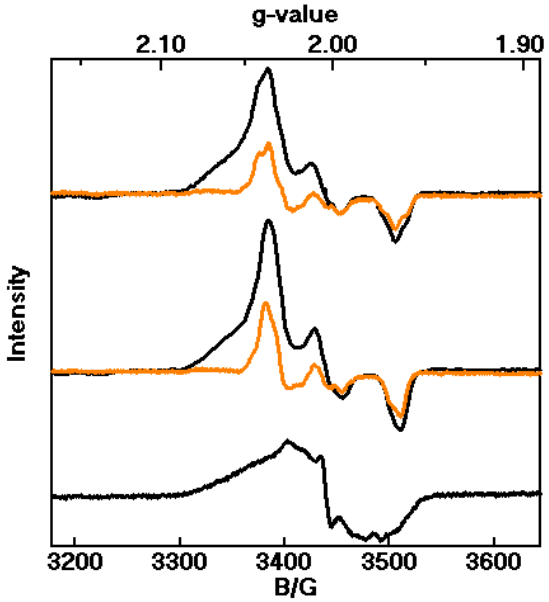

Figure 4.29. EPR spectra of S = 1/2 species, (top) [Co-HPCD(4FC)O_2], (middle) [Co-HPCD(d_3-4FC)O_2] (bottom) [H200N-Co-HPCD(4FC)O_2] collected at 20 K (black), and 80 K (orange) at 2 mW power.

Table 4.6. Electronic absorption spectra of observed intermediates, catechol, semiquinone, and quinone model complexes.

Complex[a]	**λ_{max} (nm) (ε, $M^{-1}cm^{-1}$)**	**Ref.**
Co^{4FC}Int2	**467(~11000)**	**This work**
Co^{4ClC}Int2	**456(~9000)**	**This work**
Co^{4BrC}Int2	**453(~8000)**	**This work**
[H200N-Fe(III)HPCD(HPCA-SQ)(H)peroxo]	**310(7000), 395(3200), 610(1100)**	**149**
[H200N-Fe(III)HPCD(4NSQ)(H)peroxo]	**405(15000), 675(1000)**	**162**
[Y257F-Fe(II)HPCD(HPCA-Q)(H)peroxo]	**425(10500)**	**161**
[Fe(III)-HPCD(4FC)]	**430(1900), 680(2000)**	**This work**
Fe(III)-MndD-DOPA	675(750)	**281**
DTBC	290(2500)	282
DTBC +OH^-	275(5000), 320(4900)	282
4XC	280(~2100)	This work
$[Mn(CO)_3(THF)DTBC]$	436(6250), 546(8300)	283
$[Mn(CO)_2(P(OEt)_3)_2DTBC]^+$	416(5500), 514(4200)	283
$[Co(III)(CTH)DTBC]^+$	272, 306, 378, 413, 518, 781	271
$[Co(III)(CTH)TCC]^+$	309, 318, 382, 532, 676	271
[Co(III)(trien)cat]I	296(5500), 348(260), 564(175)	269
$[Co(III)(en)_2PCA]I\ H_2O$	318(9590), 412, 544(188)	269
$[Co(III)(CTH)DTBC]^+$	305(10500), 413(460), 518(200), 781(240)	284
$[Co(III)(CTH)TCC]^+$	318(8500), 382(460), 532(200), 675(245)	284
$[Ru(II)(py)_4TCC]$	350(8700), 388(15500), 446(20900)	285
$[Ru(II)(py)_4DTBC]$	344(7950), 410(12300), 484(13500), 580(4675)	285
$[Ru(III)(bpy)(catechol)_2]^-$	400, 680, 780	286
[Cu(II)(DBED)DTBC]	300(7900), 520(600)	287
[Cu(II)(TMCD)DTBC]	260(12000), 300(11600), 450(300)	287
4FSQ	307(~2300), 380(~800), 875(~350)	This work
HPCA-SQ	375, 645	161
$DTBSQ^-$	320(7800), 350(2800), 375(2900), 650(800), 750(400)	282
$[Mn(CO)_2(POEt_3)_2DTBSQ]^+$	330(5800), 820(3700)	283
$[Mn(CO)_3(THF)DTBSQ]$	310(9830), 524(2370) 708(1650)	283, 288
$[Cu(II)(DBED)DTBSQ]^+$	290(8000), 350(2500), 600(3200), 870(1800)	287, 289
$[Cu(II)(TMCD)DTBSQ]^+$	300(14000), 380(2900), 450(650), 800(500)	**287**
$[Co(II)(Me_3TPA)TCSQ]PF_6$	418(1300), 578–641(1000)	**290**
$[Co(II)(Me_3TPA)DTBSQ]^+$	665-525(1000), 800(1000)	**252**

Complex[a]	λ_{max} (nm) (ε, $M^{-1}cm^{-1}$)	References
$[Co(II)(Me_4cyclam)PhenSQ]PF_6$	580–660(400–500)	291
$[Co(II)Me_4cyclam)DTBSQ]PF_6$	590–690(400–500)	291
$[Zn(CTH)PhenSQ]^+$	405(3300), 476(1400), 505(1200), 613(110)	292
$[Zn(SS\text{-}CTH)TCSQ]^+$	340(6700), 412(1800), 870(370)	292
$[Zn(SS\text{-}CTH)DTBSQ]^+$	375(1480), 770(400)	292
$[Co(III)(CTH)DTBSQ]^{2+}$	385(1500), 552(1000), 833(170)	271
$[Co(III)(CTH)TCSQ]^{2+}$	394, 418(1700), 441(2500), 606(2000), 1042(180)	271
$[Co(III)(CN)_4(DTBSQ)]^{2-}$	240(2000+), 325(2000+), 536(~2000), 742(~200), 874(~200)	**251**
$[Co(III)(trien)DTBSQ]Cl_2$	300(6680), 360(1145), 512(1270)	280
[Co(III)(salen)DTBSQ]	352, 416, 494	**270**
$[Ni(CTH)DTBSQ]^+$	772(450), 472(1,300), 308(10,500)	293
$[Co(II)(Me_4cyclam)PhenSQ]PF_6$	580–660(400–500)	291
$[Rh(CTH)DTBSQ]^{2+}$	300(6800), 450(3300), 877(170)	**294**
$[Rh(CTH)TCSQ]^{2+}$	325(5800), 523(2800), 1000(440)	**294**
$[Ru(II)(py)_4TCSQ]^+$	327(17000), 976(10700)	285
$[Ru(II)(py)_4DTBSQ]^+$	320(7760), 374(14100), 926(11500), 1149(740)	285
$[Ru(II)(bpy)(SQ)_2]$	340, 475(3600), 590(11100), 955(14400), 1235(4400)	286
$[Ru(II)(bpy)(DTBSQ)_2]$	375(5700), 505(3100), 605(11600), 955(12100), 1175(6050)	286
$[Ru(II)(bpy)(TCSQ)_2]$	420(4140), 450, 585(10040), 1005(16100), 1315(4290)	286
4FQ	408(~3500)	295, 296
4ClQ	380(~3500))	295, 296
4BrQ	404(~3500)	295, 296
HPCA-Q	310, 395	149
HPCA-SQ in EtOH	375, 645	161
DTBQ	275(3000), 400(1800)	270
$[Mn(CO)_2(POEt_3)_2DTBQ]^+$	392(2900), 582(7400)	283
$[Ru(II)(py)_4TCQ]^{2+}$	404(3300), 623(11500)	285
$[Ru(II)(py)_4DTBQ]^{2+}$	360(4570), 380(3090), 673(10500)	285

[a]Abbreviations used: 4ClC, 4-chlorocatechol; 4FC, 4-flurocatechol; HPCD, homoprotocatechuate 2,3-dioxygenase from *Brevibacterium fuscum*; Fe-MndD, Iron-substituted homoprotocatechuate 2,3-dioxygenase from *Arthrobacter globiformis*; HPCA, homoprotocatechuate; DOPA, L-3,4-dihydroxyphenylalanine; THF, tetrahydrofuran; DTBC, 3,5-di-tert-butylcatechol; DTBSQ, 3,5-di-tert-butylsemiquinone; DTBQ, 3,5-di-tert-butylquinone; SQ, semiquinone; Q, quinone; TCC, tetrachlorocatechol; TCSQ, tetrachlorosemiquinone; TCQ, tetrachloroquinone; CTH, tetraazamacrocycle; SS-CTH, (SS)-5,5,7,12,12,14-hexamethyl-1,4,8,11-tetraazacyclotetradecane; py, pyridine; bpy, bipyridine; en, ethylene *diamine*; 4FSQ, 4-fluorosemiquinone; DBED, N^1,N^2-di-tert-butylethane-1,2-diamine; TMCD, N^1,N^1,N^2,N^2-tetramethylcyclohexane-1,2-diamine; Me_3TPA, *tris*(6-methyl- 2-pyridylmethyl)amine; trien, triethylenetetramine; salen, 2,2'-Ethylenebis(nitrilomethylidene)diphenol; cat, catechol; 4NSQ, 4-nitrosemiquinone; phenSQ, 9,10-phenanthrenesemiquinone; 4XC, 4-halocatechol.

All the S = 1/2 intermediates observed in these studies with wild-type and H200N-Co-HPCD appear to be colorless, in contrast to all other characterized semiquinone model complexes in the literature, which normally display several chromophores (Table 4.6). Free (unbound) semiquinones display intense chromophores in the near UV between 270 and 300 nm (~10,000 $M^{-1}cm^{-1}$) attributed to the SOMO π* to π* transition (SOMO = singly occupied molecular orbital) and weaker transitions between 350 and 400 nm (~3,000 $M^{-1}cm^{-1}$) assigned to the π to SOMO-π* transitions and a broad weak band between and 700 and 1,000 nm (<1,000 $M^{-1}cm^{-1}$) attributed to a nonbonding to π* transition.[292] Bound semiquinone complexes often display additional metal-to-ligand transitions between 400 and 700 nm (~3,000–12,000 $M^{-1}cm^{-1}$) assigned to a metal-to-ligand charge transfer (Mdπ to $SQ^{\bullet}$ SOMO-π*).[292] The large ^{19}F splitting observed for Co^{4FC}Int1 led us to suggest localization of the semiquinone radical onto C4 of the semiquinone ring.[266] sp^3 hybridization of C4 of a localized radical would disrupt the conjugated π system and lead to the loss of the typical semiquinone chromophore,[253] this would account for fact that the Co^{4XC}Int1 intermediates are colorless.

4.2.3.F Characterization of the chromophoric intermediate Co^{4XC}Int2. For comparison to the chromophore of Co^{4FC}Int2, $4FSQ^{\bullet}$ and 4FQ were prepared. 4FQ was prepared by chemical oxidizing 4FC using $NaIO_4$ in CH_2Cl_2. The UV-Vis spectrum of 4FQ (Figure 4.30) has an intense absorption band at 400 nm (ε = 3,400 M^{-1} cm^{-1}) similar to the chromophore observed for Co^{4FC}Int2 (ε_{467} ~ 11,000). The cyclic voltammogram of 4FQ shows a reversible reduction to $4FSQ^{\bullet}$ at -854 mV vs Fc^{+}/Fc (Figure 4.31).[282] Bulk electrolysis of 4FQ at -1035 mV produced $4FSQ^{\bullet}$, which has absorption bands at 307,

380, and 875 nm (Figure 4.30, ε_{307} ~2,300 M^{-1} cm^{-1}, ε_{380} ~800 M^{-1} cm^{-1}, and ε_{875} ~350 M^{-1} cm^{-1}).

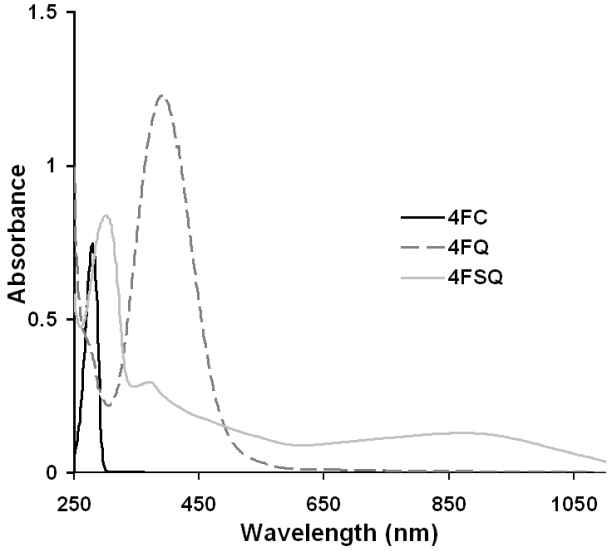

Figure 4.30. UV-Vis spectra of 4FC (black line, $\varepsilon_{280\ nm}$ = 2,100 M^{-1} cm^{-1}), 4FQ (dashed gray line, $\varepsilon_{400\ nm}$ = 3,400 M^{-1} cm^{-1}), prepared by oxidizing 4FC with sodium periodate, $4FSQ^{\bullet}$ (solid gray line, ε_{307} ~2,300 M^{-1} cm^{-1}, ε_{380} ~800 M^{-1} cm^{-1}, and ε_{875} ~350 M^{-1} cm^{-1}) prepared by bulk electrolysis by reducing 4FQ at -1035 mV (vs Fc^{+}/Fc).[296]

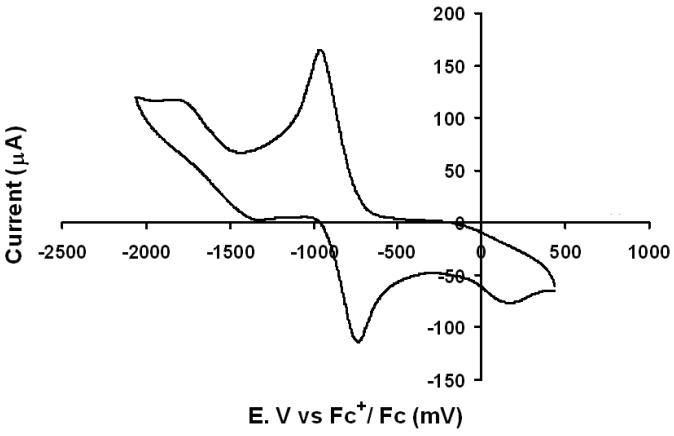

Figure 4.31. Cyclic voltammogram of anaerobic 2 mM 4FQ in CH_3CN with 0.1 M KPF_6 as supporting electrolyte.

Co^{4XC}Int2 species exhibit intense chromophores (ε ~ 9,000 M^{-1} cm^{-1}, Figure 4.32) at 453, 456, and 467 nm with 4BrC, 4ClC, and 4FC as substrates, respectively. The UV-Vis spectra of Co^{4XC}Int2 are similar to those of the independently synthesized 4XQ's prepared by oxidation with mushroom tyrosinase in 50 mM MOPS (pH 7.5) with λ_{max} values of 404, 380 and 408 nm (ε ~ 3,500 M^{-1} cm^{-1}) for 4BrQ, 4ClQ and 4FQ respectively, or by oxidizing the halogenated catechols using $NaIO_4$ in CH_2Cl_2 (Figure 4.30, 4FQ $\varepsilon_{400\ nm}$ = 3,400 M^{-1} cm^{-1}).[295, 296]

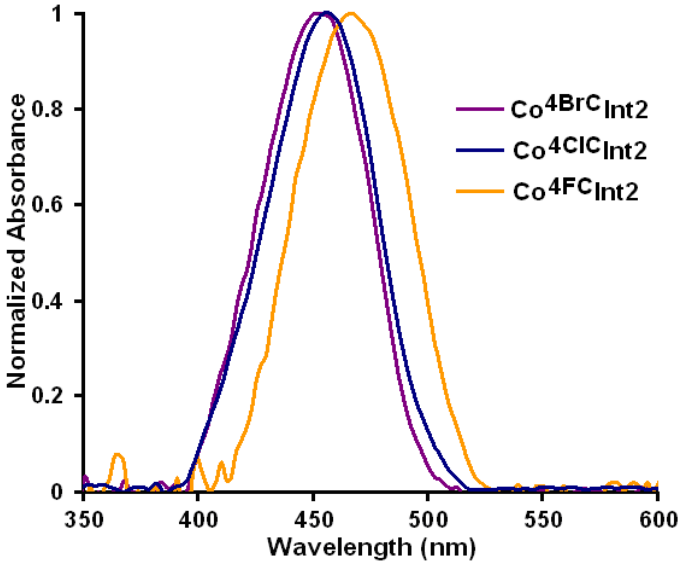

Figure 4.32. Normalized difference spectra of chromophoric intermediates at maximum yields minus spectra of the extradiol ring-cleaved products. Spectra are normalized to the λ_{max} of chromophore at 453 nm [Co-HPCD(4BrC)O_2] (purple), 456 nm [Co-HPCD(4ClC)O_2] (blue), 467 nm and [Co-HPCD(4FC)O_2] (orange).

4.2.3 G Nature of Co^{4XC}Int2. The S = 3/2 Co^{4XC}Int2 species have ^{59}Co A-values (75 G) similar to the high-spin Co(II) center in Co-HPCD (80 G) and to the [Co-HPCD(4XC) enzyme-substrate complexes (87–90 G, Table 4.3 and 4.5), suggesting that Co^{4XC}Int2

species are also high-spin Co(II) species. The EPR and UV-Vis data together suggest that the Co^{4XC}Int2 is a [high-spin Co(II)(4XQ)(hydro)peroxo] species.

4.3 Discussion

4.3.A Mechanism of O_2 activation and catechol oxidation proposed for Fe-HPCD.

Several different mechanisms of catechol oxidation and O_2 reduction can be envisioned. These mechanisms differ by the extent and of electron transfer between the two substrates to form a reactive pair that goes on to react to form the C-O bond of the proposed bridging alkylperoxo species. Based on these new spectroscopic and kinetic studies we have proposed an alternative catechol oxidation mechanism for turnover of 4XCs by Co-HPCD. In the reaction of [Fe-HPCD(HPCA)] with O_2 (Scheme 4.5), catechol oxidation and O_2 reduction are thought to occur by proton-coupled electron transfer (PCET) from the catechol substrate to O_2 via the metal center, with proton transfer to His200 to form a [Fe(II)($SQ^{\bullet}$)$O_2^{\bullet-}$] diradical pair.[149] Recombination of the radicals would then result in the spin-allowed formation of the bridging alkylperoxo intermediate. Protonation of the bridging peroxo by His200 would facilitate O-O bond cleavage leading to the formation of the the ring-cleaved product.[131, 155, 165, 181, 192] In an alternative mechanism, O_2 reduction and catechol oxidation could occur via a stepwise mechanism with transient formation of an [M(III)(catecholate)$O_2^{\bullet-}$] species. No Fe(III) species has been detected in the single turnover reaction of [wt-Fe-HPCD(HPCA)] with O_2, which suggests extremely facile electron transfer between the catechol substrate and O_2 to rapidly form a the [Fe(II)($SQ^{\bullet}$)$O_2^{\bullet-}$] diradical pair.[149]

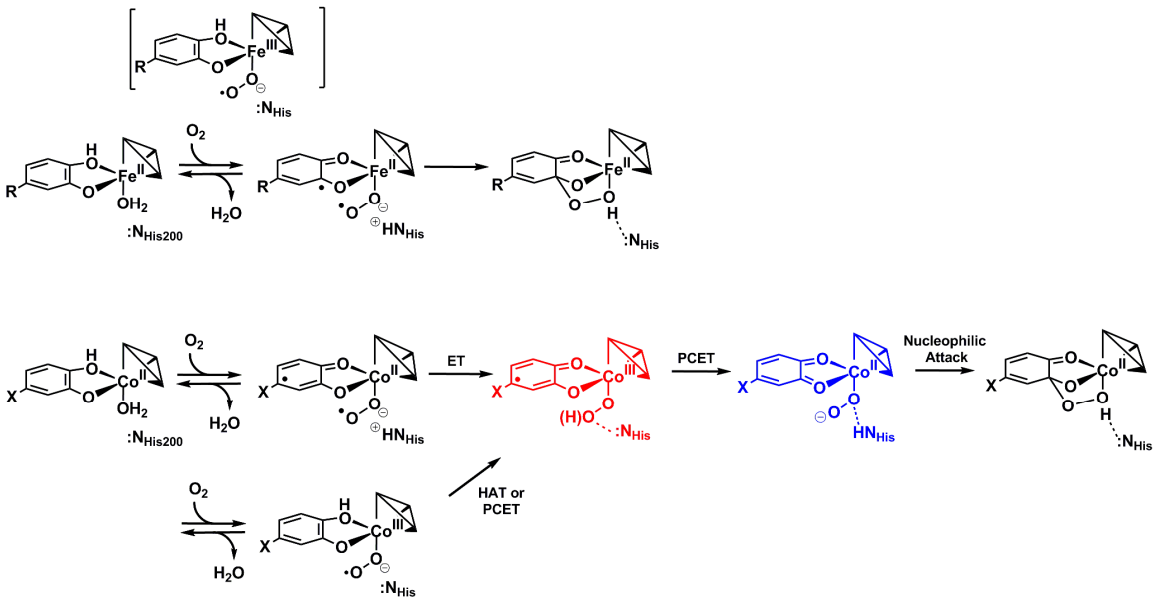

Scheme 4.5. Proposed mechanisms for formation of the bridging alkylperoxo species with Fe-HPCD (R = acetate) and Co-HPCD with 4XCs.

4.3.B Characterization of Co^{4XC}Int1 and Int2. In the current studies with Co-HPCD and the 4XC substrates, two intermediates were detected in the single turnover reaction between the enzyme-substrate complexes and O_2. The formation of the first intermediate, Co^{4XC}Int1, was found to be reversibly connected to O_2 binding. These species did not display any visible chromophore in UV-Vis stopped-flow experiments but did exhibit S = 1/2 EPR signals consistent with organic radicals based on EPR power-temperature saturation experiments. Additionally, the S = 1/2 signal with 4FC also showed splitting that was attributed to coupling of the radical to the ^{19}F nucleus. The magnitude of the ^{19}F hyperfine splitting suggested a uniquely localized semiquinone radical, where the radical is localized on the C4 by the electron withdrawing halogen substituent. Localization of the semiquinone radical would disrupt the conjugated π system and lead to the loss of the visible chromophore normally observed for delocalized semiquinone radicals.[253] Based on the UV-Vis and EPR data Co^{4XC}Int1 is assigned to a low-spin

[Co(III)(4XSQ$^{\bullet}$)(hydro)peroxo] species where the semiquinone radical is localized onto C4 of the ring.

Formation of a second intermediate, Co^{4XC}Int2, which has an intense chromophore characteristic of a halogenated quinone (4XQ) species, was observed in UV-Vis stopped-flow experiments. In EPR experiments Co^{4FC}Int2 was observed to form upon decay of Co^{4FC}Int1. Co^{4XC}Int2 displays an $S = 3/2$ EPR signal with ^{59}Co hyperfine splitting characteristic of a high-spin Co(II) center leading to the assignment of Co^{4XC}Int2 as a high-spin [Co(II)(4XQ)(hydro)peroxo] species.

4.3.C Mechanism of formation and decay of Co^{4XC}Int1 and Int2. The initial [Co(III)(4XSQ$^{\bullet}$)(hydro)peroxo] intermediate could form from a SQ$^{\bullet}$-Co(II)-$O_2^{\bullet-}$ diradical pair by electron transfer from the Co(II) center to O_2 (Scheme 4.5). Localization of the semiquinone radical on C4 of the SQ$^{\bullet}$-Co(II)-$O_2^{\bullet-}$ species could interfere with attack of the superoxide radical on the semiquinone ring resulting instead in the one-electron reduction of the superoxide species followed by oxidation of the semiquinone to form the observed [Co(III)(4XSQ$^{\bullet}$)(hydro)peroxo] and [Co(II)(4XQ)(hydro)peroxo] intermediates, respectively.

In an alternative mechanism the [Co(III)(4XSQ$^{\bullet}$)(hydro)peroxo] species could form directly from an initial low-spin [Co(III)(catecholate)$O_2^{\bullet-}$] O_2 adduct. Oxidation of the catechol substrate by either a proton-coupled electron transfer (PCET) or by hydrogen atom transfer (HAT) from the catechol substrate to the superoxide would result in the observed [Co(III)(SQ$^{\bullet}$)(hydro)peroxo] intermediate.[149] Further oxidation of the semiquinone by the M(III) center and deprotonation of the hydroperoxo by His200 by a

PCET mechanism would yield a [Co(II)(Q)peroxo] species. Nucleophilic attack of the peroxo on the quinone would then form the C-O bond of the proposed alkylperoxo intermediate.[150, 161, 163]

4.3.D Characterization of Co^{HPCA}Int1 and Int2. The first observable species in the reaction of [Co-HPCD(HPCA)] with O_2 (Co^{HPCA}Int1) in rapid freeze-quench EPR experiments formed with a yield of ~15% at 50 ms. Co^{HPCA}Int1 is an S = 1/2 organic radical species that resembles Co^{4ClC}Int1 suggesting that it too is a low-spin [Co(III)(HPCA-$SQ^{\bullet}$)(hydro)peroxo] species. Neither Co^{HPCA}Int1 or Co^{4ClC}Int1 S = 1/2 EPR signals exhibit any ^{59}Co hyperfine typical of low-spin Co(III)-$SQ^{\bullet}$ (with delocalized semiquinone radicals) or Co(III)-$O_2^{\bullet-}$ model complexes.[226, 227, 257] Both Co^{HPCA}Int1 and Co^{4ClC}Int1 exhibit no visible chromophore either expected for delocalized semiquinone species in UV-Vis stopped-flow experiments. The EPR and UV-Vis data may suggest uniquely localized organic radical species, where the radical may be localized to C2 of the semiquinone ring for Co^{HPCA}Int1 and C4 of the ring for Co^{4XC}Int1. The analogous intermediate [Fe(III)(HPCA-$SQ^{\bullet}$)(hydro)peroxo] observed with H200N-Fe-HPCD does exhibited chromophores at 395 (ε = 3,200 M^{-1} cm^{-1}) and 610 nm (ε = 1,100 M^{-1} cm^{-1}), similar to the independently synthesized HPCA-$SQ^{\bullet}$.[149, 161] The presence of a chromophore in the H200N-$SQ^{\bullet}$ complex suggests that the radical is delocalized over the ring and that H200 may play a similar role as Y257, interacting with the substrate to localize the $SQ^{\bullet}$ radical.[161, 163] In the reaction of [wt-Fe-HPCD(HPCA)] with O_2 no Fe(III) intermediates have been observed,[149] however a Mn-(III) species was observed to accumulate to a 5% yield at 10 ms (at 4 °C) with wt-Mn-HPCD, which was assigned to either a high-spin [Mn(III)(catecholate)$O_2^{\bullet-}$] or [Mn(III)($SQ^{\bullet}$)(hydro)peroxo] species.[179]

The EPR spectrum of the second intermediate observed in the reaction of [Co-HPCD(HPCA)] with O_2 (Co^{HPCA}Int2) is nearly identical to the spectrum of Co^{4ClC}Int2 and suggests that the intermediate contains a high-spin Co(II) metal center. Co^{4ClC}Int2 exhibits an intense chromophore characteristic of a quinone species, while Co^{HPCA}Int2 exhibits only a very weak chromophore at 550 nm. The [Fe(II)(Q)(hydro)peroxo] intermediate observed in the reaction of [Y257F-Fe-HPCD(HPCA)] with O_2 exhibited an intense chromophore at 425 nm (ε = 10,500 M^{-1} cm^{-1}), similar to the independently synthesized HPCA-Q.[149, 161] The optical data suggests that unlike Co^{4XC}Int2, Co^{HPCA}Int2 is not a quinone but is best assigned to the alkylperoxo species. The observation of an alkylperoxo species along with the steady-state and transient kinetic data reported for this reaction suggest that O-O bond cleavage of the alkylperoxo species is rate determining in the turnover of HPCA by Co-HPCD. Characterization of Co^{HPCA}Int1 and Int2 suggest oxidation of the catechol by Co-HPCD may proceed via a [Co(III)($SQ^{\bullet}$)(hydro)peroxo] intermediate as was also observed in the turnover of HPCA by H200N-Fe-HPCD.[149] Attack of the peroxo on the semiquinone with reduction of the metal center by the radical could form the C-O bond of the bridging alkylperoxo species, though DFT studies concluded that this species is off pathway,[150] the [Co(III)($SQ^{\bullet}$)(hydro)peroxo] species may then convert to the [Co(II)($SQ^{\bullet}$)$O_2^{\bullet-}$] reactive diradical pair as was proposed with H200N-Fe-HPCD.[149]

4.3.E Characterization of *S* = 1/2 species observed with H200N-Co-HPCD. H200N-Co-HPCD does not appear to turn over any of the catechol substrates but will still bind both catechol substrates (HPCA and the 4XCs) and O_2 to form an *S* = 1/2 species by EPR. These *S* = 1/2 species exhibits a set of ^{59}Co hyperfine splitting at 80 K similar to

low-spin Co(III)-SQ$^{\bullet}$ model complexes in the literature,[257] but different from the S = 1/2 signals observed for Co(III)-$O_2^{\bullet-}$ complexes.[226, 227] We concluded that these S = 1/2 species are also [Co(III)(SQ$^{\bullet}$)hydroperoxos] but with delocalized semiquinone radicals. The inactivity of H200N-Co-HPCD is consistent with the roles previously suggested for His200 to orienting the superoxide for attack on the substrate as was suggested in experiments with 4NC complexes with both Fe and Co H200N mutants.[149, 162, 169] Here we propose that His200 may also play a similar role as Y257 by interacting with the substrate to localize the SQ radical.[161, 163] It should also be pointed out that His200 is not required to oxidize the substrate to form these [Co(III)(SQ$^{\bullet}$)hydroperoxo] species, although when [H200N-Co-HPCD(4NC)] enzyme-substrate complex reacts with O_2 the reaction did not proceed past the [Co(III)(catecholate)$O_2^{\bullet-}$] species with the dianionically binding electron poor substrate 4NC.[130]

4.3.F Steady-state and transient kinetics for the turnover of 4XCs. In transient kinetic experiments we directly obtained rate constants for O_2 binding and dissociation to form the Co^{4XC}Int1 as well as the next two steps including oxidation of the SQ$^{\bullet}$-(hydro)peroxo to the Q-(hydro)peroxo (Co^{4XC}Int1) followed by nucleophilic attack of the peroxo on the quinone in the rate determining step. We observed a strong trend in the rate of O_2 binding where k_1 decreased from 4BrC (48 ± 2 mM^{-1} sec^{-1}) to 4FC (4.4 ± 0.2 mM^{-1} sec^{-1}). This is consistent with the trend observed in the k_{cat}/K_M^{O2} values, or the catalytic efficiency for O_2, where the rate with 4BrC (180 ± 40 mM^{-1} min^{-1}) was faster than 4FC (33 ± 5 mM^{-1} min^{-1}). These trends suggests that either electron transfer from the catechol to O_2 upon O_2 binding is faster for 4BrC or that the more basic 4BrC lowers the redox potential of the cobalt center more than the less basic and more electron-

poor substrate 4FC. The O_2 dissociation rate constant followed the same trend where k_{-1} decreased from 4BrC (37 ± 1 sec^{-1}) to 4FC (1.5 ± 0.2 sec^{-1}), suggesting that Co^{4BrC}Int1 is less stable than Co^{4FC}Int1. The rate of semiquinone oxidation (k_2) of Co^{4XC}Int1 to form the quinone, Co^{4XC}Int2 was also faster for 4BrC (8.2 sec^{-1}) than 4FC (1.4 ± 0.1 sec^{-1}), this is consistent with $4BrSQ^{\bullet}$ being easier to oxidize than $4FSQ^{\bullet}$. The rate of decay of Co^{4XC}Int2 (k_3) was found to correspond well the steady-state rate of product formation (k_{cat}) under the same conditions, suggesting that nucleophilic attack of the peroxo species on the quinone is the rate determining step in the extradiol ring-cleavage of the 4XCs by Co-HPCD. Again the reaction proceeded faster with 4BrC (0.64 ± 0.01 sec^{-1}) than 4FC (0.12 ± 0.01 sec^{-1}), though one may expect that the 4FQ would be more electrophilic than 4BrQ.

4.3.G Spin-state transition for O_2 binding and catechol oxidation. The high Co(III/II) standard redox potential and preferred low-spin state of Co(III) should be considered in the mechanism of O_2 binding and substrate oxidation with Co-HPCD, while a concerted electron transfer mechanism between the catechol and O_2 via the metal center would not require a formal change in the redox potential of the metal.[7, 131] Electron-poor substrates like the 4XCs may slow down the catechol oxidation step leading to the initial formation of a low-spin [Co(III)(catecholate)$O_2^{\bullet-}$] species.[130] However, here we observe a low-spin Co(III) species even with the electron-rich native substrate HPCA. Formation of either a low-spin [Co(III)(catecholate)$O_2^{\bullet-}$] or a low-spin [Co(III)($SQ^{\bullet}$)(hydro)peroxo] species upon reductive O_2 activation will be accompanied by a spin-state change from high-spin Co(II) in the enzyme-substrate complex to the low-spin species. The spin transition should add an additional barrier to the formation of these

species from the required reorganization energy of the ligands due to the change in the ionic radius of the metal with the spin-transition. Oxidation of the catechol substrate by electron transfer to the low-spin Co(III)-$O_2^{\bullet-}$ center to form a high-spin [Co(II)($SQ^{\bullet}$)$O_2^{\bullet-}$] diradical pair should be accompanied by a spin-transition and as well. The observed low-spin [Co(III)($SQ^{\bullet}$)(hydro)peroxo] intermediate ultimately forms with one-electron oxidation of the both the catechol and metal center with proton transfer to either His200 or to the peroxo moiety. We propose that the [Co(III)($SQ^{\bullet}$)(hydro)peroxo] species forms from the initial low-spin [Co(III)(catecholate)$O_2^{\bullet-}$] followed by either oxidation of the substrate by either a PCET transfer mechanism, with electron transfer from the catechol to the superoxide or by a HAT transfer mechanism, where the superoxide adduct oxidizes the substrate directly. The resulting [Co(III)($SQ^{\bullet}$)(hydro)peroxo] species would still be low-spin, but instead of a π-acidic O_2 or $O_2^{\bullet-}$ ligand it would have a π-basic (hydro)peroxo ligand which could lower the Co-ligand field and spin-transition barrier.

It is possible to estimate the size of the different barriers along the reaction coordinate by applying the Arrhenius equation (Equation 4.2)[264] to the rate constants obtained from transient stopped flow experiments performed at 4 and 22 °C (Figure 4.9). A large but reversible barrier was calculated for the formation of Co^{4ClC}Int1 upon O_2 binding to the enzyme-substrate complex, where 72 kJ/mol and 103 kJ/mol are the barriers associateted with O_2 binding and dissociation, respectively (Figure 4.10). The barrier calculated for the next step involving oxidation of the semiquinone to form the quinone species (Co^{4ClC}Int2) is half as high (31 kJ/mol) as the barrier associated with O_2 binding. All three of these barriers should be associated with spin-transitions. The large barrier for O_2 binding to form the low-spin Co(III)-$SQ^{\bullet}$ species (Co^{4ClC}Int1) followed by

a smaller barrier for oxidation of the semiquinone by the Co(III) center to form the high-spin Co(II)-Q intermediate (Co^{4ClC}Int2) supports a self-compensating-rates mechanism; whereas Co(II) would be expected to be a poor reducing agent in reductive O_2 binding, the generated Co(III) species should be a strong oxidant in the subsequent substrate oxidation step.[169, 179]

4.3.H Additional insights in to the mechanism of catechol oxidation. The different pH activity profiles (Figure 4.6) of the substituted catechols (HPCA, 4ClC and 4NC) may give more detail into the mechanism of oxidation of these three catechol substrates (Scheme 4.6). Electron-poor 4NC binds dianionically to the metal center and thus has no proton available for either a PCET or HAT mechanism for catechol oxidation; instead 4NC oxidation proceeds by slow electron transfer.[130] O_2 binding to [Co-HPCD(4NC)] was found to be rate limiting until very high O_2 concentrations (~15 atm O_2 at 22 °C), where the subsequent catechol oxidation step is then rate determining. On the other hand, O_2 binding to [Co-HPCD(4NC)] proceeds faster under acidic conditions due to protonation of the His200, which helps to stabilize the anionic superoxide adduct. Indeed pH titrations of [Co-HPCD(4NC)] and [H200N-Co-HPCD(4NC)] suggest that His200 is protonated at low pHs (pK_a = 6.6), leading to an increase in the rate of 4NC oxidation under acidic conditions.[130]

The less electron-poor 4ClC is expected to slow down catechol oxidation compared to HPCA but is predicted to bind monoanionically to the metal centers like HPCA at neutral pHs, allowing for either a PCET or HAT mechanism for catechol oxidation/activation. The bell-shaped pH activity profile of $4ClC$[262] suggested that at low pH when both H200 and the 4ClC catechol are protonated so no base is available to

handle the proton upon catechol oxidation. Under neutral conditions His200 is deprotonated and can act as a Lewis acid-base catalyst, while under basic conditions both His200 and 4ClC are deprotonated and the superoxide adduct is destabilized. For HPCA the curve is shifted to higher pH due its higher pK_a.

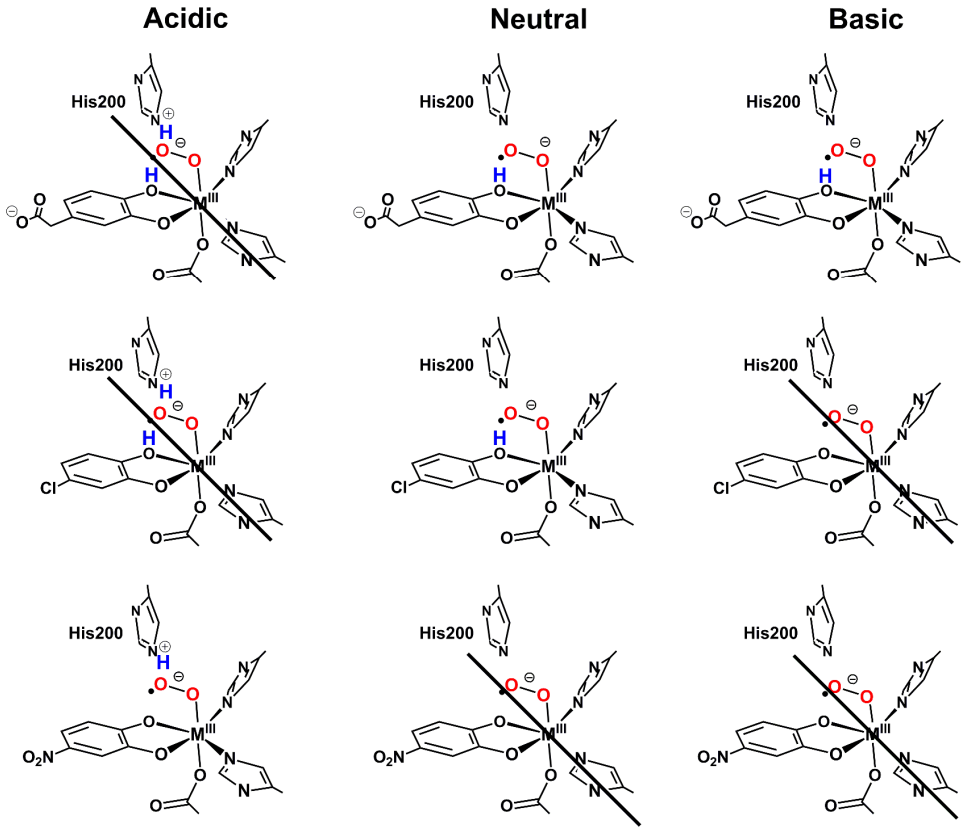

Scheme 4.6. Possible effects of pH on protonation state of catechol and His200 to explain differences in pH activity profiles of HPCA, 4ClC and 4NC.

Significant solvent kinetic isotope effects between 2.0 and 2.8 were observed on the steady state rate constant (k_{cat}) and all the individual rate constants (k_1, k_{-1}, k_2 and k_3) upon reacting the enzyme-substrate complex with O_2, as measured by transient kinetics for the turnover of 4ClC by Co-HPCD. The observed KIEs suggest that a solvent

exchangeable proton, most likely associated with 4ClC, H200 or the O_2 adduct, is transferred in each of the observed reaction steps including the rate determining step of the reaction. The observed KIEs are consistent with PCET mechanisms for catechol oxidation according to Scheme 4.5, with proton transfer from the catechol substrate to the peroxo adduct upon oxidation of the catechol to form a [Co(III)(4SQ)hydroperoxo] species (Co^{4ClC}Int1) followed by proton transfer from the hydroperoxo to H200 upon oxidation of the Co^{4ClC}Int1 to form the [Co(II)(4ClQ)peroxo] species (Co^{4ClC}Int2). The rate determining step or attack of the peroxo on the quinone could be associated with proton transfer to the proximal oxygen of the bridging peroxo to facilitate O-O bond cleavage. The observed KIE for k_1 may even suggest a HAT transfer mechanism for the formation of the [Co(III)4ClSQ)hydroperoxo] species (Co^{4XC}Int1), where Co^{4XC}Int1 may be formed by hydrogen atom abstraction from the catechol by the initial superoxide species. However, the observed KIE of 2.0 ± 0.2 is somewhat lower than the KIEs of 10.6–15 reported for PCET from phenol to a peroxyl radical and the KIE of 27.1 reported for HAT from toluene to a peroxyl radical.[297-299]

4.4 Experimental procedures

4.4.1 Reagents and general procedures. Reagents and buffers were purchased from Sigma except where otherwise noted. 4-halocatechols were purchased from TCI America and were further purified by sublimation. All reagent solutions and media were prepared using water treated with a Millipore MilliQ water system to minimize trace metal-ion contamination.

Deuterated 4FC (d_3-4FC) was prepared as reported by Heistand *et. al.* by heating an anaerobic solution of 4FC (780 mg) in D_2O (25 mL) with potassium tertbutoxide

(900 mg, ~1.3 equivalents) at 150 °C for 12 hrs in a Schlenk flask.[300] After cooling the solution was neutralized using DCl in an anaerobic glove box. The product was extracted into ethyl acetate (5 x 50 mL). The solvent was removed under vacuum and the product sublimed to give ~500 mg of deuterated 4FC as a white powder. Deuteration was confirmed by ^{1}H, ^{19}F, and ^{2}H NMR as well as by GC-MS on the esterified product according to the procedure reported by Oldenberg, *et. al.*[301]

4.4.2 Preparation of M(II)-HPCD. Metal-substituted HPCDs were prepared by growing *E. coli* BL21(DE3) carrying plasmid pWZW204 containing the HPCD gene from *Brevibacterium fuscum* as previously described.[2,4,8,17] Upon inducing protein expression with isopropyl-β-D-thiogalactopyranoside (IPTG), the cultures were supplemented with 30 mg/L of an appropriate $M(II)Cl_2$ salt. The cells were then harvested and protein purified as previously described.[18]

4.4.3 ICP-AES metal analysis. Metal incorporation was measured by ICP-AES metal analysis at the Soil Research Analytical Laboratory (College of Food, Agricultural and Natural Resource Sciences, University of Minnesota). Samples were prepared for ICP-AES analysis by digesting 2 ppm protein in 5% HNO_3 overnight and then removing precipitated protein by centrifugation.

4.4.4 Steady-state kinetics. Enzyme activity was measured in oxygenated 50 mM MOPS buffer (pH 7.5) at 4 °C and 22 °C using a Beckman DU 640 spectrophotometer. Reactions were followed by monitoring the formation of the yellow extradiol cleavage product. Extinction coefficients of the extradiol ring-cleaved products of the halogenated catechols (Table 4.7) were measured by reacting 10 μM solutions of the catechol with 1 μM Co-HPCD in 50 mM MOPS (pH 7.5) and then calculating the extinction

coefficients from the absorption spectrum after all the catechol had been consumed. The extinction coefficient of the 4ClC ring-cleaved product at the pH independent isosbestic point ($\varepsilon_{356\ nm}$ = 16,000 M^{-1} cm^{-1}) was measured by first reacting a 100 μM solution of 4ClC with 10 μM Co-HPCD in 5 mM MOPS (pH 7.5) and then transferring 100 μL of the product to 1000 μL of buffer solutions containing 25 mM of each of the following buffers: MES, BisTris, MOPS, Tris, CHES, and CAPS at pH values ranging from 5.5 to 8.5. Comparison of the absorption spectra at the different pHs revealed the pH independent isosbestic point, at which point the extinction coefficient of the extradiol ring-cleaved product was calculated.

Table 4.7. λ_{max} and extinction coefficients of extradiol ring-cleavage products of 4XC at pH 7.5.

	λ_{max}	ε (M^{-1} cm^{-1})
4BrC	379	44,800
4ClC	380	44,300
4FC	385	43,300

Catechol concentrations ranging from 1 μM to 2 mM were used to determine the $K_M^{catechol}$ with Co-HPCD concentration of 450 nM. All other steady-state assays used 3 mM 4XC to ensure pseudo first-order conditions in catechol. Mn and Co-substituted HPCDs were treated with 1 mM H_2O_2 during purification to inactivate any Fe-HPCD present in the preparation. Fe-HPCD was incubated with 1 mM ascorbate to fully reduce the enzyme prior to each assay.[131, 169] Prior to experiments with halogenated catechols, enzyme activities was first checked by assaying activity under previously reported conditions with HPCA (22 °C, 50 mM MOPS, pH 7.8).[131, 169] K_M^{O2} values were determined by performing the reaction under different O_2 concentrations by mixing

known volumes of anaerobic, air-saturated, and O_2 saturated buffer (1 atm) and at higher O_2 concentrations by equilibrating the buffer and enzyme under 2 or 3 atm of O_2 in a sealed cuvette and then inducing the reaction by the addition of the catechol substrate. A Clark-type oxygen electrode (Oxytherm from Hansatech Instruments) was also used to measure the rate of O_2 consumption in air-saturated buffer at 4 and 22 °C. Steady-state rates measured using oxygen electrode agreed well with rates measured by following formation of the yellow extradiol ring-cleaved product by UV-Vis. The apparent kinetic parameters k_{cat} and K_M were determined using nonlinear regression fits of initial velocities to the Michaelis-Menten equation from initial velocities. k_{cat} values were calculated by dividing the maximum velocity from nonlinear regression by the average metal concentration from ICP-AES metal analysis.

4.4.5 Stopped-flow experiments. Anaerobic [Co-HPCD(4XC)] was rapidly mixed with oxygenated 100 mM MOPS buffer pH/pD 7.5 using an Applied Photophysics model SX.18MV stopped-flow device at 4 and 22 °C. The concentrations of reagents after mixing were 130 μM 4XC and 220 μM Co-HPCD unless otherwise stated. The formation of the extradiol cleavage product was monitored at 380 nm using a 2 mm path length while formation and decay of the chromophoric intermediate was monitored at 475 nm, where the yellow ring-cleaved product does not absorb, using a 1 cm path length. O_2 concentrations after mixing ranged from 157 to 1,000 μM O_2 at 4 °C and 110 to 685 μM O_2 at 22 °C.[166]

4.4.6 EPR sample preparation and spectroscopic methods. Anaerobic EPR samples were made to a volume of 300 μL, with 300 μM [Co- HPCD(4XC)] in 100 mM (pH 7.5) MOPS buffer by purging enzyme and substrate under argon before mixing. Samples were

then transferred to EPR tubes in a glove box and frozen by slow immersion in liquid nitrogen. EPR spectra were recorded on a Bruker Elexsys E-500 spectrometer equipped with an Oxford Instruments ESR-10 liquid helium cryostat at X-band (9.64 GHz). Co-HPCD EPR spectra were acquired at 20 K (unless otherwise stated).

4.4.7 Rapid freeze-quench experiments. Anaerobic enzyme-substrates complexes were prepared in a Coy anaerobic glove box. The starting point EPR sample was prepared by taking an aliquot of the enzyme-substrate complex and diluted it by 1/2 using anaerobic buffer in a glove box. The sample was then transferred it to a sealed EPR tube, which was frozen by slowly submerging the EPR tube in liquid nitrogen. The rest of the pre-formed enzyme-substrate complex was loaded in to a syringe of a RFQ apparatus (model 1019) cooled to 4 °C. The enzyme-substrate complex was rapidly mixed with an equal volume of O_2-saturated buffer (1 atm at 4 °C) and passed through a calibrated ageing loop before being rapidly frozen on two counter-rotating aluminum wheels partially submerged in liquid nitrogen.[149] Scraping the wheels with liquid nitrogen cooled plastic scrapers produced a powdered sample that was packed into EPR tubes submerged in liquid nitrogen. Rapid freeze-quench samples aged for less than 1.5 sec were prepared on the RFQ apparatus as previously described.[149] Samples aged for longer times were prepared by rapidly mixing equal volumes of the O_2-saturated buffer and enzyme substrate complex in an EPR tube at 4 °C and then rapidly freezing the sample by quickly immersing it in an isopentane liquid nitrogen-cooled slurry (~160 °C). These reactions were filmed using a video camera, the video was then reviewed and the reaction timed using a stopwatch to more accurately measure the age of the sample upon freezing.

4.4.8 Spin quantification. The yield of different EPR species was quantified similar to the previously described in Section 3.2.9,[130] by first integrating the spectra of the starting enzyme-substrate complexes (diluted by one half or to the same concentration as the rapid freeze-quenched samples) and the final time point sample to get the total cobalt concentration. The S = 1/2 species was quantified by integrating the g = 2 region separately from the rest of the spectrum. The yield of the S = 1/2 species was quantified according to the procedure of Aasa and Vänngård, which corrects the intensity of the integrated areas of highly anisotropic EPR spectra by multiplying by a correction factor that scales the area based on the g-values of each species.[224] The normalized change in concentration of the enzyme-substrate complex, Co^{4FC}Int1, Co^{4FC}Int2, and the final enzyme product (Co-HPCD) were calculated by monitoring the change in intensity of EPR features unique to each species ([Co-HPCD(4FC)] at g = 10.9, Co^{4FC}Int1 at g = 2.035 and 1.965, Co^{4FC}Int2 at g = 5.68, and Co-HPCD at g = 5.19.) and then dividing the intensity at each time point by the maximum intensity observed for each feature. This procedure directly gives the normalized yield of the enzyme-substrate complex and Co-HPCD through out the reaction, assuming that all the Co-HPCD is bound initially by substrate and that at the end point all the enzyme is unbound. The concentration of Co^{4FC}Int2 must be calculated by subtracting the yield of each species (Normalized yield of Co^{4FC}Int2 = 1 - ES - Co^{4FC}Int1 - E). The yield of Co^{4FC}Int1 was measured by integrating the S = 1/2 signal by the procedure as described above.

4.4.9 EPR power saturation experiments. Power saturation experiments were setup by carefully tuning the instrument and regulating the temperature. Two scans were taken of the g = 2 region at each microwave power from 100 nW (53 dB) to159.4 mW (1 dB).

Power saturation experiments were preformed between 2.5 and 35 K. The intensity of the species of interest in each spectrum was measured by taking the difference between the highest peak and lowest trough associated with the spectrum of the species. The intensity for each power saturation experiment was normalized by dividing by the maximum intensity of the species observed at each temperature. The $P_{1/2}$ values were then obtained by fitting each set of data at each temperature to Equation 4.3 using SigmaPlot version 10.0 from Systat Software, Inc.

4.4.10 Preparation of 4FQ and 4FSQ$^{\bullet}$. 4FQ was prepared by oxidizing 4FC with mushroom tryosinases in 50 mM MOPS (pH 7.5) as previously reported by Stratford *et. al.* or by oxidation with sodium periodate as previously reported by Peiken *et. al*.[295, 296] 4FQ is unstable in H_2O, decaying rapidly over 10–30 minutes.[295] 4FSQ$^{\bullet}$ was prepared by first preparing 4FQ by oxidizing 4FC (15 mg) in 2 mL dichloromethane and 300 μL H_2O with 0.3 g sodium periodate. The reaction was stirred for 5 minutes in which time it turned dark orange. The reaction was then treated with sodium bicarbonate and then dried with anhydrous magnesium sulfate. 4FQ was treated with base to remove any acid from solution since protonated SQ$^{\bullet}$ disproportionates to form catechol and quinone.[282] The dichloromethane solvent was then evaporated under vacuum and the 4FQ re-dissolved in 3 mL of dry anaerobic acetonitrile with 0.1 mM tetra(n-butyl)ammonium hexafluorophosphate ($TBAHFP_6$) as the supporting electrolyte. The cyclic voltammogram (CV) was performed on a CS-1200 Computer-Controlled Potentiostat Electroanalytical System from Cypress Systems Inc. The CV was collected on the anaerobic solution by scanning between 500 to -2000 mV at 500 mV/sec (100 μA/V) similar to the procedure outlined by Stallings *et. al*. using Ag/AgCl reference electrode

(in acetonitrile), a carbon working electrode and platinum auxiliary electrode.[282] The voltammogram was then referenced to Fc^{+}/Fc (64 mV) by the addition of ferrocene. $4FSQ^{\bullet}$ was prepared by reducing the solution of 4FQ by bulk electrolysis using a platinum gauze working electrode with the potential poised at -1035 mV in a stirred anaerobic flask for 1hr.[282] The chemical oxidation, CV and bulk electrolysis were performed in CH_2Cl_2 or CH_3CN since 4FQ is not stable in H_2O.[295, 296] The CV measurements had to be performed anaerobically since $4FSQ^{\bullet}$ is oxidized to 4FQ in air.[282]

Chapter 5

Kinetic and Spectroscopic Characterization of Intermediates Species Observed in the Reaction of [Mn-HPCD(4XC)] with O_2

5.1 Introduction

The steady-state and transient kinetics experiments reported in Chapter 4 for reactions of Co-HPCD with 4XCs have also been repeated with Mn-HPCD. Surprisingly the turnover of 4XCs by Mn-HPCD is considerably slower than that of Co-HPCD despite the 360 mV higher M(III/II) standard redox potential of Co than Mn. With Co-HPCD, two intermediates were observed, namely Co^{4XC}Int1, which is associated with a low-spin [Co(III)(4XSQ$^{\bullet}$)(hydro)peroxo] species based on EPR, and Co^{4XC}Int2, which is assigned to a high-spin [Co(II)(4XQ)(hydro)peroxo] species based on the similarity of its visible chromophore to independently synthesized 4XQs and EPR data indicating a high-spin Co(II) center. The slower decay of the chromophoric intermediate with Mn-HPCD has allowed us to further characterize the species by resonance Raman spectroscopy.

5.2 Results

5.2.1 Steady-state kinetics. The apparent Michaelis-Menten kinetic parameters obtained by varying the concentration of either substrate (Figure 5.1) or O_2 (Figure 5.2) for reactions of Mn-HPCD enzymes with 4XCs at 4 °C and 22 °C are reported in Table 5.1. Both Mn-HPCD and Co-HPCD have significantly lower apparent affinities (larger $K_M^{catechol}$) for the halogenated catechols (4XC) than for the native substrate HPCA. Moreover, Mn-HPCD has an order of magnitude weaker apparent affinity for all catechol

substrates compared to Co-HPCD. Under saturating conditions at 22 °C the k_{cat} values for Mn-HPCD decrease across the series from 4BrC (86 ± 3 min^{-1}) to 4ClC (74 ± 4 min^{-1}) to 4FC (54 ± 4 min^{-1}), as would be expected with an increase in the electronegativity of the halogen substituent slowing down the rate of catechol oxidation. In every case Mn-HPCD catalyzes the extradiol ring cleavage of the same series of substrates at least 3-fold more slowly than Co-HPCD.

Table 5.1. Steady-state kinetic values for Mn- and Co-HPCD measured in 50 mM MOPS buffer (pH 7.5) at 22 °C and 4 °C.

Temperature		**22 °C**		**4 °C**	
Constant	**Substrate**	**Mn-HPCD**	**Co-HPCD**	**Mn-HPCD**	**Co-HPCD**
$K_M^{catechol}$ **(mM O_2)**	4BrC	0.16 ± 0.01	0.016 ± 0.001		
	4ClC	0.14 ± 0.01	0.017 ± 0.001		
	4FC	0.15 ± 0.01	0.070 ± 0.007		
	HPCA*	0.035 ± 0.005	0.005 ± 0.001		
K_M^{O2} **(mM O_2)**	4BrC	2.65 ± 0.13	0.79 ± 0.02	0.24 ± 0.03	0.18 ± 0.04
	4ClC	1.50 ± 0.15	0.98 ± 0.06	0.84 ± 0.06	0.12 ± 0.01
	4FC	1.25 ± 0.18	1.25 ± 0.15	1.0± 0.2	1.5 ± 0.2
	HPCA*	0.050 ± 0.004	1.2 ± 0.1		
k_{cat} **(min^{-1})**	4BrC	86 ± 3	297 ± 4	3.5 ± 0.1	33 ± 1
	4ClC	74 ± 4	436 ± 11	11.6 ± 0.3	35.9 ± 0.6
	4FC	54 ± 4	284 ± 15	8.0 ± 0.6	50 ± 3
	HPCA*	370 ± 10	1120 ± 70		
k_{cat}/K_M^{O2} **(mM^{-1} min^{-1})**	4BrC	32 ± 2	370 ± 10	15 ± 2	180 ± 40
	4ClC	49 ± 6	440 ± 30	14 ± 1	300 ± 30
	4FC	43 ± 7	230 ± 30	8 ± 2	33 ± 5
	HPCA*	7400 ± 600	900 ± 100		
$k_{cat}/K_M^{catechol}$ **(μM^{-1} min^{-1})**	4BrC	0.540 ± 0.04	18.6 ± 12		
	4ClC	0.530 ± 0.05	25.9 ± 2.3		
	4FC	0.36 ± 0.04	4.06 ± 4.6		
	HPCA*	10.6 ± 1.5	224 ± 47		

* measured at pH 7.8.[8] Reported error values for k_{cat} and K_M are from nonlinear regression fitting of data to the Michaelis-Menten equation. Error values for k_{cat}/K_M where calculated using error propagation.

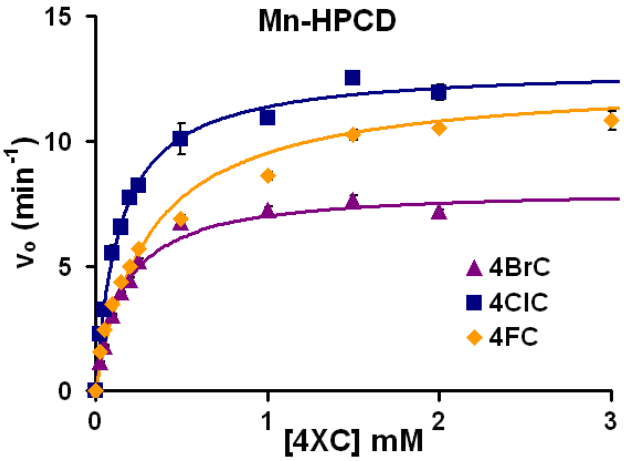

Figure 5.1. Michaelis-Menten plots varying 4XC concentration for the reaction of Mn-HPCD with 4XC. Reaction conditions air-saturated buffer (285 µM O_2) 22 °C, 50 mM MOPS buffer (pH 7.5). Rates were measured from initial velocities at different catechol concentrations by following the formation of the yellow extradiol ring-cleaved product by UV-Vis spectroscopy. Lines represent fits of data to the Michaelis-Menten equation.

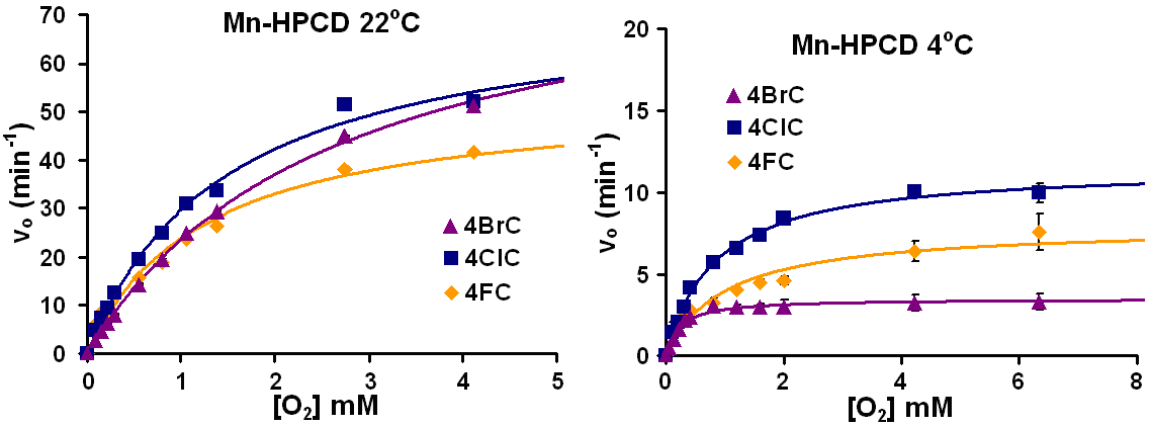

Figure 5.2. Michaelis-Menten plots varying O_2 concentration for Mn-HPCD (right) in the presence of 3 mM 4XC. Reaction conditions 4 and 22 °C, 50 mM MOPS buffer pH (pD) 7.5. Rates were measured from initial velocities at different O_2 concentrations ranging from 0.086–4.12 mM (3 atm) by following the formation of the yellow extradiol ring-cleaved product by UV-Vis spectroscopy. Rates of the reaction were also confirmed by monitoring the consumption of O_2 using a Clark-type oxygen electrode in air-saturated buffer. Lines represent fits of data to the Michaelis-Menten equation.

In previous studies with the native substrate HPCA, Co-HPCD was observed to have a much lower apparent affinity for O_2 (K_M^{O2}) of 1.20 ± 0.10 mM, compared to 0.050 and 0.06 ± 4 mM O_2 for Mn- or Fe-HPCD, respectively.[131, 169] Additionally, Co-HPCD was found to have a catalytic efficiency (k_{cat}/K_M^{O2}) observed in the steady-state turn over of HPCA that is an order of magnitude smaller than for Mn- and Fe-HPCD. In single turnover studies Co-HPCD exhibited a large O_2 concentration dependence on the rate of observed formation of the yellow extradiol ring cleavage product of HPCA, while Mn- and Fe-HPCD showed little or no O_2 concentration dependence.[166, 169] These experiments suggested that the rate determining step for the turnover of the native substrate HPCA by Mn- and Fe-HPCD is late in the catalytic cycle, presumably product formation or release, while the rate determining step in the reaction with Co-HPCD is earlier in the reaction cycle, associated with a step reversibly connected to the O_2 binding and before the first irreversible step in the mechanism.

The apparent affinity for O_2 (K_M^{O2}) of the [Mn-HPCD(4XC)] complex has decreased significantly compared to [Mn-HPCD(HPCA)], by almost two orders of magnitude in the case of 4BrC. This is accompanied by a large decrease in the k_{cat}/K_M^{O2} values of Mn-HPCD by two orders of magnitude. As a consequence, the k_{cat}/K_M^{O2} values for the [Mn-HPCD(4XC)] are an order of magnitude lower than the k_{cat}/K_M^{O2} values for Co-HPCD with the same 4XC substrates, suggesting that the rate determining step for the turnover of the halogenated substrate analogues by Mn-HPCD has moved to an earlier phase of the reaction, namely the O_2 activation and catechol oxidation steps.

5.2.2 Pre-steady state kinetics. Pre-steady state kinetic experiments monitoring the formation of the yellow extradiol ring-cleaved product show a ~100 ms lag phase in the turnover of both HPCA and 4ClC by Mn-HPCD, before the formation of the yellow chromophore (Figure 5.3). The lack of an initial burst phase suggests that product release is not rate determining in the turnover of HPCA or 4ClC by Mn-HPCD, though product formation (formation of the product chromophore) still could be.

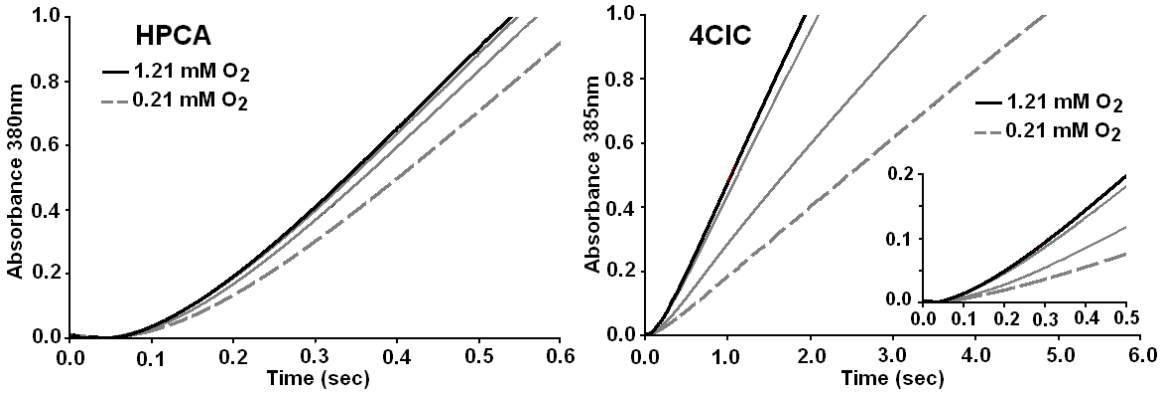

Figure 5.3 Pre-steady state kinetic experiments monitoring the formation of yellow ring-cleaved product performed at 4°C in 100 mM MOPS buffer at pH 7.5. Reaction with Mn-HPCD and HPCA (left) and 4ClC (right) with 65 μM Mn-HPCD, 5 mM catechol and O_2 concentrations ranging from 0.21 to 1.21 mM O_2 after mixing on a stopped-flow instrument. The inset in the 4ClC panel highlights the initial lag phase before product formation. A similar pre-steady state lag phase with no burst was observed with Co-HPCD and HPCA or 4ClC.

5.2.3 Stopped-flow experiments. Stopped-flow experiments were performed by rapidly mixing the anaerobic [Mn-HPCD(4XC)] enzyme-substrate complex with O_2 saturated buffer (pH 7.5 at 4 °C). [Mn-HPCD(4ClC)] reacts with O_2 to form an intermediate with an intense chromophore at 470 nm (Figure 5.4) in the first 7 sec, which decays to the yellow extradiol ring-cleaved product (ε_{380} = 44,300 M^{-1} cm^{-1}) over 2 minutes, with an

apparent isosbestic point at 440 nm. The single turnover reaction of [Mn-HPCD(4ClC)] with O_2 (Figure 5.5) was monitored at 475 nm to follow the formation and decay of the intermediate species. In the single wavelength traces an initial burst phase (~200 ms) was observed in the formation of the 470 nm chromophore, requiring the use of a triple exponential to get a good fit to the data (Figure 5.5). Closer inspection of the photodiode array data (Figure 5.4) show that the burst phase is associated with the formation of an initial chromophore at 455 nm (Mn^{4ClC}Int1) in the first 200 ms, followed by formation of the 470 nm chromophore (Mn^{4ClC}Int2).

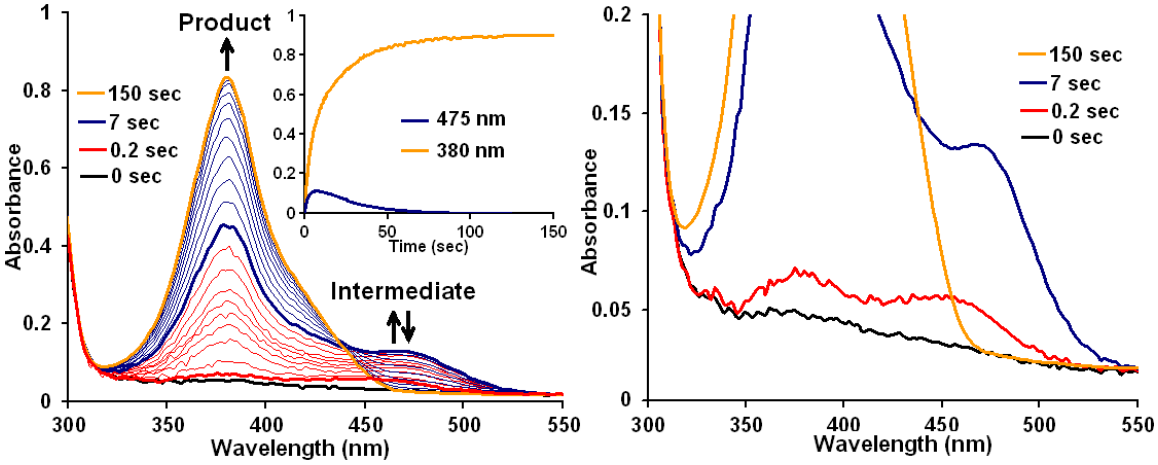

Figure 5.4. (Left) Photodiode array stopped-flow kinetic data for anaerobic [Mn-HPCD(4ClC)] rapidly mixed with O_2-saturated buffer (1atm O_2). Inset shows single wavelength traces monitoring intermediate at 475 nm and extradiol ring-cleaved product at 380 nm. (Right) Magnification of intermediate chromophores: Mn^{4ClC}Int1 at 455 nm and Mn^{4ClC}Int2 at 470 nm. Final concentrations of reagents after mixing: 30 µM 4ClC, 65 µM HPCD and 1 mM O_2. Reaction conditions: 100 mM MOPS (pH 7.5), 4 °C.

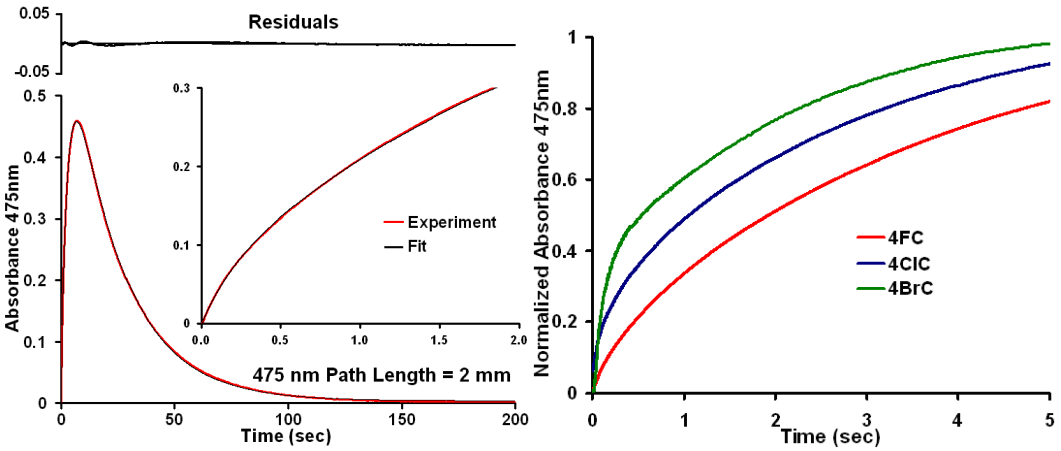

Figure 5.5. Stopped-flow kinetic data for [Mn-HPCD(4ClC)] rapidly mixed with oxygenated buffer. (Left) Single wavelength traces monitoring formation and decay of intermediate at 475 nm (2 mm path length). Inset shows the burst phase in the formation of the chromophoric intermediate. Final concentrations of reagents after mixing: 600 μM 4XC, 720 μM Mn-HPCD and 1.0 mM O_2. Reaction conditions: 100 mM MOPS (pH 7.5), 4 °C. (Right) Initial burst phase observed in reaction with 4BrC, 4ClC and 4FC. The burst phase is longest and has a larger amplitude for [Mn-HPCD(4BrC)] rapidly mixed with O_2.

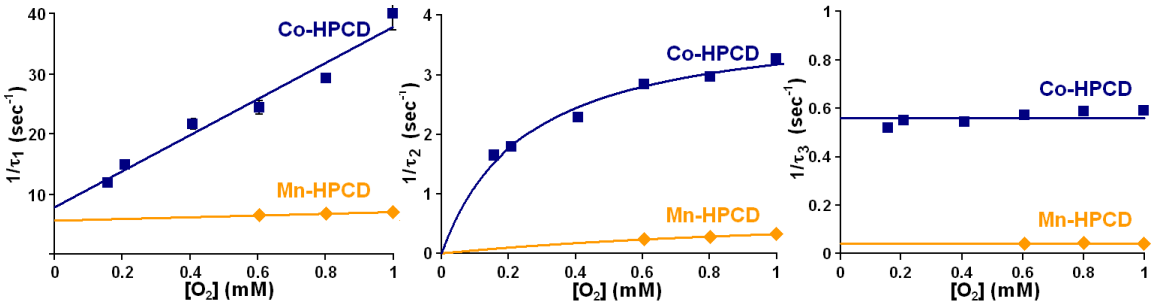

Figure 5.6. Reciprocal relaxation times for the phases in the reaction of [Co/Mn-HPCD(4ClC)] with O_2, plotted as a function of O_2 concentration. Final concentrations of reagents after mixing: 600 μM 4ClC, 720 μM Mn-HPCD and 600–1,000 μM O_2 for reactions with Mn-HPCD and 130 μM 4ClC, 220 μM Co-HPCD and 200–1,000 μM O_2. Reaction conditions: 100 mM MOPS (pH 7.5) and 4 °C. Lines represent fit of data to linear or hyperbolic functions.

Table 5.2 Rate constants for the single turnover and steady-state reactions of [Mn-/Co-HPCD(4XC)] with O_2.

Protein	Sub	k_1 (mM^{-1} sec^{-1})	k_{-1} (sec^{-1})	k_2 (sec^{-1})	k_3 (sec^{-1})	k_{cat} (sec^{-1})	K_D^{O2} (mM)
Mn-HPCD	**4FC**	0.58 ± 0.05	0.24 ± 0.02	0.64 ± 0.02	0.011 ±0.002	0.13 ± 0.01	0.41 ± 0.05
Mn-HPCD	**4ClC**	1.5 ± 0.1	5.6 ± 0.1	0.8 ± 0.2	0.043 ± 0.001	0.193 ± 0.005	0.27 ± 0.07
Co-HPCD	**4ClC**	30 ± 3	8 ± 2	4.0 ± 0.2	0.58 ± 0.03	0.60 ± 0.01	3.7 ± 0.3

The setup of appropriate experimental conditions for the single turnover and O_2 concentration dependence experiments is complicated by the low apparent affinities of Mn-HPCD for the halogenated substrates (Table 5.1) and the low solubility of O_2 in water. Mn-HPCD shows very low apparent affinities for the halogenated substrates with $K_M^{catechol}$ values of ~150 μM, while Co-HPCD shows an order of magnitude higher apparent affinity than Mn-HPCD with $K_M^{catechol}$ ranging from 16 to 70 μM. To get a high fraction of bound substrate, relatively high substrate and Mn-HPCD concentrations (720 μM Mn-HPCD and 600 μM 4XC) were used. This in turn limits the range of O_2 concentration which can be used and still have excess O_2 for O_2 concentration dependence experiments (Figure 5.6). Due to the limitations described above it is difficult to extract meaningful rate constants from the O_2 concentration dependence plots of the three observed $1/\tau$ (Figure 5.6) for the reaction of [Mn-HPCD(4XC)] with O_2.

Table 5.2 shows the calculated rate constants for the turnover of 4ClC assuming that the O_2 dependence plot of $1/\tau_1$ is linear, $1/\tau_2$ is parabolic and $1/\tau_3$ shows no O_2 concentration dependence as was observed for Co-HPCD. All the rate constants except k_{-1} are an order of magnitude smaller for Mn-HPCD than Co-HPCD, where the rate constant for O_2 dissociation (k_{-1}) is larger than the second order rate constant for O_2

binding (k_1). The difference in the observed transient kinetic rates between Mn- and Co-HPCD is consistent with the steady-state kinetic values for turnover of 4ClC, where the second order rate constants for O_2 binding (k_1 and k_{cat}/K_M^{O2}) are both smaller for Mn-HPCD, the affinity and apparent affinity for O_2 (K_D^{O2} and K_M^{O2}) are both larger for Mn-HPCD, and the rate constants associated with the rate determining step (k_{cat} and k_3) are both smaller for Mn-HPCD than Co-HPCD. It should be pointed out that there is some inconsistency in the observed steady-state and transient kinetics rate for turn over of 4ClC by Mn-HPCD, where the k_{cat} value for the turnover of 4ClC by Mn-HPCD (3.3 μM Mn-HPCD, 3 mM 4ClC) at pH 7.5 and 4 °C is 4.5-fold larger than the slowest rate (k_3) observed in the transient kinetic experiments under similar reaction conditions (720 μM Mn-HPCD, 600 μM 4ClC, and 1.0 mM O_2 at pH 7.5 and 4 °C). We reason that this difference may be due to the low fraction of bound substrate in the preformed enzyme-substrate complex resulting in multiple turnovers in the "single turnover" experiment.

5.2.4 X-band EPR spectra of Mn-HPCD enzyme-substrate complexes. X-band EPR spectra of anaerobic Mn-HPCD enzyme-substrate complexes with catechol, 4FC, 4ClC and 4BrC are shown in Figure 5.7. Mn-HPCD exhibits an $S = 5/2$ EPR signal with an intense feature at $g = 2.0$ from the $<\pm 1/2>$ doublet of the $S = 5/2$ multiplet that exhibits ^{55}Mn ($I = 5/2$) hyperfine splitting. Binding of catechol substrates results in a decrease in the intensity of the $g = 2.0$ feature and the appearance of new features at $g = 2.6$, 4.3 and 9.2.[131, 179, 181, 247] The addition of 4ClC or 4BrC, even with relatively large concentrations

(5 mM), to Mn-HPCD resulted in little perturbation of its EPR spectrum, consistent with the high $K_M^{catechol}$ values observed for the 4XC substrates (Table 5.1).

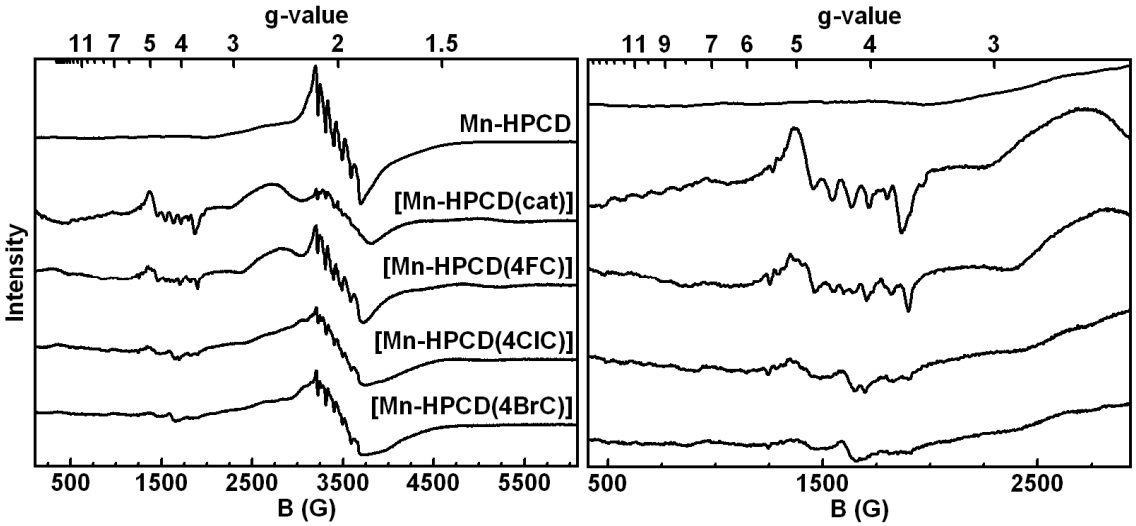

Figure 5.7. Left panel: EPR spectra obtained at 9.64 GHz and 10 K of anaerobic ES complexes of (top to bottom) Mn-HPCD, [Mn-HPCD(catechol)], [Mn-HPCD(4FC)], [Mn-HPCD(4ClC)], and [Mn-HPCD(4BrC)]. (Left) Magnification of low-field region of EPR spectra of Mn-HPCD and enzyme-substrate complexes. EPR samples were prepared with 400 μM Mn-HPCD and 5 mM 4XC.

5.2.5 Rapid freeze-quench experiments with [Mn-HPCD(4XC)] and O_2. Figure 5.8 shows representative EPR spectra from freeze-quench experiments with [Mn-HPCD(4FC)] rapidly mixed with O_2 saturated buffer (pH 7.5 at 4 °C). The anaerobic [Mn-HPCD(4FC)] enzyme-substrate complex exhibits S = 5/2 EPR signals at g = 21, 9.2, 4.3, 2.4 and 2.0 with resolved ^{55}Mn hyperfine splitting observed in the g = 9.2 (87 G), 4.3 (~70 G) and 2.0 (~84 G) features. Upon mixing the enzyme-substrate complex with O_2, the features at g = 21 and 9.2 disappear rapidly (within 10 ms), and a new S = 5/2 signal appears with a distinct set of ^{55}Mn hyperfine splitting (A = 85 G) at g = 4.2. The intensity of the new S = 5/2 species monitored at g = 4.2 increases up to a

reaction time of 2 sec and then decays over the next 100 sec (Figure 5.9). The g = 4.2 signal has a considerable shorter lifetime than the chromophoric intermediate of Mn^{4FC}Int2 observed in stopped-flow experiments and thus has been assigned to the Mn^{4FC}Int1 species associated with the 455 nm chromophore in UV-Vis stopped-flow experiments. Closer inspection of the data following the signal at g = 2.0 shows an initial decrease in the intensity of the g = 2.0 signal over the first second to one-third its original intensity, which then grows over the next 15 sec to roughly three times its initial intensity. The g = 2.0 signal then decreases in intensity till the end of the reaction. Mn^{4FC}Int1 and Mn^{4FC}Int2 form and decay on the same time scales as predicted using the rate constants from the stopped-flow experiments (Figure 5.10).

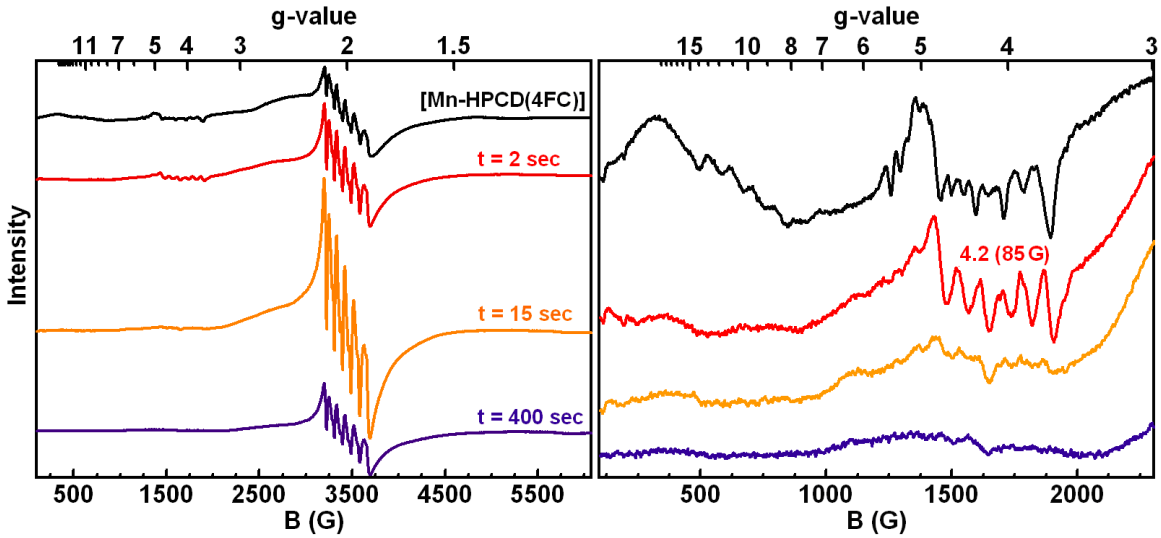

Figure 5.8. (Left) EPR spectra of rapid freeze-quench samples of anaerobic enzyme-substrate complex [Mn-HPCD(4FC)] (black) rapidly mixed with O_2-saturated buffer, showing formation of Mn^{4FC}Int1 (red, g = 4.2) at 2 sec, as well as Mn^{4FC}Int2 (orange, g = 2.0) at 20 sec and its subsequent decay to Mn-HPCD (purple) and the extradiol ring-cleaved product after 200 sec. Reaction conditions: 4 °C, 100 mM MOPS (pH 7.5), final concentration upon mixing 0.91 mM Mn-HPCD, 1.0 mM 4FC (~1.1 equivalents), and 1.0 mM O_2. EPR spectra were all collected at 10 and 0.2 mW power. (Right) Magnification of low-field regions of the EPR spectra.

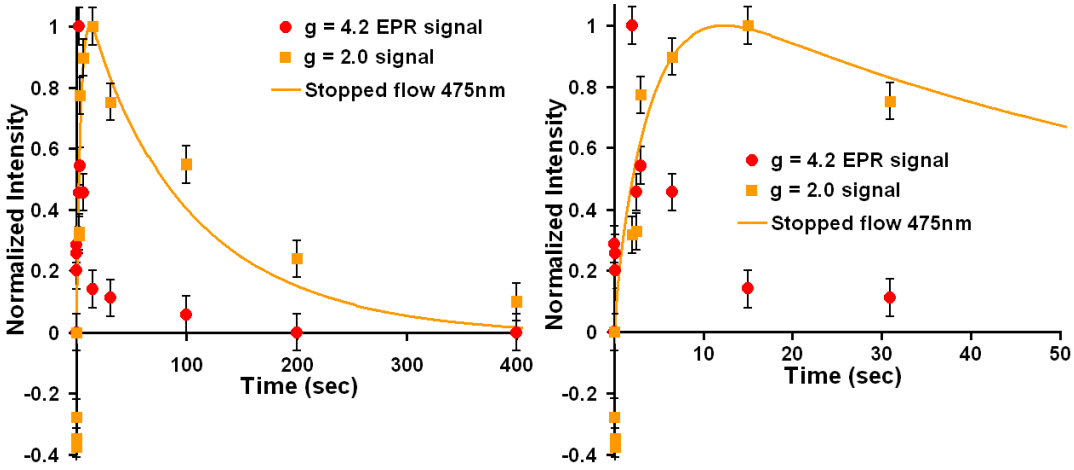

Figure 5.9. Normalized transient kinetic data from stopped-flow and EPR experiments. Monitoring the formation and decay of Mn^{4FC}Int1 (●) and Mn^{4FC}Int2 (■) by following their EPR signals at g = 4.2 and g = 2.0 (Figure 5.8), respectively. Also showing formation and decay of chromophore at 475 nm observed upon mixing [Mn-HPCD(4FC)] with O_2-saturated buffer. The stopped-flow and EPR data following Mn^{4FC}Int1 at g = 4.2 were normalized by dividing the intensity of the signal by its maximum intensity. The g = 2.0 signal was normalized by first subtracting the initial intensity of signal and then dividing by the maximum intensity of the signal minus the initial intensity of the signal at g = 2.0. Error bars represent average signal to noise associated with the EPR data.

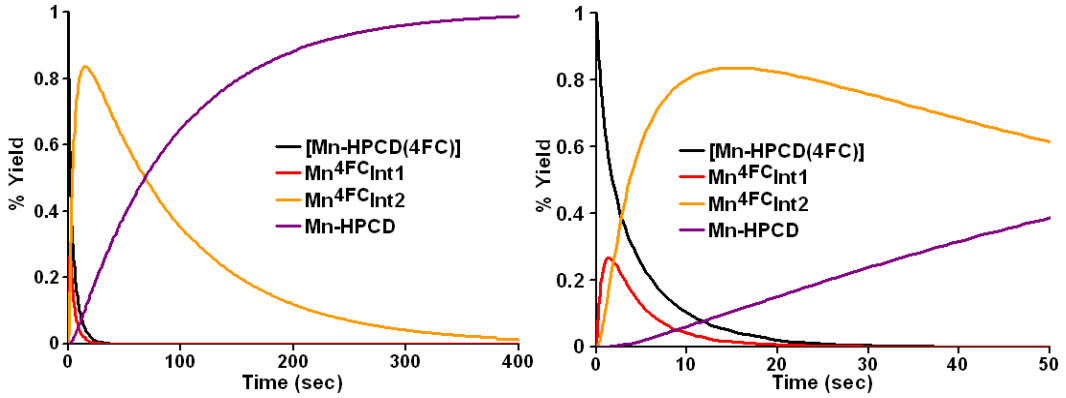

Figure 5.10. Simulated reaction time course for the reaction of [Mn-HPCD(4FC)] with O_2. Using rates constants determined from stopped-flow experiments (Table 5.2). A 24% yield of Co^{4FC}Int1 is predicted at 1.6 sec and a 77% yield of Co^{4FC}Int2 is predicted at 17 sec. Simulated using 0.91 mM [Mn-HPCD(4FC)] and 1.0 mM O_2.

The EPR data for the reaction time course of [Mn-HPCD(4FC)] with O_2 is convoluted due to overlapping features of the different species, making it difficult to quantify the yields of species without simulating the different spectra in each sample. The observed ^{55}Mn hyperfine splitting of Mn^{4FC}Int1 at g = 4.2 (85 G) is similar to that of the anaerobic enzyme-substrate complex (~73 G), which suggests that Mn^{4FC}Int1 has a high-spin Mn(II) center. A similar species was also observed at g = 4.3 (88 G) with the substrate 4ClC. This is in contrast to the S = 5/2 species (Mn^{HPCA}Int1) observed in rapid freeze-quench experiments reported with [Mn-HPCD(HPCA)] with O_2, which exhibited smaller ^{55}Mn hyperfine splitting of 60 G at g = 4.29.[179] The smaller ^{55}Mn hyperfine splitting suggested a decrease in the spin density at the Mn center or ferromagnetic coupling between a high-spin Mn(III) center and either a superoxide or a semiquinone radical.[179] The EPR spectrum of Mn^{4FC}Int2 closely resembles the spectrum of Mn-HPCD with the exception of the intensity of the feature at g = 2.0. This suggests that Mn^{4FC}Int2 also contains a high-spin Mn(II) center.

5.2.6 Resonance Raman spectroscopy of Mn^{4XC}Int2. Co^{4ClC}Int2 exhibits an intense chromophore at at 456 nm ($\varepsilon \sim 9{,}000\ M^{-1}\ cm^{-1}$), similar to the chromophores observed for Mn^{4ClC}Int1 at 455 nm and Mn^{4ClC}Int2 at 470 nm, the chromophore is further shifted to 480 nm with Mn^{4FC}Int2 (Figure 5.11). Resonance Raman spectroscopy was attempted on frozen samples of the Co^{4FC}Int2 prepared by rapidly freezing the sample in a liquid nitrogen cooled isopentane slurry, using 413.1, 457.9 and 488.0 nm laser excitation. Only peaks corresponding to the ring-cleaved product were significantly enhanced above the intense florescence background in these experiments. We then attempted solution resonance Raman experiments using 488.0 nm laser excitation, which were performed by

rapidly mixing anaerobic [Mn-HPCD(4ClC)] complex with O_2-saturated buffer in a flat-bottomed NMR tube. Spectra were collected by taking 5 sec scans until the reaction was complete. The reaction was repeated ~60 times and the spectra of scans from each reaction taken during the same time frames were added together. The baseline corrected resonance Raman spectra taken over the course of the reaction of [Mn-HPCD(4ClC)] with O_2 are shown in Figure 5.12. A set of new intense bands is observed to form and decay on the same time scale as Mn^{4ClC}Int2 observed in stopped-flow experiments (Figure 5.13). Over the entire course of the reaction, another set of bands forms that corresponds to the ring-cleaved product. None of the intermediate peaks were observed using 457.9 or 514.5 nm laser lines due to strong protein fluorescence background at 457.9 nm and poor resonance enhancement at 514.5 nm. The solution resonance Raman experiments were also performed using 4FC and 4BrC (Figures 5.14 and 5.15).

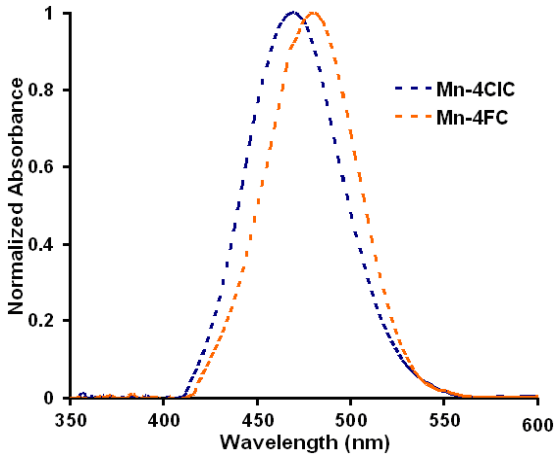

Figure 5.11. Normalized difference spectra of chromophoric intermediates at maximum yields minus spectra of the extradiol ring-cleaved products. Spectra are normalized to the λ_{max} of chromophore at 470 nm [Mn-HPCD(4ClC)O_2] (blue, dotted line), and 480 nm [Mn-HPCD(4FC)O_2] (orange, dotted line).

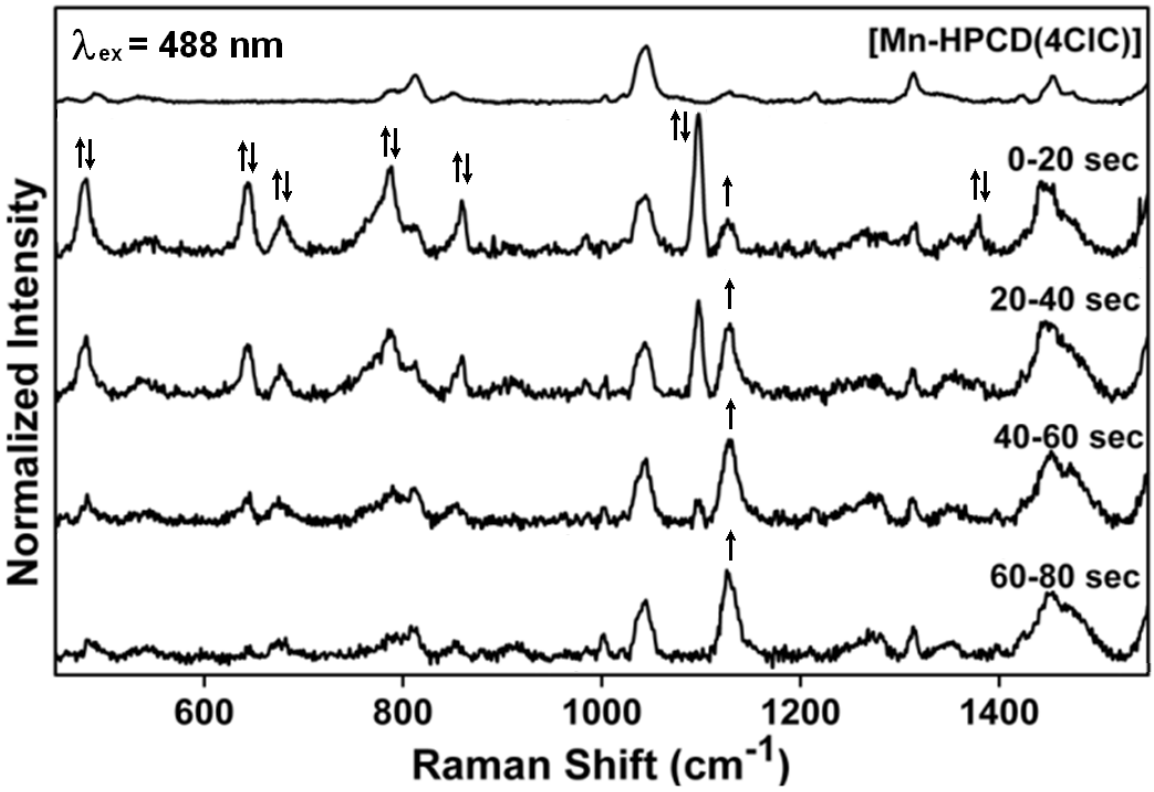

Figure 5.12. Baseline corrected resonance Raman spectra collected using the 488 nm argon laser line of the intermediate generated when anaerobic enzyme-substrate complex [Mn-HPCD(4ClC)] was rapidly mixed with O_2 saturated buffer. Reaction conditions: 100 mM MOPS (pH 7.5), 4 °C. Concentrations upon mixing: 1 mM O_2, 250 μM, Mn-HPCD and 230 μM 4ClC. Spectra were collected over 20 sec (four 5 sec scans) intervals collected for ~60 separate reactions. Spectra are all normalized to the buffer peak at 1,045 cm^{-1}. The intense peak growing in at 1,135 cm^{-1} corresponds to the ring-cleaved product.

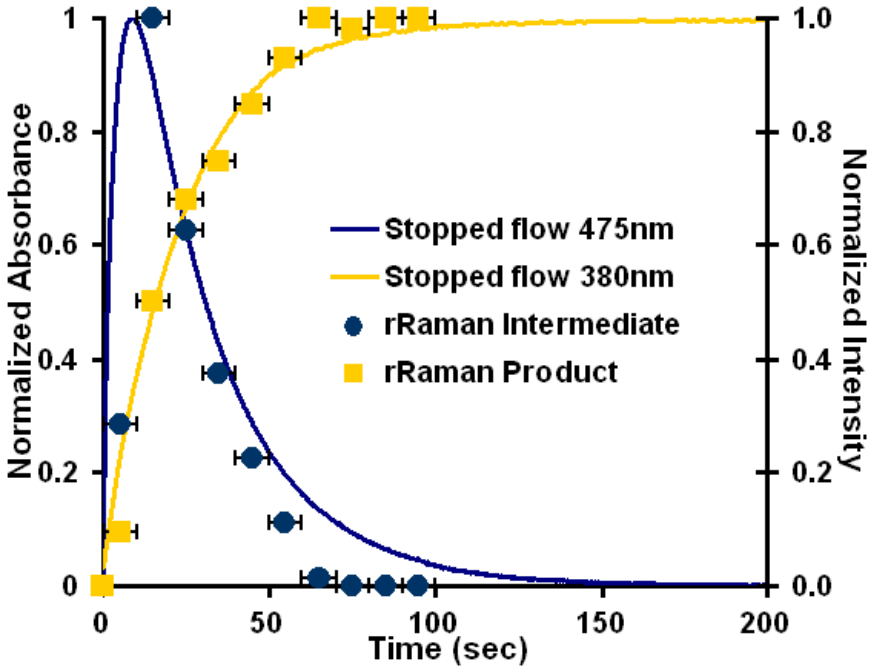

Figure 5.13. Formation and decay of the $Mn^{4ClC}In2$ intermediate and formation of the extradiol ring-cleaved product monitored by stopped-flow UV-Vis (solid lines) and by resonance Raman methods (symbols) shown in Figure 5.12. Vibrations of the intermediates and the extradiol ring-cleaved product observed by resonance Raman spectroscopy form and decay on the same time scale as chromophoric intermediates observed in stopped-flow experiments under the same conditions. Reaction conditions: 100 mM MOPS (pH 7.5), 4 °C. Concentrations upon mixing: 1 mM O_2, 250 μM Mn-HPCD and 230 μM 4XC.

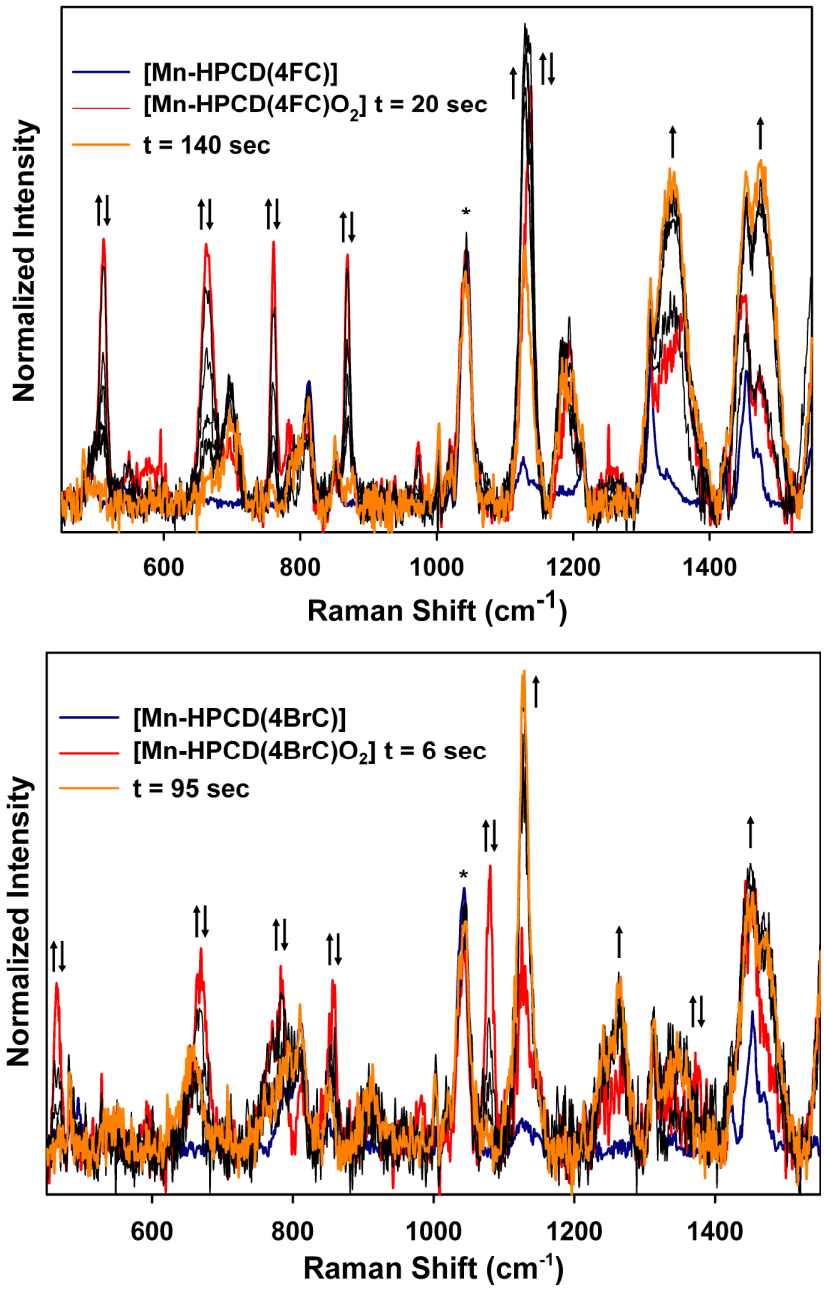

Figure 5.14. Baseline corrected resonance Raman spectra of the reaction between [Mn-HPCD(4XC)] and O_2 with 4FC (top) or 4BrC (bottom). Reaction conditions: 100 mM MOPS (pH 7.5), 4 °C. Concentrations upon mixing: 1 mM O_2, 250 µM, Mn-HPCD and 230 µM 4XC. Spectra were collected using 488 nm argon laser excitation with 20 sec scans for 4FC and 12 sec scans with 4BrC from ~60 separate reactions. Spectra are all normalized to the buffer peak at 1,045 cm^{-1}. With 4FC the intermediate peak (1,137cm^{-1}) and extradiol ring-cleaved product peak (1,135 cm^{-1}) overlap significantly as well as peaks from the buffer, intermediate and product above 1,300 cm^{-1}.

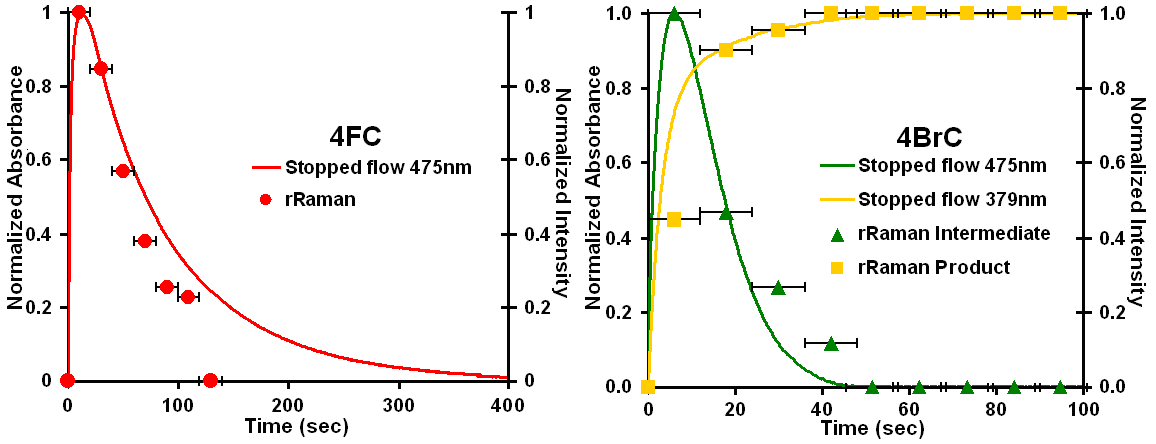

Figure 5.15. Formation and decay of the [Mn-HPCD(4XC)O_2] intermediate as monitored by stopped-flow UV-Vis (solid lines) and resonance Raman (symbols) methods with 4FC (left) and 4BrC(right) for spectra shown in Figure 5.14. Also shown in the right panel is the formation of the extradiol ring-cleaved product monitored by stopped-flow and by resonance Raman for the reaction with 4BrC. Intermediates and extradiol ring-cleaved products observed by resonance Raman form and decay on the same time scale as chromophoric intermediates observed in stopped-flow experiments under the same conditions. Reaction Conditions: 100 mM MOPS (pH 7.5) at 4 °C. Concentrations upon mixing: 1 mM O_2, 250 μM, Mn-HPCD and 230 μM 4XC.

Upon mixing an anaerobic solution of [Mn-HPCD(4FC)] with oxygenated buffer, intense resonance enhanced bands of the intermediate are observed at 512, 663, 760, 868, 1,137, 1,194, 1,363, and 1,442 cm^{-1} associated with Mn^{4FC}Int2 (Figure 5.14). Figure 5.16 shows the resonance Raman difference spectra for [M-HPCD(4XC)O_2] intermediates after subtracting the spectra of the extradiol ring-cleaved product and buffer. Although the intense band at 1,137 cm^{-1} is in the range expected for the ν(O-O) vibration of a metal-superoxide (1,090 to 1,160 cm^{-1}),[227, 302-306] it proved to be insensitive to $^{18}O_2$ labeling experiments (Figure 5.16E). Instead the 1,137 cm^{-1} band was observed to shift to lower wavenumbers (1,097 and 1,079 cm^{-1}) upon changing the halogen substituent to

heavier Cl or Br atoms. A similar behavior is observed for the band at 512 cm^{-1}. Deuteration of the catechol ring of 4FC resulted in significant shifts in all the observed bands. This suggests that the vibrations originate from a chromophore derived from the catechol substrates such as an oxidized semiquinone or quinone species. In addition, no shifts were observed in the spectra when Co-HPCD was used instead of Mn-HPCD (Figure 5.16F).

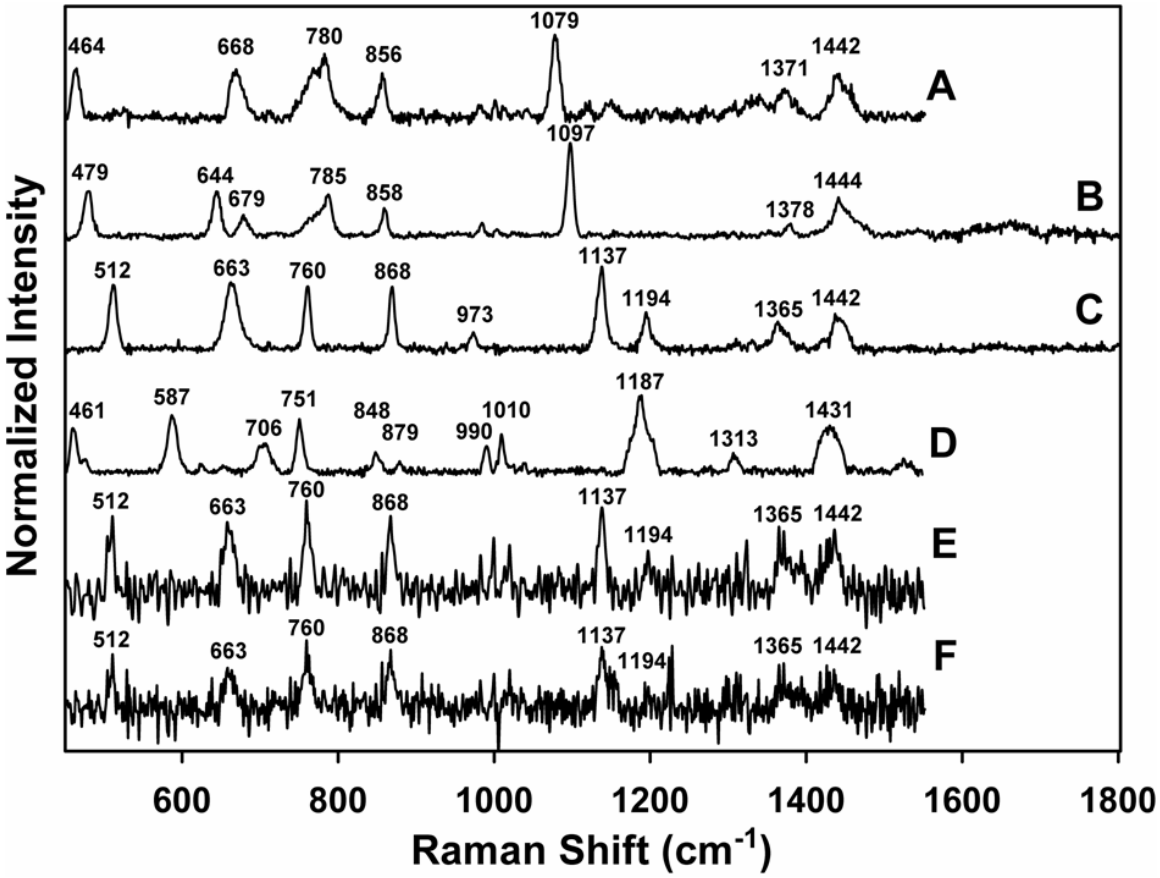

Figure 5.16. Resonance Raman difference spectra of $Mn^{4XC}Int2$ and $Co^{4FC}Int2$ intermediates minus spectra of 100 mM MOPS (pH 7.5) and ring-cleaved products. (A) $Mn^{4BrC}Int2$, (B) $Mn^{4ClC}Int2$, (C) $Mn^{4FC}Int2$, (D) $Mn^{d34FC}Int2$, (E) $Mn^{4FC}Int^{18}O_2$, and (F) $Co^{4FC}Int2$.

Bands attributed to mixed ν(C-O) ring + ν(C-C) vibrational modes observed between 1,200 and 1,700 cm^{-1} can be useful in distinguishing the oxidation state of the catechol ligand (Table 5.3). Whereas [M(III)catecholate] complexes typically exhibit two bands, at 1,250 cm^{-1} and 1,480 cm^{-1}, the bands for [M-semiquinone] complexes typically fall around 1,440 cm^{-1} and those for [M-quinone] complexes are between 1,600 and 1,700 cm^{-1}.[285, 289, 307, 308] The bands at 1,363 and 1,442 cm^{-1} observed for Mn^{4FC}Int2 suggest that the catechol ligand of the intermediate has been oxidized to a semiquinone. The Co/Mn^{4XC}Int2 intermediates have vibrations similar to the previously characterized [Cu(II)(DBED)TBSQ] complex, which has bands at 508, 557, 577, 748, 1,375, and 1,475 cm^{-1} (Table 5.3). The 508 and 557 cm^{-1} vibrations of [Cu(II)(DBED)TBSQ] were assigned to chelate vibrational modes from the five-membered metal-ligand ring and the 577 and 748 cm^{-1} bands to ring vibrations.[289]

Table 5.3. Vibrational data for catecholate, semiquinone and quinone model complexes and intermediates Mn^{4XC}Int2 and Co^{4FC}Int2.

Complex[a]	Vibrations (cm^{-1})										Ref
coordinated catechols							1250		1440–1480		285, 307, 308
coordinated semiquinones						1100–1200			1400–1500		289, 308
coordinated quinones										1600–1675	307
free quinones										~1675	308
Mn^{4BrC}Int2	464	668	768 780	856		1079		1371	1442		Fig 5.15
Mn^{4ClC}Int2	479	664 679	785	858		1097		1378	1444		Fig 5.15
Mn^{4FC}Int2	512	663	760	868	973	1137 1194		1365	1442		Fig 5.15
$Mn^{4FC}Int2^{18}O_2$	512	663	760	868	973	1137 1194		1365	1442		Fig 5.15
Mn^{d34FC}Int2	461	587	706 751	848 879	990 1010	1187		1313	1431		Fig 5.15
Co^{4FC}Int2	512	663	760	868		1137 1194		1365	1442		Fig 5.15
[Fe(III)-HPCD(4FC)]	533	570	647			1137	1272	1322	1423/1474		Fig 5.18
Fe(III)-MndD-DOPA	530	569 586	646 666				1273	1318	1423/1464		281
$[Mn(CO)_3THF(DTBC)]$	530/580	611					1254	1316	1410/1434/ 1463/1551		283
$[Mn(CO)_2(POEt_3)_2(DTBC)]^+$	526	607					1254	1318	1413/1434/ 1462/1546		283
$[Co(III)(CTH)(DTBC)]^+$							1250				271
$[Co(III)(CTH)(TCC)]^+$							1250				271
[Co(III)(trien)cat]I							1250		1480		269
$[Co(III)(en)_2PCA]I\ H_2O$							1295		1495	1680	269
$[Ru(II)(py)_4(TCC)]$						1072	1125	1351			285

Complex[a]	Vibrations (cm^{-1})										Ref
$[Ru(III)(bpy)(catechol)_2]^-$			735 768				1253	1385	1415/1464 1559		286
$[Co(III)(trien)DTBSQ]Cl_2$									1440		280
[Cu(II)(DBED)TBSQ]	508	557	748					1375	1435		289
$[Co(III)(DTBSQ)(CN)_4]^{2-}$									1485/1456		251
$[Ru(II)(bpy)(SQ)_2]$	527		728 743	772		1099 1113	1208	1315	1415/1448 1532		286
$[Ru(II)(bpy)(DTBSQ)_2]$	505		773		1024	1099 1142		1360 1375	1464/1518/ 1583		286
$[Ru(II)(bpy)(TCSQ)_2]$			767	798	979	1188		1322 1384	1396 1421		286
4FQ							1306	1329 1367	1393/1508/ 1566/1590	1632 1661	295, 296
DTBQ										1670 1695	270
$[Mn(CO)_2(POEt_3)_2(DTBQ)]^+$	453/525/ 571/589	638	742			1154		1310 1362	1410		283
catechol	586		752	775	1043	1065	1276			1614	this work
4BrC	591	635		786	886	1071	1282	1351		1607	this work
4ClC	580/604	663		790	905	1087	1282	1367		1605	this work
4FC	517	605	732	791	969	1099	1301	1365		1621	this work
d_3-4FC	497	583	726	860			1257			1610	this work

[a]Abbreviations used: 4ClC, 4-chlorocatechol; 4FC, 4-fluorocatechol; $d_3$4FC, deuterated 4-fluorocatechol HPCD, homoprotocatechuate 2,3-dioxygenase from *Brevibacterium fuscum*; Fe-MndD, Iron-substituted homoprotocatechuate 2,3-dioxygenase from *Arthrobacter Globiformis*; HPCA, homoprotocatechuate; DOPA, L-3,4-dihydroxyphenylalanine; THF, tetrahydrofuran; DTBC, 3,5-di-tert-butylcatechol; DTBSQ, 3,5-di-tert-butylsemiquinone; DTBQ, 3,5-di-tert-butylquinone; SQ, semiquione; Q, quinone; TCC, tetrachlorocatechol; TCSQ, tetrachlorosemiquinone; TCQ, tetrachloroquinone; CTH, tetraazamacrocycle; py, pyridine; bpy, bipyridine; en, ethylene *diamine*; 4FSQ, 4-fluorosemiquinone; DBED, ; Me_3TPA, *tris*(6-methyl- 2-pyridylmethyl)amine; trien, triethylenetetramine; salen, 2,2'-Ethylenebis(nitrilomethylidene)diphenol; cat, catechol; 4NSQ, 4-nitrosemiquinone; phenSQ, 9,10-phenanthrenesemiquinone; 4XC, 4-halocatechol.

The [Cu(II)(DBED)TBSQ] species lacks an intense vibration at ~1,100 cm^{-1} observed for the Co/Mn^{4XC}Int2 intermediates that were sensitive to the halogen substituent of the 4XC and may be due to a vibrational mode involving the C-X bond. [Ru(II)(bpy)$(TCSQ)_2$] (TCSQ = tetrachloro-*o*-semiquinone) also exhibits a band at 1,188 cm^{-1} in support of the assignment of the ~1,100 cm^{-1} peak to a ν(C-X) vibrational mode,.[286] The aryl halides (X-C_6H_5, X = F, Cl, Br, I) exhibit two substituent-dependent vibrational modes, which are absent from benzene, where the ν_1(C-X) vibrational modes decrease from 1,211 cm^{-1} with F-C_6H_5 to 1,057 cm^{-1} with I-C_6H_5 and the ν_2(C-X) vibrational decrease from 803 cm^{-1} with F-C_6H_5 to 647 cm^{-1} with I-C_6H_5.[309] The Raman spectra of the 4XC substrates (Table 5.3) also show two substituent-dependent vibrational modes that shifts from 1,099 and 969 cm^{-1} with 4FC to 1,071 and 886 $cm^{-1}$with 4BrC. This further supports the assignment of the ~1,110 cm^{-1} vibration to a vibrational mode involving the C-X bond.

5.2.7 Resonance Raman spectrum of 4FQ. Unbound 4FQ has an intense chromophore at 408 nm (ε_{408nm} ~3,500 M^{-1} cm^{-1}). The resonance Raman spectrum collected of 4FQ in dichloromethane (λ_{ex} = 457.9 nm, Figure 5.17) exhibits intense vibrations between 1,508 and 1,661 cm^{-1}, which would be expected to down shift by ~60 cm^{-1} upon coordination to a metal center.[310] The absence of vibrational bands between 1,600 and 1675 cm^{-1} typical of metal-quinone complexes further suggest that the Mn/Co^{4XC}Int2 intermediate may not be a quinone species.

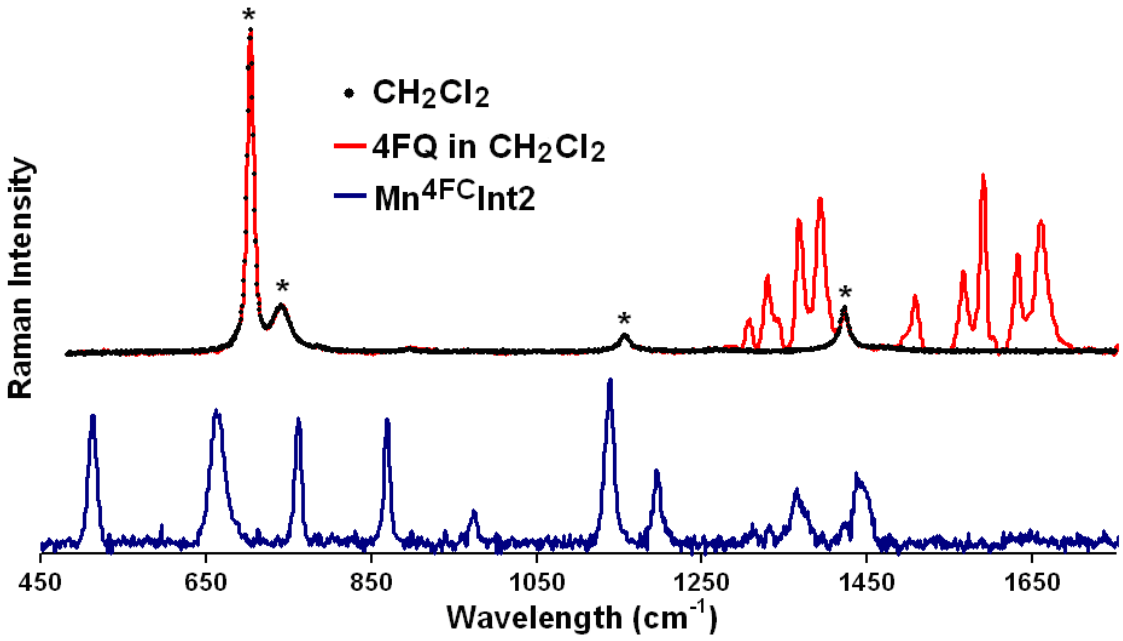

Figure 5.17. Raman spectra collected using 457.9 nm (100 mW) argon ion laser line of 4-fluoroquinone (4FQ, red line) in CH_2Cl_2 (*) prepared by oxidizing 4FC with sodium periodate in CH_2Cl_2.[296] 4FQ vibrations observed at 1,303, 1,329, 1,367, 1393, 1,508, 1,566, 1,590, 1,632, and 1,661 cm^{-1}. The resonance Raman spectrum of Mn^{4FC}Int2 (blue line) collected using 488.0 nm laser excitation is shown for comparison.

5.2.8 Resonance Raman of [Fe(III)-HPCD(4FC)]. For comparison to the intermediate species, the [Fe(III)-4FC] complex was also prepared by first oxidizing Fe-HPCD with potassium persulfate and then adding 4FC to the oxidized enzyme. [Fe(III)-HPCD(4FC)] exhibits an intense blue chromophore with two absorption bands at 430 and 680 nm (Figure 5.18, ε_{430nm} = 1,900 M^{-1} cm^{-1} and ε_{680nm} = 2,000 M^{-1} cm^{-1}) similar to the chromophore observed after inactivation of Fe-HPCD during steady-state turnover of 4ClC (Figure 4.3). The resonance Raman spectrum of [Fe(III)-HPCD(4FC)] (Figure 5.19) is typical of Fe(III)-catecholates.[281, 311-314] In fact it is nearly identical to the spectrum of the self-hydroxylated blue-green metal substituted extradiol-cleaving catechol dioxygenase complex [Fe(III)-MndD-DOPA] ($\varepsilon_{675\ nm}$ = 750 M^{-1} cm^{-1})

(Table 4.6), except for the addition of a band at 1,137 cm^{-1} that may be assigned to a vibrational mode involving the C-F bond of the halogenated catecholate.[281]

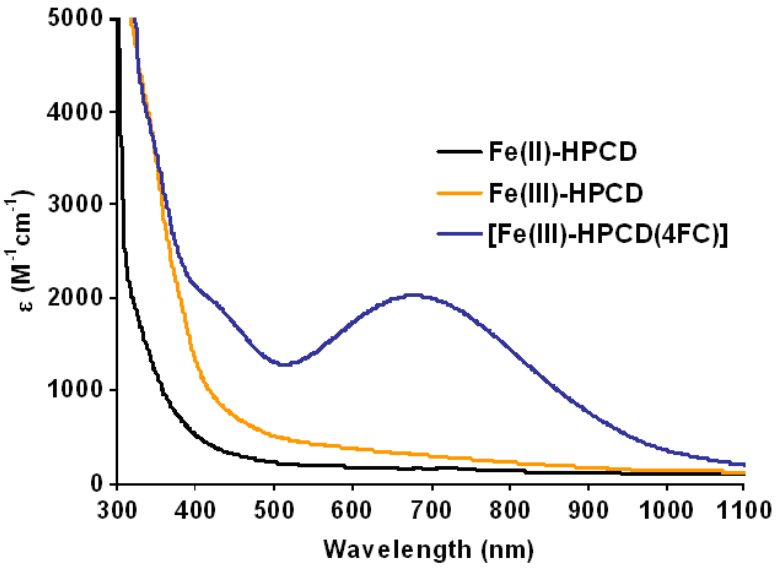

Figure 5.18. UV-Vis spectra of Fe(II)-HPCD (black), and Fe(III)-HPCD (orange) prepared using by oxidizing Fe(II)-HPCD with 4 equivalents of $K_2S_2O_8$. Anaerobic enzyme-substrate complex of [Fe(III)-HPCD(4FC)] (blue, ε_{430nm} = 1,900 M^{-1} cm^{-1} and ε_{680nm} = 2,000 M^{-1} cm^{-1}).

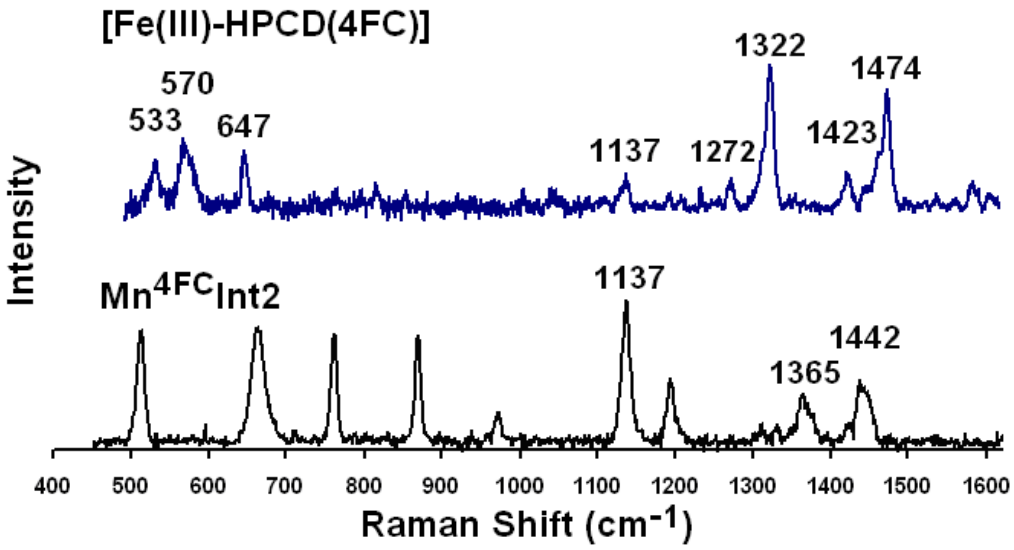

Figure 5.19. Resonance Raman spectra of [Fe(III)-HPCD(4FC)] (blue) collected using 647.1 nm laser excitation. Resonance Raman spectrum of Mn^{4FC}Int2 (black) collected using 488.0 nm laser excitation is shown for comparison.

UV-Vis spectroscopy suggests that the free 4FQ and the Co/Mn^{4XC}Int2 intermediates have similar chromophores, whereas the resonances Raman data of the intermediates are more consistent with a [M-semiquinone] formulation. One possible explanation for the inconsistency of the resonance Raman and UV-Vis data of the Co/Mn^{4XC}Int2 intermediates could be due to photoreduction of the quinone by the intense laser beam. This hypothesis was tested by using K_2SO_4 as an internal standard for resonance Raman experiments on a frozen sample of M^{4FC}Int2 (M = Mn, Co) and then comparing the intensity of the enhanced vibrations of the intermediate to the internal standard after extended exposure to the laser. Resonance Raman experiments on frozen samples of Co^{4FC}Int2 were unsuccessful in observing any of the vibrations of the intermediates. Fortunately, the chromophore of Mn^{4FC}Int2 is shifted substantially to lower energies away from the absorption of the protein in the near-UV at 280 nm and the

chromophore of the extradiol ring-cleaved product at 385 nm allowing us to collect resonance Raman spectra on frozen samples of Mn^{4FC}Int2 with less fluorescence background. No change in the ratio of the intensity of the intermediate vibration at 873 cm^{-1} relative to the intensity of the internal standard peak at 984 cm^{-1} was observed for one minute scans over 15 minutes of exposure to the laser (488.0 nm 100 mW) (Figure 5.20), suggesting that no significant photoreduction occurred.

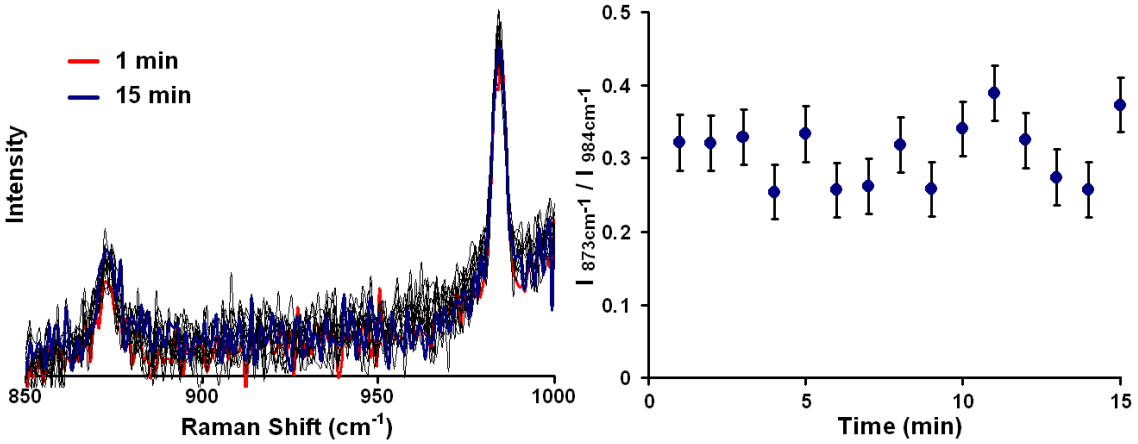

Figure 5.20. (Left) Resonance Raman spectra collected using 488.0 nm argon laser line at 100mW power on a frozen sample of Mn^{4FC}Int2 frozen at 2 sec with K_2SO_4 internal standard (984 cm^{-1}). Spectra were collected every minute for 15 min at 77 K. (Right) Ratio of intermediate peak at 873 cm^{-1} to internal standard peak at 984 cm^{-1} over 15 min showing no change in intensity of intermediate peak during prolonged irradiation with the laser.

5.3 Discussion

5.3.1 Reactivity of Mn-HPCD with 4XCs. In Chapter 4 we reported steady-state and transient kinetic experiments with Co-HPCD and the 4XCs and the characterization of two intermediates in the reaction of the enzyme-substrate complexes with O_2. Based on the available UV-Vis, EPR and kinetic data Co^{4XC}Int1 was assigned to a low-spin [Co(III)($SQ^{\bullet}$)(hydro)peroxo] species and Co^{4XC}Int2 was assigned to a high-spin

[Co(II)(Q)(hydro)peroxo] species. Here we examined the analogous reaction of the 4XCs with Mn-HPCD. Mn-HPCD was found to turn over the 4XC substrates to produce the extradiol-ring cleaved products but at significantly slower rates than for Co-HPCD. The apparent affinity ($K_M^{catechol}$) of Mn-HPCD toward both 4XCs and O_2 decreased dramatically compared to the native substrate HPCA.[131] This could be rationalized by a loss of substrate specificity conferred by the proteins anion binding pocket as well as slower electron transfer from the electron deficient catechol substrates upon O_2 binding. The lower k_{cat} and higher K_M values for the 4XCs compared to HPCA result in a decrease in the catalytic efficiency for both O_2 (k_{cat}/K_M^{O2}), and the catechol ($k_{cat}/K_M^{catechol}$) suggesting that the rates of both O_2 and catechol binding have decreased and that the rate determining step for the turnover of the 4XCs by Mn-HPCD has shifted from a step late in the product formation sequence with HPCA to a step reversibly connected with O_2 binding in the turnover of the 4XCs.

5.3.2 Characterization of transient intermediates Mn^{4XC}Int1 and Int2. Two intermediate species were detected in transient kinetic experiments upon reaction of [Mn-HPCD(4XC)] enzyme-substrate complexes with O_2, as was also observed with the reaction with Co-HPCD. Whereas Co^{4XC}Int1 was colorless, Mn^{4XC}Int1 exhibits a chromophore at 455 nm for 4ClC EPR studies suggested that Co^{4XC}Int1 has a low-spin Co(III) metal center, while Mn^{4XC}Int1 is a high-spin Mn(II) species. Therefore Co^{4XC}Int1 and Mn^{4XC}Int1 do not appear to be analogous species. The similar chromophores exhibited by Mn^{4XC}Int1 and Int2 could suggest that they are just different isomers of the same species where one species is a quinone-hydroperoxo and the other is quinone-peroxo species or one has a side-on and the other an end-on bound O_2-species.

Co^{4XC}Int2 and Mn^{4XC}Int2 on the other hand have very similar intense chromophores and both have EPR spectra consistent with high-spin M(II) centers. Based on the UV-Vis and EPR data these species can be assigned to [M(II)(Q)(hydro)peroxo] species. Resonance Raman characterization of the M^{4XC}Int2 species shows that the chromophore originates from an oxidized catechol species. The observed resonance enhanced vibrations between 1350–1450 cm^{-1} suggests that the M^{4XC}Int2 are metal-semiquinones, which conflicts with the initial assignment of these intermediates to [M(II)(Q)(hydro)peroxo] species. Based then on the EPR and resonance Raman data these species might be assigned to the illusive [M(II)($SQ^{\bullet}$)$O_2^{\bullet-}$] diradical pair, where the two radicals are antiferromagnetically coupled to each other. This species may be trapped by localization of the semiquinone radical onto C4 of the ring by the electron withdrawing halogen substituent, as was suggested for the Co^{4XC}Int1 semiquinone intermediates, slowing the attack of the superoxide on the substrate. Other possible explanations to explain the apparent contradiction between the UV-Vis data and resonance Raman data may be extensive backbonding from the metal center into the quinone π* orbital or strong hydrogen bonding interactions with the quinone from the His200 or Tyr257, which weaken (C-O) vibration.

5.3.3 Identity of the reactive pair. The steady-state and transient kinetic experiments suggest that the rate determining step under saturating O_2 conditions in the turnover of the 4XC by Mn- and Co-HPCD is the decay of M^{4XC}Int2, which was assigned to either a [M(II)(4XQ)(hydro)peroxo] or a [M(II)($SQ^{\bullet}$)$O_2^{\bullet-}$] species. If M^{4XC}Int2 is a [M(II)(4XQ)(hydro)peroxo] species, then the rate determining step would be formation of the bridging alkylperoxo species formed by nucleophilic attack of the peroxo on the

quinone. However, if M^{4XC}Int2 is formulated as [M(II)($SQ^{\bullet}$)$O_2^{\bullet-}$], the rate determining step would be pairing of the two radicals. A definite trend in the decay of M^{4XC}Int2 was observed in stopped-flow experiments where k_3 was the slowest for 4FC and the fastest with 4BrC; this trend is inconsistent with attack of a peroxo on a quinone since one may expect this step would be faster with the more electrophilic 4FQ species**.** Localization of the semiquinone radical to C4 of the ring may be more efficient with $4FSQ^{\bullet}$ consistent with the trend observed in the decay of M^{4XC}Int2 by slowing the attack of the superoxide on the ring.

5.3.4 More questions. The kinetic and spectroscopic experiments reported here with the 4XCs and the metal-substituted catechol dioxygenases may provoke more questions than they answer. Besides difficulties definitively assigning the nature of M^{4XC}Int2, the observed differences in reactivity of the three metals in the turnover of the 4XCs are puzzling. Whereas Fe-HPCD quickly becomes inactive during the turnover of 4XCs, the turnover of the 4XCs by Co-HPCD was found to be faster than Mn-HPCD, despite the higher standard redox potential of Co. These differences in reactivity result in unanswered questions as to the effect of the different electronic and physical properties of the metal center and the catechol substrate on the individual rates and even mechanism of the reaction. Some specifically questions that need to be addressed include: the effects of the different redox potentials, spin states, and Lewis acidities of the three metals on the reaction rates and the mechanism. As well as the effect of the substrates analogues different redox potentials, pK_as and different specificities for the substrate binding pocket on the reaction rates and the mechanism. DFT studies may be useful to interpret the spectroscopic and kinetic data reported in Chapters 3 and 4, and to test the validity of the

arguments used to assign the intermediates. Specific questions of interest include: (1) the effects of localizing the semiquinone radical to different positions of the semiquinone ring on the calculated optical, vibrational, and EPR spectra, (2) the effect of a spin-transition observed for Co-HPCD on the reaction coordinate or mechanism,[130] and (3) the effect of ferromagnetic or antiferromagnetic coupling of the $SQ^{\bullet}$ to the metal center on its optical spectrum of the $SQ^{\bullet}$.[287]

5.4 Intermediates Trapped and Characterized with M-HPCDs.

Table 5.4 lists all the intermediate species trapped and characterized to date in transient kinetic solution studies using Fe-, Mn-, and Co-substituted HPCDs, active site mutants and catecholic substrate analogues. Table 5.4 also gives optical data as well as electronic structure information deduced from EPR and Mössbauer spectroscopic characterization that can be used to assign the metal oxidation and spin state, as well as the oxidation states of the catechol substrate and the bound O_2-adduct.

With the wild-type system (ie wt-Fe-HPCD and HPCA) the only observable O_2-intermediate (Fe^{HPCA}Int1) in solution studies forms in ~70% yield at 10 ms.[149, 166] Stopped flow experiments suggested that that Fe^{HPCA}Int1 is colorless and that its formation is not reversibly connected to O_2 binding. Fe^{HPCA}Int1 was characterized by Mössbauer to have a high-spin-Fe(II) metal center. Based on the kinetic and spectroscopic evidence Fe^{HPCA}Int1 was assigned to the proposed bridging alkylperoxo species.[149] The rapid formation of a bridging alkylperoxo species suggested that Nature had tuned the active site to rapidly activate both substrates to form the alkylperoxo species. The authors suggested that O_2 activation and substrate oxidation proceed

simultaneously with electron transfer from the catechol substrate to O_2 via the metal center upon O_2 binding to form a [Fe(II)($SQ^{\bullet}$)- $O_2^{\bullet-}$] diradical species with the $SQ^{\bullet}$ radical localized to C2 of the ring by interactions between the $SQ^{\bullet}$ with second sphere amino acid residues Y257.[149, 161, 163] Likewise H200 interaction with the superoxide adduct aligns it to attack the semiquinone radical.[130, 149, 162, 165] The paramagnetic high-spin Fe(II) active site and second sphere amino acid residues are thus poised to rapidly perform this transformation.

Upon disrupting the native system by either substituting the metal center,[130, 169, 179] mutating the key active site amino acid residues H200[130, 149, 162] or Y257,[161, 163] or replacing the native substrate with more electron-poor substrate analogs, the reaction energy surface is perturbed, resulting in the stabilization of other electronic tautomers of the ternary enzyme-substrate-O_2 complex. Each trapped intermediate is at a different stage along the reductive O_2 activation and substrate oxidation pathway, all are catalytically competent to form the extradiol ring-cleaved product though at much decreased rates than the native system. Nearly every possible electronic configuration has now been observed from an initial [M(II)(catecholate)O_2] species ($Y257F^{HPCA}$Int1)[161], several [M(III)(catecholate)$O_2^{\bullet-}$] superoxide species (Mn^{HPCA}Int1,[179] H200NFe^{4NC}Int1,[162, 167] Co^{4NC},[130] and H200NCo^{4NC} [130]), a possible diradical pair species [M(II)($SQ^{\bullet}$)$O_2^{\bullet-}$] (Co/Mn^{4XC}Int2), several [M(II)($SQ^{\bullet}$)(hydro)peroxo] species (H200NFe^{HPCA}Int1,[149, 167] Mn^{HPCA}Int1,[179] Co^{4XC}Int1, H200NCo^{HPCA}), and several possible [M(II)(Q)peroxo] species (Y257FFe^{HPCA}Int2,[161, 163] Mn^{4XC}Int1, Mn^{4XC}Int2,Co^{4XC}Int2).

Table 5.4 Intermediates characterized in solution reactions of M-HPCD enzyme-substrate complexes with O_2.

Intermediate	Metal Spin/Oxidation State	λ_{max} (nm) (ε, $M^{-1}cm^{-1}$)	Assignment	Ref
Fe^{HPCA}Int1	hs-Fe^{II}	no	[Fe(II)-alkylperoxo]	149, 166
H200NFe^{HPCA}Int1	hs-Fe^{III} afc radical (S = 2)	395 (3,200), 610(1,100)	[Fe(III)($SQ^{\bullet}$)(hydro)peroxo]	149, 167
H200NFe^{HPCA}Int2	hs-Fe^{II}	no	[Fe(II)-alkylperoxo]	149, 167
H200NFe^{4NC}Int1	hs-Fe^{III} afc radical (S = 2)	506 (~10,000), 630 (~1,200)	[Fe(III)(4NC)$O_2^{\bullet-}$]	162, 167
H200NFe^{4NC}Int2	hs-Fe^{III} afc radical (S = 2)	405 (~15,000), 675 (~1,000)	[Fe(III)($SQ^{\bullet}$)(hydro)peroxo]	162, 167
Y257FFe^{HPCA}Int1	hs-Fe^{II}	no	[Fe(II)(HPCA)O_2]	161
Y257FFe^{HPCA}Int2	hs-Fe^{II}	425 (~10,500)	[Fe(III)(Q)(hydro)peroxo]	161
Mn^{HPCA}Int1	hs-Mn^{III} fc radical (S = 5/2)	no	[Mn(III)(HPCA)$O_2^{\bullet-}$] or [Mn(III)($SQ^{\bullet}$)(hydro)peroxo]	169
Mn^{HPCA}Int2	hs-MnII (S = 5/2)	no	[Mn(II)-alkylperoxo]	169
Mn^{4XC}Int1	hs-Mn^{II} (S = 5/2)	455 (~5,000)	[Mn(II)(Q)(hydro)peroxo] or [Mn(II)($SQ^{\bullet}$)$O_2^{\bullet-}$]	This work
Mn^{4XC}Int2	hs-Mn^{II} (S = 5/2)	470–480 (~20,000)	[Mn(II)(Q)(hydro)peroxo] or [Mn(II)($SQ^{\bullet}$)$O_2^{\bullet-}$]	This work
Co^{HPCA}Int1	ls-Co^{III} (S = 1/2)	no	[Co(III)($SQ^{\bullet}$)(hydro)peroxo]	This work
Co^{HPCA}Int2	hs-Co^{II} (S = 3/2)	550 nm	[Co(II)-alkylperoxo]	This work
Co^{4XC}Int1	ls-Co^{III} radical	no	[Co(II)(SQ)(hydro)peroxo]	This work
Co^{4XC}Int2	hs-Co^{II} (S = 3/2)	453–467 (8,000–11,000)	[Co(II)(Q)(hydro)peroxo] or [Co(II)($SQ^{\bullet}$)$O_2^{\bullet-}$]	This work
H200NCo^{HPCA}	ls-Co^{III} (S = 1/2)	no	[Co(III)($SQ^{\bullet}$)(hydro)peroxo]	This work
Co^{4NC}	ls-Co^{III} (S = 1/2)	390 (~7,000), 526 (~13,000) pH 6.0	[Co(III)(4NC)$O_2^{\bullet-}$]	130
H200NCo^{4NC}	ls-Co^{III} (S = 1/2)	390 (~7,000), 530 (~14,000) pH 6.0	[Co(III)(4NC)$O_2^{\bullet-}$]	130

[a]Abbreviations used: HPCA, homoprotocatechuate; 4NC, 4-nitrocatechol; 4XC, 4-halocatechol (X = F, Cl, or Br); HPCD, SQ, semiquinone; Q, quinone; hs, high-spin; ls, low-spin; afc, antiferromagnetically coupled; fc, ferromagnetically coupled.

5.5 Experimental Procedures

5.5.1 Preparation of M(II)-HPCD. Metal-substituted HPCDs were prepared by growing *E. coli* BL21(DE3) carrying plasmid pWZW204 containing the HPCD gene from *Brevibacterium fuscum* as previously described.[2,4,8,17] Upon inducing protein expression with isopropyl-β-D-thiogalactopyranoside (IPTG), the cultures were supplemented with 30 mg/L of an appropriate $M(II)Cl_2$ salt. The cells were then harvested and protein purified as previously described.[18] Some of the Mn-HPCD used in these experiments was prepared by was former Que lab member Dr. Erik R. Farquhar.

5.5.2 ICP-AES metal analysis. Metal incorporation was measured by ICP-AES metal analysis at the Soil Research Analytical Laboratory (College of Food, Agricultural and Natural Resource Sciences, University of Minnesota). Samples were prepared for ICP-AES analysis by digesting 2 ppm protein in 5% HNO_3 overnight and then removing precipitated protein by centrifugation.

5.5.3 Steady-state kinetics. Enzyme activity was measured in oxygenated 50 mM MOPS buffer (pH 7.5) at 4 °C and 22 °C using a Beckman DU 640 spectrophotometer. Reactions were followed by monitoring the formation of the yellow extradiol cleavage product (Table 4.7).

Catechol concentrations ranging from 1 μM to 3 mM were used to determine the $K_M^{catechol}$ with Mn-HPCD concentration ranging from 1.6 to 3.3 μM [Mn]. All other steady-state assays used 3 mM 4XC to be under pseudo first order catechol concentrations. Metal-substituted Mn-HPCD was treated with 1 mM H_2O_2 during purification to inactivate any Fe-HPCD present in the preparation. Fe-HPCD was

incubated with 1 mM ascorbate to fully reduce the enzyme prior to each assay.[131, 169] Prior to experiments with halogenated catechols enzyme activity were checked by assaying activity under previously reported conditions with HPCA (22 °C 50 mM MOPS pH 7.8).[131, 169] K_M^{O2} values were determined by performing the reaction under different O_2 concentrations by mixing known volumes of anaerobic, air-saturated and O_2 saturated buffer (1 atm) and at higher O_2 concentrations by equilibrating the buffer and enzyme under 2 or 3 atm of O_2 in a sealed cuvette and then inducing the reaction by the addition of the catechol substrate. A Clark-type oxygen electrode (Oxytherm from Hansatech Instruments) was also used to measure the rate of O_2 consumption in air-saturated buffer at 4 and 22 °C. Steady-state rates measured using oxygen electrode agreed well with rates measured by following formation of the yellow extradiol ring-cleaved product by UV-Vis. The apparent kinetic parameters k_{cat} and K_M were determined using nonlinear regression fits of initial velocities to the Michaelis-Menten equation from initial velocities. k_{cat} values were calculated by dividing the maximum velocity from nonlinear regression by the average metal concentration from ICP-AES metal analysis.

5.5.4 Presteady-state kinetics. Solutions of Mn- or Co-HPCD in air-saturated 100 mM MOPS buffer (pH 7.5) was rapidly mixed with 10 mM solutions of HPCA or 4ClC using an Applied Photophysics model SX.18MV stopped-flow device at 4 °C. The formation of the yellow extradiol ring-cleaved product was monitored at 380 nm for HPCA and 385 nm for 4ClC. Final concentrations of reagents upon mixing were 5 mM catechol, 0.21 to 1.21 mM O_2, 65 μM Mn-HPCD, or 115 nM Co-HPCD for reactions with HPCA and 2.3 μM Co-HPCD for reactions with 4ClC.

5.5.5 Stopped-flow experiments. Anaerobic [Mn-HPCD(4XC)] was rapidly mixed with oxygenated 100 mM MOPS buffer (pH 7.5) using an Applied Photophysics model SX.18MV stopped-flow device at 4 °C. The concentrations of reagents after mixing were 600 μM 4XC and 720 μM Mn-HPCD. The formation of the extradiol cleavage product was monitored at 380 nm using a 2 mm path length while formation and decay of the chromophoric intermediate was monitored at 475 nm where the yellow ring-cleaved product does not absorb, using a 1 cm path length. O_2 concentrations after mixing ranged from 604 to 1,000 μM O_2 at 4 °C.[166]

5.5.6 EPR sample preparation and spectroscopic methods. Anaerobic EPR samples were made to a volume of 300 μL, with 300 μM [Mn- HPCD(4XC)] in 100 mM MOPS buffer (pH 7.5) by purging enzyme and substrate under argon before mixing. Samples were then transferred to EPR tubes in a glove box and frozen by slow immersion in liquid nitrogen. EPR spectra were recorded on a Bruker Elexsys E-500 spectrometer equipped with an Oxford Instruments ESR-10 liquid helium cryostat at X-band (9.64 GHz). Mn-HPCD EPR spectra were acquired at 10 K and 0.2 mW power, 10 G modulation amplitude, and 100 kHz modulation frequency.

5.5.7 Rapid freeze-quench experiments. Anaerobic enzyme-substrates complexes were prepared in a Coy anaerobic glove box. The starting point EPR sample was prepared by taking an aliquot of the enzyme-substrate complex and diluted it by 1/2 using anaerobic buffer in a glove box. The sample was then transferred to a sealed EPR tube, which was frozen by slowly submerging the EPR tube in liquid nitrogen. The rest of the pre-formed enzyme-substrate complex was loaded in to a syringe of a RFQ apparatus

(model 1019) cooled to 4 °C. The enzyme-substrate complex was rapidly mixed with an equal volume of O_2-saturated buffer (1 atm at 4 °C) and passed through a calibrated ageing loop before being rapidly frozen on two counter-rotating aluminum wheels partially submerged in liquid nitrogen.[149] Scraping the wheels with liquid nitrogen cooled plastic scrapers produced a powdered sample that was packed into EPR tubes submerged in liquid nitrogen. Rapid freeze-quench samples aged for less than 1.5 sec were prepared on the RFQ apparatus as previously described.[149] Samples aged for longer times were prepared by rapidly mixing equal volumes of the O_2-saturated buffer and enzyme substrate complex in an EPR tube at 4 °C and then rapidly freezing the sample by quickly immersing it in an isopentane liquid nitrogen-cooled slurry (~160 °C). These reactions were filmed using a video camera. The video was then reviewed and the reaction timed using a stopwatch to more accurately measure the age of the sample upon freezing.

5.5.8 Resonance Raman experiments. Resonance Raman spectra were collected on an Acton AM-506 spectrophotometer (1,200 groove rating) using Kaiser Optical Systems holographic supernotch filters and a Princeton Instruments liquid N_2-cooled CCD detector (LN^{-1}100PB) with 4 cm^{-1} spectral resolution. Spectra were collected at 100 mW laser power using a Spectra Physics 2030–15 argon ion laser (488.0 nm). Raman frequencies were referenced to indene standard with an accuracy of ±1 cm^{-1}. Raman spectra were collected at 4 °C by 90° scattering from a flat bottomed NMR tube. Spectra were collected using 5–20 sec scan intervals collected for ~60 separate reactions of 150 μL solutions of preformed anaerobic [M-HPCD(4XC)] complex with 150 μL oxygen-saturated 100 mM MOPS (pH 7.5) buffer (1 atm 4 °C). Concentrations upon

mixing: 1 mM O_2, 250 μM, [M] M-HPCD and 230 μM 4XC. Spectra of the transient Mn^{4XC}Int2 where collected from 450–1,500 cm^{-1} except for 4ClC and 4FC where a second overlapping window was obtained up to 1,800 cm^{-1}. The florescent background was subtracted before normalizing spectra to the nonresonance enhanced buffer peak at 1,045 cm^{-1} and splicing normalized spectra together. Baseline corrections (polynomial fits) were applied using Gram/32 Spectral Notebook (ThermoGalactic). Difference resonance Raman spectra of resonance enhanced transient intermediates were obtained by subtracting the spectra of the ring-cleaved product and buffer.

References

(1) Van der Donk, W. A.; Krebs, C; Bollinger, J. M. Jr., Substrate activation by iron superoxo intermeidates. *Curr. Opin. Struct. Biol.* **2010,** *20*, 673–683.

(2) Bugg, T. D. H., Dioxygenase enzymes: Catalytic mechanisms and chemical models. *Tetrahedron* **2003,** *59*, 7075–7101.

(3) Bruijnincx, P. C. A.; van Koten, G.; Klein Gebbink, R. J. M., Mononuclear non-heme iron enzymes with the 2-His-1-carboxylate facial triad: Recent developments in enzymology and modeling studies. *Chem. Soc. Rev.* **2008,** *37*, 2716–2744.

(4) Bugg, T. D. H.; Gang, L., Solving the riddle of the intradiol and extradiol catechol dioxygenases: How do enzymes control hydroperoxide rearrangements? *Chem. Commun.* **2001,** 941–952.

(5) Bugg, T. D. H.; Ramaswamy, S., Non-heme iron-dependent dioxygenases: Unravelling catalytic mechanisms for complex enzymatic oxidations. *Curr. Opin. Chem. Biol.* **2008,** *12*, 134–140.

(6) Fetzner, S., Ring-cleaving dioxygenases with a cupin fold. *Appl. Environ. Microbiol.* **2012,** *78*, 2505–2514.

(7) Lipscomb, John D., Mechanism of extradiol aromatic ring-cleaving dioxygenases. *Curr. Opin. Chem. Biol.* **2008,** *18*, 644–649.

(8) Vaillancourt, F. H., The ins and outs of ring-cleaving dioxygenases. *Crit. Rev. Biochem. Mol. Biol.* **2006,** *41*, 241–267.

(9) Xin, M.; Bugg, T. D. H., Evidence from mechanistic probes for distinct hydroperoxide rearrangement mechanisms in the intradiol and extradiol catechol dioxygenases. *J. Am. Chem. Soc.* **2008,** *130*, 10422–10430.

(10) Leuenberger, M. G.; Engeloch-Jarret, C.; Woggon, W.- D., The reaction mechanism of the enzyme-catalyzed central cleavage of β-carotene to retinal. *Angew. Chem. Int. Edit.* **2001,** *40*, 2613–2617.

(11) Marasco, E. K.; Schmidt-Dannert, C., Identification of bacterial carotenoid cleavage dioxygenase homologues that cleave the interphenyl α, β double bond of stilbene derivatives via a monooxygenase reaction. *ChemBioChem* **2008,** *9*, 1450–1461.

(12) Schmidt, H.; Kurtzer, R.; Eisenreich, W.; Schwab, W., The carotenase AtCCD1 from *Arabidopsis thaliana* is a dioxygenase. *J. Biol. Chem.* **2006,** *281*, 9845–9851.

(13) Cicchillo, R. M.; Zhang, H.; Blodgett, J.A. V.; Whitteck, J. T.; Li, G.; Nair, S. K.; van der Donk, W. A. ; Metcalf, W. W., An unusual carbon-carbon bond cleavage reaction during phosphinothricin biosynthesis. *Nature* **2009,** *459*, 871–874.

(14) Du, L.; Gao, J.; Liu, Y.; Zhang, D.; Liu, C., The reaction mechanism of hydroxyethylphosphonate dioxygenase: A QM/MM study. *Org. Biolmol. Chem.* **2012,** *10*, 1014–1024.

(15) Hirao, H.; Morokuma, K., Ferric superoxide and ferric hydroxide are used in the catalytic mechanism of hydroxyethylphosphonate dioxygenase: A density functional theory investigation. *J. Am. Chem. Soc.* **2010,** *132*, 17901–17909.

(16) Hirao, H.; Morokuma, K., ONIOM(DFT:MM) study of 2-hydroxyethylphosphonate dioxygenase: What determines the destinies of different substrates? *J. Am. Chem. Soc.* **2011,** *133*, 14550–14553.

(17) Nair, S. K.; van der Donk, W. A., Structure and mechanism of enzymes involved in biosynthesis and breakdown of the phosphonates fosfomycin, dehydrophos, and phosphinothricin. *Arch. Biochem. Biophys.* **2011,** *505*, 13–21.
(18) Peck, S. C.; Cooke, H. A.; Cicchillo, R. M.; Malova, P.; Hammerschmidt, F.; Nair, S. K.; van der Donk, W. A., Mechanism and substrate recognition of 2-hydroxyethylphosphonate dioxygenase. *Biochemistry* **2011,** *50*, 6598–6605.
(19) Whitteck, J. T.; Cicchillo, R. M.; van der Donk, W. A., Hydroperoxylation by hydroxyethylphosphonate dioxygenase. *J. Am. Chem. Soc.* **2009,** *131*, 16225–16232.
(20) Whitteck, J. T.; Malova, P.; Peck, S.C.; Cicchillo, R. M.; Hammerschmidt, F.; van der Donk, W. A., On the stereochemistry of 2-hydroxyethylphosphonate dioxygenase. *J. Am. Chem. Soc.* **2011,** *133*, 4236–4239.
(21) Hausinger, R. P., Fe(II)/α-ketoglutarate-dependent hydroxylases and related enzymes. *Crit. Rev. Biochem. Mol. Biol.* **2004,** *39*, 21–68.
(22) Hewitson, K. S.; Granatino, N.; Welford, R. W. D.; McDonough, M. A.; Schofield, C. J., Oxidation by 2-oxogluterate oxygenases: Non-haem iron systems in catalysis and signaling. *Phil. Trans. R. Soc. A* **2005,** *363*, 807–828.
(23) Li, T.; Huo, L.; Pulley, C.; Liu, A., Decarboxylation mechanisms in biological system. *Bioorg. Chem.* **2012,** *43*, 2–14.
(24) Mantri, M.; Zhang, Z.; McDonoug, M. A.; Schofield, C. J., Autocatalysed oxidative modifications to 2-oxogluterate dependent oxygenases. *FEBS J.* **2012,** *279*, 1563–1575.
(25) Ye, S.; Riplinger, C.; Hansen, A.; Krebs, C.; Bollinger, J. M. Jr., Electronic structure analysis of the oxygen-activation mechanism by Fe^{II}- and α-ketoglutarate (αKG)-dependent dioxygenases. *Chem. Eur. J.* **2012,** *18*, 6555–6567.
(26) Numazawa, M.; Nagaoka, M.; Sohtome, N., Aromatase reaction of 3-deoxyandrogens: Steric mode of the C-19 oxygenation and cleavage of the C10-C19 bond by human placental aromatase. *Biochemistry* **2005,** *44*, 10839–10845.
(27) Korzekwa, K. R.; Trager, W. F.; Smith, S. J.; Osawa, Y.; Gillette, J. R., Theoretical studies on the mechanism of conversion of androgens to estrogens by aromatase. *Biochemistry* **1991,** *30*, 6155–6162.
(28) Ghosh, D.; Griswold, J.; Erman, M.; Pangborn, W., Structural basis for androgen specificity and oestrogen synthesis in human aromatase. *Nature* **2009,** *457*, 219–223.
(29) Akhtar, M.; Wright, J. N.; Lee-Robichaud, P., A review of mechanistic studies on aromatase (CYP19) and 17α-hydroxylase-17,20-lyase (CYP17). *J. Steroid Biochem.* **2011,** *125*, 2–12.
(30) Akhtar, M.; Njar, V. C. O.; Wright, J. N., Mechanistic studies on aromatase and related C–C bond cleaving P-450 enzymes. *J. Steroid Biochem.* **1993,** *44*, 375–387.
(31) Zhang, Y.; Colabroy, K. L.; Begley, T. P.; Ealick, S. E., Structural studies on 3-hydroxyanthranilate-3,4-dioxygenase: The catalytic mechanism of a complex oxidation involved in NAD biosynthesis. *Biochemistry* **2005,** *44*, 7632–7643.
(32) Li, X.; Guo, M.; Fan, J.; Tang, W.; Wang, D.; Ge, H.; Rong, H.; Teng, M.; Niu, L.; Liu, Q.; Hao, Q., Crystal structure of 3-hydroxyanthranilic acid 3,4-dioxygenase from *Saccharomyces cerevisiae*: A special subgroup of the type III extradiol dioxygenases. *Protein Sci.* **2006,** *15*.

(33) Moonen, M. J. H.; Synowsky, S. A.; van den Berg, W. A. M.; Westphal, A. H.; Heck, A. J. R.; van den Heuvel, R. H. H.; Fraaije, M. W.; van Berkel, W. J. H., Hydroquinone dioxygenase from *Pseudomonas fluorescens* ACB: A novel member of the family of nonheme-iron(II)-dependent dioxygenases. *J. Bacteriol* **2008,** *190*, 5199–5209.
(34) Da Vela, S.; Ferraroni, M.; Kolvenbach, B. A.; Keller, E.; Corvini, P. F. X.; Scozzafava, A.; Briganti, F., Crystallization and preliminary X-ray crystallographic analysis of hydroquinone dioxygenase from *Sphingomonas sp.* TTNP3. *Acta. Cryst.* **2012,** *68*, 588–590.
(35) Machonkin, T. E.; Doerner, A. E., Substrate specificity of *Sphingobium chlorophenolicum* 2,6-dichlorohydroquinone 1,2-dioxygenase. *Biochemistry* **2011,** *50*, 8899–8913.
(36) Machonkin, T.; Holland, P.; Smith, K.; Liberman, J.; Dinescu, A.; Cundari, T.; Rocks, S., Determination of the active site of; *Sphingobium chlorophenolicum*; 2,6-dichlorohydroquinone dioxygenase (PcpA). *J. Biol. Inorg. Chem.* **2010,** *15*, 291–301.
(37) Matera, I.; Ferraroni, M.; Bürger, S.; Scozzafava, A.; Stolz, A.; Briganti, F., Salicylate 1,2-dioxygenase from *Pseudaminobacter salicylatoxidans*: Crystal structure of a peculiar ring-cleaving dioxygenase. *J. Mol. Biol.* **2008,** *380*, 856–868.
(38) Chen, J.; Li, W.; Wang, M.; Zhu, G.; Liu, D.; Sun, F.; Hao, N.; Li, X.; Rao, Z.; Zhang, X. C., Crystal structure and mutagenic analysis of GDOsp, a gentisate 1,2-dioxygenase from *Silicibacter pomeroyi*. *Protein Sci.* **2008,** *17*, 1362–1373.
(39) Steiner, R. A.; Kalk, K. H.; Dijkstra, B. W., Anaerobic enzyme-substrate structures provide insight into the reaction mechanism of the copper-dependent quercetin 2,3-dioxygenase. *Proc. Natl. Acad. Sci. U.S.A.* **2002,** *99*, 16625–16630.
(40) Siegbahn, P. E. M., Hybrid DFT study of the mechanism of quercetin 2,3-dioxygenase. *Inorg. Chem.* **2004,** *43*, 5944–5953.
(41) Schaab, M. R.; Barney, B. M.; Francisco, W. A., Kinetic and spectroscopic studies on the quercetin 2,3-dioxygenase from *Bacillus subtilis*. *Biochemistry* **2006,** *45*, 1009–1016.
(42) Kumar, M. R.; Zapata, A.; Ramirez, A. J.; Bowen, S. K.; Francisco, W. A.; Farmer, P. J., Nitrosyl hydride (HNO) replaces dioxygen in nitroxygenase activity of manganese quercetin dioxygenase. *Proc. Natl. Acad. Sci. U.S.A.* **2011,** *108*, 18926–18931.
(43) Fiorucci, Sébastien; Golebiowski, Jérome; Cabrol-Bass, Daniel; Antonczak, Serge, Oxygenolysis of flavonoid compounds: DFT description of the mechanism for quercetin. *ChemPhysChem* **2004,** *5*, 1726-1733.
(44) Sakamoto, H.; Takahashi, K.; Higashimoto, Y.; Harada, S.; Palmer, G.; Noguchi, M., A kinetic study of the mechanism of conversion of alpha-hydroxyheme to verdoheme while bound to heme oxygenase. *Biochem. Bioph. Res. Co.* **2005,** *338*, 578–583.
(45) Sakamoto, H.; Omata, Y.; Hayashi, S.; Harada, S.; Palmer, G.; Noguchi, M., The reactivity of α-hydroxyhaem and verdohaem bound to haem oxygenase-1 to dioxygen and sodium dithionite. *Eur. J. Biochem.* **2002,** *269*, 5231–5239.
(46) Matsui, Toshitaka; Unno, Masaki; Ikeda-Saito, Masao, Heme oxygenase reveals its strategy for catalyzing three successive oxygenation reactions. *Acc. Chem. Res.* **2009,** *43*, 240–247.

(47) Matsui, T.; Iwasaki, M.; Sugiyama, R.; Unno, M.; Ikeda-Saito, M., Dioxygen activation for the self-degradation of heme: Reaction mechanism and regulation of heme oxygenase. *Inorg. Chem.* **2010,** *49*, 3602–3609.
(48) Bianchetti, C. M.; Yi, L.; Ragsdale, S. W.; Phillips, G. N., Comparison of apo- and heme-bound crystal structures of a truncated human heme oxygenase-2. *J. Biol. Chem.* **2007,** *282*, 37624–37631.
(49) Liu, Y.; Moënne-Loccoz, P.; Loehr, T. M.; Ortiz de Montellano, P. R., Heme oxygenase-1, intermediates in verdoheme formation and the requirement for reduction equivalents. *J. Biol. Chem.* **1997,** *272*, 6909–6917.
(50) Millett, E. S.; Efimov, I.; Basran, J.; Handa, S.; Mowat, C. G.; Raven, E. L., Heme-containing dioxygenases involved in tryptophan oxidation. *Curr. Opin. Chem. Biol.* **2012,** *16*, 60-66.
(51) Lewis-Ballester, A.; Batabyal, D.; Egawa, T.; Lu, C.; Lin, Y.; Marti, M. A.; Capece, L.; Estrin, D. A.; Yeh, S.-R., Evidence for a ferryl intermediate in a heme-based dioxygenase. *Proc. Natl. Acad. Sci. U.S.A.* **2009,** *106*, 17371–17376.
(52) Kuo, H. H.; Mauk, A. G., Indole peroxygenase activity of indoleamine 2,3-dioxygenase. *Proc. Natl. Acad. Sci. U.S.A.* **2012,** *109*, 13966–13971.
(53) Han, S.; Eltis, L. D.; Timmis, K. N.; Muchmore, S. W.; Bolin, J. T., Crystal structure of the biphenyl-cleaving extradiol dioxygenase from a PCB-degrading pseudomonad. *Science* **1995,** *270*, 976–980.
(54) Geng, J.; Dornevil, K.; Liu, A., Chemical rescue of the distal histidine mutants of tryptophan 2,3-dioxygenase. *J. Am. Chem. Soc.* **2012,** *134*, 12209–12218.
(55) Fu, R.; Gupta, R.; Geng, J.; Dornevil, K.; Wang, S.; Zhang, Y.; Hendrich, M. P.; Liu, A., Enzyme reactivation by hydrogen peroxide in heme-based tryptophan dioxygenase. *J. Biol. Chem.* **2011,** *286*, 26541–26554.
(56) Efimov, I.; Basran, J.; Sun, X.; Chauhan, N.; Chapman, S. K.; Mowat, C. G.; Raven, E. L., The mechanism of substrate inhibition in human indoleamine 2,3-dioxygenase. *J. Am. Chem. Soc.* **2012,** *134*, 3034–3041.
(57) Chung, L. W.; Li, Xin; Sugimoto, H.; Shiro, Y.; Morokuma, K., Density functional theory study on a missing piece in understanding of heme chemistry: The reaction mechanism for indoleamine 2,3-dioxygenase and tryptophan 2,3-dioxygenase. *J. Am. Chem. Soc.* **2008,** *130*, 12299–12309.
(58) Capece, L.; Lewis-Ballester, A.; Batabyal, D.; Di Russo, N.; Yeh, S.-R.; Estrin, D.; Marti, M., The first step of the dioxygenation reaction carried out by tryptophan dioxygenase and indoleamine 2,3-dioxygenase as revealed by quantum mechanical/molecular mechanical studies. *J. Biol. Inorg. Chem.* **2010,** *15*, 811–823.
(59) Warui, D. M.; Li, N.; Nørgaard, H.; Krebs, C.; Bollinger, J. M. Jr.; Booker, S. J., Detection of formate, rather than carbon monoxide, as the stoichiometric coproduct in conversion of fatty aldehydes to alkanes by a cyanobacterial aldehyde decarbonylase. *J. Am. Chem. Soc.* **2011,** *133*, 3316–3319.
(60) Schirmer, A.; Rude, M. A.; Li, X.; Popova, E.; del Cardayre, S. B. , Microbial biosynthesis of alkanes. *Science* **2010,** *329*, 559–562.
(61) Li, N.; Nørgaard, H.; Warui, D. M.; Booker, S. J.; Krebs, C.; Bollinger, J. M. Jr., Conversion of fatty aldehydes to alka(e)nes and formate by a cyanobacterial aldehyde

decarbonylase: Cryptic redox by an unusual dimetal oxygenase. *J. Am. Chem. Soc.* **2011,** *133*, 6158–6161.
(62) Li, N.; Chang, W.-C.; Warui, D. M.; Booker, S. J.; Krebs, C.; Bollinger, J. M. Jr., Evidence for only oxygenative cleavage of aldehydes to alk(a/e)nes and formate by cyanobacterial aldehyde decarbonylases. *Biochemistry* **2012,** *51*, 7908–7916.
(63) Krebs, C.; Bollinger Jr, J. M.; Booker, S. J., Cyanobacterial alkane biosynthesis further expands the catalytic repertoire of the ferritin-like 'di-iron-carboxylate' proteins. *Curr. Opin. Chem. Biol.* **2011,** *15*, 291–303.
(64) Eser, B. E.; Das, D.; Han, J.; Jones, P. R.; Marsh, E. N. G., Oxygen-independent alkane formation by non-heme iron-dependent cyanobacterial aldehyde decarbonylase: Investigation of kinetics and requirement for an external electron donor. *Biochemistry* **2011,** *50*, 10743–10750.
(65) Das, D.; Eser, B. E.; Han, J.; Sciore, A.; Marsh, E. N. G., Oxygen-independent decarbonylation of aldehydes by cyanobacterial aldehyde decarbonylase: A new reaction of diiron enzymes. *Angew. Chem. Int. Edit.* **2011,** *50*, 7148–7152.
(66) Xu, Q.; Schwarzenbacher, R.; Sri Krishna, S.; McMullan, D.; Agarwalla, S.; Quijano, K.; Abdubek, P.; Ambing, E.; Axelrod, H.; Biorac, T.; Canaves, J. M.; Chiu, H.-J.; Elsliger, M.-A.; Grittini, C.; Grzechnik, S. K.; DiDonato, M.; Hale, J.; Hampton, E.; Han, G. W.; Haugen, J.; Hornsby, M.; Jaroszewski, L.; Klock, H. E.; Knuth, M. W.; Koesema, E.; Kreusch, A.; Kuhn, P.; Miller, M. D.; Moy, K.; Nigoghossian, E.; Paulsen, J.; Reyes, R.; Rife, C.; Spraggon, G.; Stevens, R. C.; van den Bedem, H.; Velasquez, J.; White, A.; Wolf, G.; Hodgson, K. O.; Wooley, J.; Deacon, A. M.; Godzik, A.; Lesley, S. A.; Wilson, I. A., Crystal structure of acireductone dioxygenase (ARD) from *Mus musculus* at 2.06 Å resolution. *Proteins* **2006,** *64*, 808–813.
(67) Pochapsky, T. C.; Pochapsky, S. S.; Ju, T.; Hoefler, C.; Liang, J., A refined model for the structure of acireductone dioxygenase from *Klebsiella* ATCC 8724 incorporating residual dipolar couplings. *J. Biomol. NMR* **2006,** *34*, 117–127.
(68) Ju, T.; Goldsmith, R. B.; Chai, S. C.; Maroney, M. J.; Pochapsky, S. S.; Pochapsky, T. C., One protein, two enzymes revisited: A structural entropy switch interconverts the two isoforms of acireductone dioxygenase. *J. Mol. Biol.* **2006,** *363*, 823–834.
(69) Grubel, K.; Ingle, G. K.; Fuller, A. L.; Arif, A. M.; Berreau, L. M., Influence of water on the formation of O_2-reactive divalent metal enolate complexes of relevance to acireductone dioxygenases. *Dalton T.* **2011,** *40*, 10609–10620.
(70) Dai, Y.; Wensink, P. C.; Abeles, R. H., One protein, two enzymes. *J. Biol. Chem.* **1999,** *274*, 1193–1195.
(71) Dai, Y.; Pochapsky, T. C.; Abeles, R. H., Mechanistic studies of two dioxygenases in the methionine salvage pathway of *Klebsiella pneumoniae*. *Biochemistry* **2001,** *40*, 6379–6387.
(72) Berreau, L. M.; Borowski, T.; Grubel, K.; Allpress, C. J.; Wikstrom, J. P.; Germain, M. E.; Rybak-Akimova, E. V.; Tierney, D. L., Mechanistic studies of the O_2-dependent aliphatic carbon carbon bond cleavage reaction of a nickel enolate complex. *Inorg. Chem.* **2011,** *50*, 1047–1057.

(73) Al-Mjeni, F.; Ju, T.; Pochapsky, T. C.; Maroney, M. J., XAS Investigation of the structure and function of Ni in acireductone dioxygenase. *Biochemistry* **2002,** *41*, 6761–6769.
(74) Straganz, G. D.; Nidetzky, B., Reaction coordinate analysis for β-diketone cleavage by the non-heme Fe^{2+}-dependent dioxygenase Dke1. *J. Am. Chem. Soc.* **2005,** *127*, 12306–12314.
(75) Straganz, G. D.; Hofer, H.; Steiner, W.; Nidetzky, B., Electronic substituent effects on the cleavage specificity of a non-heme Fe^{2+}-Dependent β-diketone dioxygenase and their mechanistic implications. *J. Am. Chem. Soc.* **2004,** *126*, 12202–12203.
(76) Straganz, G. D.; Glieder, A.; Brecker, L.; Ribbons, D. W.; Steiner, W., Acetylacetone-cleaving enzyme Dke1: A novel C-C-bond-cleaving enzyme from *Acinetobacter johnsonii*. *Biochem. J.* **2003,** *369*, 573–581.
(77) Leitgeb, S.; Straganz, G. D.; Nidetzky, B., Biochemical characterization and mutational analysis of the mononuclear non-haem Fe^{2+} site in Dke1, a cupin-type dioxygenase from *Acinetobacter johnsonii*. *Biochem. J.* **2009,** *418*, 403–411.
(78) Leitgeb, S.; Nidetzky, B., Enzyme catalytic promiscuity: The nonheme Fe^{2+} center of β-diketone-cleaving dioxygenase Dke1 promotes hydrolysis of activated esters. *Chem. Bio. Chem.* **2010,** *11*, 502–505.
(79) Diebold, A. R.; Neidig, M. L.; Moran, G. R.; Straganz, G. D.; Solomon, E. I., The three-his triad in Dke1: Comparisons to the classical facial triad. *Biochemistry* **2010,** *49*, 6945–6952.
(80) Hopper, D. J.; Kaderbhai, M. A., 2,4'-Dihydroxyacetophenone dioxygenase from *Alcaligenes sp.* 4HAP: A novel enzyme with an atypical dioxygenase sequence. *Biochem. J.* **1999,** *344*, 397–402.
(81) Cooke, H. A.; Peck, S. C.; Evans, B. S.; van der Donk, W. A., Mechanistic investigation of methylphosphonate synthase, a non-heme iron-dependent oxygenase. *J. Am. Chem. Soc.* **2012,** *134*, 15660–15663.
(82) Brown, P. M.; Caradoc-Davies, T. T.; Dickson, J. M. J.; Cooper, G. J. S.; Loomes, K. M.; Baker, E. N., Crystal structure of a substrate complex of *myo*-inositol oxygenase, a di-iron oxygenase with a key role in inositol metabolism. *Proc. Natl. Acad. Sci. U.S.A.* **2006,** *103*, 15032–15037.
(83) Xing, G.; Hoffart, L. M.; Diao, Y.; Prabhu, K. S.; Arner, R. J.; Reddy, C. C.; Krebs, C.; Bollinger, J. M. Jr., A coupled dinuclear iron cluster that is perturbed by substrate binding in *myo*-inositol oxygenase. *Biochemistry* **2006,** *45*, 5393–5401.
(84) Bollinger, J. M. Jr.; Diao, Y.; Matthews, M. L.; Xing, G.; Krebs, C., *myo*-Inositol oxygenase: A radical new pathway for O_2 and C-H activation at a nonheme diiron cluster. *Dalton T.* **2009,** 905–914.
(85) Naber, N. I.; Swan, J. S.; Hamilton, G. A., L-*myo*-inosose-1 as a probable intermediate in the reaction catalyzed by *myo*-inositol oxygenase. *Biochemistry* **1986,** *25*, 7201–7207.
(86) Pojer, F., CloR, a bifunctional non-heme iron oxygenase involved in clorobiocin biosynthesis. *J. Biol. Chem.* **2003,** *278*, 30661–30668.

(87) Diebold, A. R.; Straganz, G. D.; Solomon, E. I., Spectroscopic and computational studies of α-keto acid binding to Dke1: Understanding the role of the facial triad and the reactivity of α-diketones. *J. Am. Chem. Soc.* **2011,** *133*, 15979–15991.
(88) Di Giuro, C. M. L.; Buongiorno, D.; Leitner, E.; Straganz, G.D., Exploring the catalytic potential of the 3-His mononuclear nonheme Fe(II) center: Discovery and characterization of an unprecedented maltol cleavage activity. *J. Inorg. Biochem.* **2011,** *105*, 1204–1211.
(89) Ward, J. L.; Gaskin, P.; Brown, R.G. S.; Jackson, G. S.; Hedden, P.; Phillips, A. L.; Willis, C. L.; Beale, M. H., Probing the mechanism of loss of carbon-20 in gibberellin biosynthesis. Synthesis of gibberellin 3α,20-hemiacetal and 19,20-lactol analogues and their metabolism by a recombinant GA 20-oxidase. *J. Chem. Soc., Perkin Trans. 2* **2002,** 232–241.
(90) Prescott, A. G.; John, P., Dioxygenases: Molecular structure and role in plant metabolism. *Annu. Rev. Plant Physiol.* **1996,** *47*, 245–271.
(91) MacMillan, J., Biosynthesis of the gibberellin plant hormones. *Nat. Prod. Rep.* **1997,** *14*, 221–243.
(92) Shah, D. D.; Conrad, J. A.; Heinz, B.; Brownlee, J. M.; Moran, G. R., Evidence for the mechanism of hydroxylation by 4-hydroxyphenylpyruvate dioxygenase and hydroxymandelate synthase from intermediate partitioning in active site variants. *Biochemistry* **2011,** *50*, 7694–7704.
(93) Neidig, M. L.; Decker, A.; Choroba, O. W.; Huang, F.; Kavana, M.; Moran, G. R.; Spencer, J. B.; Solomon, E. I., Spectroscopic and electronic structure studies of aromatic electrophilic attack and hydrogen-atom abstraction by non-heme iron enzymes. *Proc. Natl. Acad. Sci. U.S.A.* **2006,** *103*, 12966–12973.
(94) Johnson-Winters, K.; Purpero, V. M.; Kavana, M.; Nelson, T.; Moran, G. R., (4-Hydroxyphenyl)pyruvate dioxygenase from *Streptomyces avermitilis*: The basis for ordered substrate addition. *Biochemistry* **2003,** *42*, 2072–2080.
(95) Johnson-Winters, K.; Purpero, V. M.; Kavana, M.; Moran, G. R., Accumulation of multiple intermediates in the catalytic cycle of (4-hydroxyphenyl)pyruvate dioxygenase from *Streptomyces avermitilis*. *Biochemistry* **2005,** *44*, 7189–7199.
(96) Fritze, I. M., The crystal structures of *Zea mays* and Arabidopsis 4-hydroxyphenylpyruvate dioxygenase. *Plant Physiol.* **2004,** *134*, 1388–1400.
(97) Zhang, Z.; Ren, J.-S.; Clifton, I. J.; Schofield, C. J., Crystal structure and mechanistic implications of 1-aminocyclopropane-1-carboxylic acid oxidase–The ethylene-forming enzyme. *Chem. Biol.* **2004,** *11*, 1383–1394.
(98) Seo, Y. S.; Yoo, A.; Jung, J.; Sung, S.-K.; Yang, D. R.; Kim, W. T.; Lee, W., The active site and substrate-binding mode of 1-aminocyclopropane-1-carboxylate oxidase determined by site-directed mutagenesis and comparative modeling studies. *Biochem. J.* **2004,** *380*, 339–346.
(99) Rocklin, A. M.; Tierney, D. L.; Kofman, V.; Brunhuber, N. M. W.; Hoffman, B. M.; Christoffersen, R. E.; Reich, N. O.; Lipscomb, J. D.; Que, L. Jr., Role of the nonheme Fe(II) center in the biosynthesis of the plant hormone ethylene. *Proc. Natl. Acad. Sci. U.S.A.* **1999,** *96*, 7905–7909.

(100) Rocklin, A. M.; Kato, K.; Liu, H.-W.; Que, L. Jr.; Lipscomb, J. D., Mechanistic studies of 1-aminocyclopropane-1-carboxylic acid oxidase: Single turnover reaction. *J. Biol. Inorg. Chem.* **2004,** *9*, 171–182.
(101) Mirica, L. M.; McCusker, K. P.; Munos, J. W.; Liu, H.-W.; Klinman, J. P., ^{18}O kinetic isotope effects in non-heme iron enzymes: Probing the nature of Fe/O_2 intermediates. *J. Am. Chem. Soc.* **2008,** *130*, 8122–8123.
(102) Mirica, L. M.; Klinman, J. P., The nature of O_2 activation by the ethylene-forming enzyme 1-aminocyclopropane-1-carboxylic acid oxidase. *Proc. Natl. Acad. Sci. U.S.A.* **2008,** *105*, 1814–1819.
(103) Brisson, L.; El Bakkali-Taheri, N.; Giorgi, M.; Fadel, A.; Kaizer, J.; Réglier, M.; Tron, T.; Ajandouz, El H.; Simaan, A. J., 1-Aminocyclopropane-1-carboxylic acid oxidase: Insight into cofactor binding from experimental and theoretical studies. *J. Biol. Inorg. Chem.* **2012,** *17*, 939–949.
(104) Borowski, T.; Blomberg, M. R. A.; Siegbahn, Per E. M., Reaction mechanism of apocarotenoid oxygenase (ACO): A DFT study *Chem. Eur. J.* **2008,** *14*, 2264–2276.
(105) Bassan, A.; Borowski, T.; Schofield, C. J.; Siegbahn, Per E. M., Ethylene biosynthesis by 1-aminocyclopropane-1-carboxylic acid oxidase: A DFT study. *Chem. Eur. J.* **2006,** *12*, 8835–8846.
(106) Baráth, G.; Kaizer, J.; Pap, J. S.; Speier, G.; El Bakkali-Taheri, N.; Simaan, A. J., Bio-inspired amino acid oxidation by a non-heme iron catalyst modeling the action of 1-aminocyclopropane-1-carboxylic acid oxidase. *Chem. Commun.* **2010,** *46*, 7391–7393.
(107) Nagahama, K.; Ogawa, T.; Fujii, T.; Tazaki, M.; Tanase, S.; Morino, Y.; Fukuda, H., Purification and properties of an ethylene-forming enzyme from *Pseudomonas syringae* pv. *phaseolicola* PK2. *J. Gen. Microbiol.* **1991,** *137*, 2281–2286.
(108) Nagahama, K.; Ogawa, T.; Fujii, T.; Tazaki, M.; Goto, M.; Fukuda, H., L-Arginine is essential for the formation in vitro of ethylene by an extract of *Pseudomonas syringae*. *J. Gen. Microbiol.* **1991,** *137*, 1641–1646.
(109) Nazli, Z.; Arshad, M.; Khalid, A., 2-keto-4-methylthiobutyric acid-dependent biosynthesis of ethylene in soil. *Biol. Fert. Soils* **2003,** *37*, 130–135.
(110) Ince, J. E.; Knowles, C. J., Ethylene formation by cell-free extracts of *Escherichia coli*. *Arch. Microbiol.* **1986,** *146*, 151–158.
(111) Fukuda, H.; Takahashi, M.; Fujii, T.; Ogawa, T., Ethylene production from L-methionine by *Cryptococcus albidus*. *J. Ferment. Bioeng.* **1989,** *67*, 173–175.
(112) Primrose, S. B., Evaluation of the role of methional, 2-keto-4-methylthiobutyric acid and peroxidase in ethylene formation by *Escherichia coli*. *J. Gen. Microbiol.* **1977,** *98*, 519–528.
(113) Devore, N. M.; Scott, E. E., Structure of cytochrome p450 17A1 with prostate cancer drugs abiraterone and TOK-001. *Nature* **2012,** *482*, 116–119.
(114) Mukherjee, A.; Angeles-Boza, A. M.; Huff, G. S.; Roth, J. P., Catalytic mechanism of a heme and tyrosyl radical-containing fatty acid α-(di)oxygenase. *J. Am. Chem. Soc.* **2010,** *133*, 227–238.
(115) Huff, G. S.; Doncheva, I. S.; Brinkley, D. W.; Angeles-Boza, A. M.; Mukherjee, A.; Cramer, C. J.; Roth, J. P., Experimental and computational investigations of oxygen

reactivity in a heme and tyrosyl radical-containing fatty acid α-(di)oxygenase. *Biochemistry* **2011,** *50*, 7375–7389.
(116) Gupta, A.; Mukherjee, A.; Matsui, K.; Roth, J. P., Evidence for protein radical-mediated nuclear tunneling in fatty acid α-oxygenase. *J. Am. Chem. Soc.* **2008,** *130*, 11274–11275.
(117) Woo, E. J.; Dunwell, J. M.; Goodenough, P. W.; Marvier, A. C.; Pickersgill, R. W., Germin is a manganese containing homohexamer with oxalate oxidase and superoxide dismutase activities. *Nat. Struct. Biol.* **2000,** *7*.
(118) Svedružić, D.; Jónsson, S.; Toyota, C. G.; Reinhardt, L. A.; Ricagno, S.; Lindqvist, Y.; Richards, N. G. J., The enzymes of oxalate metabolism: Unexpected structures and mechanisms. *Arch. Biochem. Biophys.* **2005,** *433*, 176–192.
(119) Moussatche, P.; Angerhofer, A.; Imaram, W.; Hoffer, E.; Uberto, K.; Brooks, C.; Bruce, C.; Sledge, D.; Richards, N. G. J.; Moomaw, E. W., Characterization of *Ceriporiopsis subvermispora* bicupin oxalate oxidase expressed in *Pichia pastoris*. *Arch. Biochem. Biophys.* **2011,** *509*, 100–107.
(120) Tanner, A.; Bowater, L.; Fairhurst, S. A.; Bornemann, S., Oxalate decarboxylase requires manganese and dioxygen for activity overexpession and characterization of *Bacillus subtilis* YvrK and YoaN. *J. Biol. Chem.* **2001,** *276*, 43627–43634.
(121) Reinhardt, L. A.; Svedruzic, D.; Chang, C. H.; Cleland, W. W.; Richards, N. G. J., Heavy atom isotope effects on the reaction catalyzed by the oxalate decarboxylase from *Bacillus subtilis*. *J. Am. Chem. Soc.* **2003,** *125*, 1244–1252.
(122) Just, V. J., A closed conformation of *Bacillus subtilis* oxalate decarboxylase OxDC provides evidence for the true identity of the active site. *J. Biol. Chem.* **2004,** *279*, 19867–19874.
(123) Sawyer, D. T., *Oxygen Chemistry*. Oxford University Press: New York, 1991.
(124) Bertini, I.; Gray, H. B.; Stiefel, E. I.; Valentine, J. S., *Biological inorganic chemistry: Structure and reactivity*. University Science Books: Sausalito, 2007.
(125) Costas, M.; Mehn, M. P.; Jensen, M P.; Que, L. Jr., Dioxygen activation at mononuclear nonheme iron active sites: Enzymes, models, and intermediates. *Chem. Rev.* **2004,** *104*, 939–986.
(126) O'Brien, J. R.; Schuller, D. J.; Yang, V. S.; Dillard, B. D.; Lanzilotta, W. N., Substrate-induced conformational changes in *Escherichia coli* taurine/α-ketoglutarate dioxygenase and insight into the oligomeric structure. *Biochemistry* **2003,** *42*, 5547–5554.
(127) Stranzl, G. R. Strukturuntersuchungen an Enzymen im Kristall und in Loesung. Karl Franzens University Ph.D. dissertation, Karl Franzens University, 2002.
(128) Kloer, D. P., The structure of a retinal-forming carotenoid oxygenase. *Science* **2005,** *308*, 267–269.
(129) Zhu, X.; Van Pee, K.-H.; Naismith, J. H., The ternary complex of PrnB (the second enzyme in the pyrrolnitrin biosynthesis pathway), tryptophan, and cyanide yields new mechanistic insights into the indoleamine dioxygenase superfamily. *J. Biol. Chem.* **2010,** *285*, 21126–21133.

(130) Fielding, A. J.; Lipscomb, J. D.; Que, L. Jr., Characterization of an O_2 adduct of an active cobalt-substituted extradiol-cleaving catechol dioxygenase. *J. Am. Chem. Soc.* **2012,** *134*, 796–799.
(131) Emerson, J. P.; Kovaleva, E. G.; Farquhar, E. R.; Lipscomb, J. D.; Que, L. Jr., Swapping metals in Fe- and Mn-dependent dioxygenases: Evidence for oxygen activation without a change in metal redox state. *Proc. Natl. Acad. Sci. U.S.A.* **2008,** *105*, 7347–7352.
(132) Ravichandran, K. G.; Boddupalli, S. S.; Hasermann, C. A.; Peterson, J. A.; Deisenhofer, J., Crystal structure of hemoprotein domain of P450M-3, a prototype for microsomal P450's. *Science* **1993,** *261*, 731–736.
(133) Joint Center for Structural Genomics, PDB 2OC5 In *Crystal structure of hypothetical protein (NP_895059.1) from Prochlorococcus marinus MIT9313 at 1.68 A resolution*, RCSB Protein Data Bank: 2006.
(134) Anand, R.; Dorrestein, P. C.; Kinsland, C.; Begley, T. P.; Ealick, S. E., Structure of oxalate decarboxylase from *Bacillus subtilis* at 1.75 Å resolution. *Biochemistry* **2002,** *41*, 7659–7669.
(135) Ohlendorf, D. H.; Lipscomb, J. D.; Weber, P. C., Structure and assembly of protocatechuate 3,4-dioxygenase. *Nature* **1988,** *336*, 403–405.
(136) Brown, C. K.; Vetting, M. W.; Earhart, C. A.; Ohlendorf, D. H., Biophysical analysis of designed and selected mutants of protocatechuate 3,4-dioxygenase. *Annu. Rev. Microbiol.* **2004,** *58*, 555–585.
(137) Paria, S.; Halder, P.; Paine, T. K., Oxidative carbon-carbon bond cleavage of a α-hydroxy ketone by a functional model of 2,4'-dihydroxyacetophenone dioxygenase. *Angew. Chem. Int. Edit.* **2012,** *51*, 6195–6199.
(138) Bauer, I.; Max, N.; Fetzner, S.; Lingens, F., 2,4-Dioxygenases catalyzing N-heterocyclic-ring cleavage and formation of carbon monoxide. *Eur. J. Biochem.* **1996,** *240*, 576–583.
(139) Frerichs-Deeken, U.; Ranguelova, K.; Kappl, R.; Hüttermann, J.; Fetzner, S., Dioxygenases without requirement for cofactors and their chemical model reaction: Compulsory order ternary complex mechanism of 1H-3-hydroxy-4-oxoquinaldine 2,4-dioxygenase involving general base catalysis by histidine 251 and single-electron oxidation of the substrate dianion. *Biochemistry* **2004,** *43*, 14485–14499.
(140) Hart, R. C.; Stempel, K. E.; Boyer, P. D.; Cormier, M. J., Mechanism of the enzyme-catalyzed bioluminescent oxidation of coelenterate-type luciferin. *Biochem. Bioph. Res. Commun.* **1978,** *81*.
(141) Silva, P . J.; Ramos, M. J., A comparative density-functional study of the reaction mechanism of the O_2-dependent coproporphrinogen III oxidase. *Bioorg. Med. Chem.* **2008,** *16*.
(142) Malito, E.; Alfieri, A.; Fraaije, M. W.; Mattevi, A., Crystal structure of a Baeyer-Villiger monooxygenase. *Proc. Natl. Acad. Sci. U.S.A.* **2004,** *101*, 13157–13162.
(143) Sheng, D.; Ballou, D. P.; Massey, V., Mechanistic studies of cyclohexanone monooxygenase: Chemical properties of intermediates involved in catalysis. *Biochemistry* **2001,** *40*, 11156–11167.

(144) Fetzner, S.; Steiner, R., Cofactor-independent oxidases and oxygenases. *Appl. Microbiol. Biot.* **2010,** *86*, 791–804.
(145) Schulz, F.; Leca, F.; Hollmann, F.; Reetz, M. T., Towards practical biocatalytic Baeyer-Villiger reactions: applying a thermostable enzyme in the gram-scale synthesis of optically-active lactones in a two-liquid-phase system. *Beilstein J. Org. Chem.* **2005,** *1*, 10.
(146) Donoghue, Nuala A.; Norris, David B.; Trudgill, Peter W., The purification and properties of cyclohexanone oxygenase from *Nocardia globerula* CL1 and *Acinetobacter* NCIB 9871. *Eur. J. Biochem.* **1976,** *63*, 175–192.
(147) Fetzner, S.; Steiner, R., Cofactor-independent oxidases and oxygenases. *Appl. Microbiol. Biot.* **2012,** *86*, 791–804.
(148) Corina, D. L.; Miller, S. L.; Wright, J. N.; Akhtar, M., The mechanism of cytochrome P-450 dependent C-C bond cleavage: studies on 17α-hydroxylase-17,20-lyase. *J. Am. Chem. Soc.* **1991,** 782–783.
(149) Mbughuni, M.; Chakrabarti, M.; Hayden, J. A.; Meier, K. K.; Dalluge, J. J.; Hendrich, M. P.; Münck, E.; Lipscomb, J. D., Oxy intermediates of homoprotocatechate 2,3-dioxygenase: Facile electron transfer between substrates. *Biochemistry* **2011,** *50*, 10262–10274.
(150) Christian, G. J.; Ye, S.; Neese, F., Oxygen activation in extradiol catecholate dioxygenases - A density functional study. *Chem. Sci.* **2012,** *3*, 1600–1611.
(151) Georgiev, V.; Borowski, T.; Blomberg, M. R. A.; Siegbahn, Per E. M., A comparison of the reaction mechanisms of iron- and manganese-containing 2,3-HPCD: An important spin transition for manganese. *J. Biol. Inorg. Chem.* **2008,** *13*, 929–940.
(152) Pau, M. Y. M.; Davis, M. I.; Orville, A. M.; Lipscomb, J. D.; Solomon, E. I., Spectroscopic and electronic structure study of the enzyme-substrate complex of intradiol dioxygenases: Substrate activation by a high-spin ferric non-heme iron site. *J. Am. Chem. Soc.* **2007,** *129*, 1944–1958.
(153) Geletneky, C.; Berger, S., The mechanism of ozonolysis revisited by ^{17}O NMR spectroscopy. *Eur. J. Org. Chem.* **1998,** *1998*, 1625–1627.
(154) Criegee, Rudolf, Mechanism of ozonolysis. *Angew. Chem. Int. Edit.* **2003,** *14*, 745–752.
(155) Siegbahn, P. E. M.; Haeffner, F., Mechanism for catechol ring-cleavage by non-heme iron extradiol dioxygenases. *J. Am. Chem. Soc.* **2004,** *126*, 8919–8932.
(156) Borowski, T.; Wójcik, A.; Miłaczewska, A.; Georgiev, V.; Blomberg, M. R. A.; Siegbahn, Per E. M., The alkenyl migration mechanism catalyzed by extradiol dioxygenases: A hybrid DFT study. *J. Biol. Inorg. Chem.* **2012,** *17*, 881–890.
(157) Bassan, A.; Borowski, T.; Siegbahn, Per E. M., Quantum chemical studies of dioxygen activation by mononuclear non-heme iron enzymes with the 2-His-1-carboxylate facial triad. *Dalton T.* **2004,** 3153–3162.
(158) Borowski, T.; Georgiev, V.; Siegbahn, Per E. M., On the observation of a gem diol intermediate after O-O bond cleavage by extradiol dioxygenases. A hybrid DFT study. *J. Mol. Model.* **2010,** *16*, 1673–1677.

(159) Borowski, T.; Georgiev, V.; Siegbahn, Per E. M., Catalytic reaction mechanism of homogentisate dioxygenase: A hybrid DFT study. *J. Am. Chem. Soc.* **2005,** *127*, 17303–17314.
(160) Akhtar, M.; Corina, D. L.; Miller, S. L.; Shyadehi, A. Z.; Wright, J. N., Incorporation of label from $^{18}O_2$ into acetate during side-chain cleavage catalysed by cytochrome P-450 17α(17α-hydroxylase-17,20-lyase). *J. Chem. Soc., Perkin Trans 1* **1994,** 263–267.
(161) Mbughuni, M. M.; Meier, K. K.; Münck, E.; Lipscomb, J. D., Substrate-mediated oxygen activation by homoprotocatechuate 2,3-dioxygenase: Intermediates formed by tyrosine 257 variant. *Biochemistry* **2012,** *51*, 8743–8754.
(162) Mbughuni, M. M.; Chakrabarti, M.; Hayden, J. A.; Bominaar, E. L.; Hendrich, M. P.; Münck, E.; Lipscomb, J. D., Trapping and spectroscopic characterization of an Fe(III)-superoxo intermediate from a non-heme mononuclear iron-containing enzyme. *Proc. Natl. Acad. Sci. U.S.A.* **2010,** *107*, 16788–16793.
(163) Kovaleva, E. G.; Lipscomb, J. D., Structural basis for the role of tyrosine 257 of homoprotocatechuate 2,3-dioxygenase in substrate and oxygen activation. *Biochemistry* **2012,** *51*, 8755–8763.
(164) Kovaleva, E. G.; Lipscomb, J. D., Intermediate in the O-O bond cleavage reaction of an extradiol dioxygenase. *Biochemistry* **2008,** *47*, 11168–11170.
(165) Kovaleva, E. G.; Lipscomb, J. D., Crystal structure of Fe(II) dioxygenase superoxo, alkykperoxo, and bound product intermediates. *Science* **2007,** *316*, 453–457.
(166) Groce, S. L.; Miller-Rodeberg, M. A.; Lipscomb, J. D., Single-turnover kinetics of homoprotocatechuate 2,3-dioxygenase. *Biochemistry* **2004,** *43*, 15141–15153.
(167) Groce, S. L.; Lipscomb, J. D., Aromatic ring cleavage by homoprotocatechuate 2,3-dioxygenase: Role of H200 in the kinetics of interconversion of reaction cycle intermediates. *Biochemistry* **2005,** *44*, 7175–7188.
(168) Groce, S. L.; Lipscomb, J. D., Conversion of extradiol aromatic ring-cleaving homoprotocatechuate 2,3-dioxygease into an intradiol cleaving enzyme. *J. Am. Chem. Soc.* **2003,** *125*, 11780–11781.
(169) Fielding, A. J.; Kovaleva, E. G.; Farquhar, E. R.; Lipscomb, J. D.; Que, L. Jr., A hyperactive cobalt-substituted extradiol-cleaving catechol dioxygenase. *J. Biol. Inorg. Chem.* **2011,** *16*, 341–355.
(170) Smith, M. R., The biodegradation of aromatic hydrocarbons by bacteria. *Biodegradation* **1990,** *1*, 191–206.
(171) Orville, A. M.; Lipscomb, J. D., Mechanistic aspects of dihydroxybenzoate dioxygenases. *Met. Ions Biol. Syst.* **1992,** *28*, 243–298.
(172) Fernández-Cañón, J.; Granadino, B.; de Bernabé, D. B.-V.; Renedo, M.; Fernández-Ruiz, E.; Peñalva, M.; de Córdoba, S. R., The molecular basis of alkaptonuria. *Nat. Genet.* **1996,** *14*, 19–24.
(173) Schwarcz, R.; Okuno, E.; White, R. J.; Bird, E. D.; Whetsell, W. O., Jr., 3-Hydroxyanthranilate oxygenase activity is increased in the brains of Huntington disease victums. *Proc. Natl. Acad. Sci. U.S.A.* **1988,** *85*, 4079-4081.

(174) Vetting, M. W.; Wackett, L. P.; Que, L. Jr.; Lipscomb, J. D.; Ohlendorf, D. H., Crystallographic comparison of manganese- and iron-dependent homoprotocatechuate 2,3-dioxygenase. *J. Bacteriol.* **2004,** *186*, 1945–1958.
(175) Miller, M. A.; Lipscomb, J. D., Homoprotocatechuate 2,3-dioxygenase from *Brevibacterium fuscum*: A dioxygenase with catalase activity *J. Biol. Chem.* **1996,** *271*, 5524–5535.
(176) Hegg, E. L.; Que, L. Jr., The 2-His-1-carboxylate facial triad: An emerging structural motif in mononuclear non-heme iron(II) enzymes. *Eur. J. Biochem.* **1997,** *250*, 625–629.
(177) Whiting, A. K.; Boldt, Y. R.; Hendrich, M. P.; Wackett, L. P.; Que, L. Jr., Manganese(II)-dependent extradiol cleaving catechol dioxygenase from *Arthrobacter globiformis* CM-2. *Biochemistry* **1996,** *35*, 160–170.
(178) Bratsch, S. G., Standard electrode potentials and temperature coefficients in water at 298.15 K. *J. Phys. Chem. Ref. Data* **1989,** *18*, 1–21.
(179) Gunderson, W. A.; Zatsman, A. I.; Emerson, J. P.; Farquhar, E. R.; Que, L. Jr.; Lipscomb, J. D.; Hendrich, M. P., EPR detection of intermediates in the enzymatic cycle of an extra dioxygenase. *J. Am. Chem. Soc.* **2008,** *130*, 14465–14467.
(180) Deeth, R. J.; Bugg, T. D. H., A density functional investigation of the extradiol cleavage mechanism in non-heme iron catechol dioxygenases. *J. Biol. Inorg. Chem.* **2003,** *8*, 409–418.
(181) Emerson, J. P.; Wagner, M. L.; Reynolds, M. F.; Que, L. Jr.; Sadowsky, M. J.; Wackett, L. P., The role of histidine 200 in MndD, the Mn(II)-dependent 3,4-dihydroxyphenylacetate 2,3-dioxygenase from *Arthrobacter globiformis* CM-2, a site-directed mutagenesis study. *J. Biol. Inorg. Chem.* **2005,** *10*, 751–760.
(182) Georgiev, V.; Borowski, T.; Siegbahn, Per E. M., Theoretical study of the catalytic reaction mechanism of MndD. *J. Biol. Inorg. Chem.* **2006,** *11*, 571–585.
(183) Koehntop, K. D.; Emerson, J. P.; Que, L. Jr., The 2-his-1-carboxylate facial triad: A versatile platform for dioxygen activation by mononuclear non-heme iron(II) enzymes. *J. Biol. Inorg. Chem.* **2005,** *10*, 83–97.
(184) Vance, C. K.; Miller, A.-F., A simple proposal that can explain the inactivity of metal-substituted superoxide dismutases. *J. Am. Chem. Soc.* **1998,** *120*, 461–467.
(185) Yikilmaz, E.; Porta, J.; Grove, L. E.; Vahedi-Faridi, A.; Bronshteyn, Y.; Brunold, T. C.; Borgstahl, G. E. O.; Miller, A.-F., How can a single second sphere amino acid substitution cause reduction midpoint potential changes of hundreds of millivolts? *J. Am. Chem. Soc.* **2007,** *129*, 9927–9940.
(186) Jackson, T. A.; Brunold, T. C., Combined spectroscopic/computational studies on Fe- and Mn-dependent superoxide dismutases: Insights into second-sphere tuning of active site properties. *Acc. Chem. Res.* **2004,** *37*, 461–470.
(187) Merkens, H.; Kappl, R.; Jakob, R. P.; Schmid, F. X.; Fetzner, S., Quercetinase QueD of *Streptomyces sp*. FLA, a monocupin dioxygenase with a preference for nickel and cobalt. *Biochemistry* **2008,** *47*, 12185–12196.
(188) Groves, J. T., High-valent iron in chemical and biological oxidations. *J. Inorg. Biochem.* **2006,** *100*, 434–447.

(189) Dawson, J. H., Probing structure-function relations in heme-containing oxygenases and peroxidases. *Science* **1988,** *240*, 433–439.
(190) Meunier, B.; Visser, S. P.; Shaik, S., Mechanism of oxidation reactions catalyzed by cytochrome P450 enzymes. *Chem. Rev.* **2004,** *104*, 3947–3980.
(191) Arciero, D. M.; Orville, A. M.; Lipscomb, J. D., [^{17}O]water and nitric oxide binding by protocatechuate 4,5-dioxygenase and catechol 2,3-dioxygenase. Evidence for binding of exogenous ligands to the active site Fe^{+2} of extradiol dioxygenases. *J. Biol. Chem.* **1985,** *260*, 14035–14044.
(192) Arciero, D. M.; Lipscomb, J. D., Binding of ^{17}O-labeled substrate and inhibitors to protocatechuate 4,5-dioxygenase-nitrosyl complex. *J. Biol. Chem.* **1986,** *261*, 2170–2178.
(193) Wang, Y. Z.; Lipscomb, J. D., Cloning, overexpression, and mutagenesis of the gene for homoprotocatechuate 2,3-dioxygenase from *Brevibacterium fuscum Protein. Expr. Purif.* **1997,** *10*, 1–9.
(194) Kabsch, W., Automatic processing of rotation diffraction data from crystals of initially unknown symmetry and cell constants. *J. Appl. Cryst.* **1993,** *26*, 795–800.
(195) Murdhudov, G. N.; Vain, A. A.; Dodson, E. J., Refinement of macromolecular structures by the maximum-likelihood method. *Acta. Cryst.* **1997,** *D53*, 240–255.
(196) Collaborative Computational Project; Number, 4, *Acta. Cryst.* **1994,** *D50*, 760–763.
(197) Emsley, P.; Cowtan, K., Coot: Model-building tools for molecular graphics. *Acta. Cryst.* **2004,** *D60*, 2126–2132.
(198) Horrocks, W. D. Jr.; Ishley, J. N.; Holmquist, B.; Thompson, J. S., Structural and electronic mimics of the active site of cobalt(II)-substituted zinc metalloenzymes. *J. Inorg. Biochem.* **1980,** *12*, 131–141.
(199) Bertini, I.; Luchinat, C., High spin cobalt(II) as a probe for the investigation of metalloproteins. *Adv. Inorg. Biochem.* **1984,** *6*, 71–111.
(200) Sellin, S.; Eriksson, L. E.; Aronsson, A. C.; Mannervik, B., Octahedral metal coordination in the active site of glyoxalase I as evidenced by the properties of Co(II)-glyoxalase I. *J. Biol. Chem.* **1983,** *258*, 2091–2093.
(201) Crawford, P. A.; Yang, K.-W.; Sharma, N.; Bennett, B., Spectroscopic studies on cobalt(II)-substituted metallo-β-lactamase ImiS from *Aeromonas veronii* bv. *sobria*. *Biochemistry* **2005,** *44*, 5168–5176.
(202) Myers, W. K.; Duesler, E. N.; Tierney, D. L., Integrated paramagnetic resonance of high-spin Co(II) in axial symmetry: Chemical separation of dipolar and contact electron-nuclear couplings. *Inorg. Chem.* **2008,** *47*, 6701–6710.
(203) Bencini, A.; Bertini, I.; Canti, G.; Gatteschi, D.; Luchinat, C., The EPR spectra of the inhibitor derivatives of cobalt carbonic anhydrase. *J. Inorg. Biochem.* **1981,** *14*, 81–93.
(204) Bennett, B., EPR of Co(II) as a structural and mechanistic probe of metalloprotein activity sites: Characterization of an amino peptidase. *Curr. Top. Biophys.* **2002,** *26*, 49–57.
(205) Bennett, B.; Holz, R. C., Inhibition of the aminopeptidase from *Aeromonas proteolytica* by L-leucinephosphonic acid, a transition state analogue of peptide hydrolysis. *J. Am. Chem. Soc.* **1998,** *120*, 12139–12140.

(206) Jacobsen, F. E.; Breece, R. M.; Myers, W. K.; Tierney, D. L.; Cohen, S. M., Model complexes of cobalt-substituted matrix metalloproteinases: Tools for inhibitor design. *Inorg. Chem.* **2006,** *45*, 7306–7315.
(207) Farquhar, E. R. Metal substitution studies of an extradiol dioxygenase and X-ray absorption studies of high-valent nonheme iron complexes, In chapter 3 XAS studies of Co(II)-substituted homoprotocatechuate 2,3-dioxygenase and related model complexes. University of Minnesota Ph.D. dissertation, University of Minnesota, **2010**.
(208) Zang, J. H.; Kurtz, D. M. Jr.; Maroney, M. J.; Whitehead, J. P., Metal substitutions at the diiron site of hemerythrin. A dicoblat(II) derivative. *Inorg. Chem.* **1992,** *31*.
(209) Leitch, S.; Bradley, M. J.; Rowe, J. L.; Chivers, P. T.; Maroney, M. J., Nickel-specific response in the transcription regulator, *Escherichia coli* NikR. *J. Am. Chem. Soc.* **2007,** *129*, 5085–5095.
(210) Iwig, J. S.; Leitch, S.; Herbst, R. W.; Maroney, M. J.; Chivers, P. T., Ni(II) and Co(II) sensing by *Escherichia coli* RcnR. *J. Am. Chem. Soc.* **2008,** *130*, 7592–7606.
(211) della Longa, S. ; Bianconi, A.; Palladino, L.; Simonelli, B.; Congiu Castellano, A.; Borghi, E.; Barteri, M.; Beltramini, M.; Rocco, G. P.; Salvato, B.; Bubacco, L.; Magliozzo, R. S.; Peisach, J., An X-ray absorption near edge structure spectroscopy study of metal coordination in Co(II)-substituted *Carcinus maenas* hemocyanin. *Biophys. J.* **1993,** *65*, 2680–2691.
(212) Sato, N.; Uragami, Y.; Nishizaki, T.; Takahashi, Y.; Sazaki, G.; Sugimoto, K.; Nonaka, T.; Masai, E.; Fukuda, M.; Senda, T., Crystal structures of the reaction intermediate and its homologue of an extradiol-cleaving catecholic dioxygenase. *J. Mol. Biol.* **2002,** *321*, 621–636.
(213) Vaillancourt, F. H.; Barbosa, C. J.; Spiro, T. G.; Bolin, J. T.; Blades, M. W.; Turner, R. F. B.; Eltis, L. D., Definitive evidence for monoanionic binding of 2,3-dihydroxybiphenyl to 2,3-dihydroxybiphenyl 1,2-dioxygenase from UV resonance Raman spectroscopy, UV/Vis absorption spectroscopy, and crystallography. *J. Am. Chem. Soc.* **2002,** *124*, 2485–2496.
(214) Shu, L.; Chiou, Y. M.; Orville, A. M.; Miller, M. A.; Lipscomb, J. D.; Que, L .Jr., X-ray absorption spectroscopic studies of the Fe(II) active site of catechol 2,3-dioxygenase. *Biochemistry* **1995,** *34*, 6649–6659.
(215) Uragami, Y.; Senda, T.; Sugimoto, K.; Sato, N.; Nagarajan, V.; Masai, E.; Fukuda, M.; Mitsui, Y., Crystal structure of substrate free and complex forms of reactivated BphC, an extradiol type ring-cleavage dioxygenase. *J. Inorg. Biochem.* **2001,** *83*, 269–279.
(216) Price, J. C.; Barr, E. W.; Tirupati, B.; Bollinger, J. M. Jr.; Krebs, C., The first direct characterization of a high-valent iron intermediate in the reaction of an alpha-ketogluterate-dependent dioxygenase: A high-spin Fe(IV) complex in taurine/alpha-ketogluterate dioxygenase (TauD) from *Escherichia coli*. *Biochemistry* **2003,** *42*, 7497–508.
(217) Kalliri, E.; Grzyska, P. K.; Hausinger, R. P., Kinetic and spectroscpoic investigation of Co(II), Ni(II), and N-oxalylglycine inhibition of the Fe(II)/alpha-ketoglutarate dioxygenase, TauD. *Biochem. Bioph. Res. Co.* **2005,** *338*, 191–197.

(218) Segel, I. H., *Enzyme kinetics: Behavior and analysis of rapid equilibrium and steady-state enzyme systems*. Wiley-Interscience New York, 1993.
(219) Northrop, D. B., On the meaning of K_M and V/K in enzyme kinetics. *J. Chem. Ed.* **1998,** *75*, 1153–1157.
(220) Weiss, M. S., *J. Appl. Cryst.* **2001,** *34*, 130–135.
(221) *CRC Handbook of Chemistry and Physics*. 76th ed.; Boca Raton, FL, 1995.
(222) Kuzumic, P., Program DYNAFIT for the analysis of enzyme kinetic data application to HIV proteinase. *Anal. Biochem.* **1996,** *237*, 260–273.
(223) Lee, S-K.; Lipscomb, J. D., Oxygen activation catalyzed by methane monooxygenase hydoxylase component: Protein delivery during the O-O bond cleavage steps. *Biochemistry* **1999,** *38*, 4423–4432.
(224) Aasa, R.; Vanngard, T., EPR signal intensity and powder shapes: A reexamination. *J. Magn. Reson.* **1975,** *19*, 308–315.
(225) Niswander, R. H.; Taylor, L. T., ESR studies of cobalt dioxygen complexes containing pentadentate schiff base ligands. *J. Magn. Reson.* **1977,** *26*, 491–503.
(226) Smith, T. D.; Pilbrow, J. R., Recent developments in the studies of molecular oxygen adducts of cobalt (II) compounds and related systems. *Coord. Chem. Rev.* **1981,** *39*, 295–383.
(227) Jones, R. D.; Summerville, D. A.; Basolo, F., Synthetic oxygen carriers related to biological systems. *Chem. Rev.* **1979,** *79*, 139–179.
(228) Hoffman, B. M.; Damon, L. D.; Basolo, F., Electron paramagnetic resonance studies of some cobalt(II) schiff base compounds and their monomeric adducts. *J. Am. Chem. Soc.* **1970,** *92*, 61–65.
(229) Tovrog, B. S.; Kitko, D. J.; Drago, R. S., Nature of the bound O_2 in a series of cobalt dioxygen adducts. *J. Am. Chem. Soc.* **1976,** *98*, 5144–5153.
(230) Chien, J. C. W.; Dickinson, L. C., Electron paramagnetic resonance of single crystal oxycobaltmyoglobin and deoxycobaltmyoglobin. *Proc. Natl. Acad. Sci. U.S.A.* **1972,** *69*, 2783–2787.
(231) Dickinson, L. C.; Chien, J. C. W., Electron paramagnetic resonance crystallography of ^{17}O-enriched oxycobaltomyoglobin: Stereoelectronic structure of the cobalt dioxygen system. *Proc. Natl. Acad. Sci. U.S.A.* **1980,** *77*, 1235–1239.
(232) Hoffman, B. M.; Szymanski, T.; Basolo, F., Consideration of a report on the formulation of monomeric cobalt-dioxygen adducts. Continued support for Co(III)-O_2^-. *J. Am. Chem. Soc.* **1975,** *97*, 673–674.
(233) Tovrog, B. S.; Drago, R. S., Evidence against the O_2^- formulation of cobalt(II) adducts of dioxygen. *J. Am. Chem. Soc.* **1974,** *96*, 6765–6766.
(234) Ochiai, E.-I., Electronic structure and oxygenation of bis(salicylaldehyde)ethylenediimino cobalt(II). *J. Inorg. Nucl. Chem.* **1973,** *35*, 1727–1739.
(235) Dogutan, D. K.; Stoian, S. A.; McGuire, R. Jr.; Schwalbe, M.; Teets, T. S.; Nocera, D. G., Hangman corroles: Efficient synthesis and oxygen reaction chemistry. *J. Am. Chem. Soc.* **2010,** *133*, 131–140.

(236) Jorin, E.; Schweiger, A.; Guenthard, H. H., Single-crystal EPR of the oxygen-17-enriched dioxygen adduct of vitamin B12r: Reversible oxygen bonding, electronic and geometric structure and molecular dynamics. *J. Am. Chem. Soc.* **1983,** *105*, 4277–4286.
(237) Carter, M. J.; Rillema, D. P.; Basolo, F., Oxygen carrier and redox properties of some neutral cobalt chelates. Axial and in-plane ligand effects. *J. Am. Chem. Soc.* **1974,** *96*, 392–400.
(238) Getz, D.; Melamud, E.; Silver, B. L.; Dori, Z., Electronic structure of dioxygen in cobalt(II) oxygen carriers, singlet oxygen or O_2^-? *J. Am. Chem. Soc.* **1975,** *97*, 3846–3847.
(239) Rodley, G. A.; Robinson, W. T., Structure of a monomeric oxygen-carrying complex. *Nature* **1972,** *235*, 438–439.
(240) Basolo, F.; Pearson, R. G., *Mechanisms of inorganic reactions: A study of metal complexes in solution*. 2nd ed.; Wiley: New York, 1967; Chapter 6.
(241) Davis, M .I.; Wasinger, E. C.; Decker, A.; Pau, M. Y. M.; Vaillancourt, H. F.; Bolin, J. T.; Eltis, L. D.; Hedman, B.; Hodgson, K. O.; Solomon, E. I., Spectroscopic and electronic structural studies of 2,3-dihydroxybiphenyl 1,2-dioxygenase: O_2 reactivity of the non-heme ferrous site in extradiol dioxygenases. *J. Am. Chem. Soc.* **2003,** *125*, 11214–11227.
(242) Cornard, J-P.; Rasmiwetti; C., Merlinm J., Molecular structure and spectroscopic properties of 4-nitrocatechol at different pH: UV-Visible, Raman, DFT and TD-DFT calculations. *Chem. Phys.* **2005,** *309*, 239–249.
(243) Perrin, D. D.; Dempsey, B.; Serjeant, E. P., *pK_a prediction for organic acids and bases*. Chapman and Hall: London, 1981.
(244) Tyson, C., Nitrocatechol as a colorimetric probe for non-heme iron dioxygenases. *J. Biol. Chem.* **1975,** *5*, 1765–1770.
(245) Reynolds, M. F.; Costas, M.; Ito, M.; Jo, D.-H.; Tipton, A. A.; Whiting, A. K.; Que, L. Jr., 4-nitro catechol as a probe of Mn(II)dependent extradiol-cleaving catechol dioxygenase (MndD): Comparison with relevant Fe(II) and Mn(II) model complexes. *J. Biol. Inorg. Chem.* **2003,** *8*, 263–272.
(246) Que, L. Jr.; Widom, J.; Crawford, R. L., 3,4-Dihydroxyphenylacetate 2,3-dioxygenase. *J. Biol. Chem.* **1981,** *256*, 10941–10944.
(247) Hayden, J. A. Oxygen reactivity of manganese proteins. Ph.D. dissertation, Carnegie Mellon University, **2011**.
(248) Yam, K. C.; Addison, C. J.; Farquhar, E. R.; Mbughuni, M. M.; Fielding, A. J.; Lipscomb, J. D.; Blades, M. W.; Que, L. Jr.; Turner, R. F. B.; Eltis, L. D., Characterization of catechol binding by metal-substituted extradiol dioxygenases. *unpublished manuscript*
(249) Muñoz, P.; Huenchugula, S.; Paris, I.; Segura-Aguilar, J., Dopamine oxidation and autophagy. *Parkinson's Disease* **2012,** *2012*, 1–13.
(250) Adams, D. M.; Dei, A.; Rheingold, A. L.; Hendrickson, D. N., Bistability in the $[Co^{II}(semiquinonate)_2]$ to $[Co^{III}(catecholate)(semiquinonate)]$ valence-tautomeric conversion. *J. Am. Chem. Soc.* **1993,** *115*, 8221–8829.

(251) Arzberger, S.; Soper, J.; Anderson, O. P.; la Cour, A.; Wicholas, M., Synthesis and structure of an air-stable, free-radical cobalt(III) semiquinone complex. *Inorg. Chem.* **1999,** *38*, 757–761.
(252) Beni, A.; Dei, A.; Laschi, S.; Rizzitano, M.; Sorace, L., Tuning the charge distribution and photoswitchable properties of cobalt-dioxolene complexes by using molecular techniques. *Chem. Eur. J.* **2008,** *14*, 1804–1813.
(253) Bianchini, C.; Masi, D.; Mealli, C.; Meli, A.; Martini, G.; Laschi, F.; Zanello, P., Comprehensive experimental and interpretational study of the complex formation and transformations involving *o*-quinoid molecules and an L_3M-type metal fragment (M = cobalt). *Inorg. Chem.* **1987,** *26*, 3683–3693.
(254) Buchanan, R. M.; Pierpont, C. G., Tautomeric catecholate-semiquinone interconversion via metal-ligand electron transfer. Structural, spectral, and magnetic properties of (3,5-di-*tert*-butylcatecholato) 3,5-di-*tert*-butylsemiquinone)(bipyridyl) cobalt(III), a complex containing mixed-valence organic ligands. *J. Am. Chem. Soc.* **1980,** *102*, 4951–4957.
(255) Jung, O.-S.; Pierpont, C. G., Bistability and low-energy electron transfer in cobalt complexes containing catecholate and semiquinone ligands. *Inorg. Chem.* **1994,** *33*, 2227–2235.
(256) Mialane, P.; Anxolabréhère-Mallart, E.; Blondin, G.; Nivorojkine, A.; Guilhem, J.; Tchertanova, L.; Cesario, M.; Ravi, N.; E., Bominaar; Girerd, J.-J.; Münck, E., Structure and electronic properties of (N,N'-bis(methyl-6-tert-butyl-2-2methyl-phenolato)-N,N'-bismethyl-1,2-diaminoethane)Fe^{III}(DBSQ). Spectroelectrochemical study of the red-ox properties. Relevance to intradiol catechol dioxygenases. *Inorg. Chim. Acta* **1997,** *263*, 367–378.
(257) Pierpont, C. G., Studies on charge distribution and valence tautomerism in transition metal complexes of catecholate and semiquinonate ligands. *Coord. Chem. Rev.* **2001,** *216*, 99–125.
(258) Pierpont, C. G., Ligand redox activity and mixed valency in first-row transition-metal complexes containing tetrachlorocatecholate and radical tetrachlorosemiquinonate ligands. *Inorg. Chem.* **2011,** *50*, 9766–9772.
(259) Ruf, M.; Noll, B. C.; Groner, M. D.; Yee, G. T.; Pierpont, C. G., Pocket semiquinonate complexes of cobalt(II), copper(II), and zinc(II) prepared with the hydrotris(cumenylmethylpyrazolyl)borate ligand. *Inorg. Chem.* **1997,** *36*, 4860–4865.
(260) Land, E. J.; Ramsden, C. A.; Riley, P. A.; Stratford, M. R. L., Studies of *para*-quinomethane formation during the tyrosinase-catalyzed oxidation of 4-alkylcatechols. *Arch. Org. Chem.* **2008,** *2*, 258–267.
(261) Vaillancourt, F. H.; Labbé, G.; Drouin, N. M.; Fortin, P. D.; Eltis, L. D., The mechanism-based inactivation of 2,3-dihydroxybiphenyl 1,2-dioxygenase by catecholic substrates. *J. Biol. Chem.* **2002,** *277*, 2019–2027.
(262) Ishida, T.; Tanaka, H.; Horiike, K., Quantitative structure-activity relationship for the cleavage of C3/C4-substituted catechols by a prototypal extradiol catechol dioxygenase with broad substrate specificity. *J. Biochem.* **2004,** *135*, 721–730.

(263) Dai, S.; Vaillancourt, F. H.; Maarouf, H.; Drouin, N. M.; Neau, D. B.; Snieckus, V. S.; Bolin, J. T.; Eltis, L. D., Identification and analysis of a bottleneck in PCB biodegradation. *Nat. Struct. Biol.* **2002,** *9*, 934–939.
(264) Anslyn, E. V.; Dougherty, D. A., Energy Surfaces and Kinetic Analyses. In *Modern Physical Organic Chemistry*, University Science Books: Sausalito, CA, 2006; pp 355–419.
(265) Kovaleva, E. G., Private communication regarding substrate binding orientation of 4XC to H200N-HPCD mutants. **2013**.
(266) Stegmann, H. B.; Deuschle, G.; Schuler, P., Synthesis and EPR investigations of fluorocatecholamines. *J. Chem. Soc., Perkin Trans 2* **1994,** *3*, 547–555.
(267) Bubnov, M. P.; Teplova, K. A.; Kozhanov, G. A.; Abakumov, G. A.; Cherkasov, V. K., *o*-Semiquinonato and *o*-iminosemiquinonato rhodium complexes. EPR study of the reactions in coordination sphere of rhodium *J. Magn. Reson.* **2011,** *209*, 149–155.
(268) Abakumov, G. A.; Abakumova, L. G.; Cherkasov, V. K.; Nevodchikov, V. I., Fluorinated 3,6-di-tert-butyl-*o*-benzoquinones. *ChemInform* **1991,** *22*, 984–986.
(269) Wicklund, P. A.; Brown, D. G., Preparation and properties of a stable semiquinone complex. *Inorg. Chem.* **1976,** *15*, 396–399.
(270) Kessel, S. L.; Emberson, R. M.; Debrunner, P. G.; Hendrickson, D. N., Iron(III), manganese(III), and cobalt(III) complexes with single chelating *o*-semiquinone ligands. *Inorg. Chem.* **1980,** *19*, 1170–1178.
(271) Benelli, C.; Dei, A.; Gatteschi, D.; Pardi, L, Redox potentials and charge transfer spectra of catecholate and semiquinone adducts of a cobalt-tetraazamacrocyclic complex. *Inorg. Chim. Acta* **1989,** *163*, 99–104.
(272) Niswander, R. H.; Taylor, L. T., Characterization of isolable dioxygen cobalt complexes containing linear pentadentate ligands. *J. Am. Chem. Soc.* **1977,** *99*, 5935–5939.
(273) Hagen, W.R., Biomolecular EPR spectroscopy. In CRC Press: Boca Raton, Fl, USA, 2009.
(274) Rakhimov, R. R.; Prokof'ev, A. I.; Bah, R.; Pegram, S. A.; Hwang, J. S.; Khodak, A. A.; Alexandrov, I. A.; Aleksandrov, A. I., Dechlorination of diphenyl chlorophosphate with tin and sodium 3,6-di-tert-butyl-ortho-semiquinones. *Inorg. Chim. Acta* **2007,** *360*, 3033–39.
(275) Barfield, M.; Babaqi, A. S.; Doddrell, D. M.; Gottlieb, H. P. W., Semiempirical molecular orbital calculations of anisotropic ^{1}H, ^{13}C and ^{19}F hyperfine coupling constants in hydrocarbon and fluorocarbon radicals. *Mol. Phys.* **1981,** *42*, 153–164.
(276) Fessenden, R. W.; Schuler, R. H., ESR spectra and structure of the fluorinated methyl radicals. *J. Chem. Phys.* **1965,** *43*, 2704–2712.
(277) Goldschleger, I. U.; Akimov, A. V.; Misochko, E. Ya.; Wright, C. A., Infrared and EPR spectroscopic studies of 2-C_2H_2F and 1-C_2H_2F radicals isolated in solid argon. *J. Mol. Spectrosc.* **2001,** *205*, 269–279.
(278) Hirsh, D. J.; Brudvig, G. W., Measuring distance in proteins by saturation-recovery EPR. *Nat. Protoc.* **2007,** *2*, 1770–1781.
(279) Brown, D. G.; Hemphill, W. D., Cobalt(III) *o*-semiquinone complexes. *Inorg. Chem.* **1979,** *18*, 2039–2040.

(280) Wicklund, P. A.; Beckmann, L. S.; Brown, D. G., Preparation and properties of a stable semiquinone complex. *Inorg. Chem.* **1976,** *15*, 1996–1997.
(281) Farquhar, E. R.; Emerson, J. P.; Koehntop, K. D.; Reynolds, M. F.; Trmcic, M.; Que, L., Jr., In vivo self-hydroxylation of an Fe-substituted manganese dependent extradiol dioxygenase. *J. Biol. Inorg. Chem.* **2011,** *16*, 589–597.
(282) Stallings, M. D.; Morrison, M. M.; Sawyer, D. T., Redox chemistry of metal-catechol complexes in aprotic media. Electrochemistry of substituted catechols and their oxidation products. *Inorg. Chem.* **1981,** *20*, 2655–2660.
(283) Hartl, F.; Stufkens, D. J.; Vlcek, A. Jr., *Inorg. Chem.* **1992,** *31*, 1687–1695.
(284) Stufkens, D. J.; Snoeck, T. L.; Lever, A. B. P., Semiquinone-quinone redox species involving bis(bipyridine)ruthenium: Resonance Raman spectra. *Inorg. Chem.* **1988,** *27*, 953–956.
(285) Haga, M.; Dodsworth, E. S.; Lever, A. B. P., Catechol-quinone redox series involving bis(bipyridine)ruthenium(II) and tetrakis(pyridine)ruthenium(II). *Inorg. Chem.* **1986,** *25*
447–453.
(286) Lever, A. B. P.; Auburn, P. R.; Dodsworth, E. S.; Haga, M.; Liu, W.; Melnik, M.; Nevin, A., Bis(dioxolene)(bipyridine)ruthenium redox series. *J. Am. Chem. Soc.* **1988,** *110*, 8076–8084.
(287) Verma, P.; Weir, J.; Mirica, L. M.; Stack, T. D. P., Tale of a twist: Magnetic and optical switching in copper(II) semiquinone complexes. *Inorg. Chem.* **2011,** *50*, 9816–9825.
(288) Hartl, F.; Stufkens, D. J.; Vlcek, A. Jr., *Inorg. Chem.* **1991,** *30*, 3048–3053.
(289) Op't Holt, B. T.; Vance, M. A.; Mirica, L. M.; Heppner, D. E.; Stack, T. D. P.; Solomon, E. I., Reaction coordinate of a functional model of tyrosinase: Spectroscopic and computational characterization. *J. Am. Chem. Soc.* **2009,** *131*, 6421-6438.
(290) Dei, A.; Feis, A.; Poneti, G.; Sorace, L., Thermodynamics of valence tautomeric interconversion in a tetrachlorodioxolene:cobalt 1:1 adduct. *Inorg. Chim. Acta* **2008,** *361*, 3842–3846.
(291) Caneschi, A.; Dei, A.; Gatteschi, D.; Tangoulis, V., Antiferromagnetic coupling in a six-coordinate high-spin cobalt(II)-semiquinone complex. *Inorg. Chem.* **2002,** *41*, 3508–3512.
(292) Benelli, C.; Dei, A.; Gatteschi, D.; Pardi, L., Electronic and CD spectra of catecholate and semiquinonate adducts of zinc(II) and nickel(II) tetraaza macrocyclic complexes. *Inorg. Chem.* **1989,** *28*, 1476–1480.
(293) Benelli, C.; Dei, A.; Gatteschi, D.; Pardi, L., Synthesis, redox behavior, magnetic properties, and crystal structures of a nickel(II)-semiquinone adduct with an unusually strong ferromagnetic coupling. *Inorg. Chem.* **1988,** *27*, 2831–2836.
(294) Dei, A.; Pardi, L., Electronic structure of dioxolene adducts of rhodium(III) tetraazacmacrocyclic complexes. *Inorg. Chim. Acta* **1991,** *181*, 3–5.
(295) Stratford, M. R. L.; Riley, P. A.; Ramsden, C. A., Rapid halogen substitution and dibenzodioxin formation during tyrosinase-catalyzed oxidation of 4-halocatechols. *Chem. Res. Toxicol.* **2011,** *24*, 350–356.

(296) Peiken, W. A.; Kozarich, J. W., Selective synthesis and hydrolysis of dimethyl *cis, cis*-3-halomuconates. *J. Org. Chem.* **1989,** *54*, 510–512.
(297) Luzhkov, V. B., Theoretical study of deuterium kinetic isotope effect in peroxidation of phenol and toluene. *Chem. Phys.* **2005,** *320*, 1–8.
(298) Howard, J. A.; Ingold, K. U., The inhibited autoxidation of styrene: Part II. The relative inhibiting efficiencies of meta- and para-substituted phenols. *Can. J. Chem.* **1963,** *41*, 1744–1751.
(299) Koshino, N.; Saha, B.; Espenson, J. H., Kinetic study of the phthalimide *N*-oxyl radical in acetic acid. Hydrogen abstraction from substituted toluenes, benzaldehydes, and benzyl alcohols. *J. Org. Chem.* **2003,** *68*, 9364–9370.
(300) Heistand, R. H. II; Lauffer, R. B.; Fikrig, E.; Que, L. Jr., Catecholate and phenolate iron complexes as models for the dioxygenases. *J. Am. Chem. Soc.* **1982,** *104*, 2789–2796.
(301) Oldenberg, P. D.; Shteinman, A. A.; Que, L. Jr., Iron-catalyzed olefin *cis*-dihydroxylation using a bio-inspired N,N,O-ligand. *J. Am. Chem. Soc.* **2005,** *127*, 15672–73.
(302) Bajdor, K.; Nakamoto, K., Resonance Raman spectra of molecular oxygen adducts of Co(salen) and its derivatives in solution. *Inorg. Chim. Acta* **1984,** *82*.
(303) Bajdor, K.; Oshio, H.; Nakamoto, K., Resonance Raman spectra of dioxygen adducts of Co(salen) derivatives containing pendant oxygen donors. *Inorg. Chim. Acta* **1985,** *103*.
(304) Crumbliss, A. L.; Basolo, F., Monomeric oxygen adducts of N, N'-ethylenebis(acetylacetoneiminato) ligand cobalt(II). Preparations and properties. *J. Am. Chem. Soc.* **1970,** *92*, 55–65.
(305) Drago, R. S.; Corden, B. B., Spin-pairing model of dioxygen binding and its application to various transition-metal systems as well as hemoglobin cooperativity. *Acc. Chem. Res.* **1980,** *13*, 353–360.
(306) Kanda, W.; Okawa, H.; Kida, S., Synthesis and spectra of Co(salen) derivatives containing pendant groups and their dioxygen adducts. Pendent chain length and coordinating ability. *Inorg. Chim. Acta* **1988,** *146*, 193–198.
(307) Hartl, F.; Vlcek, A. Jr., Bonding properties of the 1,2-semiquione radical-anionic ligand in the $[M(CO)_{4-n}(L)_n(DBSQ)]$ complexes (M = Re, Mn; DBSQ = 3,5-di-*tert*-butyl-1,2-benzosemiquione; n = 0, 1, 2). A comprehensive spectroscopic (UV-Vis and IR absorption, resonance Raman, EPR) and electrochemical study. *Inorg. Chem.* **1996,** *35*, 1257–1265.
(308) Lynch, M. W.; Valentine, M.; Hendrickson, D. N., Mixed-valence semiquinone-catecholate-iron complexes. *J. Am. Chem. Soc.* **1982,** *104*, 6982–6989.
(309) Pein, B. C.; Seong, N.-H.; Dlott, D. D., Vibrational energy relaxation of liquid aryl-halides $X\text{-}C_6H_5$ (X = F, Cl, Br, I). *J. Phys. Chem. A* **2010,** *114*, 10500–10507.
(310) Shaikh, N.; Goswami, S.; Panja, A.; Sun, H. L.; Pan, F.; Gao, S.; Banerjee, P., Syntheses, crystal structures, and spectroscopic and magnetic properties of $[Mn_2^{III}(H_2L_1)(Cl_4Cat)4H_2O]$ and $[Mn_2^{III}(H_2L_2)(Cl_4Cat)_4\ 2CH_3CN\ 2H_2O]$: Temperature-dependent valence tautomerism in solution. *Inorg. Chem.* **2005,** *44*, 9714–9722.

(311) Cox, D. D.; Benkovic, S. J.; Bloom, L. M.; Bradley, F. C.; Nelson, M. J.; Que, L. Jr.; Wallick, D. E., Catecholate LMCT bands as probes for the active sites of nonheme iron oxygenases. *J. Am. Chem. Soc.* **1988,** *110*, 2026–2032.
(312) Michaud-Soret, I.; Anderson, K. K.; Que, L. Jr.; Haavik, J., Resonance Raman studies of catecholate and phenolate complexes of recombinant human tyrosine hydroxylase. *Biochemistry* **1995,** *34*, 5504–5510.
(313) Ryle, M. J.; Liu, A.; Muthukumaran, R. B.; Ho, R. Y. N.; Koehntop, K. D.; McCracken, J.; Que, L. Jr.; Hausinger, R. P., O_2- and alpha-ketogluterate-dependent tyrosyl radical formation in TauD, an alpha-keto acid-dependent non-heme iron dioxygenase. *Biochemistry* **2003,** *42*, 1854–1862.
(314) Smith, J. J.; Thomson, A. J.; Proudfoot, A. E.; Wells, T. N., Identification of an Fe(III)-dihydroxyphenylalanine site in recombinant phosphomannose isomerase from *Candida albicans*. *Eur. J. Biochem.* **1997,** *244*, 325–333.